DOT/FAA/TC-24/19

Federal Aviation Administration
William J. Hughes Technical Center
Aviation Research Division
Atlantic City International Airport
New Jersey 08405

Integrated Propulsion and Controls for Rotorcraft – Phase 2

April 2024

Final report

U.S. Department of Transportation
Federal Aviation Administration

NOTICE

This document is disseminated under the sponsorship of the U.S. Department of Transportation in the interest of information exchange. The U.S. Government assumes no liability for the contents or use thereof. The U.S. Government does not endorse products or manufacturers. Trade or manufacturers' names appear herein solely because they are considered essential to the objective of this report. The findings and conclusions in this report are those of the author(s) and do not necessarily represent the views of the funding agency. This document does not constitute FAA policy. Consult the FAA sponsoring organization listed on the Technical Documentation page as to its use.

This report is available at the Federal Aviation Administration William J. Hughes Technical Center's Full-Text Technical Reports page: actlibrary.tc.faa.gov in Adobe Acrobat portable document format (PDF).

Technical Report Documentation Page

Form DOT F 1700.7 (8-72) Reproduction of completed page authorized

1. Report No.	2. Government Accession No.	3. Recipient's Catalog No.
DOT/FAA/TC-24/19		

4. Title and Subtitle	5. Report Date
Integrated Propulsion and Controls for Rotorcraft – Phase 2	April 2024
	6. Performing Organization Code

7. Author(s)	8. Performing Organization Report No.
Kyle B. Collins, Richard P. Anderson, Richard Prazenica, K. Merve Dogan, Patric Hruswicki, Louis Spier, Shivansh Agrawal, Syed Zuhair Ali Razvi, Eren Sarioglu, Atahan Kurttisi, Xinyu Yang, Cody Kuskie	

9. Performing Organization Name and Address	10. Work Unit No. (TRAIS)
Embry Riddle Aeronautical University (Eagle Flight Research Center) 1 Aerospace Blvd, Daytona Beach, FL, 32114, USA	11. Contract or Grant No. 692M15-23-T-00002

12. Sponsoring Agency Name and Address	13. Type of Report and Period Covered
Federal Aviation Administration (FAA) David Sizoo, Dan Dellmyer, Traci Stadtmueller, Ross Schaller	Final Report (January 2023 – April 2024)
	14. Sponsoring Agency Code

15. Supplementary Notes

This project was initiated and sponsored by David Sizoo and Ross Schaller. It is part of a portfolio of research sponsored by the Flight Test Branch of the FAA's Aircraft Certification Line of Business. These projects have outcomes that enable Advanced Air Mobility Certification by identifying technical issues through hands on experiments. This approach is used to enable policy and flight test techniques to safely certify new technology.

16. Abstract

This technical report documents research conducted by Embry-Riddle Aeronautical University's Eagle Flight Research Center team in Phase 2 of the Integrated Propulsion and Controls for Rotorcraft project. The purpose of this research was to build on the progress made during Phase 1 of the project. This involved developing a hardware-validated flight dynamics simulation to assess different control strategies to fly Mission Task Elements (MTEs) as well as create methodologies that may one day aid and inform specific certification testing at the vehicle level. Methodologies to compute force and moment envelopes for different vehicle configurations were developed and enabled the team to predict potential control challenges, such as situations leading to loss of control. An optimization code was created which tailored control and power outputs to optimize torque, thrust, moment, or noise footprint. A flight test campaign was conducted to characterize each novel control strategy developed within the limitations of the vehicle's capabilities and flying environment.

17. Key Words	18. Distribution Statement
	This document is available to the U.S. public through the National Technical Information Service (NTIS), Springfield, Virginia 22161. This document is also available from the Federal Aviation Administration William J. Hughes Technical Center at actlibrary.tc.faa.gov.

19. Security Classif. (of this report)	20. Security Classif. (of this page)	21. No. of Pages	22. Price
Unclassified	Unclassified	173	Unclassified

Contents

Figures

Tables

Acronyms

Acronym	Definition
AAM	Advanced Air Mobility
AFS	Attainable force set
AMS	Attainable moment set
CCPM	Collective cyclic pitch mixing
CETI	Control equivalent turbulence input
CG	Center of gravity
CIFER	Comprehensive identification from frequency responses
CONDUIT	Control designer's unified interface
DCM	Direction cosine matrix
DEP	Distributed electric propulsion
EFRC	Eagle Flight Research Center
ERAU	Embry-Riddle Aeronautical University
eVTOL	Electric vertical take-off and landing
FAA	Federal Aviation Administration
FBW	Fly-by-wire
FDD	Fault detection and diagnosis
HQTE	Handling qualities task element
IMU	Inertial measurement unit
JIO	Joint input-output
KTAS	Knots true airspeed
LGCAT	Langley Generic Control Allocation Toolbox
LOES	Lower order equivalent system
MMA	Motor mixing algorithm
MTE	Mission task element
NLDI	Nonlinear dynamic inversion
OEI	One engine inoperative
PAVER	Personal air vehicle at Embry-Riddle
PWM	Pulse-width modulation
RCS	Reaction control system
RMS	Required moment set
RPM	Revolutions per minute
RTS	Rotor test stand

SCAS	Stability and control augmentation system
SISO	Single input single output
6DOF	Six degrees of freedom
SVO	Simplified vehicle operations
TVC	Thrust vector control
UAM	Urban air mobility
UAV	Unmanned aerial vehicle
VP1, VP2, VP3	Variable Pitch 1, Variable Pitch 2, Variable Pitch 3

1 Introduction

1.1 Electric vertical take-off and landing enabled by distributed electric propulsion

Distributed electric propulsion (DEP) has increased the design space for aerospace vehicles, specifically the class of vehicles characterized as electric Vertical Take-Off and Landing (eVTOL). This new class of vehicles not only looks different from the typical airplane or helicopter with which the aviation community is familiar, but also functions differently. To certify these aircraft for private and commercial operations, a greater understanding of how the vehicle is controlled in both nominal and off-nominal (or degraded) modes is required. The purpose of the research reported herein is to assess how the various methods of DEP thrust control scale up to the sizes required for the eVTOL mission, in addition to how well the methods perform in both normal and degraded modes of operation.

During Phase 1, the Eagle Flight Research Center (EFRC) developed two quadrotor vehicle testbeds with interchangeable DEP "pods." In addition, the EFRC also developed a rotor test stand (RTS) to characterize the steady forces and moments produced by the rotors. Simulation models were used to predict the forces and moments required to fly the transition from hover to forward flight handling qualities task elements (HQTEs).

The FAA and EFRC collaboration steered research toward the development of HQTE methods to assess fly-by-wire (FBW) eVTOL designs that may serve the urban air mobility (UAM) market in a way similar to how ADS-33 is used for design specifications on the military side (ADS-33E-PRF, 2000). The handling qualities assessment for HQTEs could be used as a means of compliance for certification. Additionally, the HQTE methodology can reduce the number of flight tests required by leveraging frequency and time-response metrics or "artifacts" from a combination of simulation, sub-component testing, and piloted simulation. Given the number and diversity of FBW eVTOL configurations, this HQTE methodology in support of flight test is an area of research interest to the FAA (Schulze, et al., 2020). The Phase 2 research discussed in this report builds on the capabilities and hardware developed during Phase 1 to further this area of knowledge (Collins, et al., 2023).

The results of this research are intended to support a greater understanding of the certification basis and methods of compliance for eVTOL and UAM vehicles that employ DEP for thrust, lift, and control. This research utilized mathematical simulation models and techniques combined with physical testing in the form of a RTS and multirotor flight test vehicles. This research also

focused on increasing the knowledge of the handling qualities certification of FBW eVTOL vehicles through a combination of modeling and simulation combined with experimental studies. Outcomes of this Phase 2 research include the following:

- Prototype multirotor vehicle testbeds
- Validated multirotor vehicle simulation models
- HQTE trajectory simulation
- eVTOL force and moment envelope predictions and displays

Future outcomes in later phases may include the following, to name a few. They are listed here for completeness, and because they are closely related to the problem of handling quality certification of novel, advanced concepts.

- Frequency/time response, stability, and performance flying qualities
- Handling qualities prediction
- Piloted simulation and handling qualities assessment

1.2 Background and motivation

The integration of DEP, digital FBW flight control systems, and autonomous flight control has allowed a new vehicle market to emerge within general aviation. This new market is mostly comprised of eVTOL vehicles. Figure 1 shows two such concepts from Jaunt Air Mobility and Vinati F-Helix. These eVTOL vehicles will have similar design features to conventional VTOL aircraft.

a.

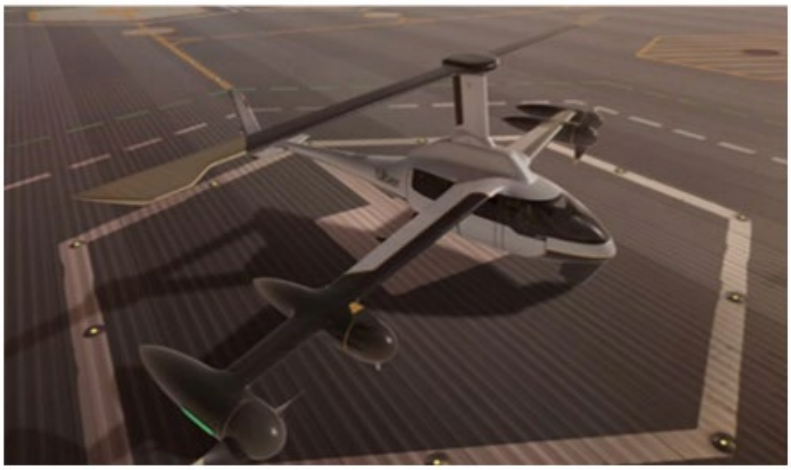

b.

Figure 1. Artistic renditions of the Jaunt Air Mobility slowed rotor compound helicopter (a) and the Vinati F-Helix propeller reaction-driven helicopter eVTOL (b) concepts

(images from https://evtol.news)

Some other new vehicle concepts bear little resemblance at all to a conventional helicopter. Due to the added degree of flexibility offered by DEP and FBW, many concept vehicles incorporate a plurality of rotors and/or propellers in their designs. Some vector the thrust from these rotors to perform lifting functions in hovering and low-speed flight modes and propulsive functions in the cruise flight modes. Some designs use DEP units to lift and other DEP units to provide thrust. Some examples of these unique design configurations can be seen in Figure 2, Figure 3, Figure 4, and Figure 5.

Figure 2. Tiltrotor Joby S4
(image from https://evtol.news)

Figure 3. Multi-rotor Volocopter
(image from https://evtol.news)

Figure 4. Lift and cruise Wisk Cora
(image from https://evtol.news)

Figure 5. Lilium Jet
(image from https://evtol.news)

All four vehicles are currently well into development and flight testing. In addition to these four vehicles, another vehicle well into development is the Helix by Pivotal, shown in Figure 6.

Figure 6. Pivotal Helix
(image from pivotal.aero)

Most UAM and eVTOL concepts utilize multirotors and FBW. While many concepts also use wings for the cruise portion of the flight, they are not needed for hovering or very low-speed flight. However, wings are used since they provide a more efficient forward flight. Nevertheless, wings can provide reasonable means of gliding to a safe landing in the event of a complete power failure from a cruise flight if the wing loading allows. In cases where a complete power failure might prove catastrophic, some vehicles employ ballistic parachutes as an added safety feature. An example of a multirotor vehicle well into development that does not utilize a wing is the EHang vehicle shown in Figure 7.

Figure 7. EHang multirotor vehicle
(image from EHang)

One aspect of multirotor vehicles that may not be immediately noticeable is how the thrust of the DEP units is adjusted. In most cases, the thrust is modified using changes in propeller/rotor revolutions per minute (RPM), which is a simple and reliable method with few moving parts.

However, this strategy has some limitations, such as the inability to produce negative thrust, no capability for producing hub moments, and slower response times as the size of the propeller increases. As the propeller size grows, the thrust response may become slower due to the larger inertia of the propeller and the greater torque required by the electric motor. In fact, there may be a point where this strategy is no longer effective, as the motor size needed to generate the necessary torque to change the RPM of a large propeller becomes too large. Overall, the use of RPM changes to modify thrust is a useful technique, but it has its limitations that should be taken into consideration when designing and operating multirotor vehicles.

Some DEP units use collective pitch control at a fixed RPM to achieve more responsive thrust control. While this strategy is more mechanically complex, with more moving parts, it allows the RPM to be maintained at a desired constant value while changing the thrust through collective pitch changes. Additionally, if the collective pitch control is somehow impaired, thrust can still be controlled through RPM changes in this degraded mode. The FAA has a lot of experience certifying fixed-wing vehicles with constant-speed propellers that use this method. Overall, while the use of collective pitch control at a fixed RPM is more complex, it offers the benefits of more responsive thrust control and the ability to maintain a constant RPM.

A third strategy developed at the EFRC involves the use of both collective and cyclic pitch on a DEP unit with a rotor featuring lead-lag hinges but no flapping hinges. While the use of collective and cyclic pitch itself is not new, as it is commonly used on helicopter rotors, its application on a DEP unit is unique. The added benefit of this strategy over the use of collective pitch alone is that the rigid rotor allows cyclic pitch changes to create significant lateral and longitudinal moments at the rotor hub, which can be used to control the vehicle in addition to using thrust alone on the DEP units. This should result in greater control authority for the vehicle. Additionally, this strategy can provide control moments within a multirotor system, even if one or more DEP units fail, without reducing thrust on the remaining DEP units. Overall, the use of both collective and cyclic pitch of the individual rotors offers the potential for greater control power and increased reliability in multirotor vehicles.

Though there are an ostensibly infinite number of vehicle configurations that can fulfill the role of an air taxi, more effort needs to be spent understanding the performance and safety factors for off-nominal (or degraded) modes of flight. This body of work cannot be ignored if UAM is to truly take hold in the realm of human transportation.

2 Problem statement

To date, over 900 concepts for eVTOL aircraft have been cataloged by the Vertical Flight Society (Vertical Flight Society, 2023). Each has unique propulsion architectures and control strategies. The airworthiness criteria and means of compliance (MOC) to certify these vehicles are still being developed. Current FAR 23/25 and FAR 27/29 rules are inadequate to certify the new UAM vehicles with simplified vehicle operations (SVO) features and vertical takeoff and landing (VTOL) capability.

As the FAA begins to investigate the handling qualities certification of eVTOL aircraft, the challenge is becoming readily apparent. Many of these vehicles have novel architectures with overactuated controls that utilize complex FBW flight control laws. Flight-testing these vehicles must be done systematically and rigorously to uncover any handling qualities inadequacies that may be present in both nominal and degraded flight models. Because of this, the FAA is interested in research that can lead to methods of discovering these handling quality deficiencies prior to flight testing. In addition to increasing the safety of the certification flight testing process, this could significantly reduce the number of flight tests required. The proposed technical approach elements, technical objectives, prototype process, and task presented in this research will provide the FAA with knowledge on how to address this challenging issue.

3 Technical approach

3.1 Component and flight test

The technical approach taken by the team at Embry-Riddle Aeronautical University's (ERAU's) EFRC is best described as building a set of capabilities that allow the team to respond to the fast-paced nature of the eVTOL community with respect to handling qualities certification research. Having already developed several capabilities during Phase 1 research, the team expanded these capabilities to include many of the elements needed to study the handling qualities certification of eVTOL configurations. These elements are shown in Figure 8.

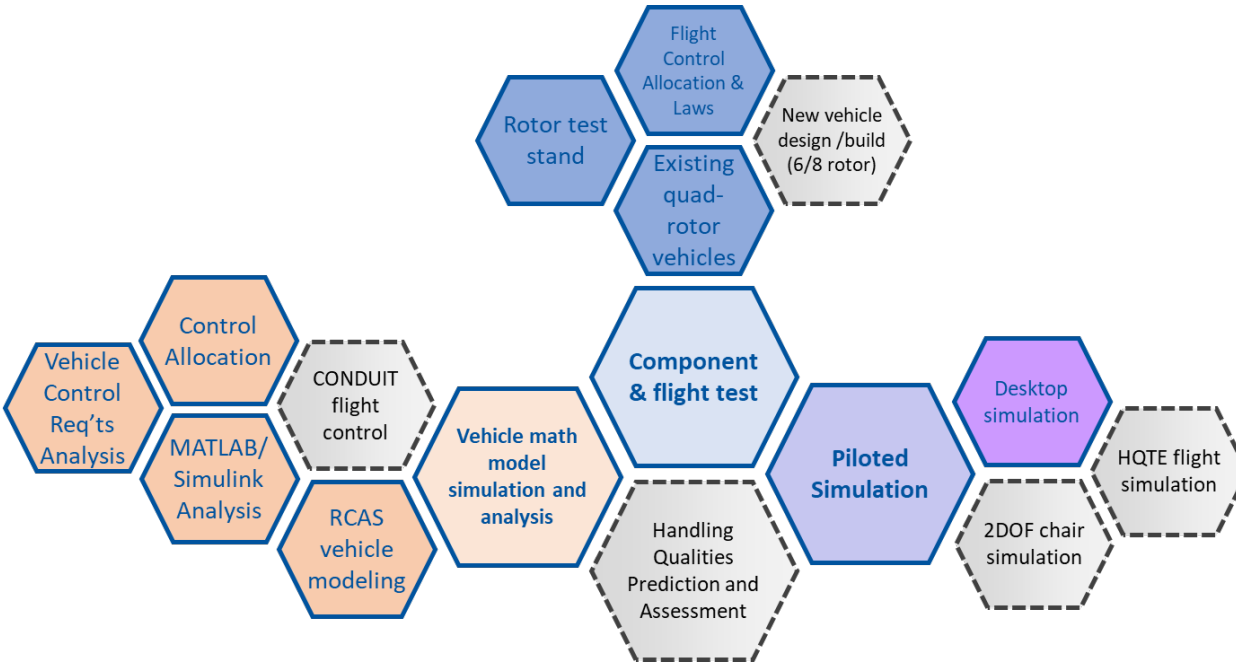

Figure 8. Elements of ERAU's technical approach

These capabilities were utilized to develop methods and processes to analyze the ability of eVTOL configurations to fly specific HQTEs in nominal and degraded modes with various control law implementations. Methods developed employ hardware-validated math models to predict the capability of typical eVTOL configurations to perform a given task (e.g. fly a trajectory or maintain a hover in the event of losing one engine) as well as study the control allocation problem. A method to alert test pilots as they approach the boundaries of an aircraft's flight envelope was also developed, which could help prevent accidents resulting from loss of control. The correlation of the results is expected to provide flight control engineers, flight test engineers, and flight test pilots with knowledge of handling qualities cliffs that might be present in a given scenario. Due to time and budget restrictions, elements in Figure 8 with dashed outlines were deemphasized in Phase 2. The main elements of the technical approach shown in Figure 8 will be described below.

3.2 Vehicle math model simulation and analysis

A major strength of the approach taken by the EFRC team is experimentation with actual hardware. During Phase 1, the team succeeded in building an RTS and two quadrotor test vehicles, as shown in Figure 9. Situated just outside the EFRC building is a large netted "drone cage" that allows the team to conduct hover flight tests of the quadrotor prototypes. While note exercised during this phase, the EFRC has the potential to construct new prototypes (Figure 10

and Figure 11) depending on specific questions that might need to be answered about configurations (e.g., lift and cruise).

Figure 9. Existing quadrotor flight test vehicles

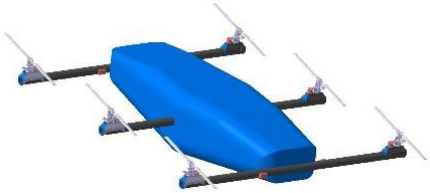

Figure 10. Potential hex-rotor vehicle.

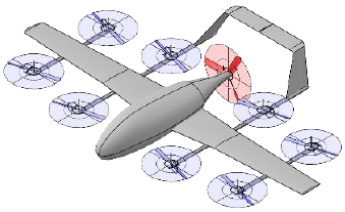

Figure 11. Potential lift and cruise vehicle

During Phase 1, the EFRC team developed rotor models in both MATLAB/Simulink and the Army's RCAS. The MATLAB/Simulink rotor model was integrated into a full six degrees of freedom (6DOF) quadrotor vehicle model in Simulink, as shown in Figure 12 (Collins, et al., 2023). This vehicle model was built generically to easily reconfigure the model to explore six-rotor and eight-rotor configurations.

The RTS has been instrumental in providing the force and moment capability of the rotors used on the quadrotor test vehicles. This data was used to validate mathematical models and simulations. During Phase 2, the team modified the MATLAB/Simulink rotor model to reflect the three-bladed rotors that were installed towards the end of Phase 1 (Collins, et al., 2023). This model was validated using RTS data from the three-bladed rotor.

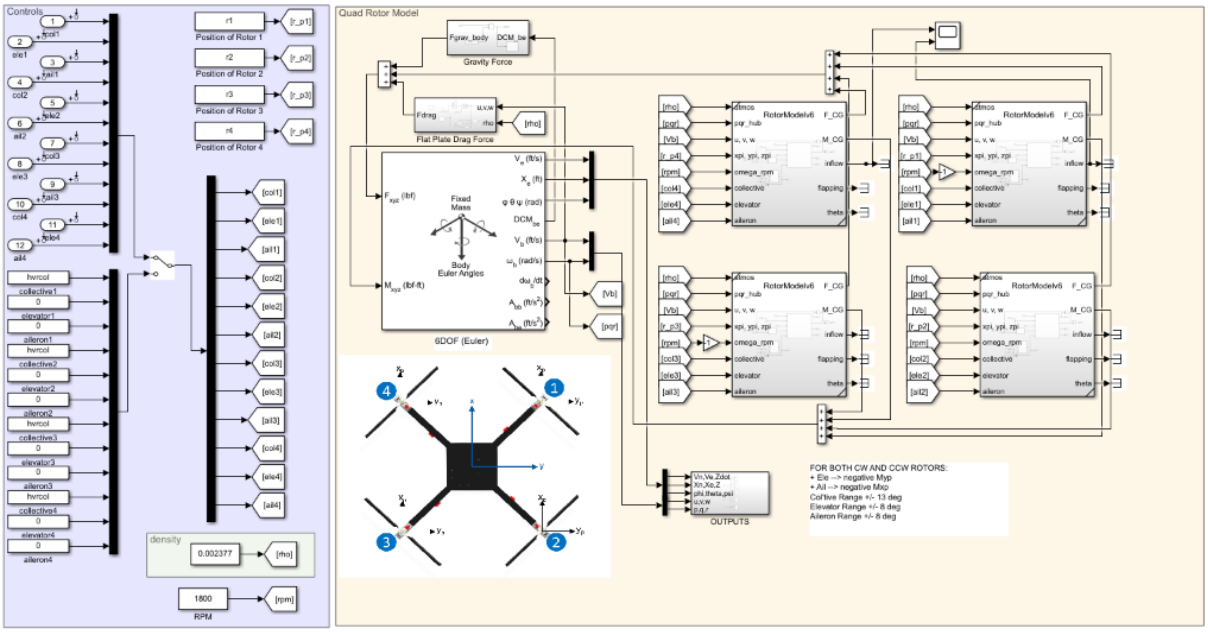

Figure 12. Quadrotor MATLAB/Simulink model developed during Phase 1

The vehicle math models were utilized to perform processes to predict force and moment envelopes of the vehicle, predict the force and moments required to fly a given HQTE, and drive piloted simulation necessary for testing control laws prior to flight test. The math model was also integral in the development of control laws and the allocation of controls for over-actuated systems which are typical of eVTOL concepts. While the flight control law determines forces and moments, control actuator settings are determined through control allocation. Specifically, control allocation improves fault tolerability and modularity of the overall control system while permitting the exploitation of actuator redundancy for improved maneuverability. Unlike the conventional commercial and military airplanes, existing prototypes, and future ideas for eVTOL, urban air mobility vehicles appear in a wide range of actuation configurations and number of actuators. This reality urges a deep investigation of control allocation techniques for overactuated (e.g., redundant) systems. In particular, several topics should be considered in designing control allocation algorithms, such as actuator health, saturation, and failure.

3.3 Handling qualities prediction and assessment

Even though the prediction of handling qualities was de-emphasized during Phase 2, the methodologies developed during Phase 2 were designed with the eventual goal of being used for handling qualities predictions. Efforts were made to obtain certain predictions of handling qualities using these methodologies. For example, the required versus attainable forces and moments prediction methodology can predict when a vehicle would run out of control power

during a given task. The pilot displays methodology could be used to alert pilots to upcoming handling qualities deficiencies (or “cliffs”) which, if exceeded, could result in loss of control.

The EFRC team envisions using methods outlined in ADS-33E as a starting point. Future research will be required to determine the correct HQTEs and metrics for novel eVTOL configurations. Piloted simulation and flight tests could be used to provide feedback on the HQ predictions to determine the flying quality metrics (e.g., Bandwidth and phase delay) and values to best predict flying qualities.

3.4 Piloted simulation

EFRC researchers created a workflow during Phase 1 that allows math model simulation to be integrated into a piloted simulation, as shown in Figure 13 (Collins, et al., 2023). The benefits of this process include control law development and testing as well as HQTE handling qualities evaluation, to name a few. This framework was utilized in Phase 2. Future work could include the creation of a full-scale piloted simulation with a motion chair, monitors, and inceptors to evaluate vehicles on a larger scale.

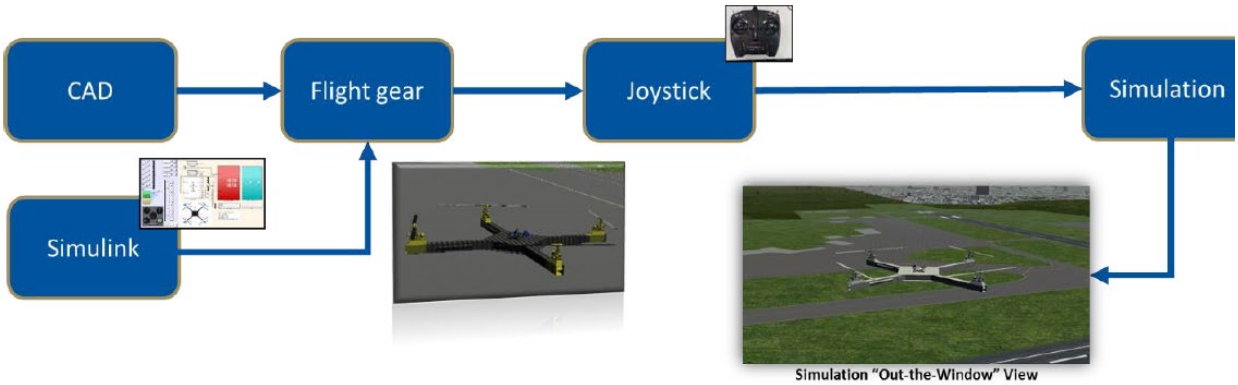

Figure 13. Piloted simulation framework developed during Phase 1

4 Performance of work tasks

4.1 Task A: Literature review

4.1.1 Handling qualities certification

FBW aircraft have several unique challenges associated with handling qualities certification, especially eVTOLs (Klyde D. H., et al., 2020). The FAA and other regulatory agencies already know how to certify FBW airplanes, as illustrated for the many models produced by Boeing, Airbus, Dassault, Gulfstream, Embraer, and Bombardier. Since the existing rules (i.e. 14 CFR Part 25) did not account for advanced FBW technology, all of these certifications required a

"patch" called a *special condition*. Due to the wide variety of eVTOL concepts being developed, utilizing special conditions for each individual design would make the certification processes very onerous and time consuming. Consequently, an alternative means to certify FBW aircraft without requiring special conditions for every single design would be beneficial. The authors propose a mission-oriented approach for FBW eVTOL certification. In a mission-oriented approach to aircraft handling qualities, means of compliance are based in part on realistic mission task elements (MTEs) (Klyde D. H., et al., 2020). MTEs and HQTEs are flight test maneuvers designed to represent the full range of tasks an aircraft is expected to perform throughout its mission and to expose any handling qualities cliffs.

The authors of this paper also make a distinction between flying qualities and handling qualities. Historically, these terms have often been used interchangeably. For the engineering community, there is typically no recognized difference between the two. To some, however, these two terms have begun to take on different meanings. *Flying qualities* is taken to mean those analytical and empirical parameters or criteria that can be measured for a given airplane (Klyde D. H., et al., 2020). All such parameters or criteria can be related to the demands the pilot places on the airplane to achieve desired performance. That is, they are *open-loop* metrics describing *pilot-in-the-loop* operations (Klyde D. H., et al., 2020). Examples include metrics such as Aircraft Bandwidth and Phase Delay as defined in ADS-33E-PRF (United States Army, 2000) and elsewhere. By contrast, *handing qualities* is meant to describe operations while the pilot is actively in the loop. This includes the definition put forth by Cooper and Harper: "Those qualities or characteristics of an aircraft that govern the ease and precision with which a pilot is able to perform the tasks required in support of an aircraft role" (Cooper & Harper, 1986). In this context, the *flying qualities* criteria are measures from which *handling qualities* of the airplane are quantified. By this definition, the criteria of ADS-33E-PRF and the fixed-wing military standard MIL-STD-1797B (United States Department of Defense, 2004) are flying qualities criteria, and the MTEs are handling qualities maneuvers (Klyde D. H., et al., 2020).

As illustrated in Figure 14, the Part 23 requirements can be divided between flying qualities and handling qualities requirements using the above descriptions. It should be noted that there will be some overlap in requirements shown in Figure 14. For example, 23.2145 Stability appears on both lists, since airplane stability must be displayed via both open- and closed-loop pilot-vehicle system maneuvering (Klyde D. H., et al., 2020).

Figure 14. Mission task elements as a means of compliance

The work of Mitchell, Klyde, Shubert, Sizoo, and Schaller (2022) discusses many of the same certification challenges introduced by Klyde D.H., et al. (2020) but discusses certain aspects of the handling qualities certification process for eVTOLs in greater detail. For example, differences between military and civil aircraft certification rules as well as flight simulator hardware and math model development are discussed. It also contains a list of recommended steps for eVTOL certification as well as considerations for formal requirements. This paper assumes a revolutionary change in certification methods requiring major steps in research and development to generate the necessary advisory circular(s).

4.1.2 Vehicle attainable force and moment predictions

Force and moment envelopes, more commonly referred to throughout literature as attainable force sets (AFS) and attainable moment sets (AMS), are graphical representations of the forces and moments that can be attained by a vehicle's effectors at any given state. These can be used for a variety of purposes, such as allocating an aircraft's flight controls, optimizing vehicle configurations by determining how to install the effectors to generate the required forces and moments, and determining whether a vehicle configuration possesses sufficient control authority to perform a required task. A method for calculating the AMS for overactuated vehicles is introduced by Durham (1993). This paper uses the example of an airplane with three effectors (aileron, horizontal tail, and rudder) to generate rolling and yawing moment, and it serves as the basis for most other literature discussing attainable force and moment sets. A modified version of this methodology was used to generate the force and moment envelopes for PAVER.

Durham's methodology is used to generate the AMS of vehicles where the moments produced by the effectors vary linearly with effector position. There are many cases for which this assumption can be made. However, for certain effector types, the forces and moments resulting from their

deflection can be highly nonlinear. One example would be the use of elevons often found on the trailing edge of delta wings to generate yawing moment. Bolender and Doman (2004) introduce a methodology that can be used to accurately compute these attainable moment sets for nonlinear effectors.

The work of Söpper, Zhang, & Holzapfel (2021) discusses the use of attainable moment sets to optimize the installation angles of an eight-rotor eVTOL aircraft to ensure sufficient control authority to perform required mission tasks (Figure 15 and Figure 16). While the purpose of the work discussed in Task D is not to use attainable moment sets to guide the configuration design of a vehicle and instead to evaluate a fixed configuration, the work presented in this paper could be considered for optimizing the design of HQTEs to be used in Advanced Air Mobility (AAM) certification.

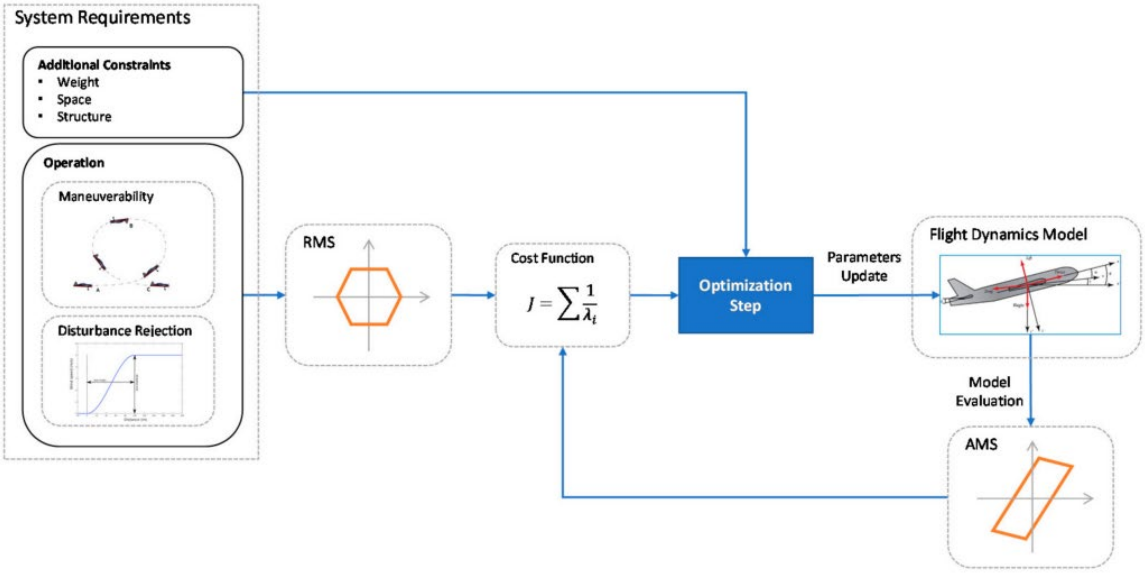

Figure 15. Workflow overview of the optimization framework proposed by Söpper, Zhang, & Holzapfel

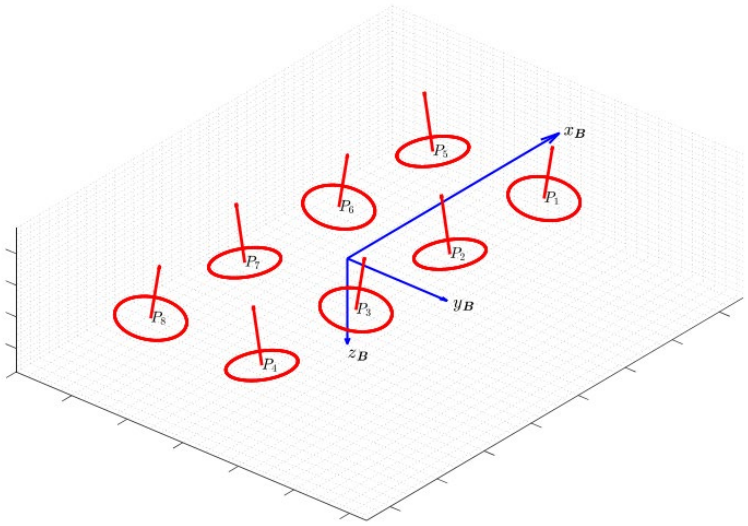

Figure 16. eVTOL propeller arrangement three-dimensional view

The work of Söpper, Zhang, Bähr, & Holzapfel (2021) introduces a methodology to develop the RMS, which describe the moments required to fulfill mission objectives, as shown in Figure 17. The RMS is comprised of the disturbance moment set and the maneuver moment set. The disturbance moment set accounts for the aerodynamic forces and moments required to overcome disturbances such as turbulence, wind gusts, and center gravity shifts. The maneuver moment set accounts for required system accelerations from top-level requirements, such as performing a given task or flying a given trajectory. These can then be compared with the AMS of a given vehicle configuration to assess its capability to fulfill mission objectives. The RMS of a system is inherent from the prescribed requirements, while the AMS can be optimized by configuring effectors. To guarantee the ability of mission fulfillment, the AMS should maximally enclose the RMS from a design point of view, which is therefore the optimization goal.

The first methodology introduced in Task D makes a comparison between the required and attainable forces and moments of a vehicle to perform a given task but calculates the attainable forces and moments using a different method that involves time simulation. The work described in Task D also attempts to extract handling qualities predictions from these comparisons of attainable forces and moments, unlike the other literature that discusses the development of the AMS and the RMS.

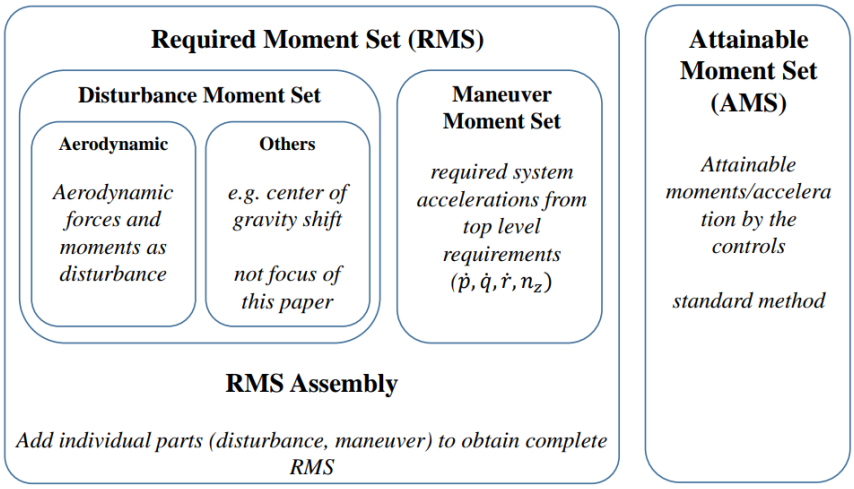

Figure 17. Overview of required and attainable moment sets and the proposed methods for obtaining the required moment set

The work of Pei, et al. (2018) introduces a program created at NASA Langley Research Center called the Generic Control Allocation Toolbox (LGCAT) in which users can quickly generate the AFS and AMS for any vehicle configuration they specify using a combination of effector types. Effector types available to the user include aerodynamic surfaces, reaction control system (RCS) thrusters, aircraft propellers/rotors, and thrust vector control. This provides the vehicle designer with quick insights into the force and moment capability of their configurations and is intended to reduce the number of iterations required in the vehicle preliminary design process. This code uses the methodology introduced in Constrained Control Allocation (Durham, 1993) to generate the AFS and AMS. Figure 19 shows how the AMS of the GL-10 eVTOL concept vehicle (shown in Figure 18 (Rothlaar, et al., 2014)) changes with the loss of the far-left rotor on the port side wing in hover flight. This results in the vehicle losing a significant amount of roll control.

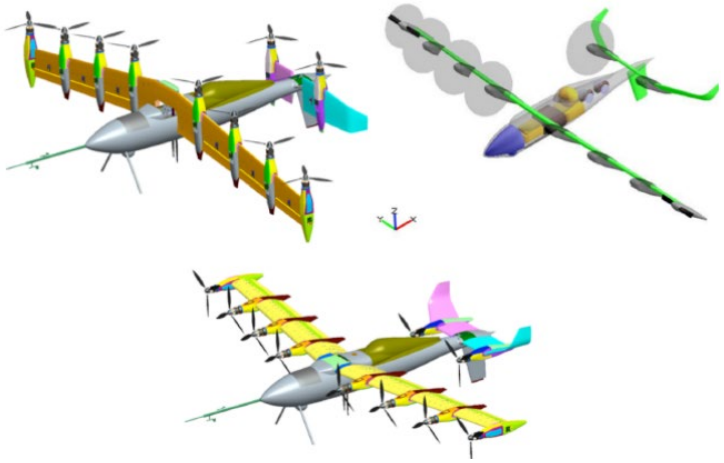

Figure 18. GL-10 modes of operation: hover, transition, and cruise (Rothlaar, et al., 2014)

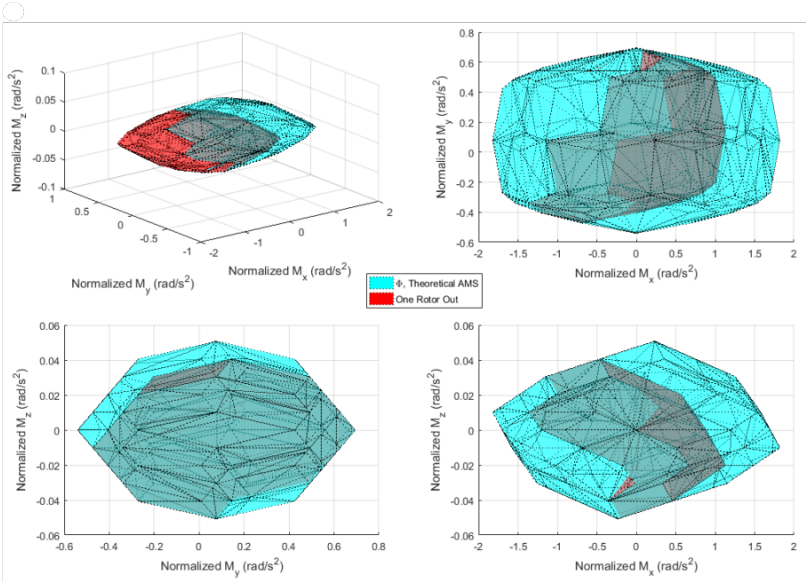

Figure 19. AMS for GL-10 Hover Mode, nominal (blue) vs. one rotor out (red)

The work of McKillip, Jr., et al. (2023) presents a method on how to use control power margin for certifying DEP aircraft. Remaining control power margin (RCP) is calculated by summing together the control power required to trim the vehicle, maneuver the vehicle, and withstand in-flight disturbances, as shown in Figure 20 (McKillip, Jr., et al., 2023).

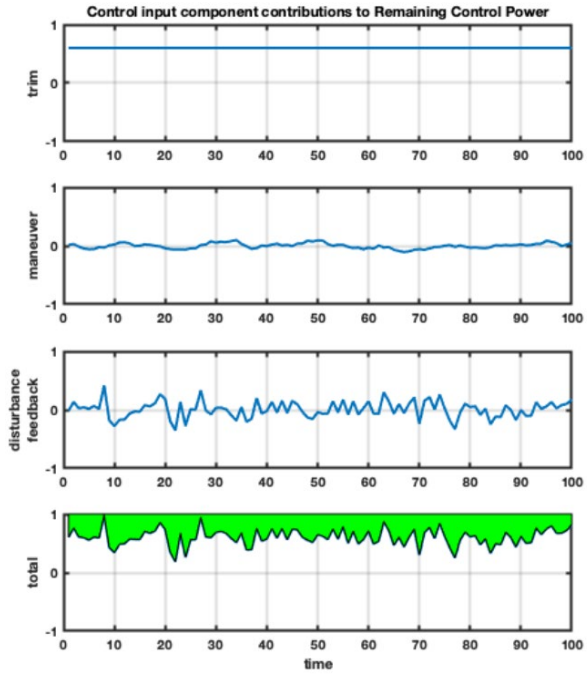

Figure 20. Contributions of control power input sources to remaining control power (highlighted in green)

RCP may be an indicator of the capability of the vehicle to accommodate operational disturbances and avoid loss of control (LOC) events. The second methodology introduced in Task D computes the control power available for a fixed-wing airplane in longitudinal motion using the wind-axis force and moment derivative equations, the engine thrust model, air data measurements, and known information about the airplane such as the maximum and minimum lift coefficients. This information is then displayed in a manner designed to provide pilots with an intuitive feel of where their airplane is located within the flight envelope and alerts them if they approach a stall or are about to overspeed the airplane. Aspects of this research could potentially be used in combination with the second methodology introduced in Task D to develop a system that alerts pilots to upcoming handling qualities cliffs.

4.1.3 Nonlinear dynamic inversion and control allocation

A key component for the stability of an overactuated aerial vehicle is the allocation operation of the desired virtual control input to vehicle effectors. During the flight, the quadcopter's performance is highly dependent on the flight control law. Researchers in *Position and attitude control of multi-rotor aerial vehicles: A survey* (Nascimento & Saska, 2019) provide an extensive survey for existing control approaches for quadcopters.

One of the powerful methods is the adaptive dynamic inversion in series feedback with nonlinear controllers (Lavretsky & Wise, 2013; Wise, et al., 1999; Das, Subbarao, & Lewis, 2009). In

general, the dynamic inversion requires the selection of the control variables to obtain the stable internal dynamics, or the internal dynamics of the linearized feedback system are stabilized by using a nominal control algorithm. Moreover, dynamic inversion technique is used for many systems that can be modeled precisely and plays a vital role for obtaining nominal (i.e., desired) control laws (Kurttisi, Perera, & Dogan, 2023). To ensure stable and safe flight, these desired control inputs should be produced and actualized by the effectors of the vehicle. Thus, control allocation plays a crucial part in guaranteeing this and assuring vehicles perform how the flight controller requires.

For a fly-by-wire multirotor system, the control allocation section acts like a digital swashplate to distribute each rotor speed command to maintain these four virtual control inputs. In (Johansen & Fossen, 2013), several linear control allocation techniques are introduced for nominal and off-nominal conditions like effector saturation for over-actuated systems. In (Dikmen, Arisoy, & Temeltas, 2009; Luukkonen, 2011), linear control allocation techniques are revealed for a quadrotor system using the lift and drag coefficients of a rotor. In Hexacopter Flight Performance Comparison with CCA vs. WCA Control Allocation (Ducard & Kryenbühl, 2020), Experimental Results on Dynamic Attitude Control Allocation for a Hexarotor Platform with Faulty Motors (Jaramillo, et al., 2022), and Control allocation for fault tolerant control of a VTOL octorotor (Marks, Whidborne, & Yamamoto, 2012), classical control allocation methods are expanded to dynamic control allocation techniques, which provide more control for off-nominal conditions like rotor degradation and faults for variable RPM multirotors. Although several control allocation approaches exist for nominal and off-nominal conditions using variable RPM mixing, few studies have been conducted on both collective and variable RPM control. Combining these two effectors can result in a higher force and moment envelope in the aspect of the control authority of the vehicle. Recently in Hover Dynamics & Flight Control of a UAM-Scale Quadcopter with Hybrid RPM & Collective Pitch Control (Walter A. , McKay, Niemiec, & and Gandhi, 2022), a hybrid control mixing method is introduced which splits frequency content of the virtual control using a complementary filter.

4.1.4 Frequency domain system identification

System identification is a versatile process for rapidly and efficiently extracting accurate dynamic models of an aircraft from the measured response to control inputs. This is used in many applications such as wind-tunnel vs flight measurement comparison, piloted simulation models, validation of physics-based models, etc. Modern FBW aircraft use system identification in their flight-vehicle development process, as this provides information regarding system performance and helps the life cycle of development from design to flight test.

The system identification method proposed by Mark Tischler (2017) is employed for this research as seen in Figure 21. The dynamic model is defined as the relation between the control inputs and the vehicle dynamic response. These models are simple input-to-output relations for a set of differential equations of motion.

An example of an input-to-output system is that of a helicopter, as seen in Figure 21, where the inputs are the lateral cyclic, longitudinal cyclic, pedal, and collective with the outputs as 14 states (Tischler, et al., 2017). The system, or black box, can be identified by excitation of the system dynamics by performing frequency sweeps and doublets. This method is known as *system identification*.

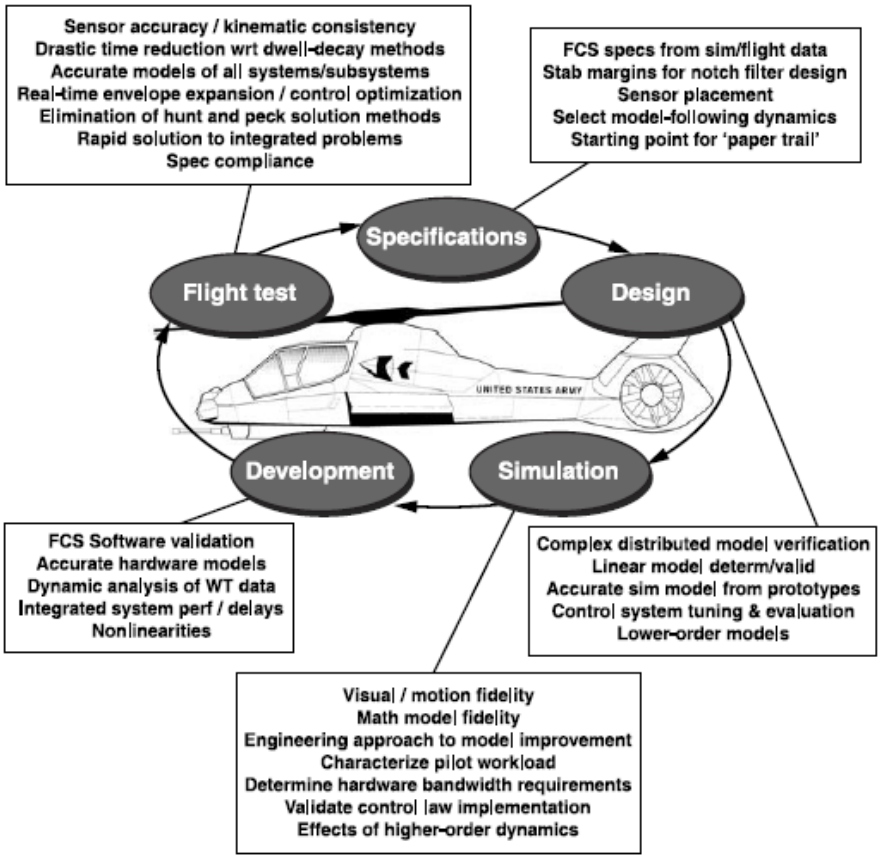

Figure 21. Roles of system identification in flight-vehicle development process

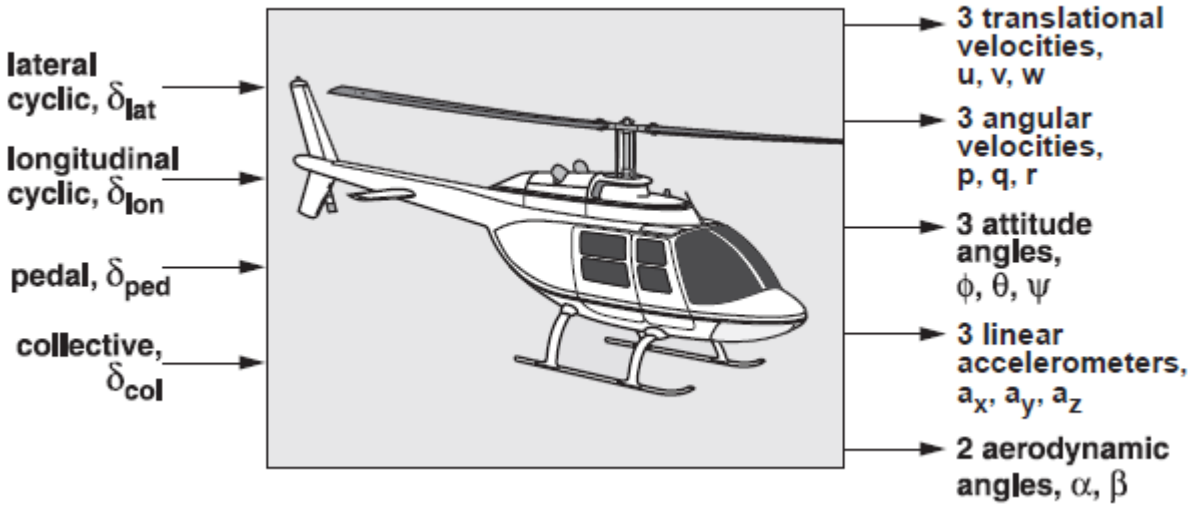

Figure 22. Input-output system of a helicopter

A good representation of a model is a transfer function model as seen in the equation below, where the numerator coefficients (b0, b1…) and denominator coefficients (a1, a2…) are determined, along with the equivalent time delay 'τ_{eq}' as given in Equation 1.

$$T(S) = \frac{(b_0 s^m + b_1 s^{m-1} + \cdots + b_m)e^{-\tau_{eq}s}}{(s^n + a_1 s^{n-1} + \cdots + a_n)} \qquad 1$$

The frequency response method is characterized by several steps, as seen in Figure 23 (Tischler, et al., 2017). First, the time history data is taken, which excites the vehicle dynamics such as doublets or frequency sweeps. Then the data is checked for consistency and errors and is reconstructed. The frequency response is then generated using FRESPID within CIFER. Depending on the problem, a single input single output (SISO) or multi input single input (MISO) analysis is performed. This method of the input-to-output process as a function of frequency is defined as *spectral analysis*.

A sweep is a time history of a sine wave with increasing frequency. This sweep can be injected either manually by the pilot or automatically through computer computer-generated sweep.

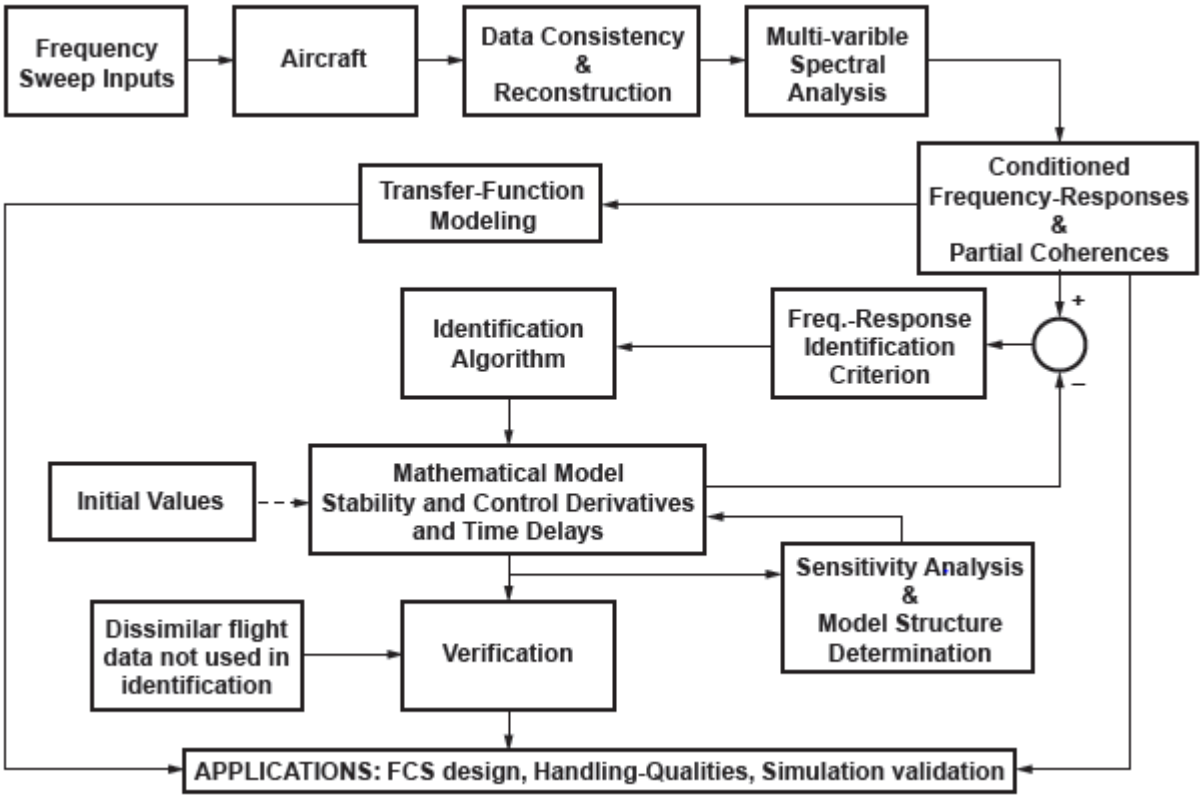

Figure 23. Flowchart of frequency-response method

4.1.5 State-space model identification

A state-space model is a mathematical representation of the system as a set of inputs and outputs. Identifying a state-space model through system identification allows for a complete dynamic representation of the system, often referred to as a *bare-airframe model*. These models are useful for designing simulation models and for system validation and troubleshooting. Other applications include handling qualities analysis and disturbance rejection analysis.

This identification utilizes the frequency responses from FRESPID and the low-order transfer function model of the system. The state-space model is expressed in terms of the stability and control derivatives of the system. The identification method through CIFER is used to identify linear time-invariant (LTI) models for any dynamic system.

An example case provided by Tischer & Remple (2012) shows the formulation of the state-space model structure from the first-order differential equations of motions. The unknown parameters in the equations are the stability and control derivatives. The initial guesses for the derivatives

were taken from previously obtained transfer function identification results. The obtained state-space model is then verified for its utility and robustness by using dissimilar flight data.

The equations of motions used in CIFER are in the following form:

$$M\dot{x} = Fx + Gu(t - \tau) \quad (2)$$

$$y = H_0 x + H_1 \dot{x} \quad (3)$$

The matrices *M*, *F*, *G* contain model parameters to be identified. The vector τ defines the equivalent delay. The matrices H_0 and H_1 in the measurement matrix y are composed of known constants such as unit conversions, gravity, and kinematics. The H_1 matrix contains simple kinematic relationship parameters for accelerometer measurements.

Once these matrices have been identified, the state-space model can be expressed as,

$$\dot{x} = Ax + Bu(t - \tau) \quad (4)$$

$$y = Cx + Du(t - \tau) \quad (5)$$

Where,

$$\mathrm{A} = \mathrm{M}^{-1}\mathrm{F} \quad (6)$$

$$B = M^{-1}G \quad (7)$$

$$C = H_0 + H_1 M^{-1} F \quad (8)$$

$$D = H_1 M^{-1} G \quad (9)$$

Where *x* is the number of states, *u* is the control vector, *A* and *B* are the state and control matrices, and *C* and *D* are the output matrices.

The bare airframe dynamics, ideally, is obtained with the SCAS-off. However, in cases where the vehicle is unstable in SCAS-off mode, having the SCAS-on is required, preferably with the gains reduced and the control surface deflections measured. This is due to SCAS typically suppressing much of low-frequency pilot inputs, resulting in a low signal-to-noise ratio in the data and degradation of identification accuracy at low frequencies.

In the case of SCAS-on, the control surface inputs are the mixer inputs — that is, the combination of pilot inputs and SCAS output — as seen in the block diagram in Figure 24 (Tischler, et al., 2017). One limitation of the closed loop identification is the cross-correlation of inputs. This could degrade the off-axis response identification. Another limitation is the potential feedback of disturbance response to the control input signals. The excitation signals will be partially correlated with the disturbance response such as turbulence or noise.

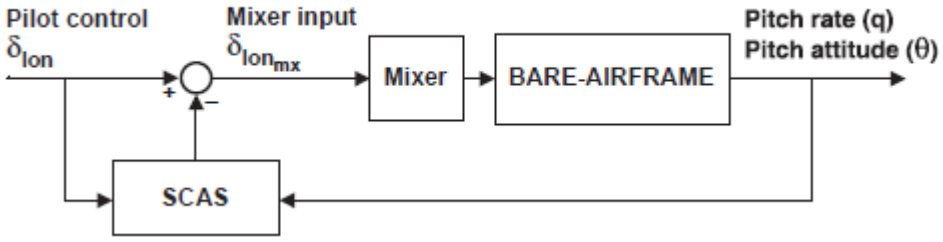

Figure 24. Example of closed-loop schematic diagram for a helicopter pitch SCAS

The transfer function identification performed for this research using CIFER is based on the lower order equivalent system (LOES). A complete rotorcraft or eVTOL dynamics for a bare-airframe system typically consists of many states. However, the overall end-to-end frequency response can be well characterized over the frequency range of interest by a simple LOES transfer function composed of only a few dominant modes. This LOES system provides a very accurate representation of the system response despite its simplicity, and they constitute a fully satisfactory end result of identification. For a LOES model identification, the recording of control surface deflections is not required. Only the measured states and pilot control inputs are sufficient. Thus, a lower order transfer function is an efficient method to obtain a satisfactory model of minimum complexity.

A transfer function can be represented by Equation 10. The poles are displayed in terms of the damping ratio and natural frequency as given by the equation below.

$$[\zeta, \omega_n] = [s^2 + 2\zeta\omega_n s + \omega_n^2] \qquad 10$$

A LOES transfer function typically has an order n of four or less for fixed-wing applications and 10 or more for helicopter applications. When the ultimate application of the model is for handling qualities analysis, the model structure should be a classical lower order equivalent system form (Tischler, et al., 2017).

The frequency range for this should be restricted to the range over which the coherence function is satisfactory ($\gamma_{xy}^2 \geq 0.6$). The transfer function models must be accurate for frequencies near the crossover frequency ω_c, generally $0.3\omega_c$ to $3.0\omega_c$. This will ensure the key characteristics are accurately modeled. A typical LOES transfer function will be in the form of an equation:

$$\frac{q}{\delta_{lon}}(s) = s\left(\frac{k(s+a)e^{-\tau_{eq}s}}{s[\zeta, \omega_n]}\right) \qquad 11$$

A cost function *J* of the transfer function is calculated, which numerically optimizes the magnitude and phase errors between the SISO transfer function model and the associated frequency response estimate (i.e., data). As a guideline, a cost function generally reflects an acceptable level of accuracy for flight dynamics modeling. If $J \leq 50$, the model is nearly indistinguishable from the flight data in the frequency domain and time domain. If $J \leq 100$, the model fit is satisfactory.

4.2 Task B: Develop and enhance existing rotor math models.

The rotor math model used in the PAVER flight dynamics model, shown in Figure 25 and Figure 26, calculates forces, moments, inflow, and flapping angles as a function of atmospheric pressure (atmos), hub angular rates (pqr_hub), hub velocity (u, v, w), hub position with respect to vehicle center of gravity (CG) (xpi, ypi, zpi), rotor RPM, and control inputs ($\theta_0, \theta_{1c}, \theta_{1s}$). Aside from RPM, there are three control inputs that control the blade pitch angle. Collective pitch (θ_0) changes the blade pitch angle of all blades together while lateral cyclic pitch (θ_{1c}) and longitudinal cyclic pitch (θ_{1s}) cause the blade pitch angle to change cyclically as a function of its azimuth angle. The rotor model numerically computes inflow which is used together with the rotor state and control inputs to obtain the flapping angles, which in turn are used to compute the forces and moments generated by the rotor.

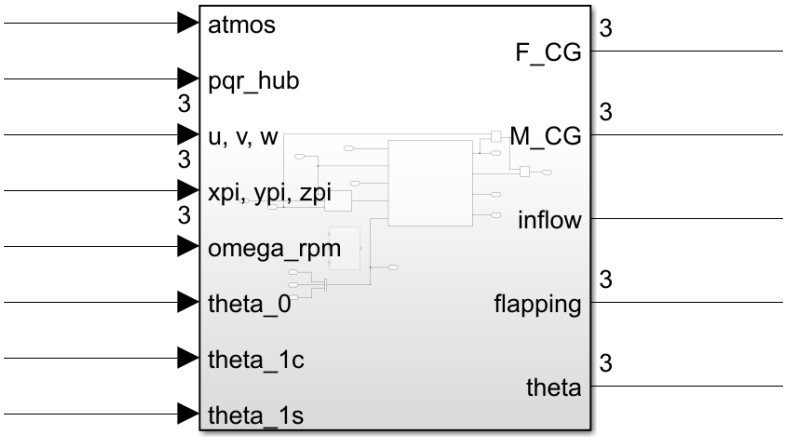

Figure 25. Rotor model block

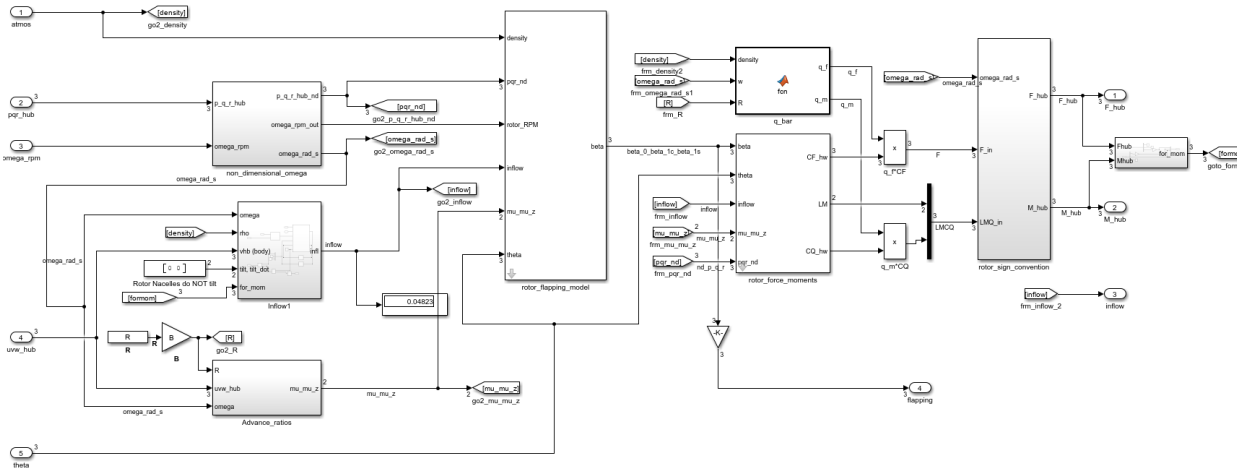

Figure 26. Rotor model detailed overview

One issue with the model is observed at the instant a collective or cyclic input is applied. The resulting force or moment spikes and then stabilizes at a steady-state value. This is believed to be caused by the transient effects in the numerical inflow model, which presents an issue when generating the force and moment envelopes for the single rotor and the entire PAVER vehicle (Task D). In order to filter out these effects, the Simulink model is run at every iteration, the resulting force or moment is recorded at T = 0.25 sec, and then stopped. This process of starting and stopping the simulation at every iteration result in the force and moment envelopes taking a long time to generate. The plots shown in Figure 27, Figure 28, Figure 29 were generated by applying a +10^{o} collective input and recording the changes in rotor thrust, rotor torque, and inflow over a period of one second.

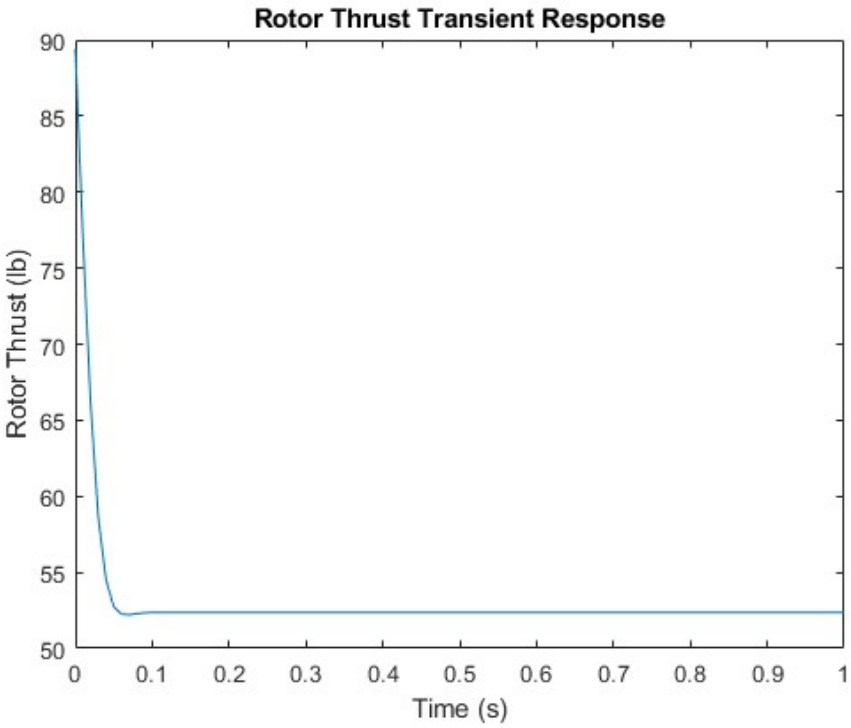

Figure 27. Rotor transient effects: thrust transient response

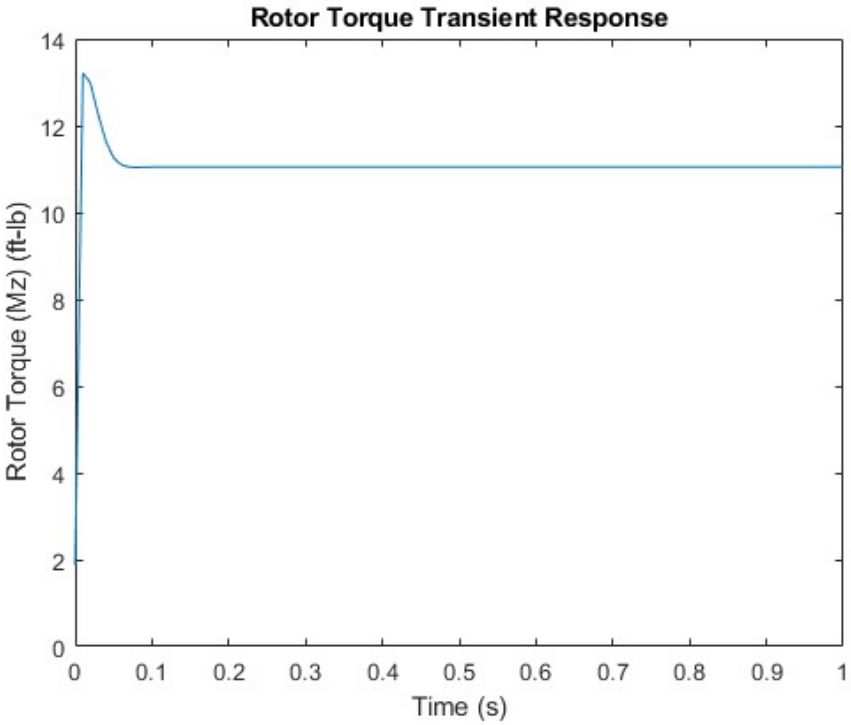

Figure 28. Rotor transient effects: torque transient response

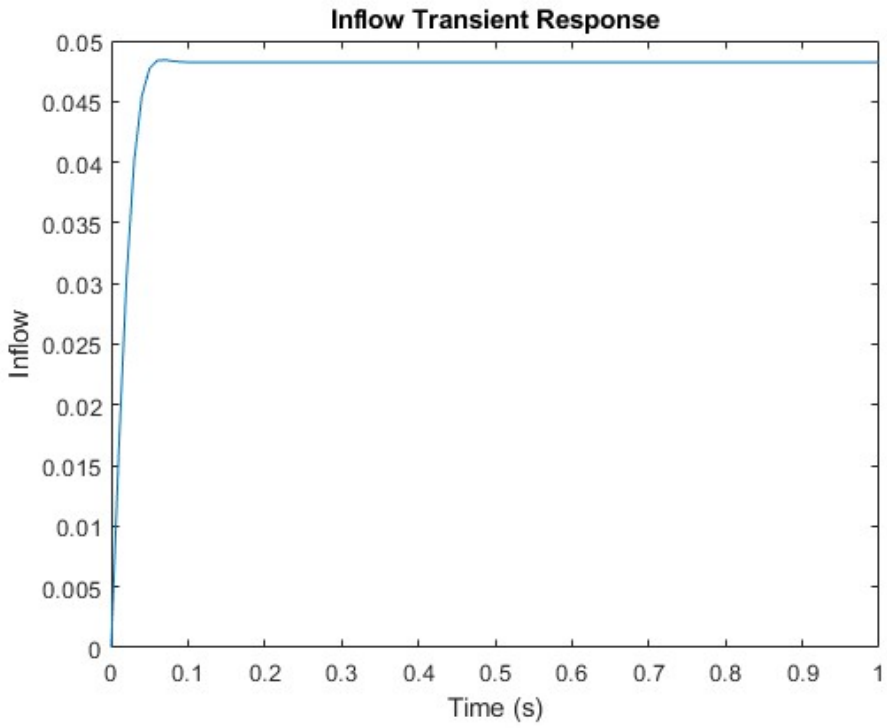

Figure 29. Rotor transient effects: inflow transient response

This mathematical model is mainly optimized for a rotor in hover and provides limited accuracy in forward flight. Since the flight testing conducted in this phase involved mainly hover flight, this rotor model proved sufficient. However, for future flight testing involving forward flight, upgraded rotor models that more accurately reflect a wider range of operating conditions would be necessary. Equations for the rotor model were derived from elements of both Lieshman (2006) and Padfield (2018), with dynamic inflow modeling from Peters & HaQuang (1988).

4.3 Task C: Rotor test stand experiments

The original two-bladed rotors on PAVER were replaced during Phase 1 by three-bladed rotors for the purpose of reducing vibrations. To validate this updated three-bladed rotor model, RPM sweeps were performed with the three-bladed S700 rotor on the RTS. RPM sweeps were performed at six different collective pitch settings and three different cyclic pitch settings, with collective pitch set to 6^{o} for the cyclic tests. The blue curves in Figure 30, Figure 31, Figure 32, and Figure 33 show the experimental RTS values, while the orange curves show the theoretical simulation values.

- a.¶

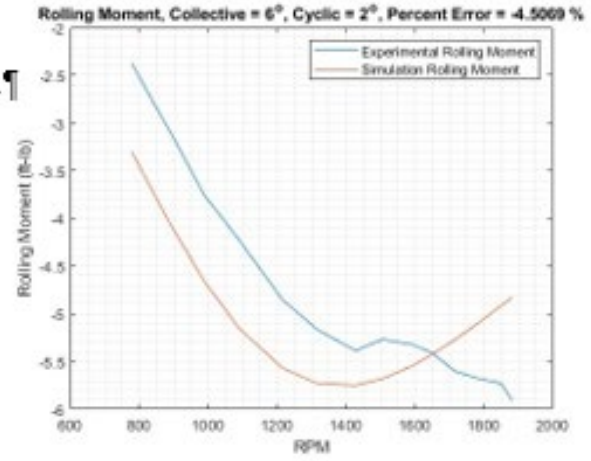

- b.¶

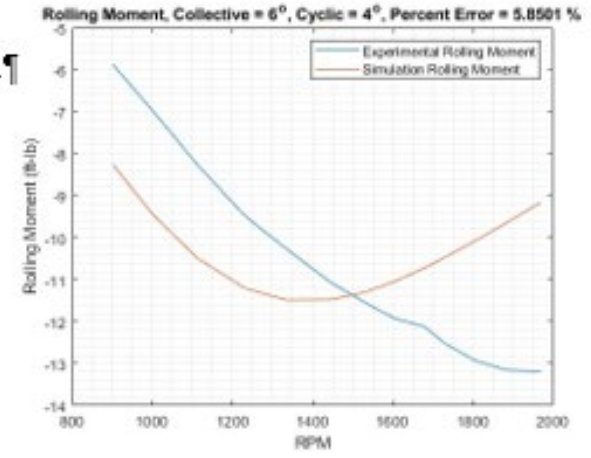

- c.¶

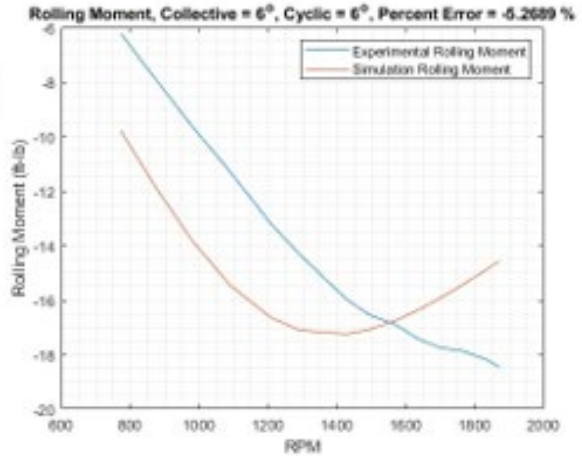

Figure 30. Rotor rolling moment validation plots

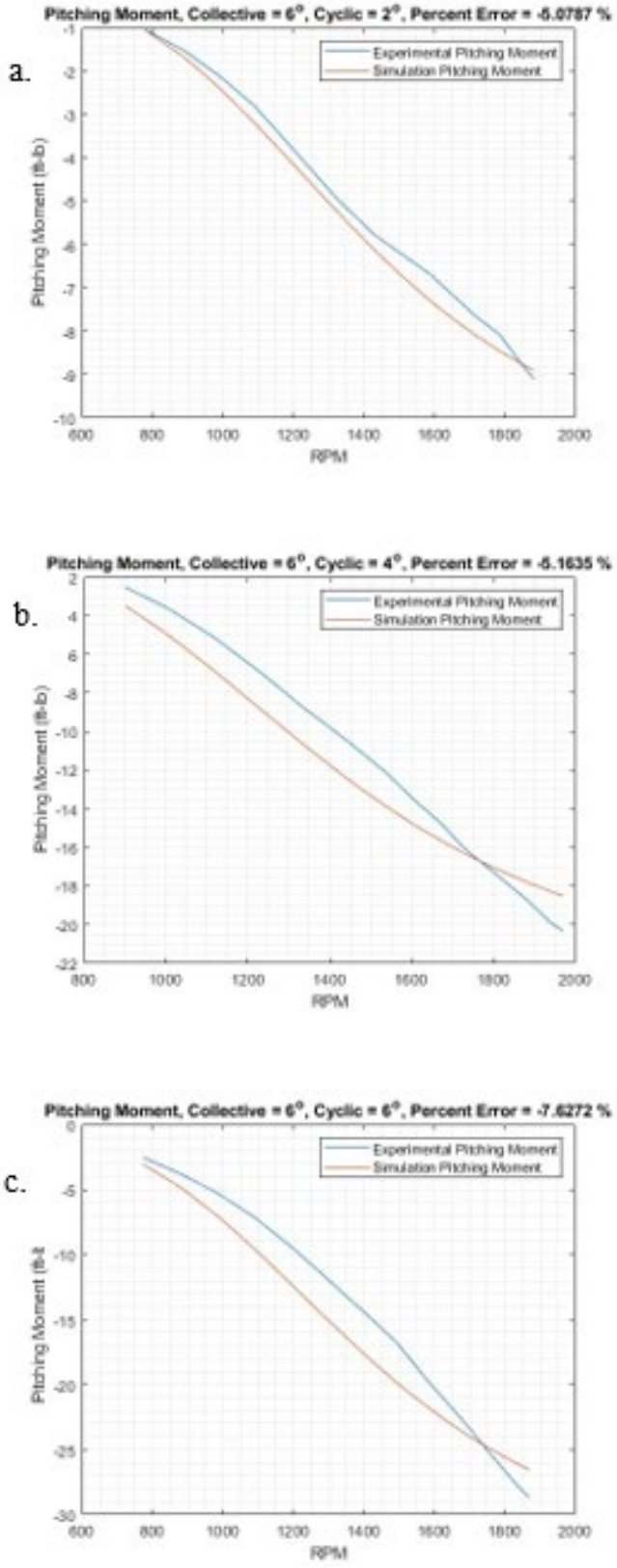

Figure 31. Rotor pitching moment validation plots

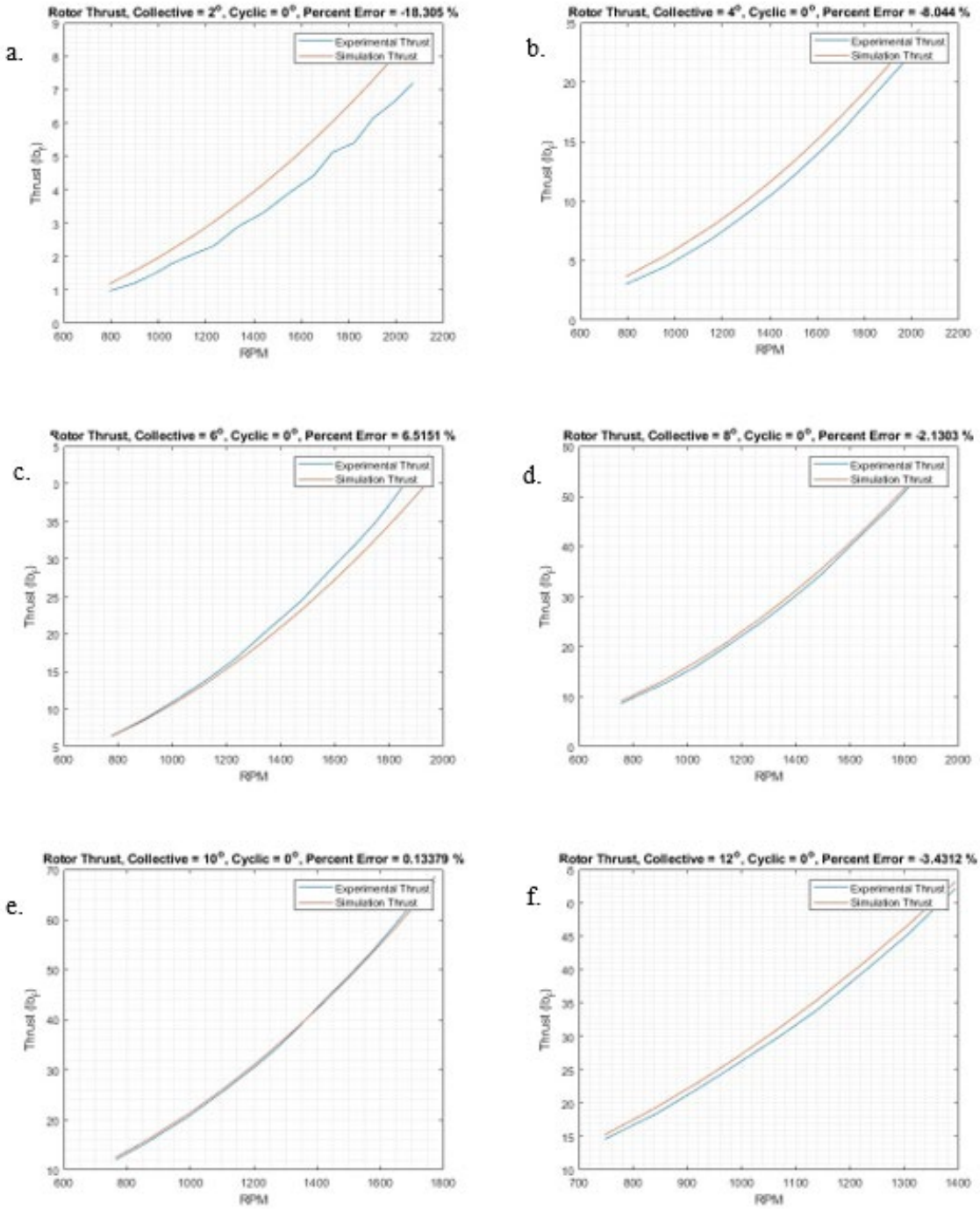

Figure 32. Rotor thrust validation plots

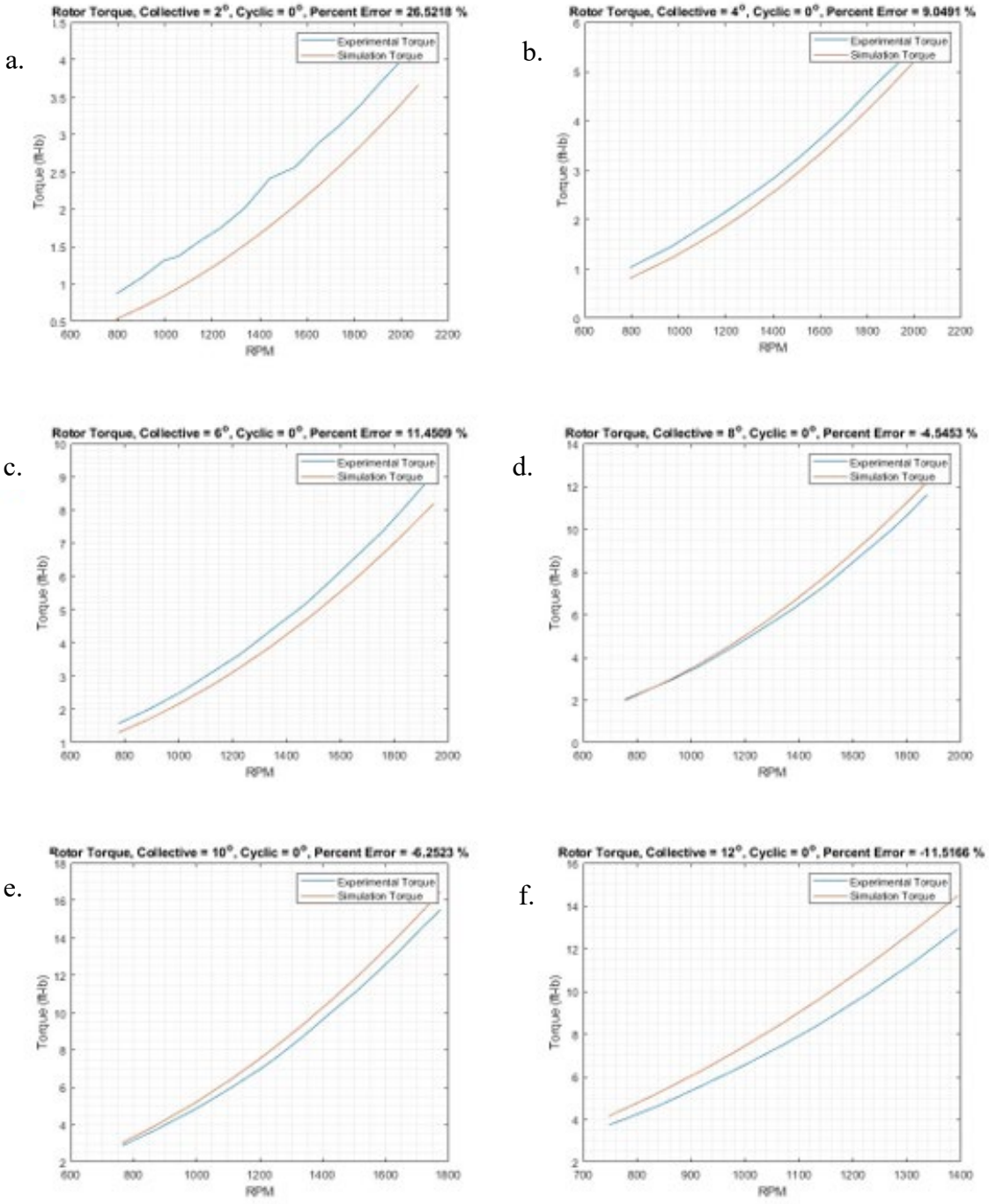

Figure 33. Rotor torque validation plots

The percent error for rolling and pitching moment is mostly consistent throughout the cyclic pitch range. Visually, the simulated pitching moment in Figure 31 follows a similar trend to the experimental pitching moment, while there is a much greater discrepancy for rolling moment in Figure 30. The thrust plots in Figure 32 show the greatest amount of percent error at 2º collective pitch and the least amount at 10º of collective pitch. The torque plots in Figure 26 show the

greatest amount of percent error at 2° of collective pitch and the least amount at 8° of collective pitch.

4.4 Task D: Develop a process to determine electric vertical take-off and landing vehicle force and moment envelopes

4.4.1 Introduction

Most AAM vehicles currently being developed are overactuated, meaning there are more control effectors than there are forces and moments to be controlled. Such vehicles look and fly differently from fixed-wing airplanes and helicopters, which the FAA and other regulatory agencies know how to certify. To certify these vehicles, their handling qualities need to be evaluated, which is often done through flight testing.

Flight testing nontraditional vehicle concepts often carries large amounts of risk. Examples of this include the Bell Boeing V-22 Osprey, the AgustaWestland (Leonardo) AW609, and the Bell 525, all shown in Figure 34 (Adams, 2015; NAVAIR, 2020; Leonardo Helicopters, n.d.).

The V-22 first flew in 1989 and spent 17 years in flight testing until its entry into service in 2007. It experienced several fatal accidents throughout its flight test program, which were mostly caused by handling qualities issues and mechanical failures.

The AW609 civilian tiltrotor made its maiden flight in 2003 and is still awaiting certification as of the time this report was published. Its flight test program was hampered by a fatal in-flight accident in 2015. While the aircraft was being tested in a high-speed dive outside its normal operating envelope, it entered Dutch roll oscillations that were not accurately predicted by the manufacturer's flight simulators, resulting in the aircraft breaking up in flight. These oscillations were believed to have been aggravated by the control laws and the actions of the pilots, and they occurred after the aircraft's tail surfaces were modified two years prior to improve performance (Agenzia Nazionale Per La Sicurezza Del Volo, 2016).

The Bell 525 is the world's first production civilian FBW helicopter. It made its maiden flight in 2015 and is still awaiting certification as of the date this report was published. Like the AW609, its flight test program was also hampered by a fatal accident caused by an in-flight breakup outside of the normal operating envelope. As the pilots were conducting one engine inoperative (OEI) tests at the aircraft's not-to-exceed speed, the aircraft began experiencing severe in-flight vibrations, resulting in loss of rotor RPM and subsequent rotor flapping that caused the rotor to impact the tail boom. The National Transportation Safety Board (NTSB) concluded that

biomechanical feedback to the collective control caused exacerbated these vibrations (National Transportation Safety Board, 2018).

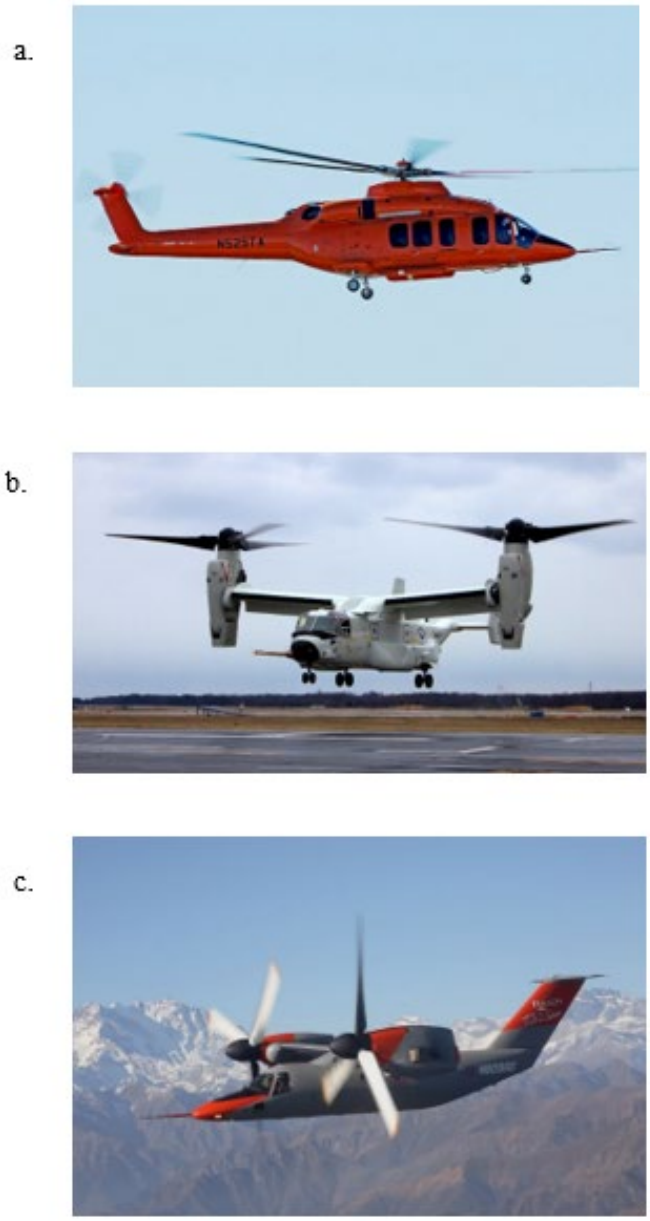

Figure 34. Current examples of FBW rotorcraft: (a) Bell 525; (b) Bell Boeing V-22 Osprey, and (c) AgustaWestland (Leonardo) AW609

If tiltrotor aircraft and even FBW helicopters that otherwise resemble conventional helicopters are taking at least a decade or longer to certify and experience accidents throughout their flight test programs, one can reasonably expect the same with eVTOLs using existing evaluation tools

and procedures. To improve flight test safety and reduce the number of flight tests required, methodologies that can predict these handling qualities deficiencies are necessary. This section discusses the development of two such methodologies.

The first methodology was designed with the intention of catching handling qualities deficiencies without the need of a test pilot and uses mathematical models to predict whether a given multirotor vehicle configuration possesses sufficient control authority to fly a given trajectory. More specifically, it uses a nonlinear dynamic inversion (NLDI)-based vehicle simulation code to predict the forces and moments required for a vehicle to fly a given trajectory together with the corresponding required vehicle states throughout the trajectory. The information provided by this code is then fed into another code that calculates the vehicle's attainable force and moment envelopes as a function of its state. The required and attainable forces and moments are then compared to predict whether the vehicle has sufficient control power to fly the trajectory. In its current iteration, this methodology's capability to predict a wide range of handling qualities deficiencies is very limited.

These limitations led to the development of a second methodology, which is designed to be used in conjunction with piloted simulation and flight testing and displays how a vehicle's force and moment envelopes change in real time as a function of its state. This would alert test pilots as they approach the boundaries of the operating envelope and could potentially reduce the likelihood of losing control of the vehicle.

4.4.2 Theoretical background: Attainable force and moment sets

Durham (1993) defines the constrained control allocation problem for overactuated vehicles and presents a methodology to solve it. An overactuated vehicle is a vehicle with more control effectors than there are degrees of freedom. A rigid aircraft has six degrees of freedom, consisting of three rotational degrees of freedom (roll, pitch, yaw) and three translational degrees of freedom (longitudinal, lateral, and vertical). In the case of a light general aviation aircraft with one effector for each rotational degree of freedom, there is only one solution to the control allocation problem (ailerons control rolling moment, elevator controls pitching moment, and rudder controls yawing moment). For vehicles with more effectors than degrees of freedom, there are multiple solutions to the control allocation problem, which means there are many ways in which the controls can be allocated to obtain the desired forces and moments. Modern tactical aircraft can have 13 or more independent control effectors. Most AAM vehicles are also highly overactuated.

Durham describes a method for calculating the AMS of an overactuated vehicle. Calculating an AMS is a necessary step for solving the control allocation problem, because in order to allocate a vehicle's flight controls, one needs to know the full capability of the vehicle's control effectors. This section does not focus on control allocation, but the calculation of attainable force and moment envelopes is useful for purposes such as assessing the maneuverability and predicting handling qualities of prototype vehicle concepts using flight simulation.

Durham's method for calculating the AMS involves cycling all the possible combinations of control effector inputs, assuming each effector is constrained to its maximum positive or negative position. The mathematics used to calculate the AMS involve a control effectiveness matrix B and a control input vector u. The control effectiveness matrix B contains linear control derivatives that determine how much force or moment can be generated by each effector or coupled set of effectors. Each column of B corresponds to a specific control effector input, while each row of B corresponds to a rotational degree of freedom or moment. For an aircraft, there are usually just three body-axis moments to be controlled (roll, pitch, and yaw) while there are m control effectors.

$$\boldsymbol{B} = \begin{bmatrix} \frac{\partial M_1}{\partial u_1} & \frac{\partial M_1}{\partial u_2} & \cdots & \frac{\partial M_1}{\partial u_m} \\ \frac{\partial M_2}{\partial u_1} & \frac{\partial M_2}{\partial u_2} & \cdots & \frac{\partial M_2}{\partial u_m} \\ \frac{\partial M_3}{\partial u_1} & \frac{\partial M_3}{\partial u_2} & \cdots & \frac{\partial M_3}{\partial u_m} \end{bmatrix} \tag{12}$$

The control input vector u is a column vector with its length determined by the number of control effectors.

$$\boldsymbol{u} = \begin{Bmatrix} \delta u_1 \\ \delta u_2 \\ \vdots \\ \delta u_m \end{Bmatrix} \tag{13}$$

Given a control effectiveness matrix B and a control input vector u, the net moment acting on the flight vehicle is computed as follows:

$$\boldsymbol{m} = \boldsymbol{Bu} \tag{14}$$

To calculate the AMS, Equation 14 is solved for each combination of admissible control inputs u, assuming that each effector can only be set to its maximum positive or negative position. The number of possible combinations of control inputs can be calculated by taking the number of admissible effector positions and raising that to the power of the number of effectors. For an aircraft with three effectors, the number of possible combinations of control inputs is $2^3 = 8$. For PAVER with differential collective control only and assuming constant RPM, there are four effectors (collective control on each rotor) and 16 possible combinations of control inputs. With cyclic control added, there are 12 effectors (collective, longitudinal cyclic pitch, and lateral cyclic pitch on each rotor) and 4096 possible combinations of control inputs. This methodology can also be used to calculate the envelope of attainable forces for a flight vehicle, which can be achieved by substituting the force for moment in Equations 12, 13, and 14. Durham's methodology requires a linearized model to obtain the control effectiveness matrix B, where the forces and moments are a linear function of effector position.

4.4.3 Durham methodology example

Durham uses the example of an airplane with ailerons operating differentially, a horizontal tail operating differentially, and a single rudder, to control rolling and yawing moment. The control effectiveness matrix for this configuration is shown below.

$$\boldsymbol{B} = \begin{bmatrix} C_{l_{\delta a}} & C_{l_{\delta HT}} & C_{l_{\delta r}} \\ C_{n_{\delta a}} & C_{n_{\delta HT}} & C_{n_{\delta r}} \end{bmatrix} \qquad 15$$

The first column of B corresponds to the ailerons δa, the second column corresponds to the horizontal tail δHT, and the third column corresponds to the rudder δr. The first row corresponds to rolling moment coefficient C_l and the second row corresponds to yawing moment coefficient C_n. The length of the control input vector u is determined by the number of control effectors (three in this case) and is a column vector.

$$\boldsymbol{u} = \begin{Bmatrix} \delta\ aileron \\ \delta\ diff.\ HT \\ \delta\ rudder \end{Bmatrix} = \begin{Bmatrix} \delta a \\ \delta HT \\ \delta r \end{Bmatrix} \qquad 16$$

The moment vector m, consisting of rolling and yawing moment coefficients, is obtained through multiplying the control effectiveness matrix B by the control vector u. It is a column vector, and its length is defined by the number of moments to be controlled (two in this case).

$$\boldsymbol{m} = \begin{Bmatrix} C_l \\ C_n \end{Bmatrix} = \boldsymbol{Bu} \tag{17}$$

Durham considers only two admissible effector positions (max positive and max negative) for each effector and uses a binary system to denote whether they are at their max positive or negative position. Any element of u equal to 0 means that the effector is at its max negative admissible position (for example, elevator in full trailing-edge down position), whereas any element of u equal to 1 means that the effector is at its max positive admissible position (for example, elevator in full trailing-edge up position). With three effectors and two admissible positions for each effector, there are $2^3 = 8$ possible combinations of control inputs.

The control vector with the aileron at its max positive position, the horizontal tail (HT) at its max negative position, and the rudder at its max positive position, labeled as u_5, would look like

$$\boldsymbol{u_5} = \begin{Bmatrix} 1 \\ 0 \\ 1 \end{Bmatrix} \tag{18}$$

The control vector with all three effectors in their max negative position, labeled as u_0, would look like

$$\boldsymbol{u_0} = \begin{Bmatrix} 0 \\ 0 \\ 0 \end{Bmatrix} \tag{19}$$

The control vector with all three effectors in their max positive position, labeled as u_7, would look like

$$\boldsymbol{u_7} = \begin{Bmatrix} 1 \\ 1 \\ 1 \end{Bmatrix} \tag{20}$$

The number with which each vector is labeled (for example, u_7), is obtained by treating the control vector is a binary number consisting of 1s and 0s and converting it to decimal form. The control vector represented by the binary number 111 would be 7 in decimal form, while 101 would be 5 and 000 would be 0 in decimal form.

Generating the AMS involves multiplying the control effectiveness matrix B by every admissible control vector u to generate all possible combinations of moments, which are then plotted in 2D or 3D space, depending on the number of moments being controlled. The outermost points are then connected to form the envelope using a type of boundary called the convex hull, which results in the AMS as shown in Figure 36. The collection of all possible combinations of control effector inputs, also known as the constrained control subset, control space, or admissible control set (ACS), can also be graphically represented as shown in Figure 35. In the case of a three-effector, two-moment problem, the control space is three-dimensional, and the AMS is two-dimensional. For a more complete three-moment problem, AMS would be three-dimensional, and the dimension of the control space would equal the number of effectors. When more than three effectors are present, the graphical depiction of the control space would be impossible for most humans to visualize and would instead be described in the form of a table.

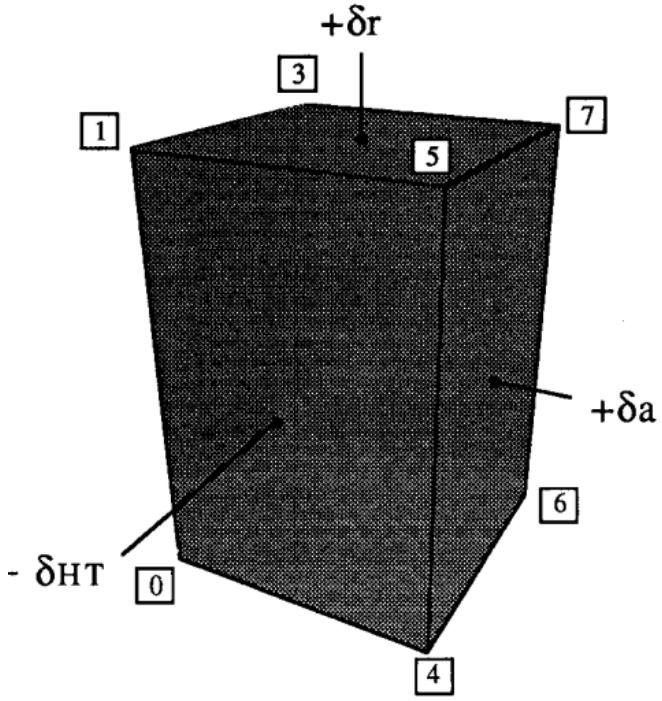

Figure 35. Constrained control subset

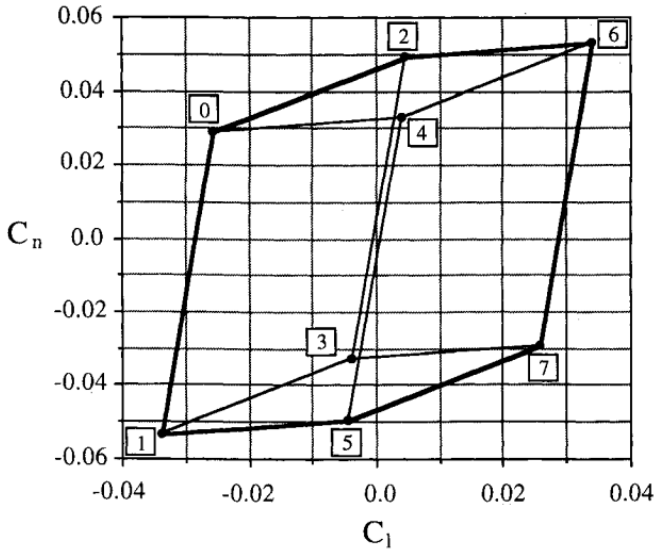

Figure 36. Attainable moment subset

Each vertex on Figure 35 represents a possible combination of control effector positions. The lines connecting these nodes are generated by moving one effector at a time whereas the surfaces, which are defined by two lines, are generated by moving two effectors at a time. All admissible control positions between the maximum and minimum effector position constraints lie on or within the boundary of Figure 36. These points map to the AMS in Figure 36, where they represent the moments that are attainable by each admissible combination of control inputs. A convex hull is used to connect the outermost points in Figure 36, which represents the AMS boundary. Unlike with the control space in Figure 36, there are two points that on in the interior of the AMS boundary.

To simplify the calculations for obtaining the AMS, Durham assumed that the moments generated by the vehicle's effectors vary linearly with effector position. There are some cases for which this assumption holds true. However, a linearized model does not always provide accurate information about a vehicle's dynamics in certain situations, such as an airplane operating at high angles of attack. To predict the attainable forces and moments for these cases, a nonlinear vehicle dynamics model can be used instead of a linearized control effectiveness matrix.

For the linear case, Durham assumed that considering only max positive or negative effector positions was sufficient to generate the attainable moment set that fully describes the vehicle's moment generation capabilities. For nonlinear models, this assumption holds true when the forces and moments resulting from max positive or negative effector deflection are indeed the maximum attainable forces or moments, which is mostly the case. Figure 37 shows the variation in rotor thrust and torque as a function of collective pitch for a helicopter rotor while hovering without any wind disturbances.

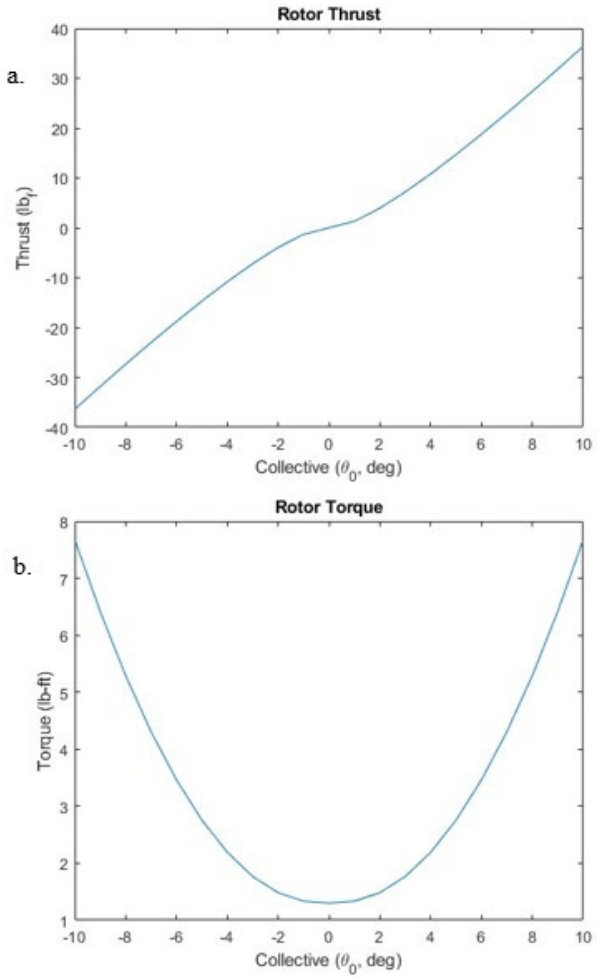

Figure 37. Rotor thrust and torque as a function of collective pitch

These curves were generated with the nonlinear rotor dynamics simulation model operating at 1500 RPM and varying collective pitch between -10° and 10°. Longitudinal and lateral cyclic pitch were kept constant. The force (thrust) and moment (torque) both vary nonlinearly with collective pitch. Using single linear slope values to build a control effectiveness matrix would not give an accurate representation of torque but would somewhat accurately represent thrust. Since the global maximum and minimum values of thrust and torque in Figure 37 correspond to their respective max positive or negative effector (collective) positions, considering only max positive or negative effector positions would give an accurate representation of the vehicle's capabilities.

One example for which this assumption would not hold true is an aircraft operating at high angles of attack in the nonlinear region of the lift curve slope. For example, if a fighter pilot flying a steep turn wants to maximize lift, holding full aft stick would cause the wings to stall, so therefore slightly less than full stick deflection would be required to maximize lift. Considering

nonlinear effects like these would require a code to seek out the global maximum and corresponding control effector position, which is beyond the scope of this study.

4.4.4 PAVER example

Since the PAVER vehicle and rotor simulation models are nonlinear, it is difficult to obtain a linear model that accurately represents the vehicle dynamics as a function of its state. Therefore, the nonlinear vehicle dynamics model of PAVER was used in place of a control effectiveness matrix to generate the forces and moments as a function of control inputs and vehicle state. The equations of motion were removed from this model, so that the vehicle's states u, v, w, p, q, r, which affect the resulting forces F_x, F_y, F_z, and moments L, M, N, are no longer calculated through numerically integrating the equations of motion and instead correspond to the states required to fly a desired trajectory. A diagram of this model is shown in Figure 38.

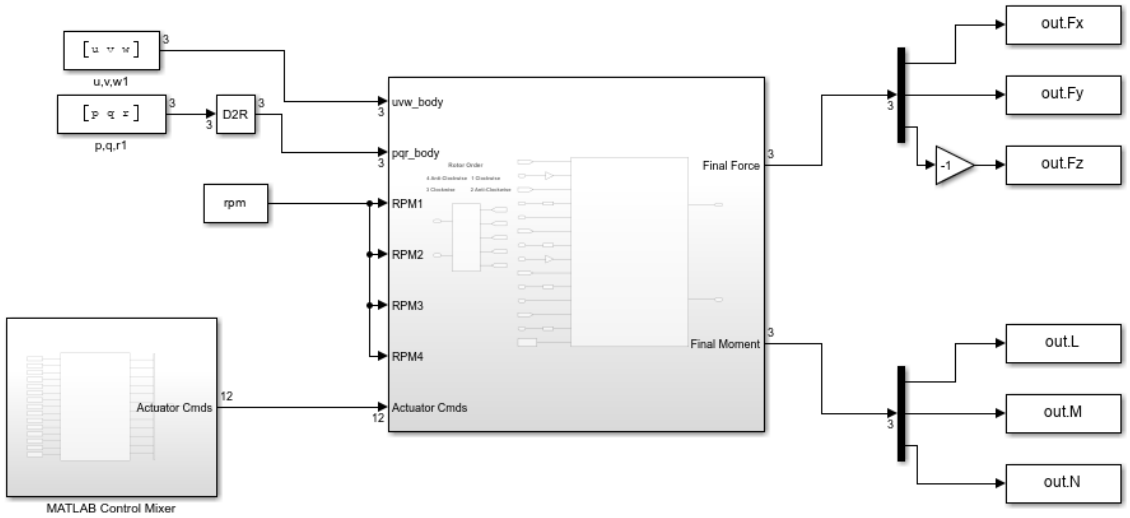

Figure 38. PAVER actuator dynamics model with equations of motion removed

The main advantage of using the nonlinear model over a linearized model is that it calculates forces and moments as a function of vehicle state, whereas a linear model would need to be created for every vehicle state and might not provide accurate predictions of the vehicle's force and moment capability. A disadvantage of this method is longer computational times, since the nonlinear vehicle model needs to be run and stopped at every iteration. To generate the force and moment envelopes for the PAVER vehicle with collective and cyclic control, the nonlinear vehicle model needs to be run 4096 times, which takes roughly seven minutes with Fast Restart mode enabled in Simulink.

The resulting force and moment envelopes are three-dimensional point clouds containing 4096 points as shown in Figure 39, with each point representing a combination of forces F_x, F_y, F_z or

moments L, M, N generated by a certain combination of control inputs. The envelope is formed by stretching a type of boundary called a convex hull around the outermost points, and is generated using the convhull() function in MATLAB. Figure 40 depicts the three-dimensional force and moment envelopes for PAVER with collective and cyclic control in hover, without any wind or turbulence. Any combination of forces or moments that lies on or within the boundary of their respective envelopes is attainable through combinations of admissible control inputs.

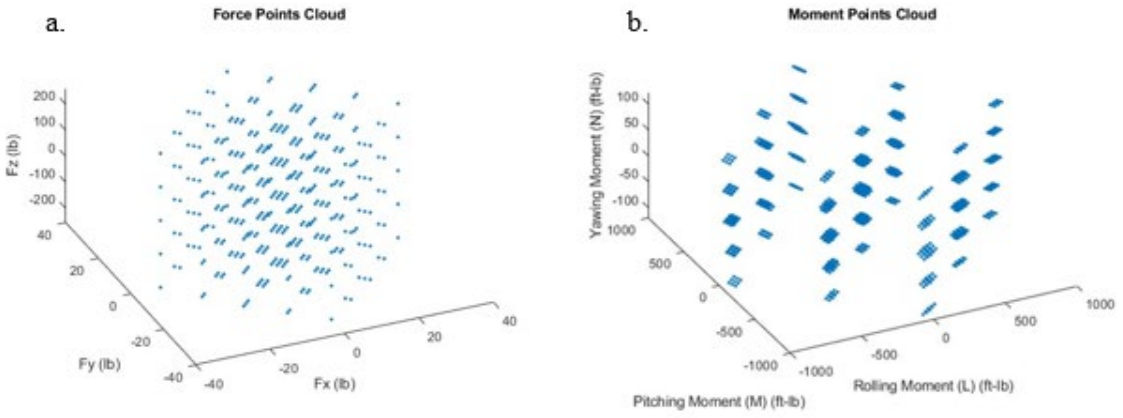

Figure 39. PAVER force (a) and moment (b) points clouds with full collective and cyclic control

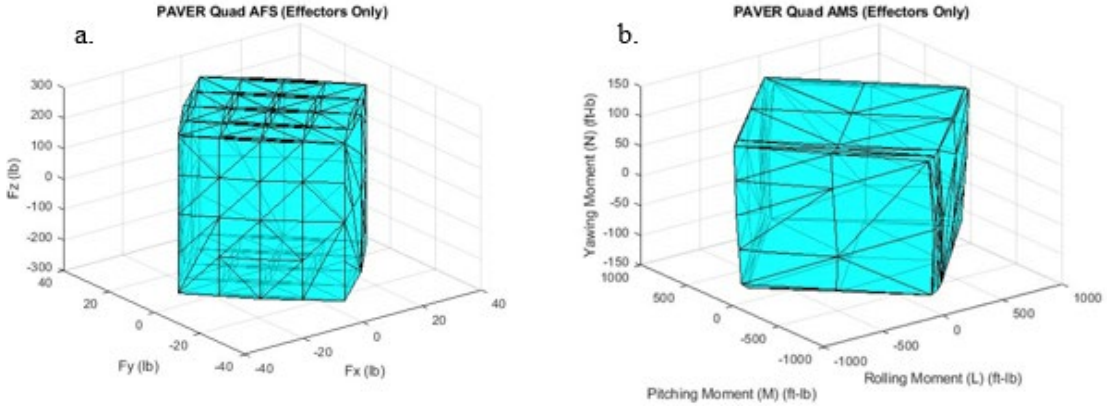

Figure 40. PAVER force (a) and moment (b) envelopes with full collective and cyclic control

4.4.5 Comparison methodology

The NLDI-based required force and moment prediction methodology (see Task H for details) outputs the forces and moments required for the vehicle to fly the trajectory together with the

corresponding required vehicle states (u, v, w) and (p, q, r). To predict whether the vehicle possesses sufficient control power to fly the trajectory, the trajectory is decomposed into a finite number of segments that can be defined by the user, where a typical choice is 100. Each segment contains information regarding the required forces, moments, and states at that specific point in the trajectory. At each segment, these six states are fed into the force and moment envelope code, which generates the envelopes of attainable forces and moments for that given state. Another code then checks whether the required forces and moments lie within the boundaries of their respective envelopes and how far from the boundaries they lie, which is a measure of control margin. This process is illustrated in Figure 41 and is repeated at each trajectory segment.

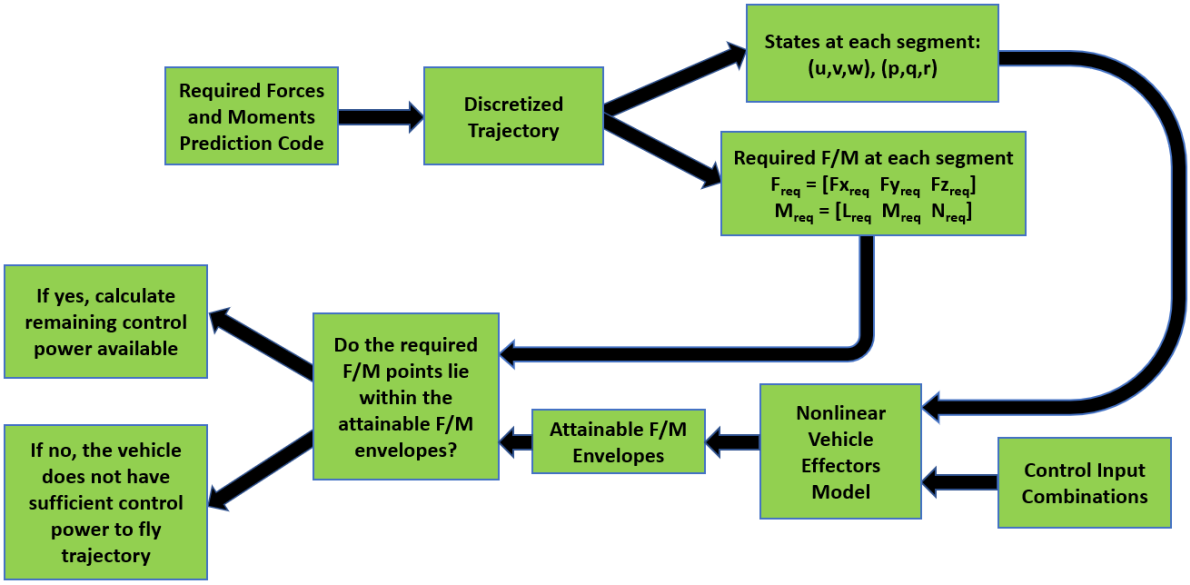

Figure 41. Required vs. attainable force and moment comparison process

This process is currently only capable of analyzing two-dimensional trajectories with three degrees of freedom of vehicle motion, involving forward/aft motion, up/down motion, and pitching motion. In the case of differential collective control (VP1 and VP2), the actuation forces are constrained to the vehicle's vertical (Z) body axis and the force and moment envelopes become one-dimensional. The force envelope is defined in terms of force along the vehicle's vertical body axis (F_z) and the moment envelope is defined in terms of pitching moment (M). This process is illustrated in Figure 42 with an arbitrary set of required and attainable forces.

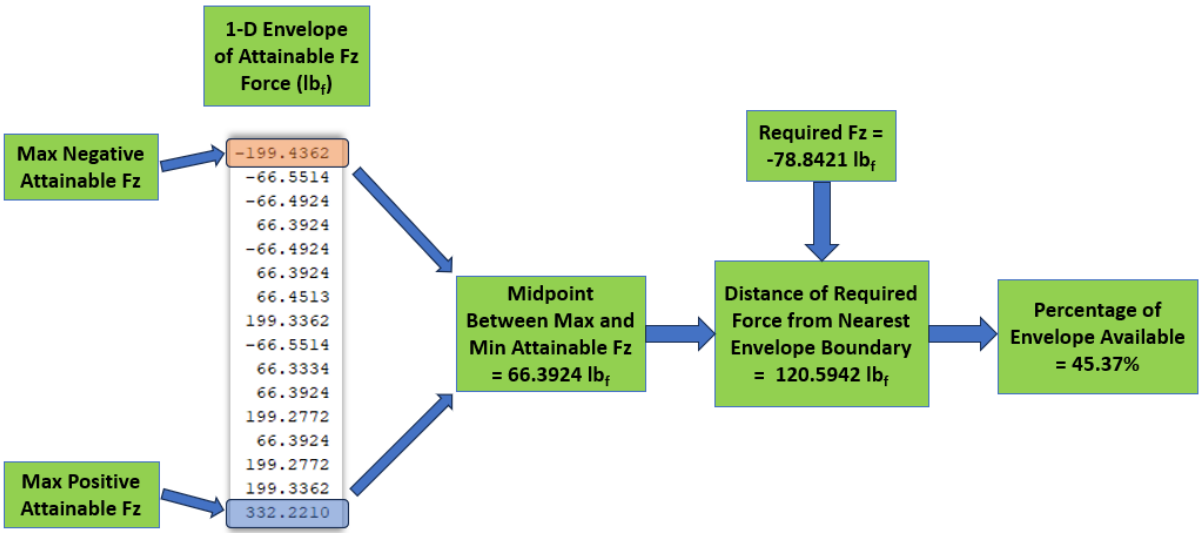

Figure 42. One-dimensional envelope evaluation process

Analyzing three-dimensional trajectories with full 6DOF vehicle dynamics and effector forces and moments about all three body axes would require a tool to determine the location of the required forces with respect to envelope boundaries in three dimensions.

This methodology was used to predict the capabilities of PAVER for two simulated flight maneuvers representative of typical MTEs. The first maneuver involved PAVER accelerating from a hover at a constant rate of 10 ft/s^2 for roughly five seconds to a velocity of 50 ft/s, followed by a deceleration back to a hover while holding a constant altitude and heading. The second maneuver involved a climb-out to a constant altitude and forward velocity while holding a constant heading, representative of the type of maneuver a UAM vehicle would perform to leave the ground and transition to forward flight. For both maneuvers, PAVER's predicted performance was analyzed for the nominal case, corresponding to all rotors working, as well as a failure case in which one rotor was inoperative. Both maneuvers assumed standard sea-level atmospheric conditions without any wind or turbulence. A third simulation case involving PAVER losing one rotor during hover was conducted to predict the vehicle's capability to maintain hover using both the RPM control and collective + cyclic pitch control strategies,

4.4.6 Simulation case 1: Acceleration and deceleration at constant altitude

To generate the thrust required to accelerate, the vehicle pitches forward to an attitude of -20° nose down to tilt the thrust vector. This is followed by a backward pitch to +20° nose up to slow the vehicle down. The velocity along the vehicle's body x-axis (u) increases proportionally to forward velocity in the inertial (Earth) reference frame. The velocity along the vehicle's body y-axis (v) is always zero. The velocity along the vehicle's body z-axis (w) is negative in the first half of the maneuver, since the top of the vehicle is subjected to the relative wind and then

becomes positive after the vehicle pitches backward, where the bottom of the vehicle becomes subjected to the relative wind.

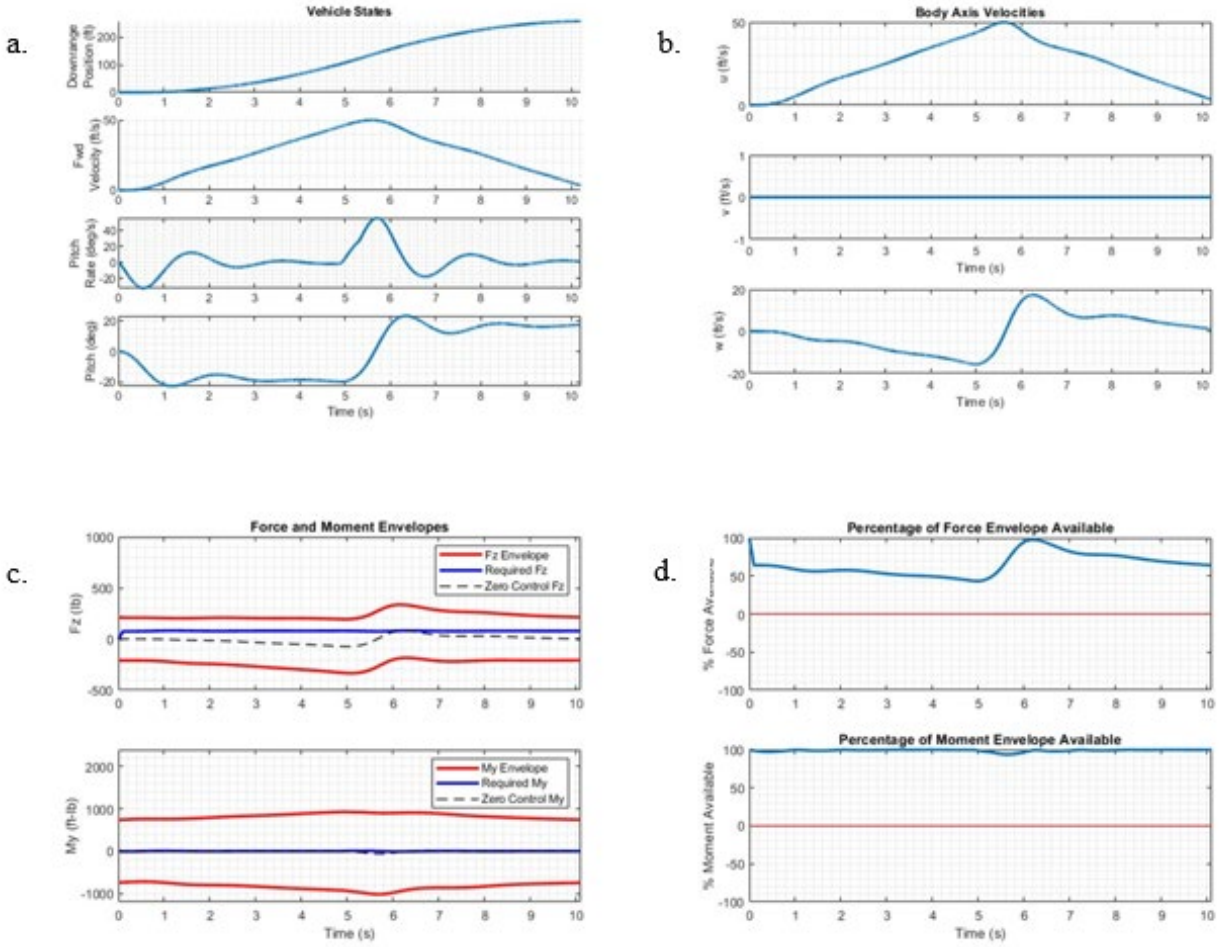

Figure 43. Results for acceleration-deceleration at constant altitude (normal condition)

The boundaries of the attainable force and moment envelopes in Figure 43 are shown by the two red lines. The upper boundary indicates the maximum available force or moment in the positive direction, while the lower boundary indicates the maximum attainable force or moment in the negative direction. The blue line shows the force or moment required to fly the trajectory, while the black dashed line shows what the force or moment acting on the vehicle would be with all controls set to neutral. The shifting of this black dashed line throughout the maneuver indicates that the vehicle is being subjected to forces and moments even without any control inputs. This is caused by airframe drag as the vehicle is subjected to relative wind and does not show in any way that the vehicle can fly the maneuver without any control inputs, which it cannot. The forces and moments that would be acting on the vehicle with neutral controls as a function of state

almost exactly correspond to the midpoints between the upper and lower bounds of each envelope.

The force envelope tends to widen in magnitude and shifts downward as the vehicle is accelerating between t = 0 and 5 seconds. This downward shift is easier to observe by looking at the black dashed *Zero Control* F_z line, which roughly corresponds to the center of the envelope. When the vehicle begins its pitch-back maneuver to decelerate, the envelope suddenly shifts upward and begins to decrease in magnitude as the vehicle slows down to hover. The widening in magnitude could be explained by the increasing inflow into the rotors as the vehicle's forward velocity increases, reducing the power required for forward flight. The upward shift is caused by the change in the direction of the body Z-axis velocity (w) resulting from the pitching motion, which removes drag from the top of the vehicle and adds it to the bottom of the vehicle. The backward pitching motion does not affect the size of the envelope but does result in the vehicle being capable of generating more force in the positive body Z-direction and less force in the negative body Z-direction.

The moment envelope also increases in size as the vehicle accelerates and the pitching motion causes a slight downward shift at t = 5 seconds. The percentage of the force or moment envelope available is calculated by finding the distance of the required force or moment from the nearest envelope boundary and expressing that as the percentage of the distance of the envelope boundary from the envelope midpoint. The percentage of available force envelope is at its minimum around t = 5 seconds, where roughly 43% of the envelope remains, and the vehicle is at its maximum speed right before the pitch maneuver. At the beginning of the trajectory, around 53% of the force envelope is available due to thrust being needed to counteract the vehicle's weight. The percentage of available moment envelope remains around 100% most of the time but experiences a slight downward shift to 93% during the pitch maneuver.

This maneuver was also simulated with one rotor inoperative, and the results from this simulation are shown in Figure 44. Overall, the results follow a similar trend to the previous ones shown in Figure 44, with the force and moment envelopes decreasing slightly due to less thrust being available. At t = 5 seconds, approximately 24% of the force envelope is available, and around 91% of the moment envelope is available. This simulation does not account for the fact that the vehicle must tilt slightly to the side to compensate for the loss of thrust from one rotor in order to maintain constant heading. This tilting of the vehicle would tilt the thrust vector to the side, resulting in even less thrust available to maneuver the vehicle.

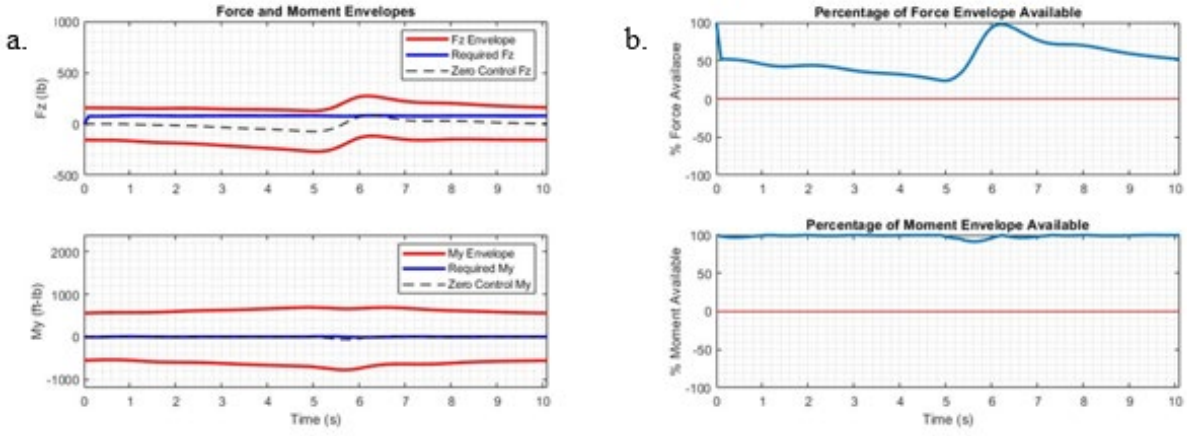

Figure 44. Results for acceleration-deceleration at constant altitude (one rotor inoperative)

4.4.7 Simulation case 2: Climb-out to constant altitude and forward velocity

This maneuver starts in a hover, which is followed by a climb to a constant altitude of 125 ft and a constant velocity of 75 ft/s, which are held for the remainder of the maneuver. To generate the thrust required to accelerate, the vehicle pitches forward to a maximum nose-down pitch angle of -24°, which then decreases to a magnitude of -8° once established at 125 ft altitude to sustain forward flight at 75 ft/s.

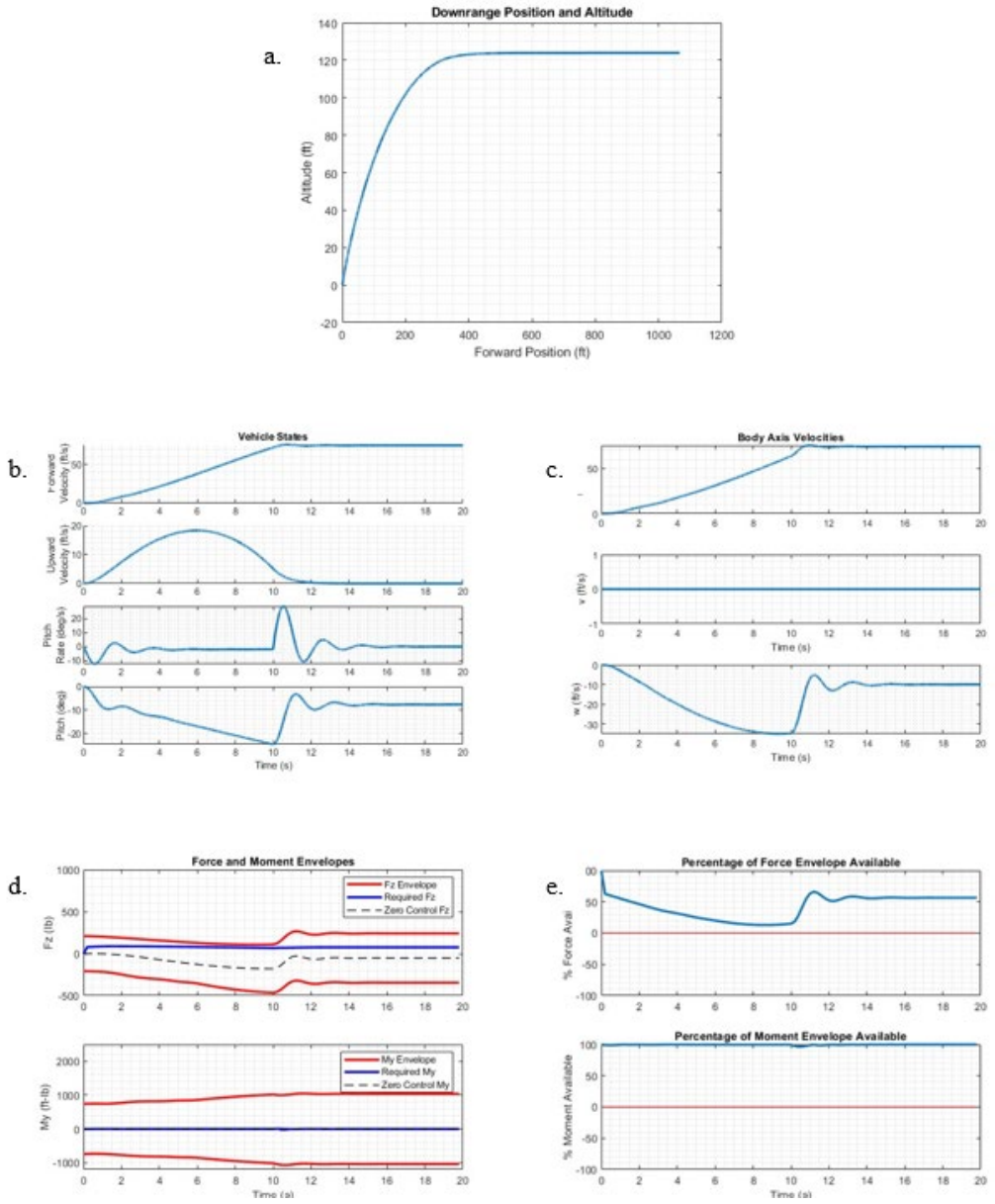

Figure 45. Results for climb-out to constant altitude and forward velocity (normal condition)

As the vehicle climbs and accelerates, the inflow into the rotors increases and causes the force and moment envelopes to widen, while the added drag on the top of the vehicle causes the force envelope to shift down. As the vehicle pitches aft and then forward again to transition to forward flight at a constant speed and altitude, the force envelope shifts up and then down again. The width of both the force and moment envelopes remains constant after t = 14 seconds, where the vehicle's speed remains constant. Between t = 8 and 10 seconds, around 12% of the force envelope is available, while almost the entire moment envelope is available. 75 ft/s was chosen as the target speed to demonstrate what would occur if the required forces and/or moments exceeded the attainable forces and/or moments. The results from the failure scenario involving

one rotor inoperative, shown in Figure 46, show the *Required* F_z line crossing the upper boundary of the force envelope during the accelerating climb. With one rotor inoperative, the vehicle is incapable of generating the thrust required to follow the desired trajectory. In a real-world situation, the vehicle would likely require a longer time to achieve the desired altitude and velocity.

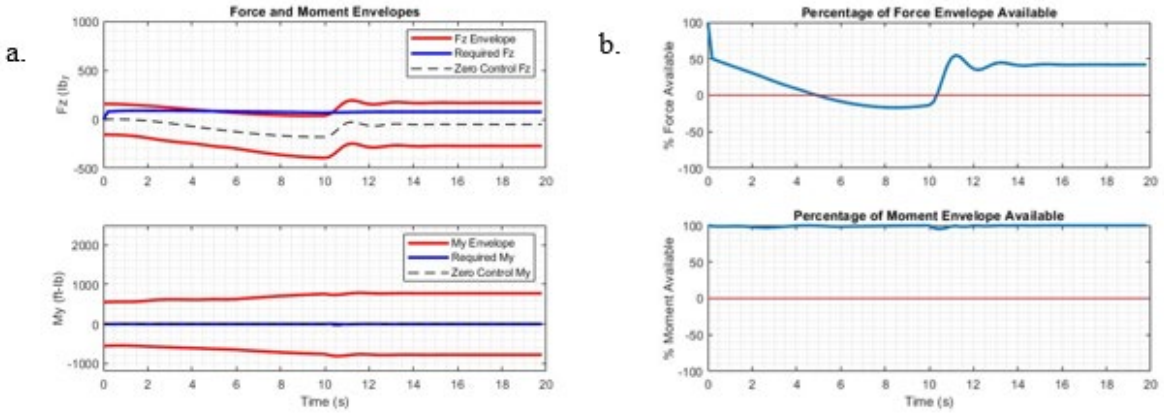

Figure 46. Results for climb-out to constant altitude and forward velocity (one rotor inoperative)

It should be noted that, if much of the rotor power is being used to produce thrust to counteract the vehicle's weight, there might not be sufficient control power remaining to pitch the vehicle without reducing the total thrust and losing altitude as a result. The force and moment envelopes shown above are independent from one another and only indicate the vehicle's capabilities assuming all the control power is available. A potential way to eliminate this issue would be to first generate the envelopes independently, then check whether force or moment generation demands the most from the vehicle's effectors, and then allocating the vehicle's controls to generate that force or moment, whichever demands the most. For example, if force generation demands the most from the vehicle's effectors, as is the case with PAVER, a control allocation algorithm could be used to find the control input combination necessary to generate that force and based on that, using the remaining available control power to generate moment envelopes.

4.4.8 Simulation case 3: Rotor failure in hover

Since the three-dimensional force and moment envelopes for PAVER with collective and cyclic pitch control consist of 4096 points and each set of envelopes taking roughly 6 minutes to generate, performing trajectory analysis using these three-dimensional envelopes would take roughly 10 hours for each trajectory, assuming the trajectory is decomposed into 100 elements. To demonstrate how three-dimensional force and moment envelopes could be used to assess

PAVER's capabilities, a very simple case was chosen, where PAVER must be trimmed in hover in the nominal case where all four rotors are working and in an off-nominal case with one of the rotors out (Rotor 4, the front left rotor).

To hover, the thrust from all four of PAVER's rotors must equal the vehicle's weight (75 lbs) and the sum of the moments acting on the vehicle must be zero. Figure 47 shows the force envelopes for both the nominal condition and the one rotor out condition. Figure 48 shows the moment envelopes for both the nominal condition and the one rotor out condition. In this test, all four rotors were operating at 1800 RPM, with a collective pitch limit of 13° and a cyclic pitch limit of 6°. *Positive Fz* is considered upward.

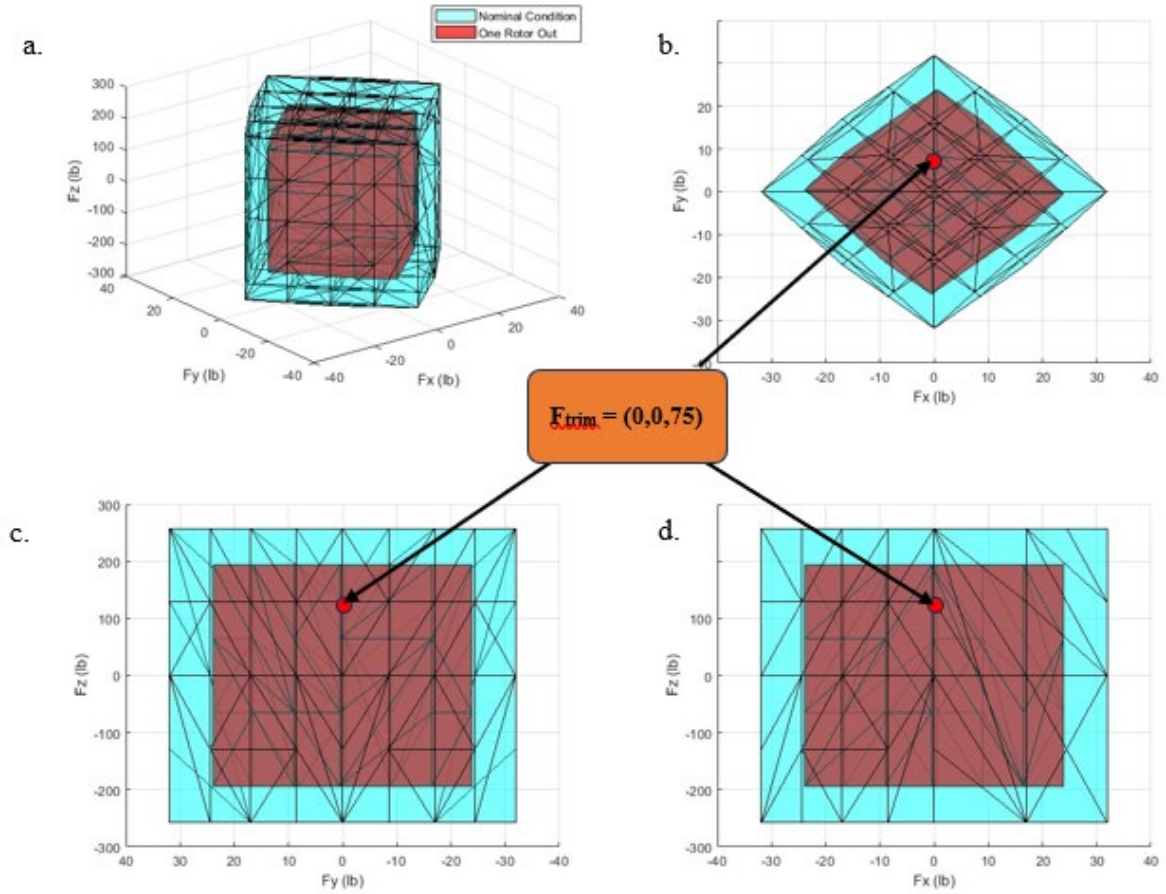

Figure 47. Force envelopes for PAVER with pitch control (nominal and OEI)

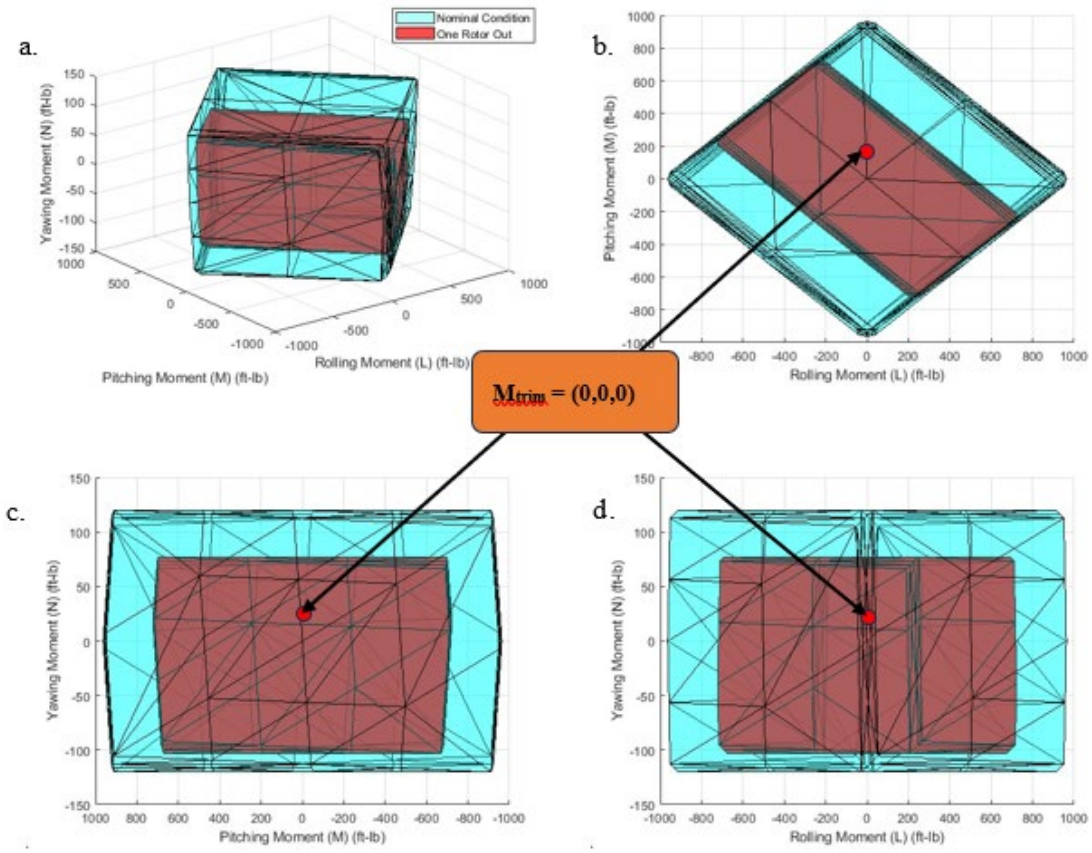

Figure 48. Moment envelopes for PAVER with pitch control (nominal and OEI)

By visual inspection, one can see that the required forces and moments (F_{trim} and M_{trim}) lie within the boundaries of the force and moment envelopes for both the nominal and one rotor out condition, meaning that in the event of losing one rotor, the remaining rotors could provide sufficient control authority to keep the vehicle trimmed in a hover. However, if all the rotor power is being used to produce thrust to counteract the vehicle's weight, there might not be sufficient control power remaining to cancel out the moments without reducing the total thrust and losing altitude. The force and moment envelopes shown above only indicate the vehicle's capabilities assuming all the control power is available. PAVER flight tests during Phase 1 showed that it is possible to trim the vehicle in hover in the event of losing one rotor (Collins, et al., 2023).

With the RPM control strategy, the blade pitch of all four rotors is set to 6° and thrust from each of the four rotors is controlled by varying RPM, with 1200 RPM being the minimum and 1800 RPM being the maximum. With four effectors (RPM control on each of the four rotors) and two admissible positions for each effector (maximum and minimum RPM), there are 16 possible combinations of control inputs and therefore 16 points that make up the force and moment

envelopes. Figure 49 shows the force envelopes for the RPM control only case, and Figure 50 shows the moment envelopes for the RPM control case. In Figure 49, the blue dots represent the range of attainable forces for the nominal condition, and the orange dots represent the range of attainable forces for the one rotor out condition. *Positive Fz* is considered upward.

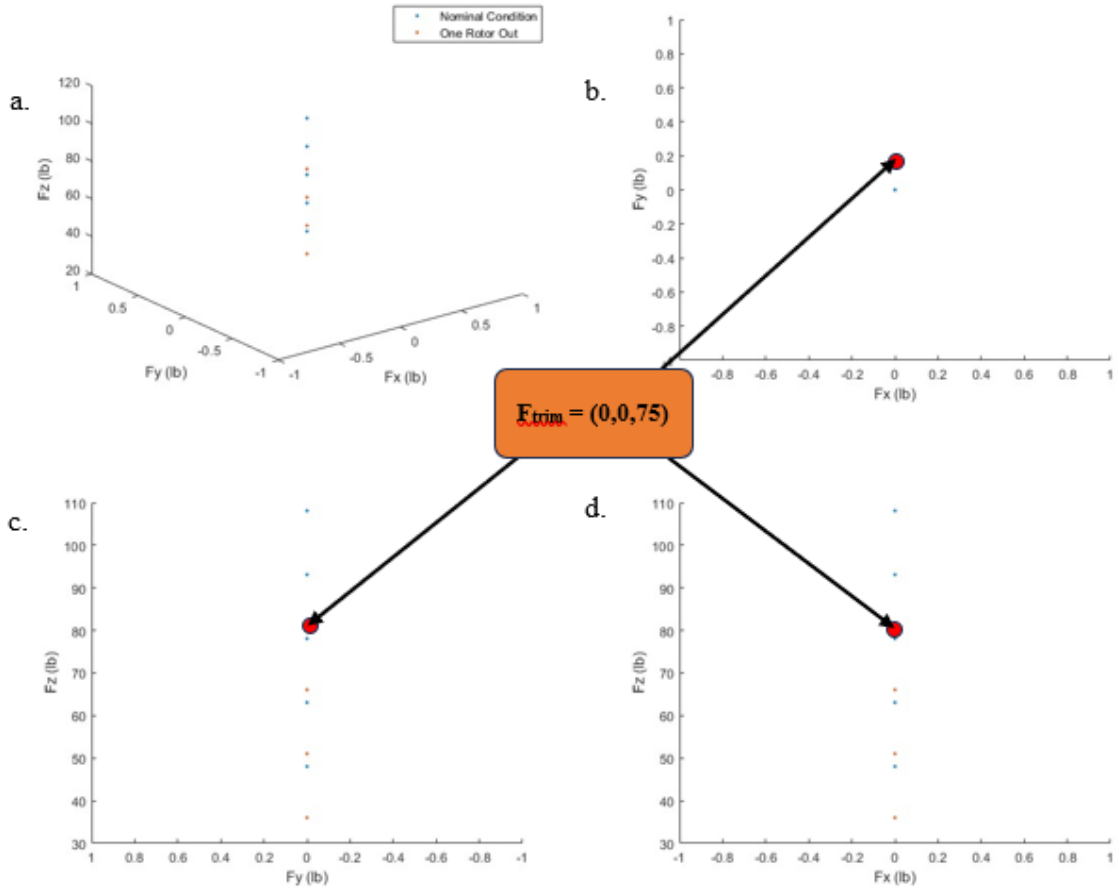

Figure 49. Force envelopes for PAVER with RPM control (nominal and OEI)

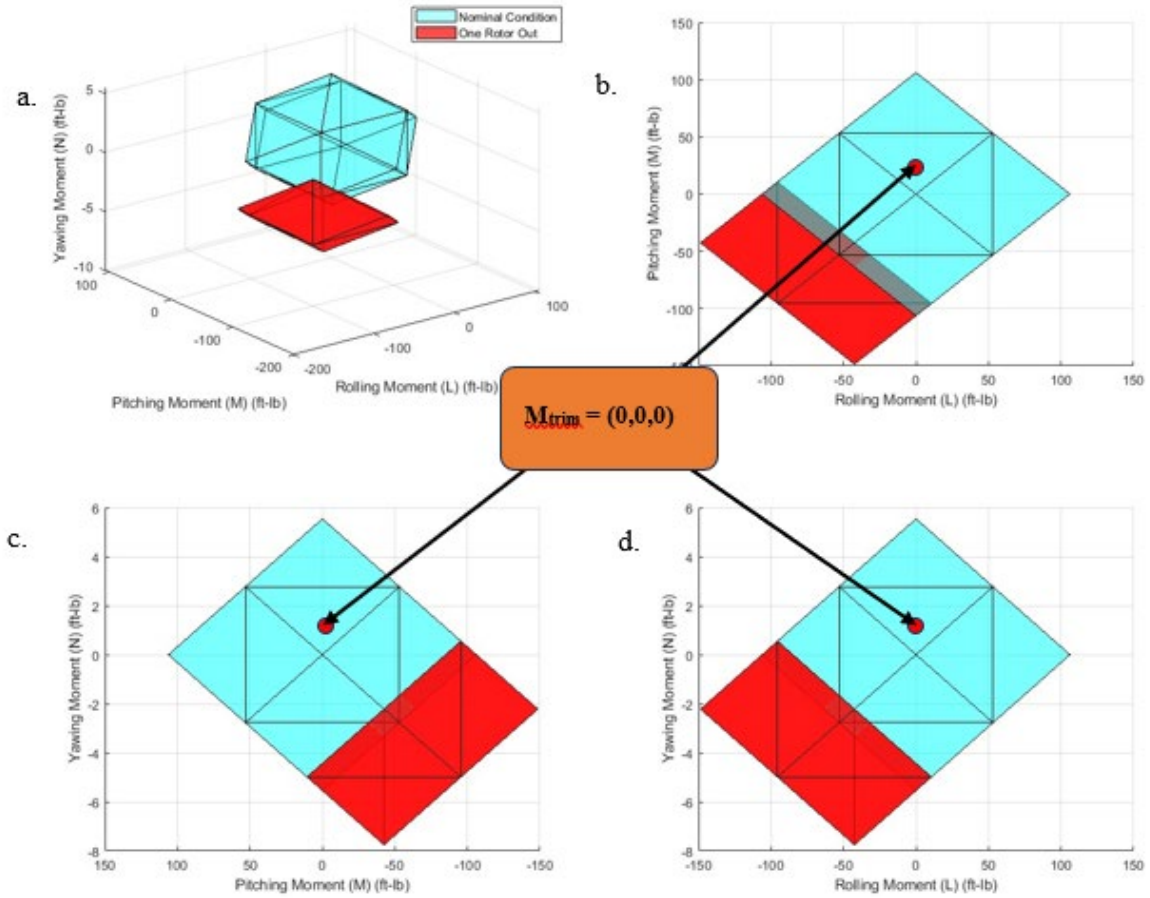

Figure 50. Moment envelopes for PAVER with RPM control (nominal and OEI)

Because the forces are constrained to the vertical body-Z axis of the vehicle, the force envelopes become one-dimensional, while the moment envelopes remain three-dimensional. By visual inspection, the rotors can produce sufficient thrust to counteract the vehicle's weight in both the nominal and one rotor out cases and cancel out the moments in the nominal case. However, the rotors are not capable of cancelling out the moments in the one rotor out case, since the point $M_{trim} = (0,0,0)$ does not fall within the boundaries of the red envelope in Figure 50. This is because with fixed-pitch RPM control, the rotors can only produce thrust in the upward direction, while with pitch control the direction of the thrust can be flipped by adjusting the blade pitch. In this case, a handling qualities cliff is present, because the pilot would lose control of the vehicle.

4.4.9 Force and moment envelope pilot displays

The previous methodology, involving the automatic prediction of forces and moments required to fly a trajectory and the comparison with the attainable force and moment envelopes can predict when a vehicle will run out of control power during any given task. Running out of

control power could result in certain handling qualities cliffs, with a good example being a one engine out scenario. However, this methodology's capability is very limited when it comes to predicting a wider range of handling qualities cliffs caused by vehicle and/or control law dynamic instability and pilot-in-the-loop effects. This is due to no pilot-vehicle interactions being considered and the force and moment envelopes mainly representing the static forces and moments acting on the vehicle. These limitations led to the development of a different methodology that displays how the force and moment envelopes of an airplane change as the pilot is flying it.

This methodology was developed using a nonlinear 6DOF model of a fixed-wing single engine airplane with a Lycoming IO-360 engine. This model takes control inputs from a joystick inceptor (elevator, aileron, rudder, throttle) and outputs the 12 vehicle states $(u, v, w, p, q, r, \phi, \theta, \Psi, x, y, h)$, along with other parameters of interest, such as true airspeed, angle of attack, sideslip angle, as well as the forces and moments acting on the vehicle. These parameters are then used to generate the force and moment envelope pilot display for airplane longitudinal motion, as shown in Figure 51.

The pilot display shows lift in both the positive and negative vertical directions, real-time drag to the right in the horizontal direction, and maximum attainable thrust to the left in the horizontal direction. The pitching moment envelope is shown in green, and its boundaries change depending on the aircraft's state. The left boundary indicates the maximum positive (nose-up) pitching moment and the right boundary indicates the maximum negative (nose-down) pitching moment. The tip of the magenta arrow shows the real-time force (combination of lift and thrust) being generated by the aircraft, while the origin of the magenta arrow moves throughout the moment envelope and shows the real-time pitching moment being generated. The origin and tip of the magenta arrow may lie within the boundaries of their respective envelopes but cannot go outside those boundaries. The black bars at the ends of the horizontal and vertical axes show where the aircraft's lift, thrust, and drag boundaries would be at the never-exceed speed.

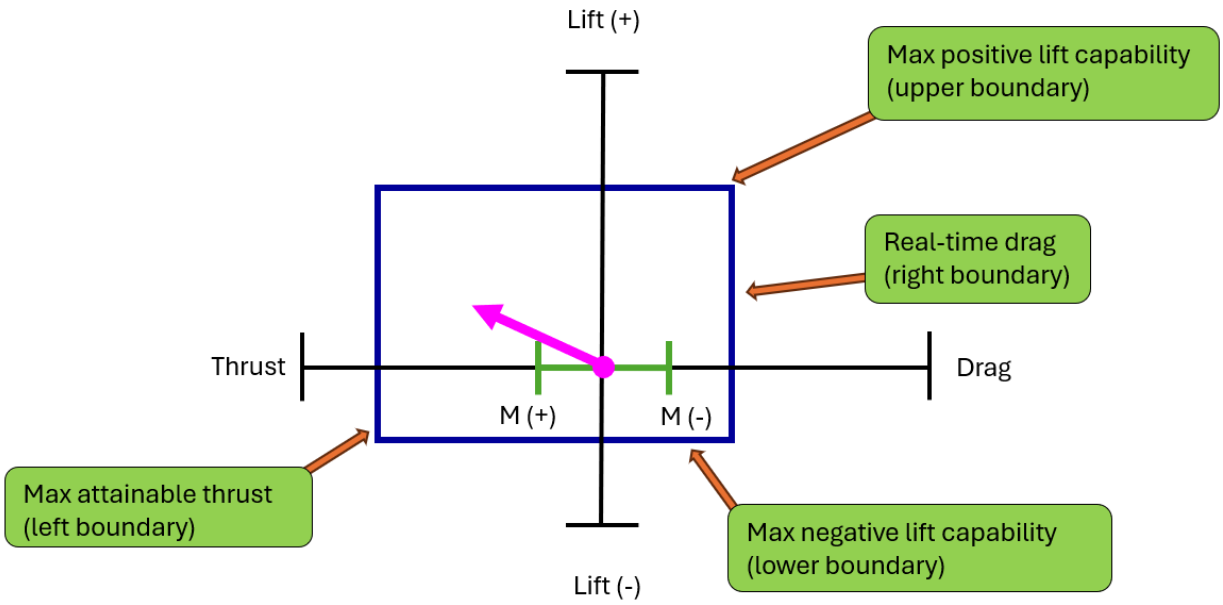

Figure 51. Pilot display description

The upper boundary of the force envelope is defined by the maximum positive lift capability, which is a function of maximum lift coefficient ($C_{L_{max}}$) and has a value of 1.7. The lift coefficient cannot go above this value, or else the aircraft will stall. Equation 21 is used to calculate this boundary. Similarly, the maximum lift coefficient in the negative direction ($C_{L_{min}}$), which is generated by negative angle of attack (α), can be used to define the lower boundary of the lift envelope and has a value of -0.5. Equation 22 is used to calculate this boundary.

$$L^{+} = \frac{1}{2}\rho V_{\infty}^{2} S C_{L_{max}} \tag{21}$$

$$L^{-} = \frac{1}{2}\rho V_{\infty}^{2} S C_{L_{min}} \tag{22}$$

Where ρ is the ambient atmospheric density, V_{∞} is the freestream velocity, and S is the wing reference area. The right-hand boundary of the force envelope is defined by the real-time drag force acting on the aircraft. The drag force (D) is calculated using Equation 23.

$$D = \frac{1}{2}\rho V_{\infty}^{2} S C_{D} \tag{23}$$

The drag coefficient (C_D) is a function of the drag coefficient at zero angle of attack (C_{D_o}) and C_{D_α}, which when multiplied by angle of attack gives lift-induced drag.

$$C_D = C_{D_o} + C_{D_\alpha}\alpha \quad (24)$$

Thrust capability is calculated using the IO-360 engine model shown in Figure 52 and setting it to max power, which causes the max thrust value to change as a function of airspeed and altitude. The engine operates continuously at 2400 RPM and a manifold pressure (MAP) of approximately 29.5 inHg corresponds to full power.

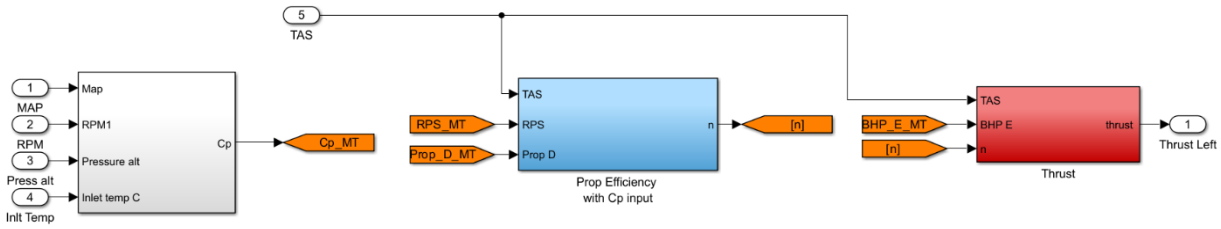

Figure 52. Lycoming IO-360 engine model

The boundaries of the moment envelope are calculated by finding the maximum positive and negative pitch control power ($C_{M_{\delta e}}$). The left boundary of the moment envelope is defined by the maximum nose-up (positive) pitching moment coefficient, which is found using Equation 25 by setting the elevator deflection (δe) to its full trailing-edge-up value. The right boundary of the moment envelope is defined by the maximum nose-down (negative) pitching moment coefficient, which is found using Equation 26 by setting δe to its full trailing-edge-down value.

$$C_M^+ = C_{M_{\delta e}}\delta e_{TEU} \quad (25)$$

$$C_M^- = C_{M_{\delta e}}\delta e_{TED} \quad (26)$$

These moment coefficients are then converted into moments using Equation 27, which makes the size of the pitching moment envelope a function of dynamic pressure.

$$M = \frac{1}{2}\rho V_\infty^2 S\bar{c}C_M \quad (27)$$

Where $\bar{c}$ is the mean geometric chord of the wing. The real-time lift and pitching moment coefficients acting on the airplane are calculated using Equation 28 and Equation 29. These are then converted from coefficients into the lift and pitching moment values that are displayed by the magenta arrow. The real-time thrust is obtained directly from the engine model.

$$C_L = C_{L_\alpha}\alpha + C_{L_{\hat{q}}} q \frac{\bar{c}}{2V_\infty} + C_{L_{\delta e}}\delta e \quad (28)$$

$$C_M = C_{M_\alpha}\alpha + C_{M_{\hat{q}}} q \frac{\bar{c}}{2V} + C_{M_{\delta e}}\delta e \quad (29)$$

The above equations and engine model calculate the forces and moments in units of lb_f and ft-lb. Before being displayed to the pilot, they are normalized with respect to the absolute maximum boundaries of the force and moment envelopes, which occur at the airplane's never-exceed speed (lift, drag, and pitching moment) and at the airplane's stall speed (thrust). Examples of how the display changes throughout flight are shown below.

Five example scenarios were chosen to demonstrate how the pilot displays would show how the flight envelope changes as a function of the airplane's state and how the location of the aircraft within its flight envelope is displayed to the pilot. These scenarios involve the airplane in straight and level flight, a high positive load factor maneuver, immediately after the high positive load factor maneuver, a high negative load factor maneuver, and approaching the never-exceed speed.

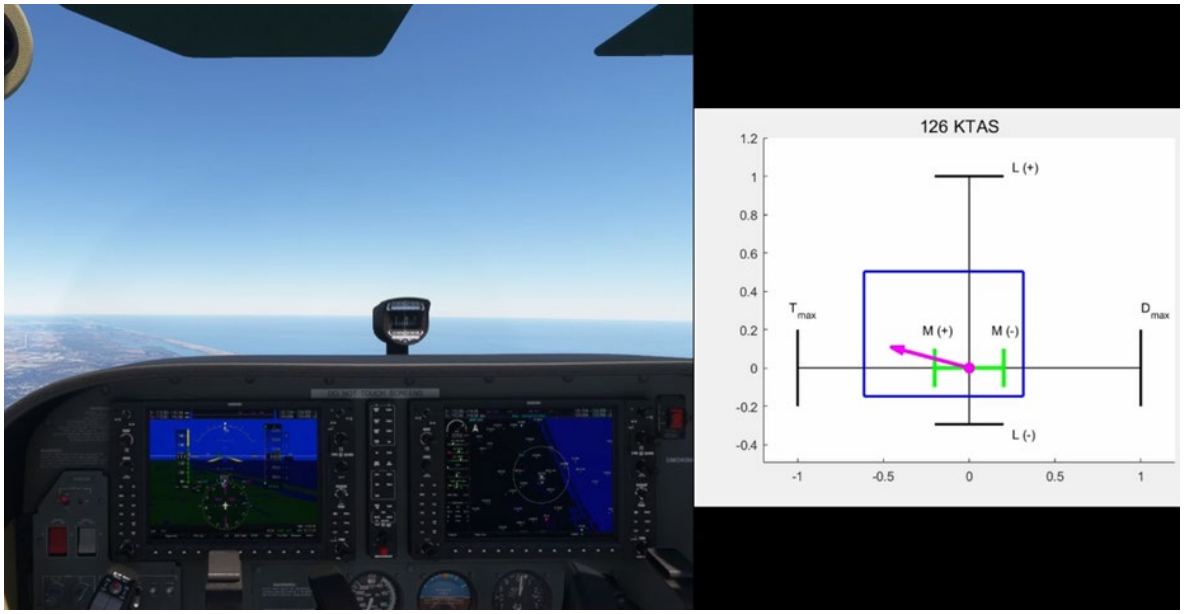

Figure 53. Pilot display for airplane in straight and level flight

In Figure 53 above, the airplane is in straight and level flight. The origin of the magenta arrow is in the middle of the green moment envelope, showing that no pitching moment is being generated by the airplane's elevator. The tip of the magenta arrow shows the thrust and lift being generated by the airplane. The airplane's knots true airspeed (KTAS) is 126.

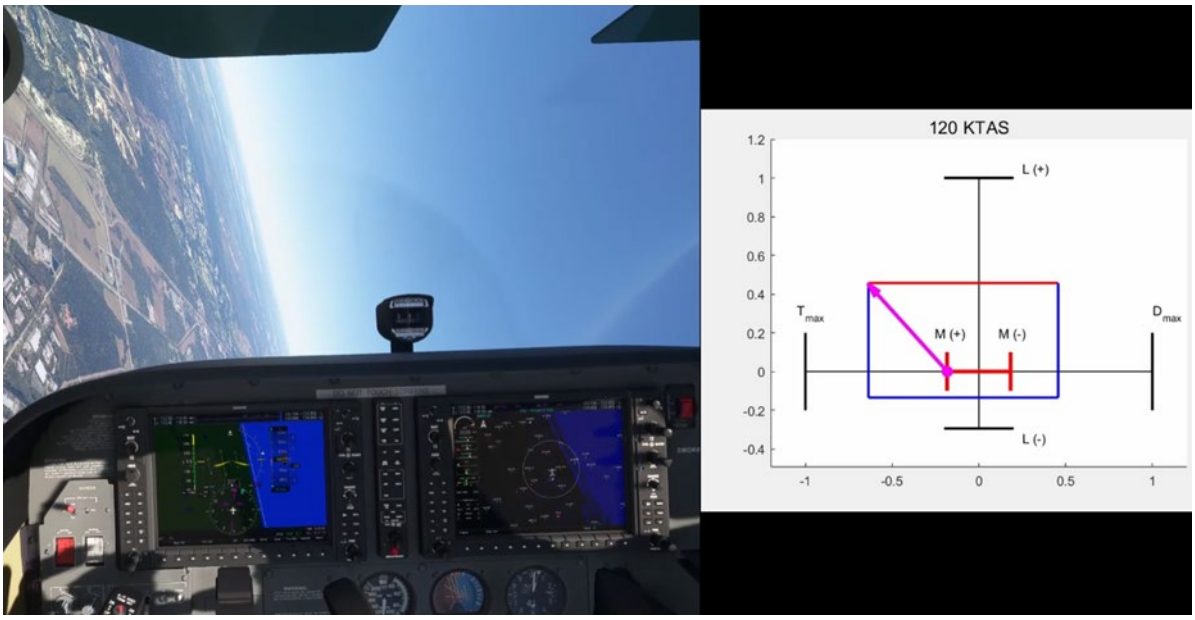

Figure 54. Pilot display for airplane in a high positive load factor maneuver

As the airplane performs a high positive load factor maneuver with full positive elevator deflection, the origin of the magenta arrow is at the left end of the moment envelope, indicating that the airplane is generating its max positive (nose up) pitching moment. The tip of the magenta arrow indicates that the airplane's engine is producing max thrust and that the wings are generating maximum lift in the positive direction. The moment envelope and the upper boundary of the force envelope turn red to show to the pilot that the airplane is on the verge of stall.

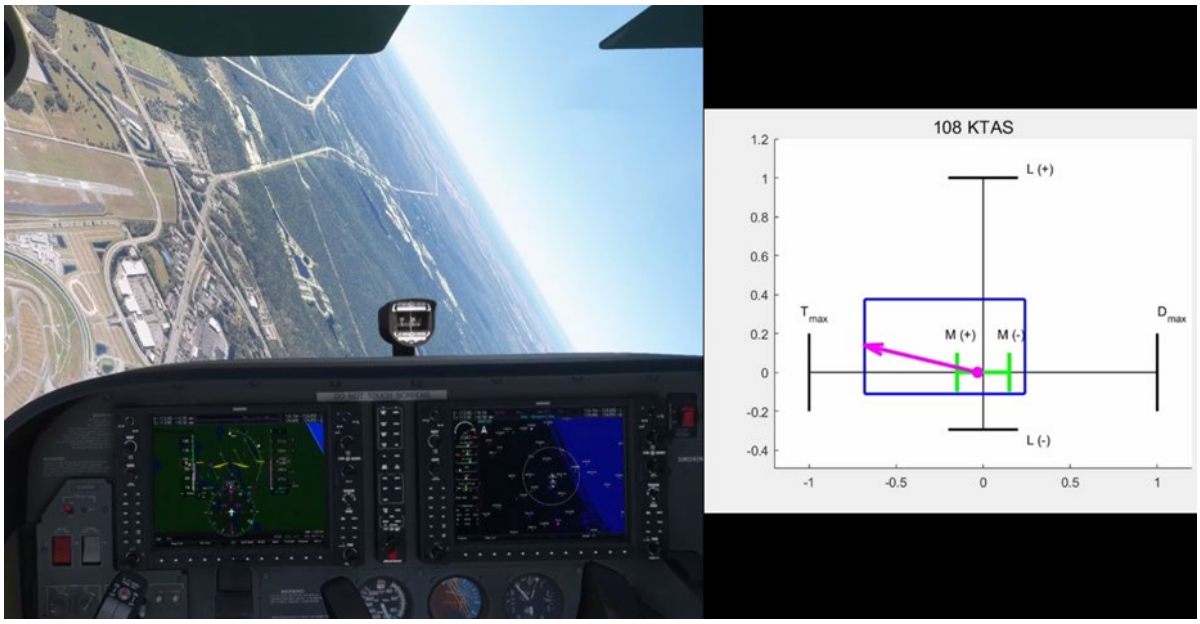

Figure 55. Pilot display for airplane immediately after high positive load factor maneuver

Immediately after the high positive load factor maneuver, the pilot lets go of the stick and the true airspeed drops to 108 KTAS from 120 KTAS before starting the maneuver. This drop in airspeed results in the lift and drag portion of the envelope becoming smaller and the thrust portion becoming slightly wider.

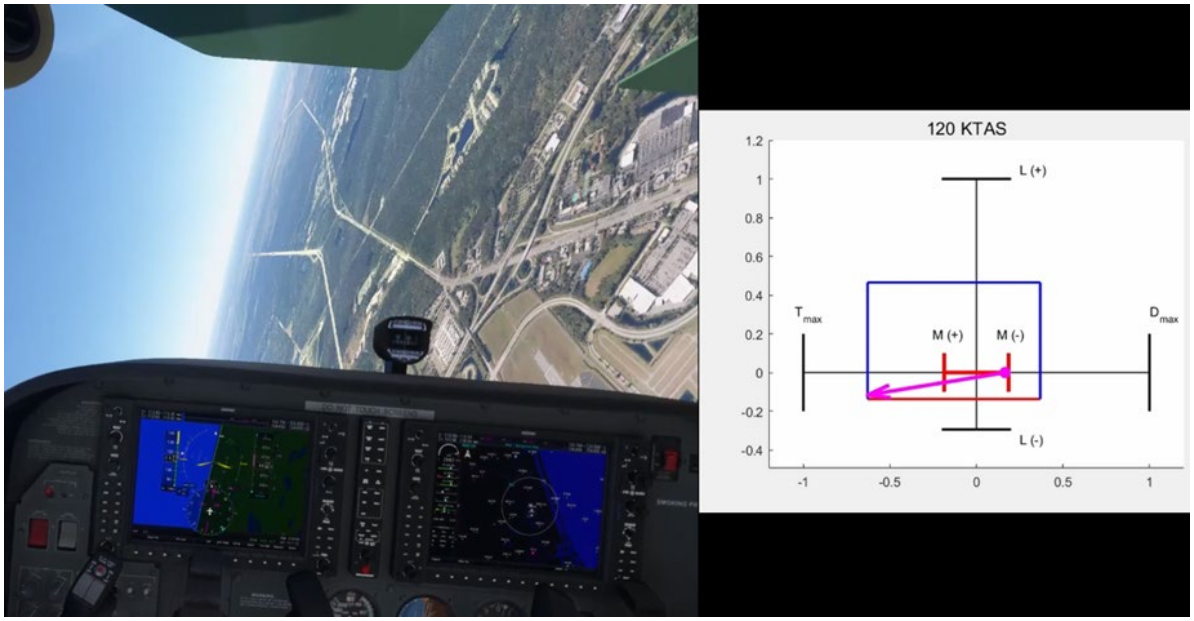

Figure 56. Pilot display for airplane in high negative load factor maneuver

As the airplane performs a high negative load factor maneuver, the origin of the magenta arrow moves to the right end of the moment envelope, indicating that the airplane is generating its max negative (nose down) pitching moment. The tip of the magenta arrow indicates that the airplane's engine is producing max thrust and that the wings are generating maximum lift in the negative direction. The moment envelope and the lower boundary of the force envelope turn red to show to the pilot that the airplane is on the verge of stall.

It should also be noted that a handling qualities cliff could involve a stall, but that not all stalls amount to handling qualities cliffs. A controlled stall, like the ones performed by flight students during training, would not be considered handling qualities cliffs. However, unexpected stalls that may occur during flight testing of nontraditional vehicle concepts that could result in loss of control could be considered handling qualities cliffs.

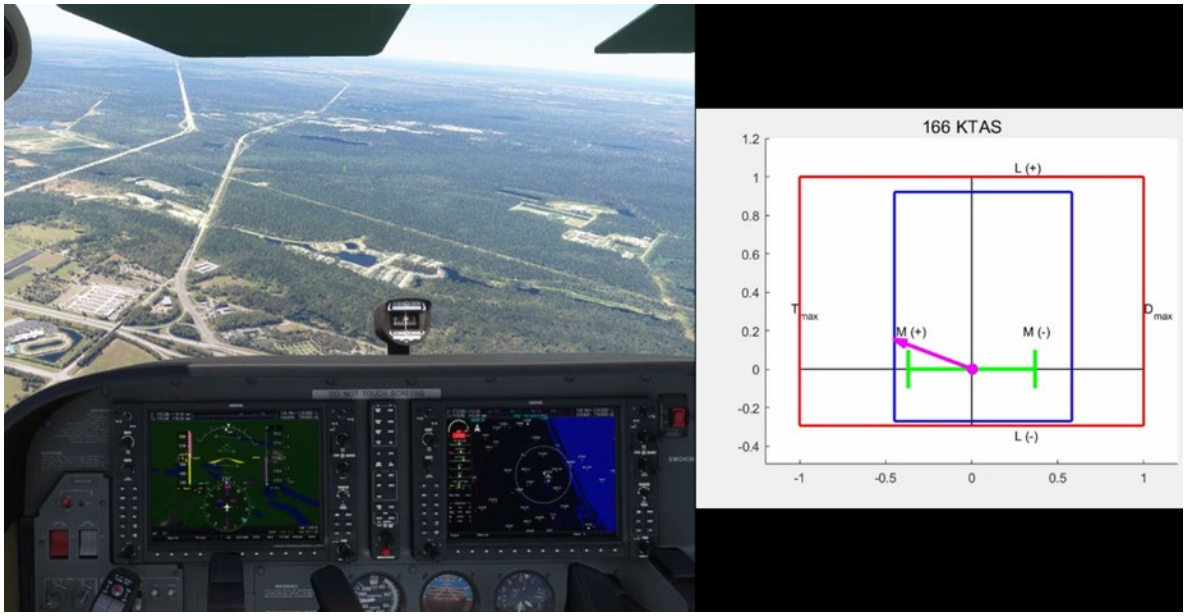

Figure 57. Pilot display for airplane approaching never-exceed speed

As the airplane approaches its never exceed speed (V_{NE}), a red box will form around the envelope, signaling to the pilot to reduce power and slowly pull out of the dive to not exceed V_{NE} or the limit load factor of the aircraft. Exceeding V_{NE} could result in flutter or other unpredictable aircraft oscillations that could amount to handling qualities cliffs. As the airplane approaches V_{NE}, the lift and drag portions of the force envelope become wider and the thrust portion becomes narrower. The moment envelope also becomes wider as a result.

4.4.10 Lessons learned

The first methodology, involving the automatic computation of required forces and moments through flight simulation and comparison with the attainable force and moment envelopes, was

intended to be a low-cost low-risk method for predicting handling qualities cliffs without the need for flight testing or any pilot input. While this methodology can predict handling qualities cliffs that could result from running out of control power and/or losing a rotor, it is unable to predict handling qualities cliffs resulting from dynamic aircraft and/or control law instability as well as pilot-in-the-loop effects. This is due to the force and moment envelopes at each given state being static in nature.

These limitations led to the development of a second methodology that displays the force and moment envelopes to the pilots as they are flying the vehicle as well as the aircraft's location with respect to the boundaries of these envelopes. This method combines real-time flight simulation or flight testing with pilot input. It could therefore help uncover a wider range of dynamic handling qualities cliffs as well as alert test pilots when the airplane is about to run out of control power, much like the first methodology. When used with ground-based simulation, it could serve as a means for test pilots to become familiar with the limits of a new aircraft's flight envelope in a safe environment and therefore improve flight test safety once the pilot sets foot in a real test aircraft.

To account for the full range of handling qualities cliffs an aircraft could be expected to encounter, either of the two methods would need to be used in combination with highly realistic aircraft flight dynamics models. During the investigation of the AW609 crash, the engineers were unable to recreate the Dutch roll oscillations that led to the in-flight breakup on the flight simulator. If the flight simulator had been able to recreate these, the accident could have been avoided.

To maximize effectiveness of the first methodology involving required vs. attainable forces and moments prediction, the following changes are recommended:

- Require forces and moments prediction code that can account for different control strategies instead of just the differential collective pitch/RPM control strategy.
- Include dynamic envelopes that consider any delays between when the pilot commands a force or moment from the effectors and when the maximum steady-state forces and moments are achieved.
- Improve computational efficiency to more efficiently analyze configurations with large numbers of effectors and allow for real-time computation of the envelopes. This could be done by finding the minimum number of points required to define the convex hull of these envelopes and feeding the control input combinations associated with these points

into the flight simulation model to generate these force and moment envelopes in real time.

- Develop realistic pilot models that can account for how a pilot might respond to a wide range of events which could include in-flight upsets, wind gusts and turbulence, effector failures, flight control failures, etc.
- Develop realistic flight simulation models that can recreate all the possible situations that could lead to handling qualities cliffs.
- Since the force and moment envelopes are independent from one another, develop an algorithm that will find out which envelope demands the most from the vehicle's effectors (in the case of PAVER, this would be force). Once this envelope is found, a control allocation algorithm would then be used to allocate the vehicle's controls to generate this force, and the moment envelope would be generated using the remaining available control power.

To maximize effectiveness of the second methodology involving the pilot displays, the following changes are recommended:

- The equations used to calculate the lift, drag, thrust, and pitching moment envelope boundaries for a fixed-wing airplane are very simple and computationally efficient. Since eVTOLs often feature multiple rotors and complex control strategies, equations that can efficiently predict the force and moment envelope boundaries of these configurations are necessary.
- Provide realistic flight simulation models that can recreate all the possible situations that could lead to handling qualities cliffs.
- Before using the pilot displays for flight testing, predict all the possible scenarios that could lead to handling qualities cliffs resulting from dynamic situations in addition to those resulting from running out of control power. This is necessary so that the pilot displays can alert pilots when they are approaching such a situation and thereby help avoid loss of control.
- In a high-speed situation, the pilot might have sufficient control authority to generate enough lift to overstress the airframe. Find a way to display structural limits as well as control law limitations to the pilot.

For piloted aircraft, predictions of handling qualities cliffs with actual test pilots in the loop will almost always be more accurate than those carried out by an automated methodology involving a

pilot model. Models that can accurately predict how a pilot might respond to a wide range of events are difficult to create since no two pilots are the same. However, it is predicted that eVTOLs will eventually become autonomous; in such cases, the pilot displays would not be of much use to a human pilot.

4.5 Task E: Nonlinear dynamic inversion control method and eVTOL control allocation process

In this section, the controller design process for a rotorcraft will be presented. First, a nonlinear dynamic inversion approach will be introduced, and then control allocation design process will be investigated. The control allocation section allows someone to convert control inputs to the actuator commands without being affected by the different types of actuation structures. As seen in Figure 58, the control input implemented to the system dynamics produces an acceleration that is converted to the velocity and position with integrations.

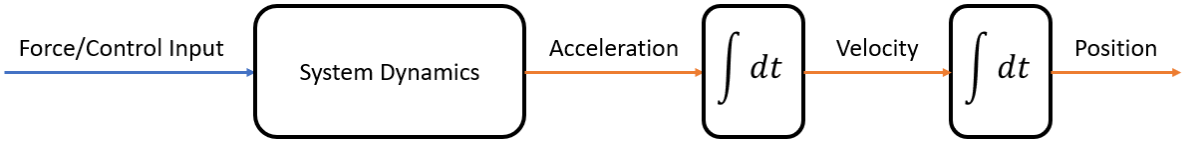

Figure 58. General representation of force/control and system states relation

NLDI Control is an algorithm that calculates the required control input (force) that cancels out the system dynamics, including the nonlinear terms for driving the vehicle to the desired position or velocity. Once the system dynamics are canceled out, the vehicle can track the acceleration commands. In the NLDI process, any type of controller can be used (e.g., PID or LQR, etc.), to produce the desired acceleration from the tracking error. Once the desired acceleration is generated, one can apply these accelerations to the system by inverting the system dynamics and actuator characteristics. This structure can be seen in Figure 59.

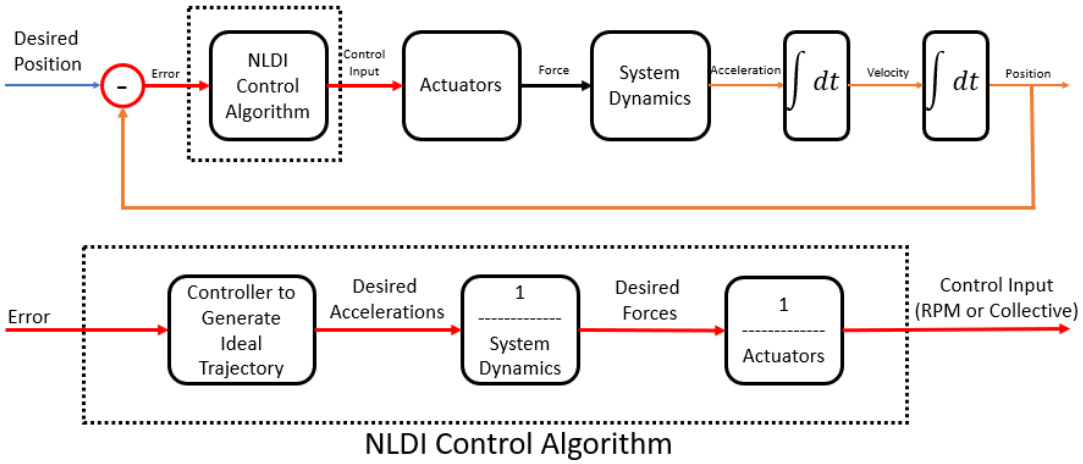

Figure 59. Overall structure of the nonlinear dynamic inversion control design and control allocation process

4.5.1 Nonlinear dynamic inversion control

This section presents a nonlinear dynamic inversion controller for controlling the attitude dynamics of a quadcopter-type aerial vehicle. First, the dynamic model, together with kinematics, is obtained. Then, a nonlinear dynamical inversion controller is designed.

4.5.1.1 Dynamic modelling

Equations of motion for the attitude dynamics of the quadcopter-type aerial vehicle can be written as

$$\tau(t) = I\dot{\omega}(t) + \omega(t) \times \big(I\omega(t)\big), \tag{30}$$

where $\tau(t) = \big[\tau_\phi(t), \tau_\theta(t), \tau_\psi(t)\big]^T \in \mathbb{R}^3$ is the torque vector, with $\tau_\phi(t)$, $\tau_\theta(t)$, $\tau_\psi(t)$ being the torques about x, y, and z axes, respectively, $\omega(t) = [p(t), q(t), r(t)]^T \in \mathbb{R}^3$ is the angular velocity vector in the body frame with $p(t)$, $q(t)$, $r(t)$ being the angular velocities about x, y, and z axes, respectively, and $I \in \mathbb{R}^{3\times3}$ is the moment of inertia matrix given by

$$I = \begin{bmatrix} I_{xx} & I_{xy} & I_{xz} \\ I_{yx} & I_{yy} & I_{yz} \\ I_{zx} & I_{zy} & I_{zz} \end{bmatrix}. \tag{31}$$

For the sake of simplicity, the aerial vehicle is assumed to be symmetric about x and y axes, which means $I_{xy} = I_{yx} = I_{xz} = I_{zx} = I_{yz} = I_{zy} = 0$, resulting in the following inertia matrix:

$$I = \begin{bmatrix} I_{xx} & 0 & 0 \\ 0 & I_{yy} & 0 \\ 0 & 0 & I_{zz} \end{bmatrix}. \quad 32$$

Inserting the moment of inertia matrix given in Equation 32 to the attitude dynamics in Equation 30 for each axis, and writing each axis separately yields

$$\tau_{\phi}(t) = I_{xx}\dot{p}(t) + \big(I_{zz} - I_{yy}\big)q(t)r(t), \quad 33$$
$$\tau_{\theta}(t) = I_{yy}\dot{q}(t) + (I_{xx} - I_{zz})p(t)r(t), \quad 34$$
$$\tau_{\psi}(t) = I_{zz}\dot{r}(t) + \big(I_{yy} - I_{xx}\big)p(t)q(t). \quad 35$$

Modifying the above equations and leaving the angular acceleration alone on the left side yields

$$\dot{p}(t) = I_{xx}^{-1}\Big(\tau_{\phi}(t) - \big(I_{zz} - I_{yy}\big)q(t)r(t)\Big), \quad 36$$
$$\dot{q}(t) = I_{yy}^{-1}\big(\tau_{\theta}(t) - (I_{xx} - I_{zz})p(t)r(t)\big), \quad 37$$
$$\dot{r}(t) = I_{zz}^{-1}\Big(\tau_{\psi}(t) - \big(I_{yy} - I_{xx}\big)p(t)q(t)\Big). \quad 38$$

These equations conclude the attitude dynamics, where nonlinear terms appear as multiplied angular velocities due to the cross-product.

In addition, derivatives of the Euler angles $\phi(t)$, $\theta(t)$, $\psi(t)$ are not exactly equal to the angular velocities $p(t)$, $q(t)$, $r(t)$ in the body frame. One can write the attitude kinematics, which defines the kinematic relation between time derivatives of the Euler angles and angular velocities in the body frame as

$$\begin{bmatrix} p(t) \\ q(t) \\ r(t) \end{bmatrix} = \begin{bmatrix} 1 & 0 & -\sin(\theta) \\ 0 & \cos(\phi) & \cos(\theta)\sin(\phi) \\ 0 & -\sin(\phi) & \cos(\phi)\cos(\theta) \end{bmatrix} \begin{bmatrix} \dot{\phi}(t) \\ \dot{\theta}(t) \\ \dot{\psi}(t) \end{bmatrix}. \quad 39$$

Writing these equations separately for each axis yields

$$p(t) = \dot{\phi}(t) - \sin(\theta)\dot{\psi}(t), \quad (40)$$

$$q(t) = \cos(\phi)\dot{\theta}(t) + \cos(\theta)\sin(\phi)\dot{\psi}(t), \quad (41)$$

$$r(t) = -\sin(\phi)\dot{\theta}(t) + \cos(\phi)\cos(\theta)\dot{\psi}(t). \quad (42)$$

This concludes the dynamics and kinematics modeling part. The following section will investigate the nonlinear dynamic inversion controller design process.

4.5.1.2 Nonlinear dynamic inversion controller design

In the previous section, the dynamics are defined; in this section, NLDI controller is designed. This controller consists of two consecutive controllers, where k_{p1}, k_{i1}, and k_{d1} are the PID control gains, producing desired torques to compensate for angular position error. One can start with designing a PID controller to produce desired angular velocity values by using the angular position error given as

$$\dot{\phi}^*(t) = k_{p1}\big(\phi_d(t) - \phi(t)\big) + k_{i1}\int\big(\phi_d(t) - \phi(t)\big) - k_{d1}p(t), \quad (43)$$

$$\dot{\theta}^*(t) = k_{p1}\big(\theta_d(t) - \theta(t)\big) + k_{i1}\int\big(\theta_d(t) - \theta(t)\big) - k_{d1}q(t), \quad (44)$$

$$\dot{\psi}^*(t) = k_{p1}\big(\psi_d(t) - \psi(t)\big) + k_{i1}\int\big(\psi_d(t) - \psi(t)\big) - k_{d1}r(t). \quad (45)$$

It is important to note that these desired angular velocities are time derivatives of the Euler angles. They are needed to use the kinematics given in Equations 40, 41, and 42, which yields

$$p^*(t) = \dot{\phi}^*(t) - \sin(\theta)\dot{\psi}^*(t), \quad (46)$$

$$q^*(t) = \cos(\phi)\dot{\theta}^*(t) + \cos(\theta)\sin(\phi)\dot{\psi}^*(t), \quad (47)$$

$$r^*(t) = -\sin(\phi)\dot{\theta}^*(t) + \cos(\phi)\cos(\theta)\dot{\psi}^*(t). \quad (48)$$

This completes the first PID loop and Equations 46, 47, and 48 provide the desired angular velocity values in the body frame. Now, one can use another proportional controller, where k_{p2} is the

proportional control gain, to produce desired angular accelerations in the body frame by using the angular velocity tracking error such as

$$\dot{p}^*(t) = k_{p2}\big(p^*(t) - p(t)\big), \quad 49$$
$$\dot{q}^*(t) = k_{p2}\big(q^*(t) - q(t)\big), \quad 50$$
$$\dot{r}^*(t) = k_{p2}\big(r^*(t) - r(t)\big). \quad 51$$

Once the desired angular accelerations are obtained through the cascaded controllers, one can use Equations 33, 34, and 35 to complete nonlinear dynamical inversion controller given by

$$\tau_{\phi}^*(t) = I_{xx}\dot{p}^*(t) + \big(I_{zz} - I_{yy}\big)q(t)r(t), \quad 52$$
$$\tau_{\theta}^*(t) = I_{yy}\dot{q}^*(t) + (I_{xx} - I_{zz})p(t)r(t), \quad 53$$
$$\tau_{\psi}^*(t) = I_{zz}\dot{r}^*(t) + \big(I_{yy} - I_{xx}\big)p(t)q(t). \quad 54$$

4.5.1.3 Simulation results

In this section, simulation results of applying nonlinear dynamic inversion control for controlling attitude dynamics of a quadcopter type aerial vehicle are provided. Results can be seen in Figure 60, Figure 61, and Figure 62.

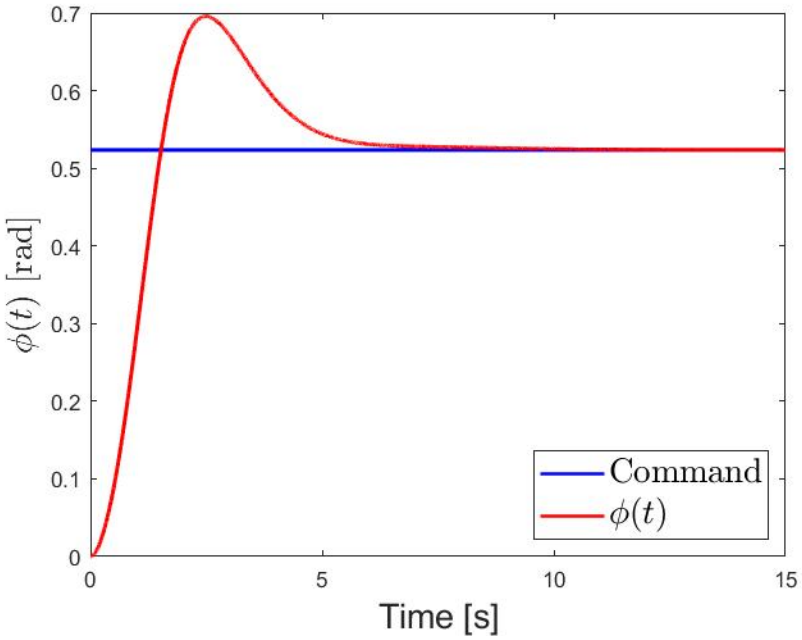

Figure 60. Roll control trajectory

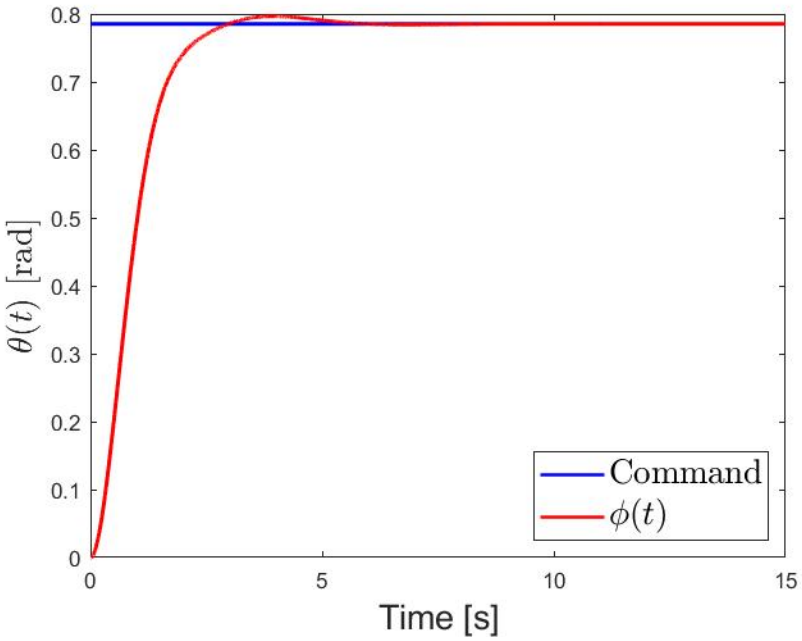

Figure 61. Pitch control trajectory

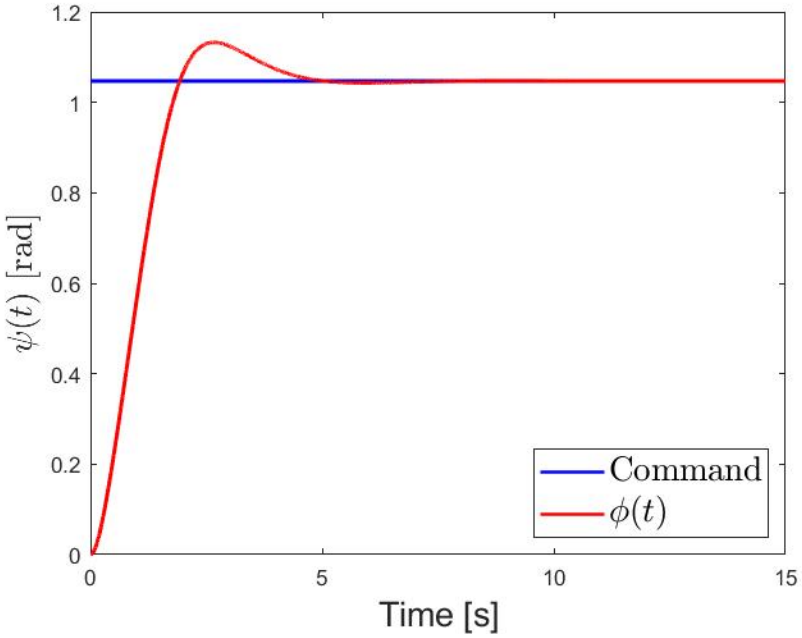

Figure 62. Yaw control trajectory

4.5.2 Control allocation

To achieve stable and safe flight, the desired commands of the pilot should be fully transferred to the aerial vehicle. In classical fixed-wing platforms, pilots can move the control surfaces using an inceptor for the desired maneuver, and there is a direct connection between the pilot and aircraft control surfaces. Another example can be given for helicopters in which the pilot can change the pitch angles of the blades using cyclic and collective sticks. On the other hand, multirotor platforms have a different approach, because it is too difficult for a pilot to control one or more rotors at the same time to adjust roll, pitch, yaw, and altitude. Additionally, multirotors are significantly more complex platforms, which necessitate FBW flight control systems. This leads to implementing digital control allocation methods rather than a mechanical solution, like a complex helicopter swashplate system, which controls four rotors at the same time for the desired maneuver.

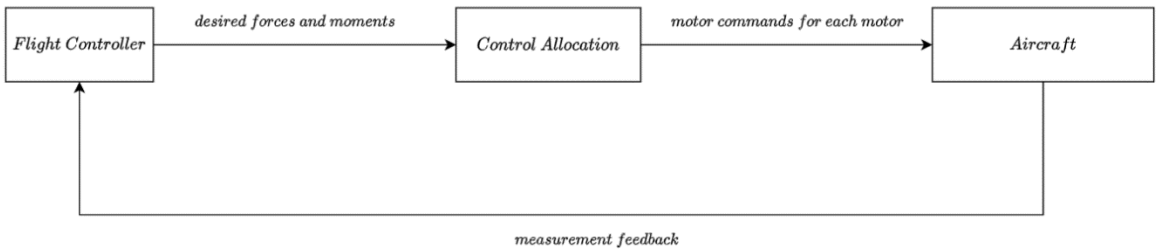

Figure 63. Control allocation scheme

General architecture of a flight system for multirotors comprises from two elements as flight controller (stability augmentation system) and control allocation sections. The flight controller is responsible for generating desired forces and moments using pilot commands for every iteration. It is essential that these virtual control inputs should be actualized by the multirotor itself. This will guarantee that vehicle will fly with the desired performance criteria. Control allocation plays a critical role in ensuring that the vehicle generates these desired moments and forces during the flight and acts like how the flight controller wants. These two sections have different responsibilities as a pilot and a digital swashplate: the flight controller is the pilot where the necessary commands are generated, and control allocation is the digital swashplate that decides what should be the control input of each rotor (Figure 63). Classical fixed-pitch multirotor platforms have only one control input (RPM command), and control allocation is responsible for calculating how much RPM each rotor needs for the desired forces and moments. This control allocation method is related to the vehicle geometry and motor characteristics, which is called the motor mixing algorithm (MMA). This algorithm is a simplified relation between forces/moments acting on the center of gravity and rotor RPMs of the vehicle. Eventually, using this relation necessary RPM for each rotor can be found by knowing virtual control inputs generated by the flight controller.

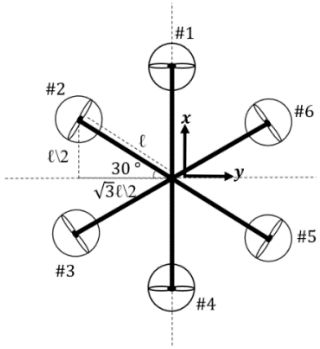

Figure 64. Hexacopter geometry

As an example, Figure 64 presents a hexacopter geometry to explain the concept of motor mixing matrix in a more realistic way.

$$\begin{bmatrix} F \\ T_{\emptyset} \\ T_{\theta} \\ T_{\varphi} \end{bmatrix} = M \begin{bmatrix} {\omega_1}^2 \\ {\omega_2}^2 \\ {\omega_3}^2 \\ {\omega_4}^2 \\ {\omega_5}^2 \\ {\omega_6}^2 \end{bmatrix} \quad 55$$

Shown is F, vertical total force, $T_{\emptyset}$ roll axis moment, T_{θ} pitch axis moment, T_{φ} yaw axis moment, and ω_i, the ith number rotor`s RPM.

$$M = \begin{bmatrix} lk_l & lk_l & lk_l & lk_l & lk_l & lk_l \\ 0 & \frac{\sqrt{3}}{2}lk_l & \frac{\sqrt{3}}{2}lk_l & 0 & -\frac{\sqrt{3}}{2}lk_l & -\frac{\sqrt{3}}{2}lk_l \\ lk_l & \frac{1}{2}lk_l & -\frac{1}{2}lk_l & -lk_l & -\frac{1}{2}lk_l & \frac{1}{2}lk_l \\ -k_d & k_d & -k_d & k_d & -k_d & k_d \end{bmatrix} \quad 56$$

Also shown is l, the length of the motor arm k_l as lift coefficient of the rotor and k_d as drag coefficient of the rotor. As stated above, this relation can be reversed, and the desired virtual forces and moments generated by the flight controller can be allocated through six rotors, and each rotor RPM can be found for each command using the relation.

$$M^{-1} \begin{bmatrix} F \\ T_{\emptyset} \\ T_{\theta} \\ T_{\varphi} \end{bmatrix} = \begin{bmatrix} {\omega_1}^2 \\ {\omega_2}^2 \\ {\omega_3}^2 \\ {\omega_4}^2 \\ {\omega_5}^2 \\ {\omega_6}^2 \end{bmatrix} \quad 57$$

This control allocation matrix is linear and very effective by using two-norm optimization (pseudo-inverse) method. In classical fixed-pitch blade multirotor configurations, the only control input is RPM command, so this matrix is enough for the control allocation of a multirotor. PAVER has multiple control input opportunities, so this mixing should be done not just for RPMs, but also for an addition of collective and lateral/longitudinal cyclic commands for reaching the desired forces and moments generated by the flight controller. The same approach with classical multirotors can be expanded and improved for PAVER. However, this time, there

will be multiple combinations of control inputs to reach the desired point. Therefore, there are some restrictions needed to decide which control input will have priority or major effect.

$$\begin{bmatrix} F_x \\ F_y \\ F_z \\ T_\emptyset \\ T_\theta \\ T_\varphi \end{bmatrix} = M \begin{bmatrix} {\omega_1}^2, \delta_{1col}, \delta_{1cyc-lat}, \delta_{1cyc-long} \\ {\omega_2}^2, \delta_{2col}, \delta_{2cyc-lat}, \delta_{2cyc-long} \\ {\omega_3}^2, \delta_{3col}, \delta_{3cyc-lat}, \delta_{3cyc-long} \\ {\omega_4}^2, \delta_{4col}, \delta_{4cyc-lat}, \delta_{4cyc-long} \\ {\omega_5}^2, \delta_{5col}, \delta_{5cyc-lat}, \delta_{5cyc-long} \\ {\omega_6}^2, \delta_{6col}, \delta_{6cyc-lat}, \delta_{6cyc-long} \end{bmatrix} \quad 58$$

where ω_i is rotor RPM, δ_{i-col} is collective command, $\delta_{i-cyc-lat}$ is lateral cyclic command, and $\delta_{i-cyc-long}$ is longitudinal cyclic command for *i*th rotor. After finding the relation between generated forces and moments with each control input, this relation can be reversed for allocating the desired forces and moments to each rotor and finding which and how much control input should be used for each rotor to maintain desired rotor forces and moments.

$$M^{-1} \begin{bmatrix} F_x \\ F_y \\ F_z \\ T_\emptyset \\ T_\theta \\ T_\varphi \end{bmatrix} = \begin{bmatrix} {\omega_1}^2, \delta_{1-col}, \delta_{1-cyc-lat}, \delta_{1-cyc-long} \\ {\omega_2}^2, \delta_{2-col}, \delta_{2-cyc-lat}, \delta_{2-cyc-long} \\ {\omega_3}^2, \delta_{3-col}, \delta_{3-cyc-lat}, \delta_{3-cyc-long} \\ {\omega_4}^2, \delta_{4-col}, \delta_{4-cyc-lat}, \delta_{4-cyc-long} \\ {\omega_5}^2, \delta_{5-col}, \delta_{5-cyc-lat}, \delta_{5-cyc-long} \\ {\omega_6}^2, \delta_{6-col}, \delta_{6-cyc-lat}, \delta_{6-cyc-long} \end{bmatrix} \quad 59$$

4.5.2.1 Relation of rotor force and RPM/collective control inputs

To construct the M matrix, the first step is to understand how much force/torque is generated by each collective and RPM commands (Figure 65 and Figure 66). These relations are called lift (k_l) and drag (k_d) coefficients.

$$Force = k_l {\omega_i}^2 \quad 60$$

$$Torque = k_d {\omega_i}^2 \quad 61$$

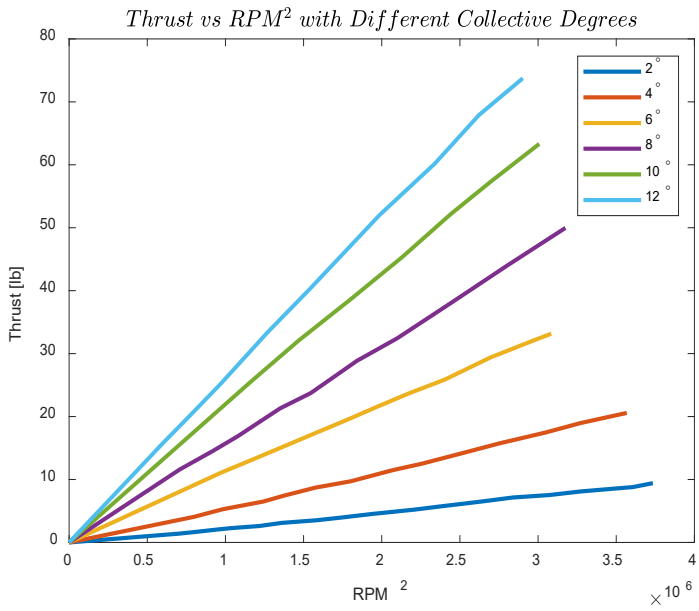

Figure 65. Thrust curves of the rotor

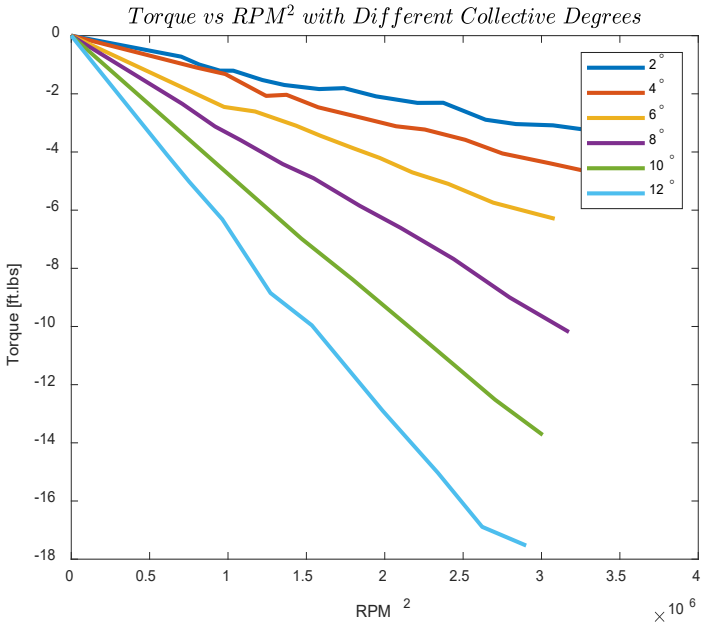

Figure 66. Torque curves of the rotor

Collective rotor experiments revealed that square of rotor RPM is linear with the generated force and torque. The collective angle for blades changes the steepness of the curve, which changes the lift and drag coefficients. The results are summarized below in Table 1 and Table 2.

Table 1: Lift coefficient table

Collective Blade Angle	**Lift Coefficient (k_l)**
2°	1.079×10^{-5}
4°	2.516×10^{-5}
6°	4.838×10^{-5}
8°	6.962×10^{-5}
10°	9.478×10^{-5}
12°	11.49×10^{-5}

Table 2: Drag coefficient table

Collective Blade Angle	**Drag Coefficient (k_d)**
2°	-1.376×10^{-6}
4°	-1.933×10^{-6}
6°	-2.872×10^{-6}
8°	-4.34×10^{-6}
10°	-6.28×10^{-6}
12°	-8.646×10^{-6}

A numerical example was created with a desired 329.1 Newton vertical force to show the difference between necessary RPMs of each rotor with different collective blade angles. Each RPM combination is shown in Table 3 to maintain the desired vertical force.

$$M^{-1}\begin{bmatrix}329.1\\0\\0\\0\end{bmatrix}=\begin{bmatrix}{\omega_1}^2\\{\omega_2}^2\\{\omega_3}^2\\{\omega_4}^2\end{bmatrix} \quad (62)$$

Table 3: RPM table with different collective angles

Collective Blade Angle	**2° each**	**4° each**	**6° each**	**8° each**	**10° each**	**12° each**
RPM_1	2780	1819	1312	1094	937	851
RPM_2	2780	1819	1312	1094	937	851
RPM_3	2780	1819	1312	1094	937	851
RPM_4	2780	1819	1312	1094	937	851

The required RPM for each rotor to maintain the desired vertical force decreases with increasing collective angle. There are no desired moments on the roll, pitch and yaw axis in this example, which results in each rotor RPM being equal. This numerical example can be expanded by adding desired moments on roll, pitch, and yaw axes or by giving different collective angles for each rotor.

Although this strategy combines the collective and RPM effector inputs for PAVER, four collective angles of each rotor are given by the user. This is a critical assumption. First, the collective angle of each rotor should be specified; then, each rotor RPM can be found by the given matrix M. Different approaches will be introduced to find both RPM and collective inputs, and specifying one of them is not necessary. This is an overactuated problem, because there will be several combinations of RPM and collective input to maintain the desired forces.

4.5.2.2 Control allocation—Optimization-based approach

The classical relationship between generated forces/moments and RPM effector input (W_i) of PAVER is stated using *M* matrix below.

$$\begin{bmatrix} F \\ L \\ M \\ N \end{bmatrix} = \begin{bmatrix} kl_1 & kl_2 & kl_3 & kl_4 \\ -\frac{\sqrt{2}}{2} lkl_1 & \frac{\sqrt{2}}{2} lkl_2 & \frac{\sqrt{2}}{2} lkl_3 & -\frac{\sqrt{2}}{2} lkl_4 \\ \frac{\sqrt{2}}{2} lkl_1 & \frac{\sqrt{2}}{2} lkl_2 & -\frac{\sqrt{2}}{2} lkl_3 & -\frac{\sqrt{2}}{2} lkl_4 \\ kd_1 & -kd_2 & kd_3 & -kd_4 \end{bmatrix} \begin{bmatrix} {W_1}^2 \\ {W_2}^2 \\ {W_3}^2 \\ {W_4}^2 \end{bmatrix} \quad (63)$$

Lift and drag coefficients will vary with the given collective effector input, and this relation can be expanded by redefining lift and drag coefficient by collective effector input C_i as

$$kl_i = aC_i + b \tag{64}$$
$$kd_i = cC_i + d \tag{65}$$

This approximation will find the specific lift and drag coefficient for the given collective effector input. The modified representation of the relation between force/moment and effector inputs can be represented as in Equation 66.

$$\begin{bmatrix} F \\ L \\ M \\ N \end{bmatrix} = \begin{bmatrix} a & a & a & a \\ -\frac{l\sqrt{2}}{2}a & \frac{l\sqrt{2}}{2}a & \frac{l\sqrt{2}}{2}a & -\frac{l\sqrt{2}}{2}a \\ \frac{l\sqrt{2}}{2}a & \frac{l\sqrt{2}}{2}a & -\frac{l\sqrt{2}}{2}a & -\frac{l\sqrt{2}}{2}a \\ c & -c & c & -c \end{bmatrix} \begin{bmatrix} W_1{}^2 C_1 \\ W_2{}^2 C_2 \\ W_3{}^2 C_3 \\ W_4{}^2 C_4 \end{bmatrix} + \begin{bmatrix} b & b & b & b \\ -\frac{l\sqrt{2}}{2}b & \frac{l\sqrt{2}}{2}b & \frac{l\sqrt{2}}{2}b & -\frac{l\sqrt{2}}{2}b \\ \frac{l\sqrt{2}}{2}b & \frac{l\sqrt{2}}{2}b & -\frac{l\sqrt{2}}{2}b & -\frac{l\sqrt{2}}{2}b \\ d & -d & d & -d \end{bmatrix} \begin{bmatrix} W_1{}^2 \\ W_2{}^2 \\ W_3{}^2 \\ W_4{}^2 \end{bmatrix} \tag{66}$$

The problem in optimization-based control allocation is to find the necessary effector combination of W_i and C_i , which maintains the desired forces and moments on vehicle to achieve desired reference tracking performance. A nonlinear optimization algorithm can help to solve the problem using a cost function. This cost function can be changed and has different responsibilities such as minimizing effector inputs or maximizing flight time of the aerial vehicle. This optimization algorithm should be implemented by considering some constraints of the vehicle such as rotor RPM limits and collective blade angle limits. These limitations are shown in Table 4. In the next section, several criteria are tested with numerical simulations using the developed cost functions.

Table 4. Constraint table of rotors

$0 \leq W_1 \leq 2000\ RPM$ (RPM Limit of 1st Rotor)	$4° \leq C_1 \leq 12°$ (Collective Angle Limit of 1st Rotor)
$0 \leq W_2 \leq 2000\ RPM$ (RPM Limit of 2nd Rotor)	$4° \leq C_2 \leq 12°$ (Collective Angle Limit of 2nd Rotor)
$0 \leq W_3 \leq 2000\ RPM$ (RPM Limit of 3rd Rotor)	$4° \leq C_3 \leq 12°$ (Collective Angle Limit of 3rd Rotor)
$0 \leq W_4 \leq 2000\ RPM$ (RPM Limit of 4th Rotor)	$4° \leq C_4 \leq 12°$ (Collective Angle Limit of 4th Rotor)

4.5.2.2.1 Collective input minimization criteria

A test algorithm was implemented in MATLAB to check whether the resultant effector inputs found by the optimization-based control allocation are valid or not. Additionally, the resultant effector control inputs should maintain the desired forces and moments generated by the controller. For this reason, rotor experiments and test data are used to compare the forces and moments generated by the rotor and the desired ones by the pilot. To solve the optimization problem and simulate it, a cost function should be chosen according to a criterion. The cost function used in numerical simulation aims to minimize the collective effector input usage, where optimization should come up with the minimum collective effector input and necessary RPM combination to maintain the desired forces and moments. The basic structure of the test algorithm is presented in Figure 67.

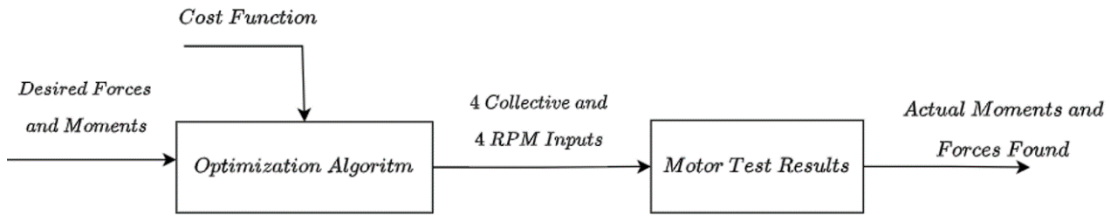

Figure 67. Optimization test architecture

The cost function that minimizes the collective pitch usage is presented as Equation 67.

$$J = \frac{1}{2}{C_1}^2 + \frac{1}{2}{C_2}^2 + \frac{1}{2}{C_3}^2 + \frac{1}{2}{C_4}^2 \qquad 67$$

For this test procedure, five tests were conducted by gradually increasing the minimum limit of collective inputs to check whether constraint optimization finds values in given constraint range or not. Additionally, rotor experiments were used to verify whether the resultant effector inputs maintain the desired forces/moments in the constraint range. For the numerical simulation tests, desired forces and moments are given in Equation 68.

$$\begin{bmatrix} F_{des} \\ L_{des} \\ M_{des} \end{bmatrix} = \begin{bmatrix} 221\ N \\ 20\ Nm \\ 10\ Nm \end{bmatrix} \tag{68}$$

The resultant effector combination found by the optimization is presented in Table 5. The preliminary results of the developed optimization problem are presented for different minimum collective blade angle constraints. For each case, 4 RPM and 4 collective inputs were successfully found by optimization algorithm in given constraint range.

Table 5: Optimization results table

Test Condition	C_1	C_2	C_3	C_4	RPM_1	RPM_2	RPM_3	RPM_4
Minimum 4° Collective Blade Angle	4°	4°	4°	4°	1334	1485	1424	1268
Minimum 6° Collective Blade Angle	6°	6°	6°	6°	1015	1151	1082	949
Minimum 8° Collective Blade Angle	8°	8°	8°	8°	850	962	906	792
Minimum 10° Collective Blade Angle	10°	10°	10°	10°	748	840	798	691
Minimum 12° Collective Blade Angle	12°	12°	12°	12°	672	759	717	625

By using the rotor experimental data, actual forces and moments generated according to found effector inputs are presented in Table 6.

Table 6: Actual force/moment table

$\boldsymbol{Test\ Condition}$	$\boldsymbol{F_{act}}$	$\boldsymbol{L_{act}}$	$\boldsymbol{M_{act}}$
Minimum 4° Collective Blade Angle	$191.9\ N$	$15.05\ Nm$	$6.2\ Nm$
Minimum 6° Collective Blade Angle	$214.4\ N$	$19.4\ Nm$	$9.7\ Nm$
Minimum 8° Collective Blade Angle	$215.79\ N$	$19.52\ Nm$	$9.76\ Nm$
Minimum 10° Collective Blade Angle	$225.86\ N$	$20.43\ Nm$	$10.22\ Nm$
Minimum 12° Collective Blade Angle	$222.39\ N$	$20.12\ Nm$	$10.06\ Nm$

The maximum error is case number 1, which is the collective angle minimum 4° case. According to the results, blade collective angle between $6° - 12°$ capture system dynamics well with interpolated curves and resultant actual forces and moments are close to desired ones. This means the optimization method successfully found RPM and collective effector combinations to meet desired forces and moments using a cost function.

The parameters of Equation 66 are presented in Table 7 for simulation purposes.

Table 7: Parameter table

Parameter	**Value**
a	$1.0720.10^{-5}$
b	$-1.4460.10^{-5}$
c	$7.2666.10^{-7}$
d	$-8.4470.10^{-7}$
l	1

4.5.2.2.2 Weighted effector minimization criteria

There may be situations where some effector types are more desirable than the others. In some cases, it may be requested to conduct the flight using more RPM input with less collective input usage or more collective input with less RPM input. This cannot be done with the previous cost function presented in the report which always aims to minimize the total usage of collective input. An extended and modified cost function is necessary for this goal, which should change

the responsibility of the effector type by a user defined parameter and at the mean time the desired forces and moments should be maintained by the resultant effector combination. The improved cost function is presented in Equation 69,

$$J = \sum_{i=1}^{4} (1\text{-G})\left(\frac{\theta_i - \theta_{min}}{\theta_{max} - \theta_{min}}\right)^2 + G\left(\frac{\omega_i - \omega_{min}}{\omega_{max} - \omega_{min}}\right)^2 \quad 69$$

where θ_i is the ith rotor collective input, θ_{min} is the minimum collective blade angle limit, θ_{max} is the maximum collective blade angle limit, ω_i is the ith rotor RPM input, ω_{min} is the minimum RPM limit, ω_{max} is the maximum RPM limit, G is the user defined weight parameter. The aim for the extended cost function is to minimize the total effector usage ratio with a given user-defined parameter that penalizes the effector usage of collective rather than RPM, or vice versa. The user-defined parameter (G) is between 0 and 1 and is responsible for adjusting the weight of the usage of effector types. When G is minimum (0), the cost function can be simplified as in Equation 70.

$$J = \sum_{i=1}^{4} \left(\frac{\theta_i - \theta_{min}}{\theta_{max} - \theta_{min}}\right)^2 \quad 70$$

When G is minimum, the contribution of RPM effectors in the cost function cancels out, and the aim of the optimization becomes to minimize the collective usage only. This will result optimization to find always the minimum collective input with a combination of RPM to maintain the desired forces and moments. On the other hand, when G is maximum (1), the contribution of collective effectors in the cost function cancels out, and the aim of the optimization becomes to minimize the RPM usage only. The simplified cost function for maximum user-defined parameter is presented in Equation 71.

$$J = \sum_{i=1}^{4} \left(\frac{\omega_i - \omega_{min}}{\omega_{max} - \omega_{min}}\right)^2 \quad 71$$

A numerical simulation is implemented to analyze the outputs of the optimization. The simulation architecture is presented in Figure 68. An NLDI controller is used to generate the desired forces and moments according to the pilot commands. The array of these virtual control inputs is given to the optimization with different user-defined parameter values, and the resultant RPM and collective inputs are collected to check whether the user-defined parameter really changes the usage of the effector types or not according to the G value. It is seen that in some cases, optimization results in noisy effector inputs, so a low pass filter is also added at the end of the structure to suppress the chattering effect of the optimization.

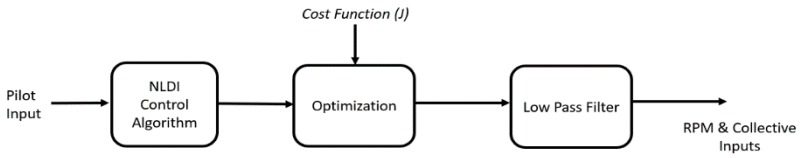

Figure 68. Numerical simulation (weighted minimization)

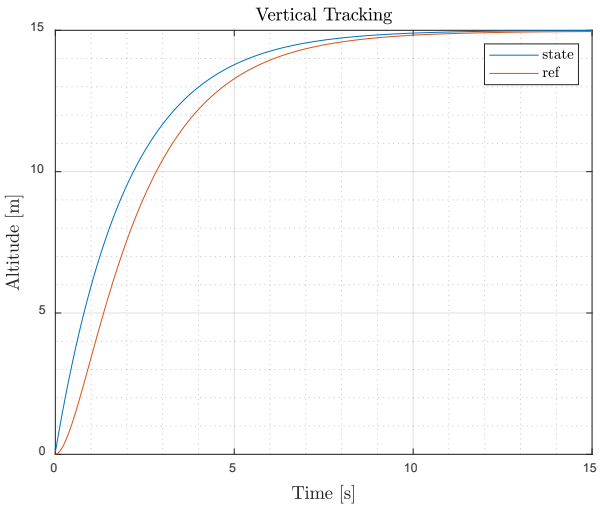

Figure 69. NLDI position tracking

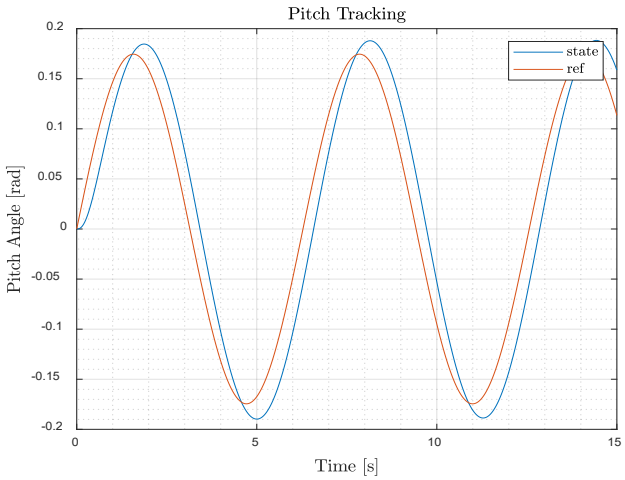

Figure 70. NLDI pitch angle tracking

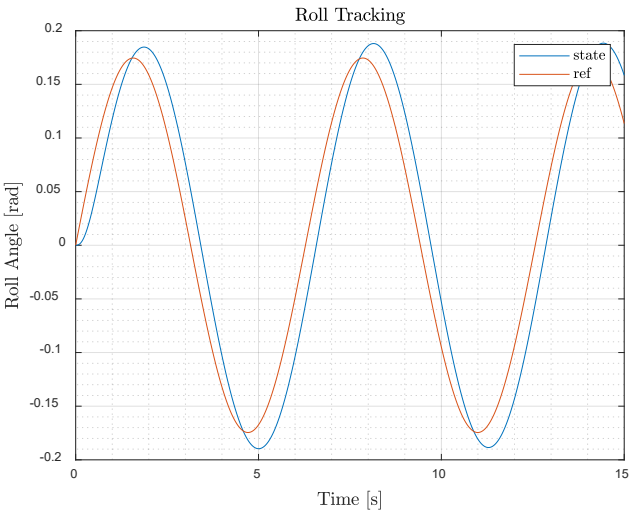

Figure 71. NLDI roll angle tracking

NLDI controller reference commands and model states for altitude, pitch angle and roll angle are presented in Figure 69, Figure 70, and Figure 71. The generated desired vertical force, roll, pitch, and yaw moments are recorded during the simulation. The recorded set of virtual controls is given to optimization with different values of user-defined parameters to understand what combination of resultant effector commands will be produced according to the given NLDI commands. The first test is conducted with user-defined parameter (G) equaling 0.25. According to the (G) value, it was expected that the resultant combination should consist of less usage of collective inputs and high usage of RPM inputs. As expected, collective inputs of four rotors are close to the minimum collective blade angle value, which is 6°, and desired control maintained by mostly RPM effector inputs. Unfiltered and filtered combinations of RPM and collective found by the optimization are presented in Figure 72 and Figure 73.

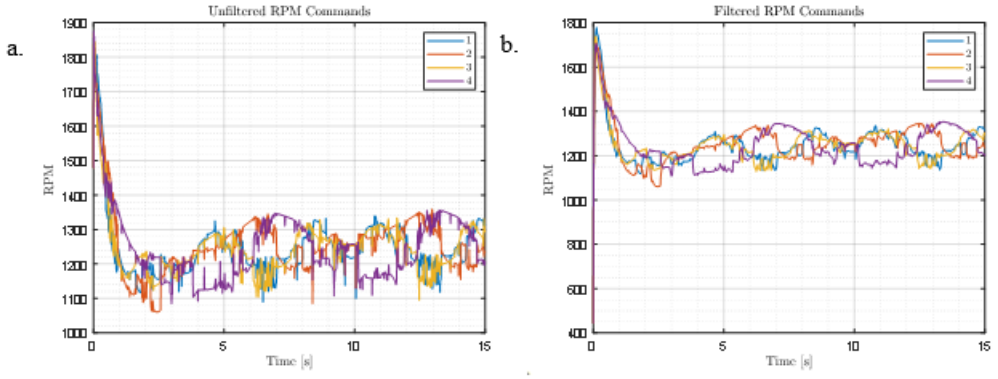

Figure 72. Unfiltered and filtered RPM input for $G = 0.25$

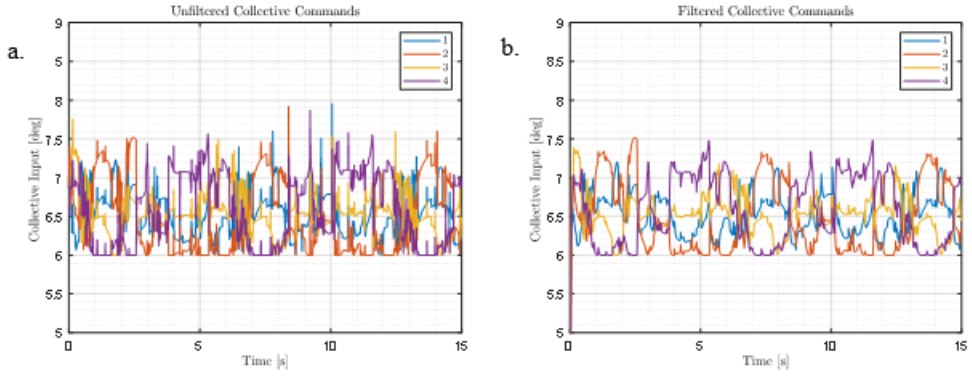

Figure 73. Unfiltered and filtered collective input for $G = 0.25$

The second test is conducted with user-defined parameter (G) equaling 0.55. According to the (G) value, it was expected that the resultant combination should have more usage of collective

inputs and less usage of RPM inputs when it is compared with the first case, which is $G = 0.25$. As explained in the beginning of this section, the higher the user-defined parameter value is, the higher the usage of collective inputs in the resultant combination. As expected, collective inputs of four rotors are higher than the previous case and in a reverse manner for the RPM inputs. Unfiltered and filtered combination of RPM and collective found by the optimization is presented in Figure 74 and Figure 75.

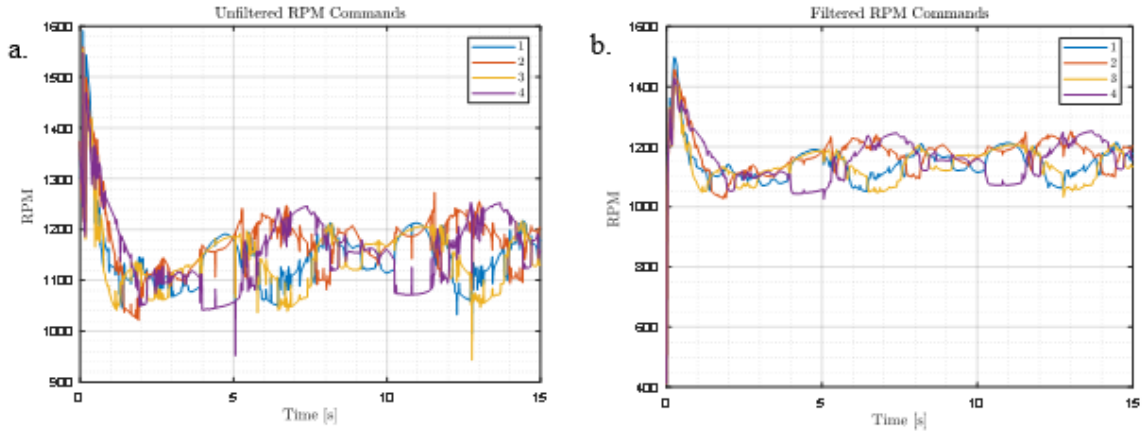

Figure 74. Unfiltered and filtered RPM input for $G = 0.55$

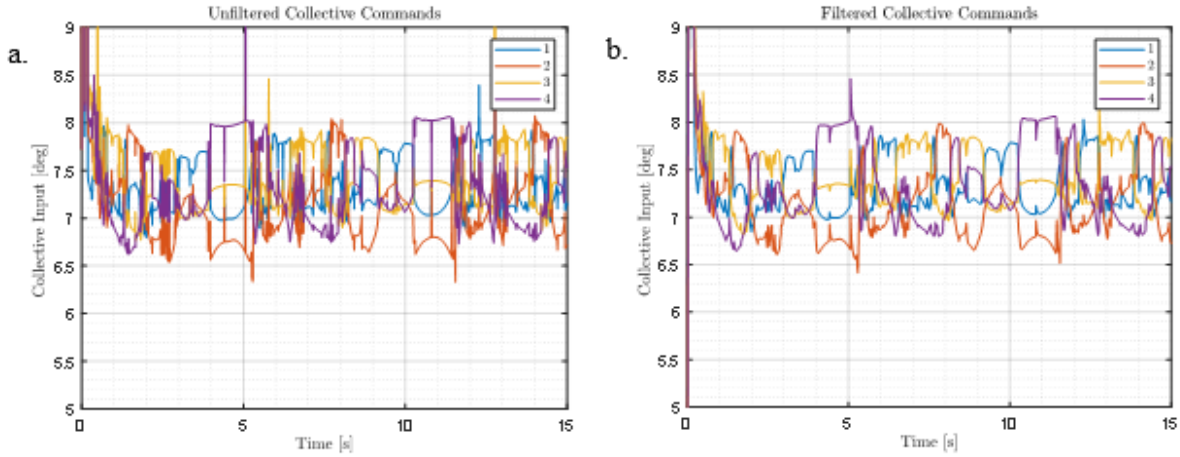

Figure 75. Unfiltered and filtered collective input for $G = 0.55$

The last test is conducted with user defined parameter (G) equals to 0.95. This value is close to 1 which means the contribution of collective usage in the cost function is significantly small and the main aim of the cost function will be to minimize the RPM usage during the test. It is expected to see that RPM values found by the optimization should be significantly smaller than

case $G = 0.25$ and $G = 0.55$. As expected, RPM values found by the optimization is the smallest in all cases. Unfiltered and filtered combination of RPM and collective found by the optimization is presented in Figure 76 and Figure 77.

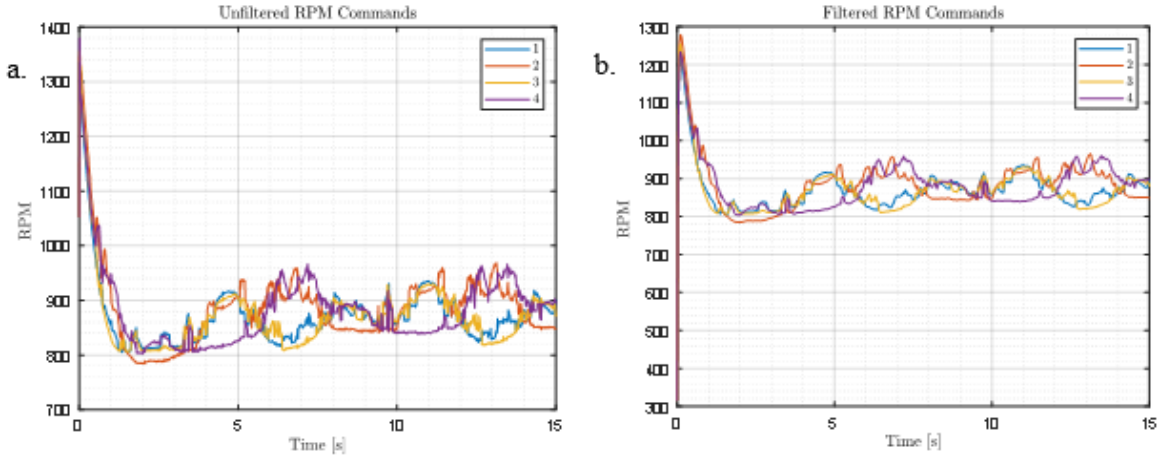

Figure 76. Unfiltered and filtered RPM input for $G = 0.95$

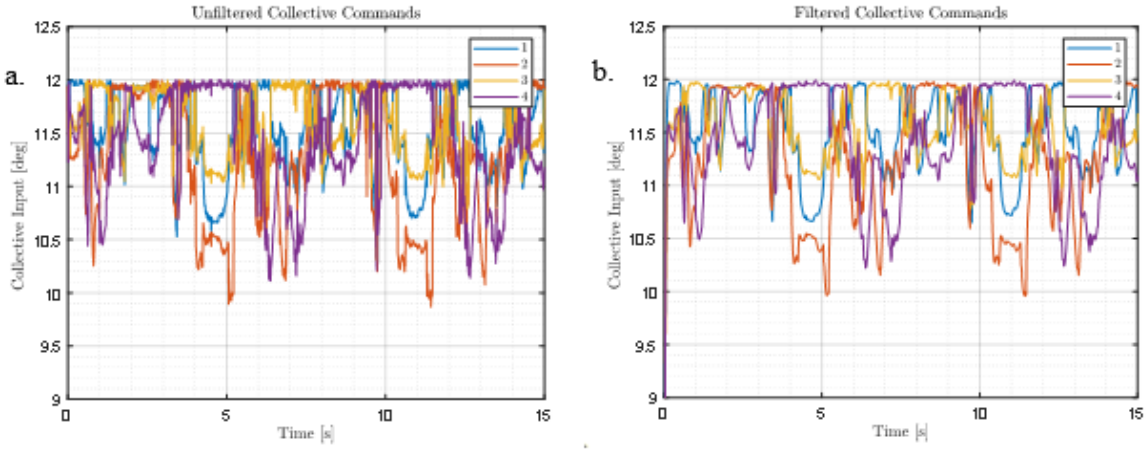

Figure 77. Unfiltered and filtered collective input for $G = 0.95$

4.5.2.2.3 Power Consumption Criteria

Rotor tests were analyzed to come up with a power consumption model for rotors to run the optimization algorithm with an advanced cost function. In Figure 78, consumed power for a rotor is presented with respect to the cube of the RPM commanded in the tests. This relation can be approximated by a power coefficient k_d as given in Equation 72.

$$P = k_p \omega^3 \quad (72)$$

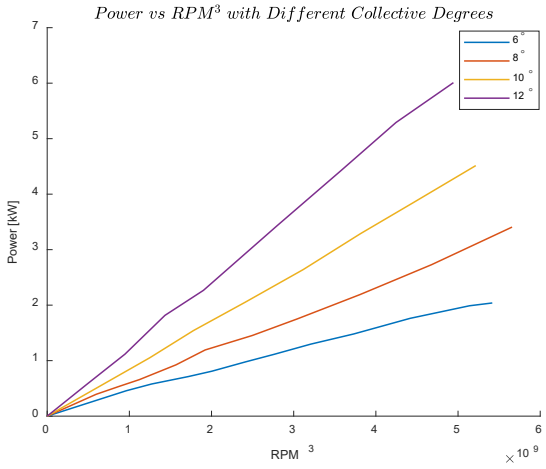

Figure 78. Power vs. RPM rotor tests

According to the data interpolation, the power coefficient of each collective blade angle is represented by Table 8. Higher collective angle of the blade results in a higher power consumption trend with a similar linear behavior.

Table 8. Power coefficient table

k_d	*Value*
6°	$3.936.10^{-10}$
8°	$5.9.10^{-10}$
10°	$8.61.10^{-10}$
12°	$12.28.10^{-10}$

The main goal of the analysis of the rotor tests is to formulate a simplified relationship between consumed power and the effector inputs. To do that, power coefficients should be approximated by the amount of given collective pitch blade command. The fitted curve between the power coefficients given by the collective blade angle is presented in Figure 79.

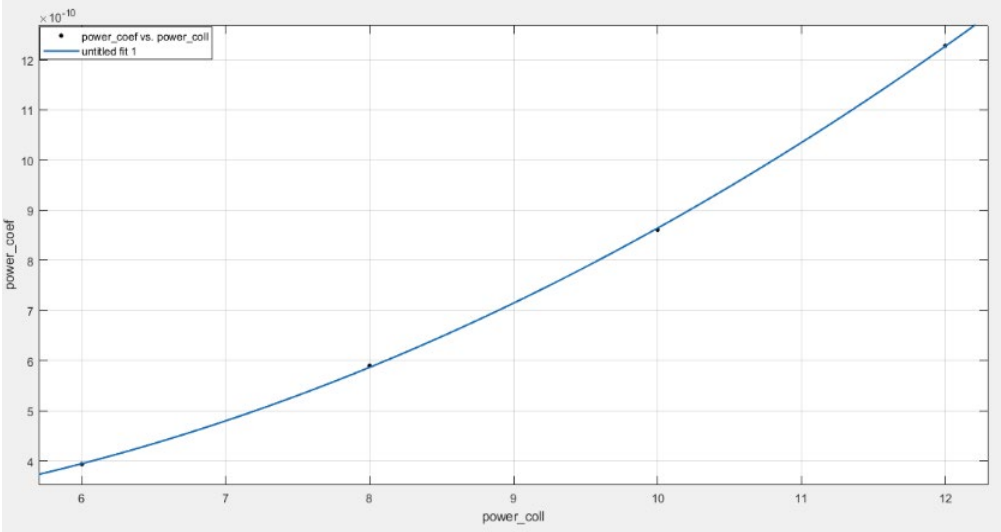

Figure 79. Power coefficient vs. collective blade angle int.

The polynomial approximation of the power coefficient given by the pitch blade angle is approximated by Equation 73,

$$k_p = 1.066 \times 10^{-11}x^2 - 5.321 \times 10^{-11}x + 3.301 \times 10^{-10} \quad 73$$

where x is the given collective pitch angle in degrees, and k_p is the power coefficient. After successfully implementing the interpolation between elements, we can write the power consumed by a rotor with given RPM and collective blade angle as

$$P = ((1.066 \times 10^{-11})C_i^2 - (5.321 \times 10^{-11})C_i + 3.301 \times 10^{-10}))\omega_i^3 \quad 74$$

where C_i is the given collective pitch angle for the *i*th rotor and ω_i is the RPM command for the *i*th rotor. Figure 80 shows a visual representation of the power consumption of the rotor with varying RPM and different blade pitch angles.

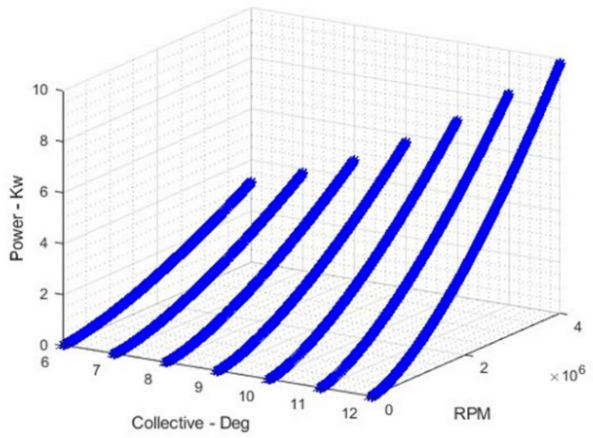

Figure 80. Power graph for the rotor

The total power consumed by the aerial vehicle can be found by summing the consumed power for each rotor. This can be formulated as

$$J = P_{TOTAL} = P_1 + P_2 + P_3 + P_4 \tag{75}$$

$$\begin{aligned} P_{TOTAL} = {} & ((1.066 \times 10^{-11}){C_1}^2 - (5.321 \times 10^{-11})C_1 + 3.301 \times 10^{-10}){\omega_1}^3 \\ & + ((1.066 \times 10^{-11}){C_2}^2 - (5.321 \times 10^{-11})C_2 + 3.301 \times 10^{-10}){\omega_2}^3 \\ & + ((1.066 \times 10^{-11}){C_3}^2 - (5.321 \times 10^{-11})C_3 + 3.301 \times 10^{-10}){\omega_3}^3 \\ & + ((1.066 \times 10^{-11}){C_4}^2 - (5.321 \times 10^{-11})C_4 + 3.301 \times 10^{-10}){\omega_4}^3 \end{aligned}$$

The cost function of J is implemented in the test algorithm to analyze whether the control allocation mixing will minimize the power consumption or not. This numerical analysis will verify whether the resultant effector inputs found will maintain the desired forces/moments but also minimize the total power consumption according to chosen criteria.

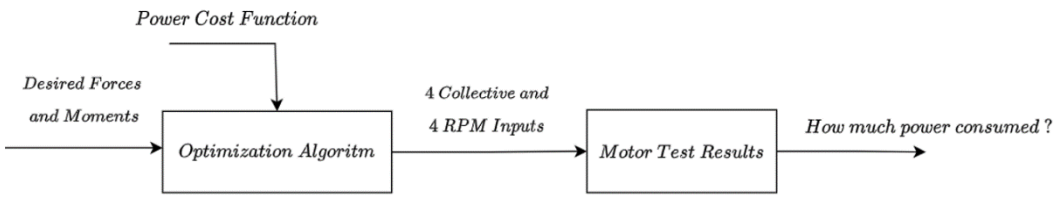

Figure 81. Power consumption test procedure

The numerical analysis procedure is summarized in Figure 81. The results of the numerical tests are presented in Table 9 and Table 10.

The test sequence starts by running the optimization algorithm from (6°-7°) collective range. The range is gradually increased by 1° for every test cycle.

The columns Col.1-Col.4 represent the resultant collective command for each rotor found by the optimization. The columns RPM1-RPM4 represent the resultant RPM command for each rotor found by the optimization. The column Power Cons. is the total power consumed by the resultant effector inputs in kilowatts. Test experiments were used to find the power consumption of the rotor by commanded effector inputs.

Table 9. Power minimization result table 1

Collective Range	RPM Range	Col.1	Col.2	Col.3	Col.4	RPM1	RPM2	RPM3	RPM4	Power Cons.
6 – 7	$0-2000^2$	6.0318	6.3089	6.0588	6.0094	1690.96	1722.85	1727.13	1653.58	7.903
6 – 8	–	7.7724	7.7617	7.7676	7.7785	1444.15	1514.85	1479.82	1407.48	7.011
6 – 9	–	8.9512	8.9356	8.9405	8.9639	1327.47	1392.73	1360.71	1293.30	6.877
6 – 10	–	9.9008	9.9975	9.9804	9.9743	1251.57	1304.46	1276.09	1215.23	6.912
6 – 11	–	10.954	10.914	10.488	10.496	1180.94	1240.34	1240.11	1180.00	6.991
6 – 12	–	11.838	11.653	11.753	11.963	1130.09	1195.02	1162.30	1095.45	7.150

** collective control initial condition of the optimization given as **minimum** value of collective range*

Collective Range	RPM Range	Col.1	Col.2	Col.3	Col.4	RPM1	RPM2	RPM3	RPM4	Power Cons.
6 – 7	$0-2000^2$	6.1176	6.1272	6.1227	6.1243	1676.08	1754.93	1715.92	1633.19	7.886
6 – 8	–	7.4799	7.4870	7.4843	7.4782	1478.20	1548.38	1513.61	1441.55	7.088
6 – 9	–	8.8357	8.9161	8.8730	8.8103	1337.66	1394.53	1366.79	1306.56	6.880
6 – 10	–	6.38	6.43	6.41	6.35	1631.47	1700.32	1666.52	1595.86	7.647
6 – 11	–	6.2401	6.3047	6.2725	6.2067	1654.96	1723.20	1689.63	1619.25	7.761
6 – 12	–	11.840	11.968	11.903	11.749	1130.03	1177.19	1154.01	1106.64	7.164

** collective control initial condition of the optimization given as **maximum** value of collective range*

In Table 9, the total consumed power is gradually decreased by the algorithm until the collective range of 6°-9°. In an ideal case, the expected outcome from the optimization is the minimum power consumption possible for each range. However, results revealed that optimization did not find the global minimum of the cost function for each iteration. According to the analysis, this

may be caused by the complexity of the cost function, in which there are many local minimum points. This will result in optimization converging on local minima and maxima points and not the global ones. Numerical results were implemented by the *MATLAB fmincon* algorithm, which is a gradient-based optimization tool. Additionally, the initial conditions of the algorithm may affect the power consumption behavior.

Table 10. Power minimization result table 2

Collective Range	RPM Range	Col.1	Col.2	Col.3	Col.4	RPM1	RPM2	RPM3	RPM4	Power Cons.
6 – 7	$0-2000^2$	6.0318	6.3089	6.0588	6.0094	1690.96	1722.85	1727.13	1653.58	7.903
7 – 8	–	7.5016	7.9564	7.6421	7.4989	1475.30	1492.62	1494.24	1439.41	7.042
8 – 9	–	8.8116	8.9735	8.8776	8.8309	1339.76	1389.32	1366.32	1304.81	6.879
9 – 10	–	9.0296	9.0724	9.0508	9.0277	1320.67	1380.35	1350.93	1287.93	6.876
10 – 11	–	10.878	10.892	10.885	10.894	1185.64	1241.75	1214.05	1155.16	7.012
11 – 12	–	11.944	11.881	11.910	11.904	1124.48	1182.02	1153.68	1098.46	7.170

** collective control initial condition of the optimization given as **minimum** value of collective range*

Collective Range	RPM Range	Col.1	Col.2	Col.3	Col.4	RPM1	RPM2	RPM3	RPM4	Power Cons.
6 – 7	$0-2000^2$	6.0318	6.3089	6.0588	6.0094	1690.96	1722.85	1727.13	1653.58	7.903
6 – 8	–	7.7724	7.7617	7.7676	7.7785	1444.15	1514.85	1479.82	1407.48	7.011
6 – 9	–	8.9512	8.9356	8.9405	8.9639	1327.47	1392.73	1360.71	1293.30	6.877
6 – 10	–	9.9008	9.9975	9.9804	9.9743	1251.57	1304.46	1276.09	1215.23	6.912
6 – 11	–	10.954	10.914	10.488	10.496	1180.94	1240.34	1240.11	1180.00	6.991
6 – 12	–	11.838	11.653	11.753	11.963	1130.09	1195.02	1162.30	1095.45	7.150

** collective control initial condition of the optimization given as **minimum** value of collective range*

To understand the complexity of the implemented cost function and its behavior, another numerical test is implemented by different constraints of collective ranges. This time, the collective range was set to 1-degree increments with different collective range intervals like (-), (-). This grid technique shows the behavior of the optimization for different collective ranges with a narrower window. Table 10 summarizes the grid results of the optimization algorithm. For each collective range, there are different power consumption results which are the local minimum of each interval found by the optimization. These local minimums change significantly for each grid and there are several local minimum points also known as the critical points. The optimization technique known as the steepest descent uses an initial guess to converge to a critical point which is the set of effector inputs for minimum power consumption. The algorithm determines the effector combination that has the lowest power consumption in a vicinity, not the minimum power consumption of all effector combinations. This is due to the architecture of the cost function leading to convergence to a local minimum rather than a global one.

4.5.2.3 Control allocation—Frequency-based approach

The second approach that can be considered on the control allocation problem is the frequency-based approach. A hybrid control mixing was considered using a complementary filter, so that it uses pitch actuators for short-term responses and RPM for trim (Walter A. , McKay, Niemiec, & and Gandhi, 2022). The acceleration commands are filtered by their frequency content to decide how much collective and how much RPM should be chosen to maintain the desired acceleration. For each rotor, the blade pitch actuator receives the high frequency (maneuver) content, while the low-frequency (trim) content is allocated to the motor speed controller.

Such a technique can guide the decision of collective and RPM effector inputs to the mixing matrix, as seen in Equation 66. The basic architecture of frequency-based control allocation approach is presented in Figure 82.

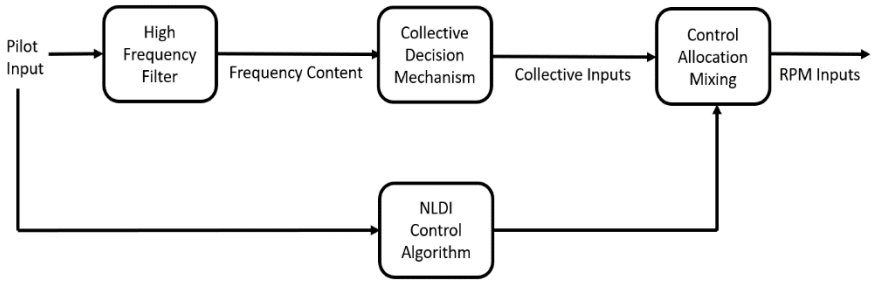

Figure 82. Frequency-based control allocation structure

The pilot input for thrust roll, pitch, and yaw commands will be decomposed to their high frequency content by a filter parameter to be an input for collective decision mechanism. The mechanism will be responsible for finding the collective angle of each rotor using the frequency contents and the geometry of the aerial vehicle. The resultant collective angles will be combined with the desired forces/moments, and control allocation mixing will find the resultant RPM combination.

4.5.2.3.1 High frequency filter

The high pass filter is a critical component in the architecture to adjust the collective control during the flight. The filter can be modified by a constant σ which allows to change the time of transition between collective and RPM. If σ is high the transition is very fast, and RPM controls are more effective. If σ is low, the transition is slow and collective inputs are more responsive.

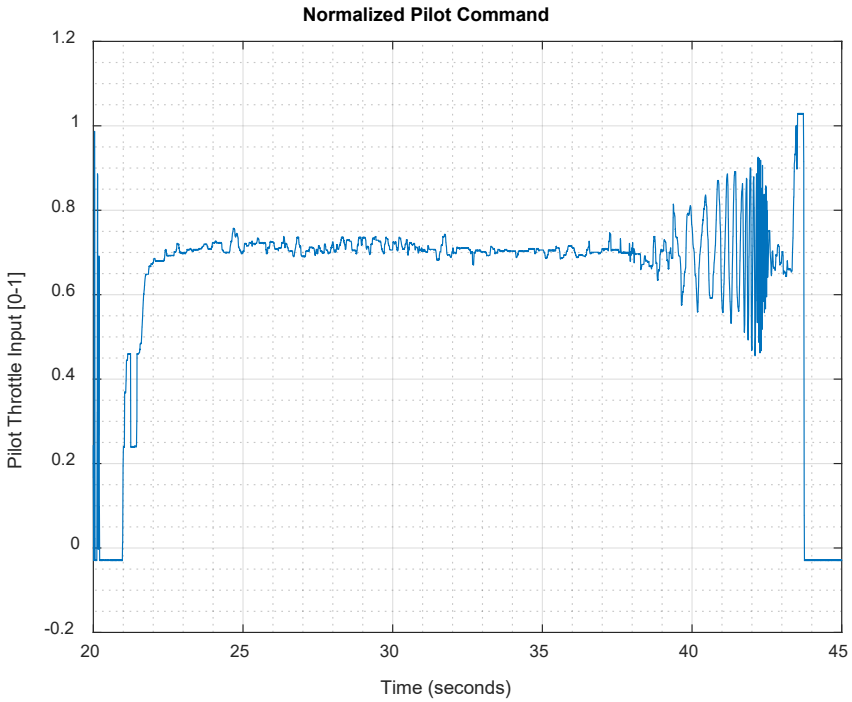

Figure 83. Normalized pilot input

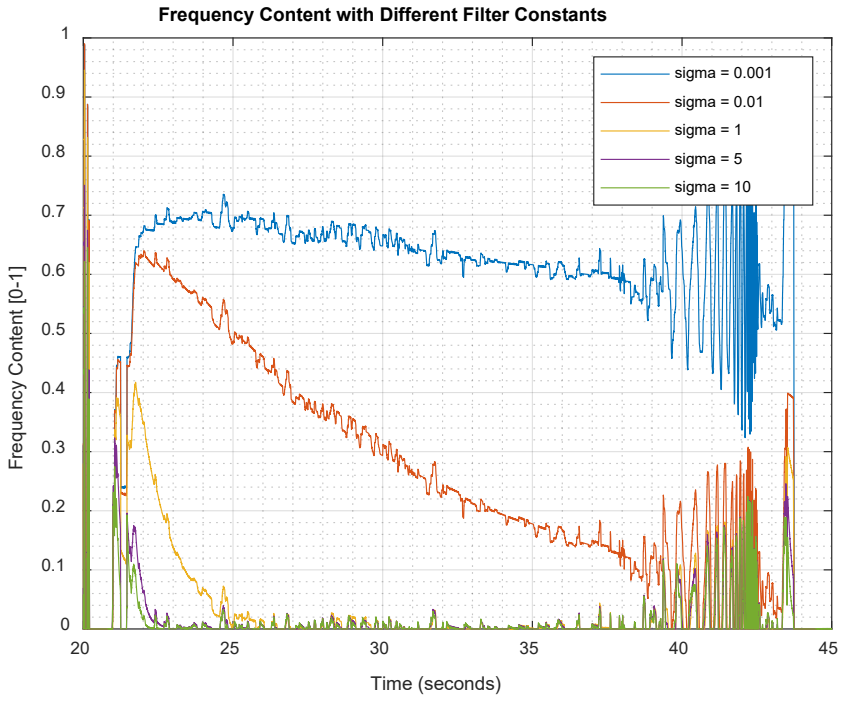

Figure 84. Frequency content data

The normalized thrust pilot input for a flight test is represented in Figure 83, and the frequency content after the filter applied with different filter constants are represented in Figure 84. As can be seen, lower σ values make the frequency content disappear slower, which means collective blade angles will be more responsive than higher values of filter constant σ. Filter constant is an important parameter to balance the tradeoff between collective and RPM control inputs.

4.5.2.3.2 Addition of the cyclic control

As given in Equation 66, the mixing relation is implemented between virtual control inputs and effector inputs of RPM/collective of each rotor of PAVER. This equation will be expanded by including cyclic inputs of the rotors, which will produce a higher moment envelope of the aerial vehicle.

$$\begin{bmatrix} F \\ L \\ M \\ N \end{bmatrix} = \begin{bmatrix} a & a & a & a \\ -\frac{l\sqrt{2}}{2}a & \frac{l\sqrt{2}}{2}a & \frac{l\sqrt{2}}{2}a & -\frac{l\sqrt{2}}{2}a \\ \frac{l\sqrt{2}}{2}a & \frac{l\sqrt{2}}{2}a & -\frac{l\sqrt{2}}{2}a & -\frac{l\sqrt{2}}{2}a \\ c & -c & c & -c \end{bmatrix} \begin{bmatrix} {W_1}^2 C_1 \\ {W_2}^2 C_2 \\ {W_3}^2 C_3 \\ {W_4}^2 C_4 \end{bmatrix} + \begin{bmatrix} b & b & b & b \\ -\frac{l\sqrt{2}}{2}b & \frac{l\sqrt{2}}{2}b & \frac{l\sqrt{2}}{2}b & -\frac{l\sqrt{2}}{2}b \\ \frac{l\sqrt{2}}{2}b & \frac{l\sqrt{2}}{2}b & -\frac{l\sqrt{2}}{2}b & -\frac{l\sqrt{2}}{2}b \\ d & -d & d & -d \end{bmatrix} \begin{bmatrix} {W_1}^2 \\ {W_2}^2 \\ {W_3}^2 \\ {W_4}^2 \end{bmatrix} + \begin{bmatrix} F_1 & F_2 & F_3 & F_4 \\ L_1 & L_2 & L_3 & L_4 \\ M_1 & M_2 & M_3 & M_4 \\ N_1 & N_2 & N_3 & N_4 \end{bmatrix} \begin{bmatrix} \partial_1 \\ \partial_2 \\ \partial_3 \\ \partial_4 \end{bmatrix} \quad (76)$$

Cyclic input is a type of control input which tilts the direction of the swashplate by a given amount of command. This control type is important and different from the others, because it can overcome the situation of a failed rotor. RPM and collective control inputs are beneficial to expand our force and moment envelope, but they are not able to overcome a rotor failure, because rotors are not capable of changing the direction of the thrust vector. In Equation 76, cyclic effector input of each rotor is represented as ∂_i and their contribution on thrust, roll, pitch, and yaw moments as a matrix. The aim is to fill each element of this matrix by using the rotor experiments to develop a complete control allocation technique that covers all collective, RPM, and cyclic commands. Thrust tests of the rotor will be analyzed to understand the relationship between generated vertical forces of the rotor by given cyclic inputs.

In Figure 85, for 6° of collective angle, generated thrust in pounds is presented with respect to the rotor RPM for different angle of cyclic controls as $0^\circ, 2^\circ, 4^\circ$and 6°. Figure 86, for 6° of collective angle, the generated torque in pounds-ft is presented with respect to the rotor RPM for different angle of cyclic controls as $0^\circ, 2^\circ, 4^\circ$and 6°.

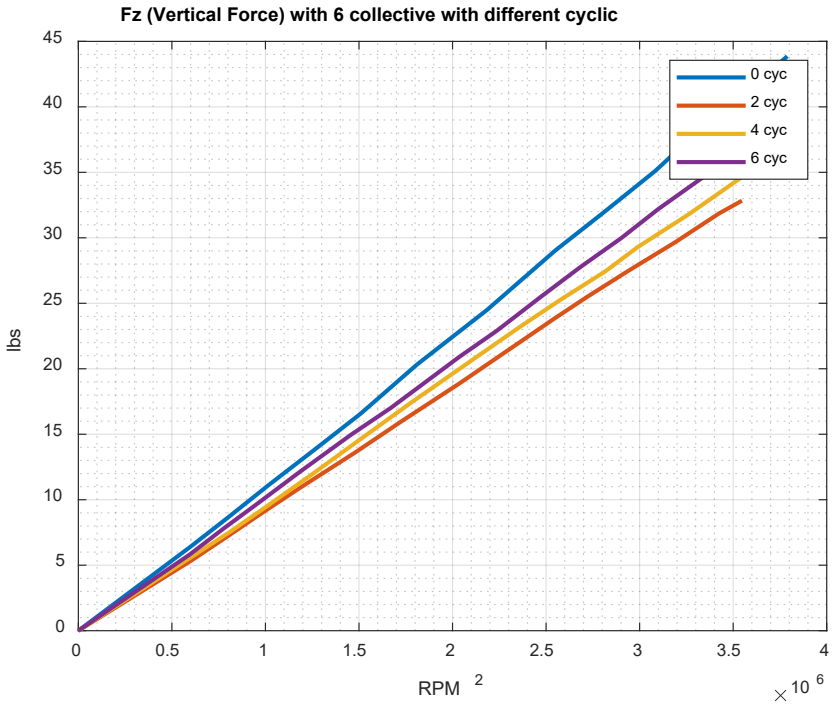

Figure 85. Thrust vs. cyclic test 1

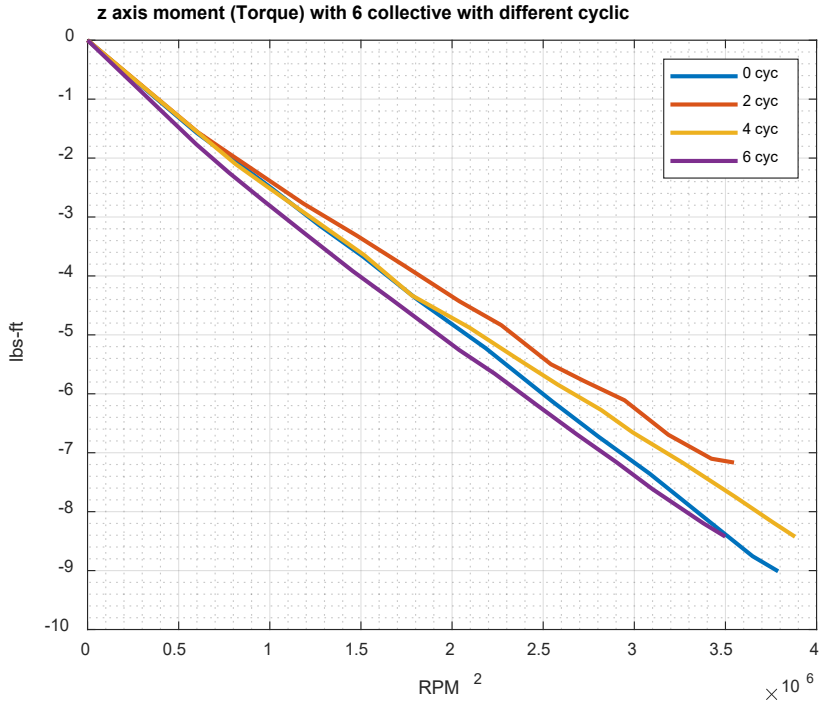

Figure 86. Torque vs. cyclic test 1

Figure 87, for 8° of collective angle, the generated thrust in pounds-ft is presented with respect to the rotor RPM for different angle of cyclic controls as $0^{\circ}, 2^{\circ}$, and 4°. Figure 88, for 8° of collective angle, generated thrust in pounds is presented with respect to the rotor RPM for different angle of cyclic controls as $0^{\circ}, 2^{\circ}$, and 4°.

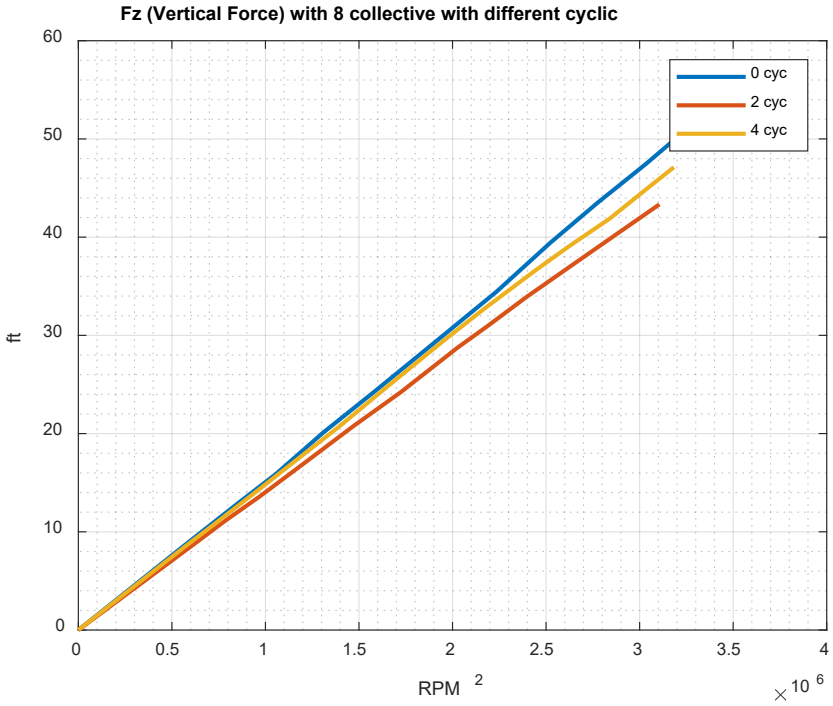

Figure 87. Thrust vs. cyclic test 2

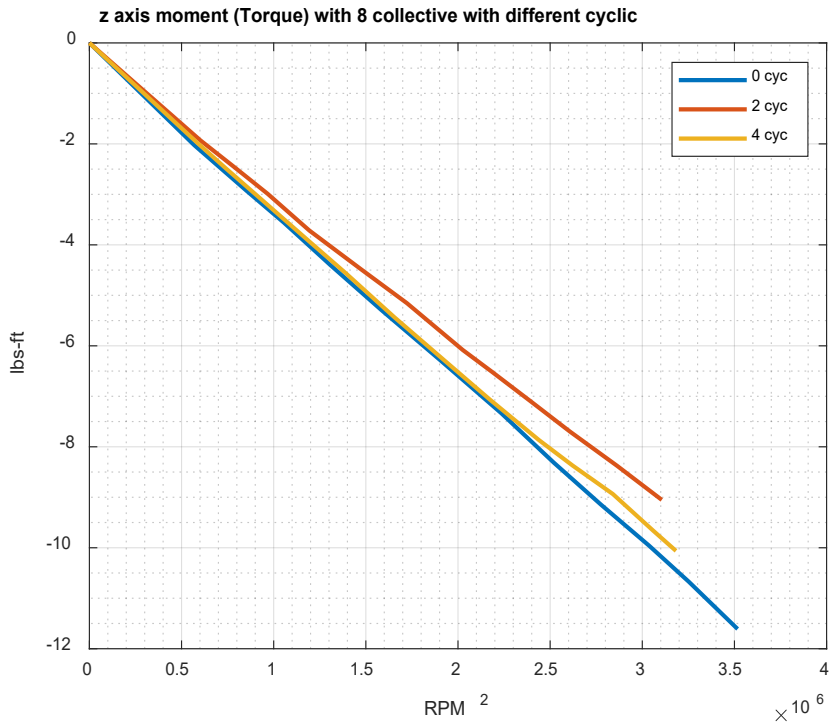

Figure 88. Torque vs. cyclic test 2

The results from the rotor tests show that the cyclic input is not affecting generated thrust and torque in high collective blade angle values. This indicates that there will be no vertical force component generated with given cyclic input, and the control allocation equation can be expanded as shown below.

$$\begin{bmatrix} F \\ L \\ M \\ N \end{bmatrix} = \begin{bmatrix} a & a & a & a \\ -\frac{l\sqrt{2}}{2}a & \frac{l\sqrt{2}}{2}a & \frac{l\sqrt{2}}{2}a & -\frac{l\sqrt{2}}{2}a \\ \frac{l\sqrt{2}}{2}a & \frac{l\sqrt{2}}{2}a & -\frac{l\sqrt{2}}{2}a & -\frac{l\sqrt{2}}{2}a \\ c & -c & c & -c \end{bmatrix} \begin{bmatrix} {W_1}^2 C_1 \\ {W_2}^2 C_2 \\ {W_3}^2 C_3 \\ {W_4}^2 C_4 \end{bmatrix} + \begin{bmatrix} b & b & b & b \\ -\frac{l\sqrt{2}}{2}b & \frac{l\sqrt{2}}{2}b & \frac{l\sqrt{2}}{2}b & -\frac{l\sqrt{2}}{2}b \\ \frac{l\sqrt{2}}{2}b & \frac{l\sqrt{2}}{2}b & -\frac{l\sqrt{2}}{2}b & -\frac{l\sqrt{2}}{2}b \\ d & -d & d & -d \end{bmatrix} \begin{bmatrix} {W_1}^2 \\ {W_2}^2 \\ {W_3}^2 \\ {W_4}^2 \end{bmatrix} + \begin{bmatrix} 0 & 0 & 0 & 0 \\ L_1 & L_2 & L_3 & L_4 \\ M_1 & M_2 & M_3 & M_4 \\ N_1 & N_2 & N_3 & N_4 \end{bmatrix} \begin{bmatrix} \partial_1 \\ \partial_2 \\ \partial_3 \\ \partial_4 \end{bmatrix} \quad (77)$$

To find the unknown coefficients of the cyclic matrix, several rotor tests are conducted. These tests are done to understand the contribution of cyclic control on rolling and pitching moments of the aerial vehicle. Different cyclic control inputs are given, and the moments generated on rotor are measured in different axes to approximate a simpler model of this relationship.

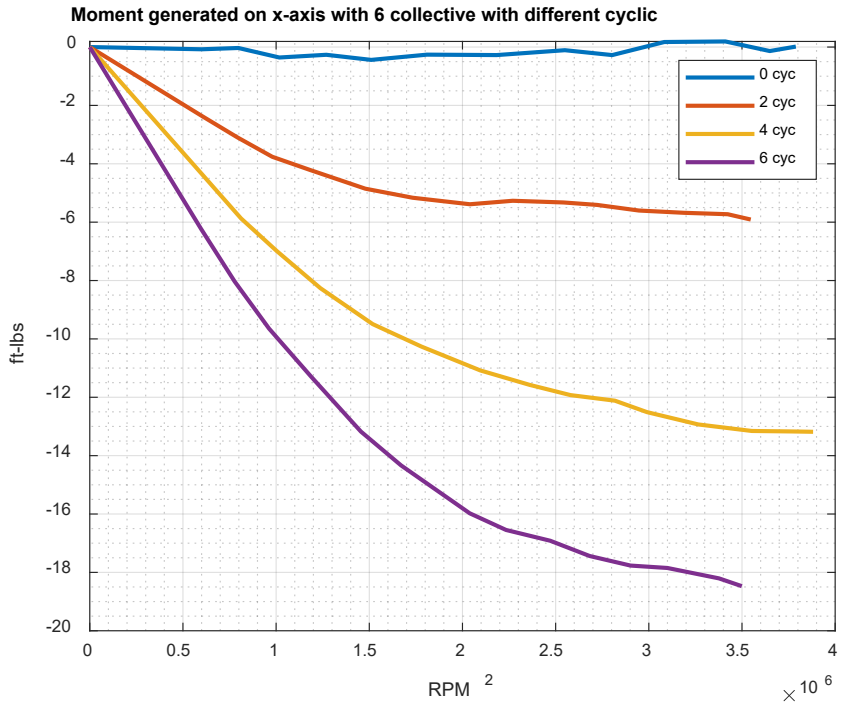

Figure 89. Moment and cyclic test 1

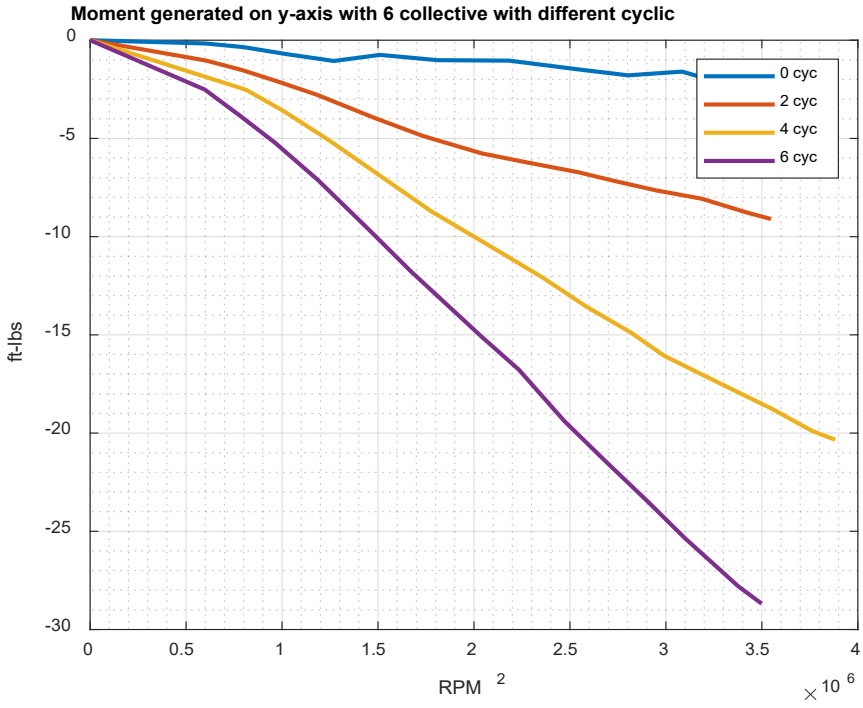

Figure 90. Moment and cyclic test 2

In Figure 89, for 6° of collective angle, the generated moment in pounds-ft in x axis is presented with respect to the rotor RPM for different angle of cyclic controls as $0^{\circ}, 2^{\circ}, 4^{\circ}$, and 6°. In Figure 90 for 6° of collective angle, the generated moment in pounds-ft in y axis is presented with respect to the rotor RPM for different angle of cyclic controls as $0^{\circ}, 2^{\circ}, 4^{\circ}$, and 6°.

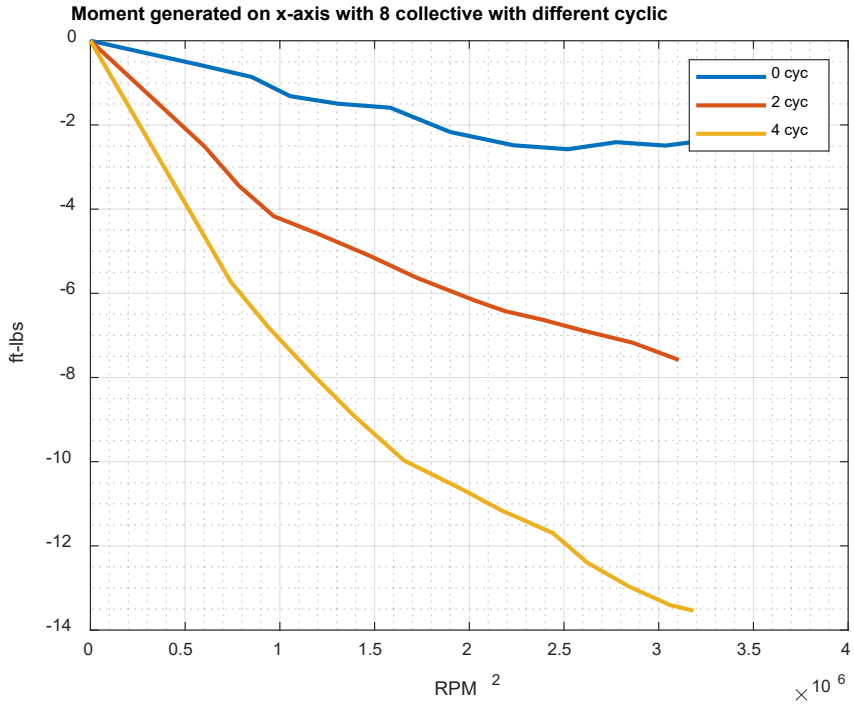

Figure 91. Moment and cyclic test 3

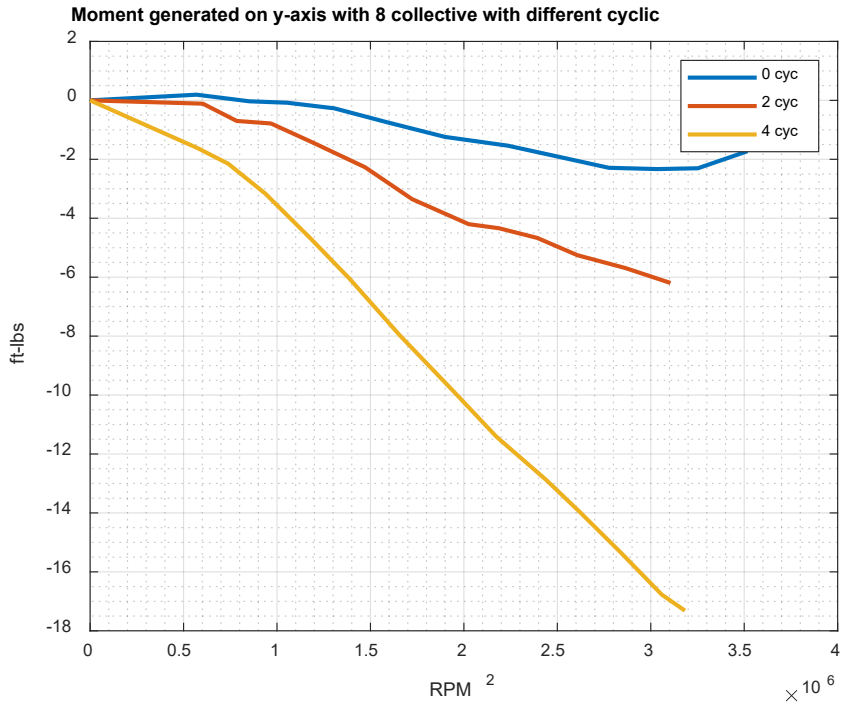

Figure 92. Moment and cyclic test 4

In Figure 91, for 8° of collective angle, the generated moment in pounds-ft in x axis is presented with respect to the rotor RPM for different angle of cyclic controls as 0°, 2°, and 4°. In Figure 92, for 8° of collective angle, the generated moment in pounds-ft in y axis is presented with respect to the rotor RPM for different angle of cyclic controls as 0°, 2°, and 4°.

The measured results of generated moments in x and y axis show a similar behavior as a second-degree polynomial for 6° and 8° of collective angles.

4.6 Task F: Perform flight tests with prototype vehicles

Phase 2 of this research has had major milestones in terms of flight testing, such as translational motion flight. This unlocked the capability of maneuvering while always keeping the attitude of the vehicle level. This mode could have applications such as proximity operations or carrying sensitive cargo.

The effectiveness of these new control strategies in off-nominal mode was of interest. The third quarter of Phase 2 was spent evaluating and enhancing the failure flight capability of the test bed. After many test flights, the PAVER was able to switch from nominal to off-nominal mode midflight and then return to nominal smoothly. Lessons learned from previous testing of different control strategies lead to the development of the control mode that could make this

possible, details of which are described below. Since the certification of such vehicles heavily depends on their capability to seamlessly compensate rotor failure, exploring and developing control laws for that is crucial.

4.6.1 Variable pitch 2 VP2 self-level controller

One of the first steps towards developing a translational controller is the self- leveling of the vehicle. This has been achieved by modifying the already developed VP2 controller during Phase 1 (Collins, et al., 2023). A self-level switch was implemented in the control law (Figure 93) that commands “zero” (level) attitude in roll and pitch when the pilot lets go of, or returns to center, the controls. The level switch can be seen in Figure 94. The accuracy, however, will depend on how well the Pixhawk has been calibrated with respect to level ground.

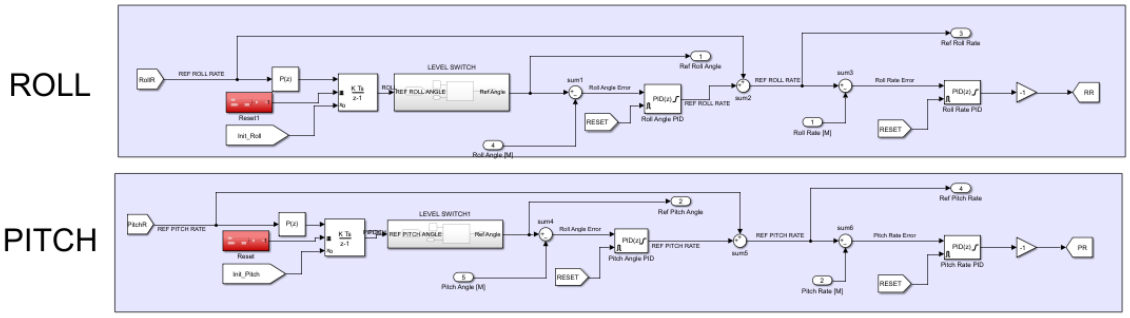

Figure 93. Cascaded feed-forwarded controller with self-level switch

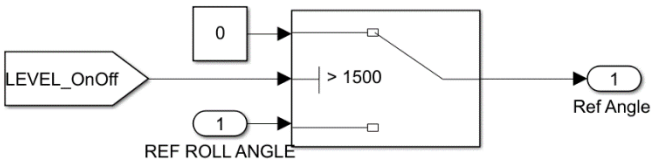

Figure 94. Level switch

Once the level switch has been activated in flight, the vehicle levels its attitude with no pilot stick inputs. However, when the self-level is deactivated in flight, the vehicle would return to its previous attitude just before the self-level was activated, which causes the vehicle to jerk. This is due to the integrator block holding the attitude just before activating the self-level. For this reason, the reset switch had to be modified to reset the integrator block to its initial condition when the self-level has been activated. This allows the vehicle to continue flying from “zero”

attitude after deactivating the self-level and avoid any jerks. The reset switch can be seen in Figure 93 in Red and in Figure 95 in expanded view.

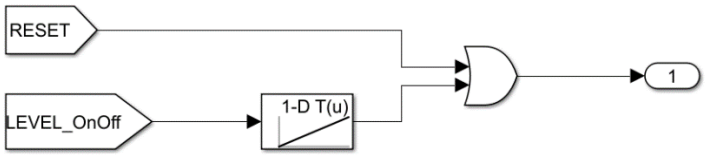

Figure 95. Integrator reset switch

Flight data recorded by the IMUs onboard the vehicle, such as pitch and roll rate, provided insights into the command tracking of the drone and its response time. The graphs below show that the flight controller gives almost equal and opposite command for roll and pitch rate as soon as the pilot commands zero (Figure 96 and Figure 97).

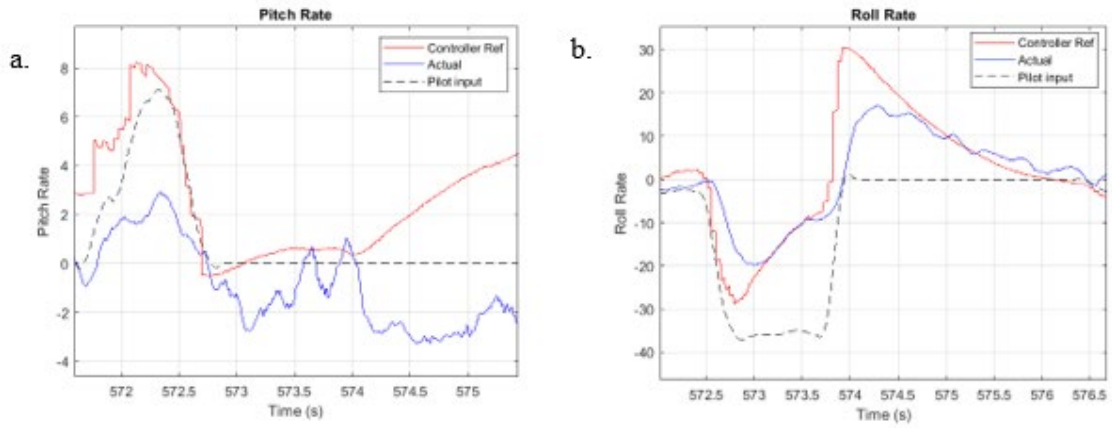

Figure 96. Pitch (a) and roll (b) rates for VP2 self-level flight

a. b.

Figure 97. a) Vehicle tracking pilot pitch command. b) Vehicle returning to level when no pilot input commanded

4.6.2 All-cyclic control (Variable Pitch 3)

The all-cyclic control, also known as Variable Pitch 3 (VP3), is a new control method that uses cyclic-only controls for maneuvering, similar to how the yaw is controlled in VP2. The thrust is still controlled by collective. A new collective cyclic pitch mixing (CCPM) algorithm had to be developed that also accounts for the gyroscopic precession.

As discussed in Section 5.10.10 of the Phase 1 report, the grouping of four rotor discs to a common airframe changes each rotor's respective gyroscopic precession by a unique value (Collins, et al., 2023). In the endeavor to identify this phase angle, tests were performed on the EFRC's RTS with a mix of collective and cyclic inputs that generated forces and moments. Computing the arctan of the forces, the phase angle was found to be between 45° and 50°. Consider commanding a negative cyclic elevator for the first rotor, as seen in Figure 98; the rotor disc will have a positive angle of attack on "+alpha" in the rotation of the rotor. On conventional rotors, due to gyroscopic precession, the maximum lift is offset by 90°, which would produce a negative pitching moment, as seen in green. However, due to the constraint of the arms, the lift is now instead offset by 45° to 50° in the direction of rotation and would produce a pitching moment as seen in red. The same would apply to a counterclockwise rotating rotor, except the phase angle would just be reversed. This offset was corrected to 90º by employing a rotation matrix within the flight software's CCPM algorithm. A phase angle of 50 º was used in the design of the control law deployed on the vehicle.

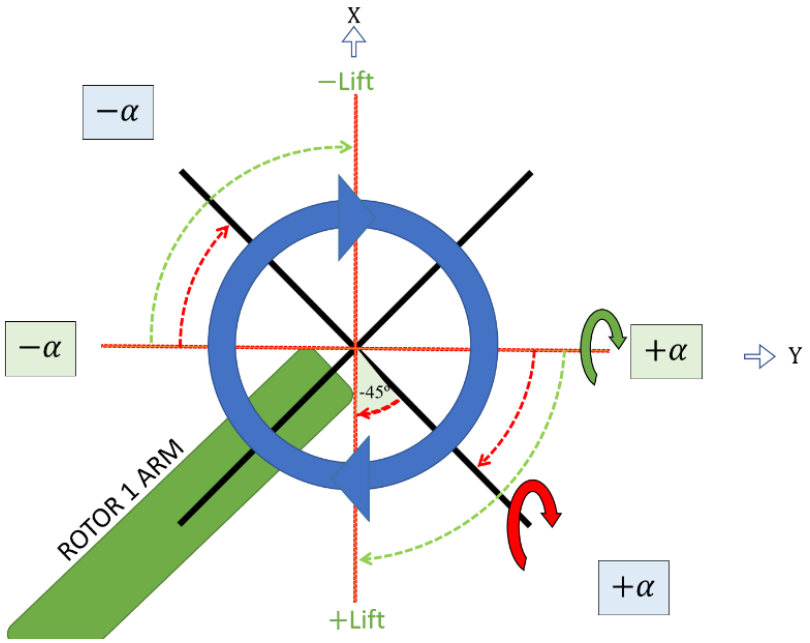

Figure 98. Gyroscopic precession

To account for the gyroscopic precession, a direction cosine matrix (DCM) has been applied to each of the pods. Figure 99 shows the DCM applied to pod 1. The axes of the pods are first aligned with respect to the body frame, then the gyroscopic precession of 50° has been applied. This is done so that the phase angle value can be changed later for optimal phase angle which would be a function of RPM and cyclic angles. The outputs are fed to the servos as PWM signals.

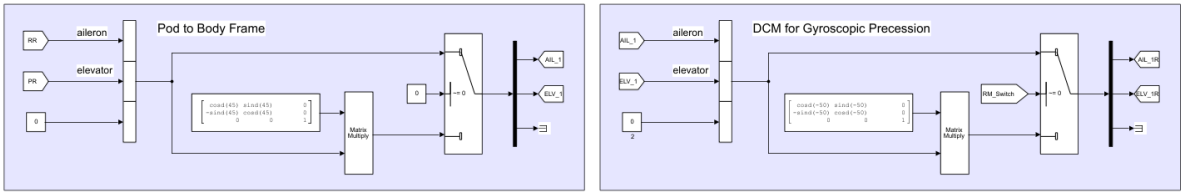

Figure 99. Gyroscopic precession applied to pod 1

A flight test was conducted to test the all-cyclic control capability of the vehicle. As this was another building block of the translational motion control, this control strategy had to have enough control authority to maneuver the vehicle with the disk tilt capability (i.e., all-cyclic). Initially the PID gains used for this control strategy were same as the ones in VP2, however it resulted in delayed response time in roll and pitch maneuvers. Here, yaw was unaffected, as it was already controlled by cyclic control in VP2. PID gains were further tuned from initial tests and were validated in flight after determining optimized gains for all-cyclic control.

4.6.3 Translational motion flight

The translation motion control was developed through the fusion of VP2 self-level control and all-cyclic VP3 control. This new control strategy enables the vehicle to maneuver while always keeping the attitude of the vehicle level. Here, the level attitude is maintained by commanding differential collective to counteract any moment observed by the onboard sensors, and translation in airspace is made possible using cyclic control. The overall thrust in this scenario was still modulated via collective pitch control.

This control law was developed to further explore the capabilities of the test vehicle and demonstrate a coordinated flight implementation in a full-scale eVTOL vehicle for better passenger comfort.

The CCPM for this control strategy can be seen in Figure 100, where the VP2 and VP3 control strategies are merged. When the vehicle is in translation mode, the pilot stick commands collective and cyclic only controls (VP3), while the controller commands roll and pitch through differential collective (VP2) to maintain a level flight.

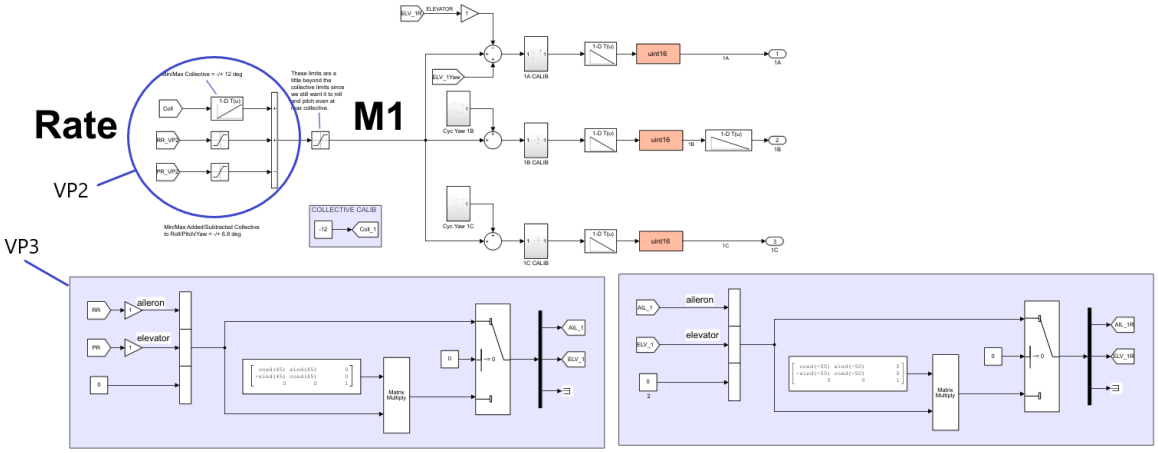

Figure 100. Translation flight CCPM

This is achieved through a state flow chart, as seen in Figure 101 and Figure 102, where switching between VP3 only and translational flight is performed.

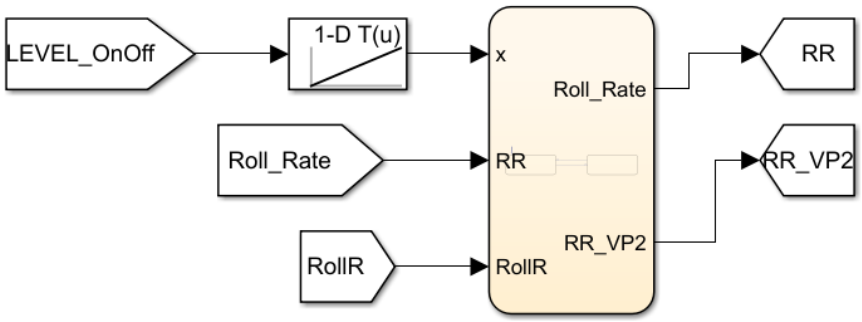

Figure 101. State flow for roll rate

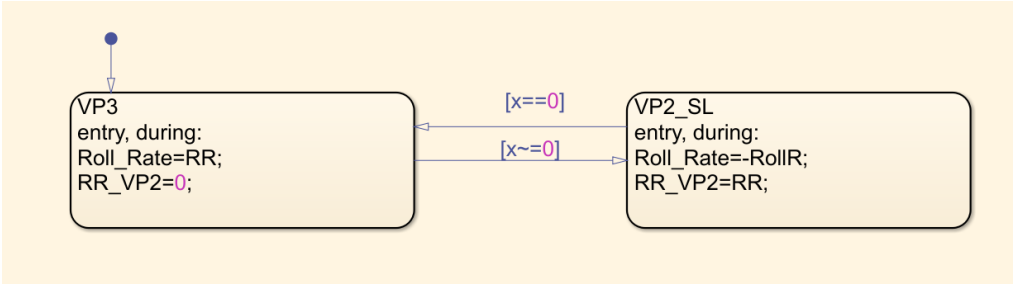

Figure 102. State flow chart

When the translation switch is activated, the pilot stick now commands only cyclic inputs (VP3), while the controller sends differential collective commands (VP2) to always maintain zero roll and pitch angle. Gain scheduling is used to switch between different PID gains for cyclic only flight and translational flight.

The translation motion flight test was conducted at a low RPM of 1300 with VP2 self-level on and cyclic only for maneuver control. The vehicle was stable with some moments generated while starting and stopping forward flight. Initial flight testing revealed that the vehicle was actively holding level attitude but had low response time in translation due to low cyclic authority. For further testing, cyclic authority (i.e., limits of swash plate deflection) was increased to give the pilot more cyclic capability, which significantly improved translation response time.

Figure 103. PAVER translational flight in EFRC drone test cage

4.6.4 PAVER off-nominal flight testing

As concluded in Phase 1 of this project, the VP2 is the only control strategy that makes failure flight possible. However, certain aspects of this control strategy had to be improved or explored further. For example, tracking of VP2 had to be improved while flying in off-nominal mode by optimizing the PID gains used while operation; the capability to switch from nominal to off-nominal mode in flight had to be tested; and finally, forward flight capability in off-nominal mode is yet to be explored.

One of the lessons learned in the process of developing the cascaded controller to accommodate failure flight was that the PIDs used in the controller give out a significant integral windup when switched from nominal to off-nominal mode. When this happens, the pilot slowly starts losing

control to the point where the vehicle is unable to track pilot input and becomes unstable. In order to overcome this issue, PID reset was turned on in the PID blocks during flights to improve tracking. This mode allowed us to maintain hover in failure mode, hands-off. PIDs were tuned for these changes.

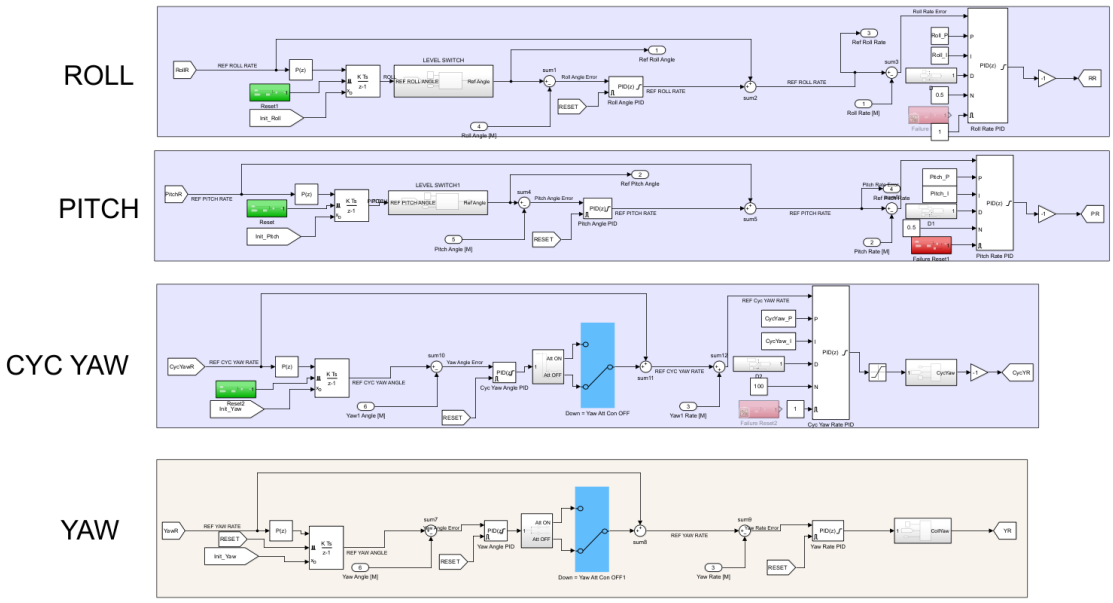

Figure 104. Updated VP2 controller

The cascaded controller was edited to keep PID reset on as shown in Figure 104 the VP2 control strategy is using differential collective for roll and pitch and using cyclic for yaw. A magnified view of the controller (Figure 105) presents the PID reset on applied to all the sections on the controller. The PIDs were tuned for this mode.

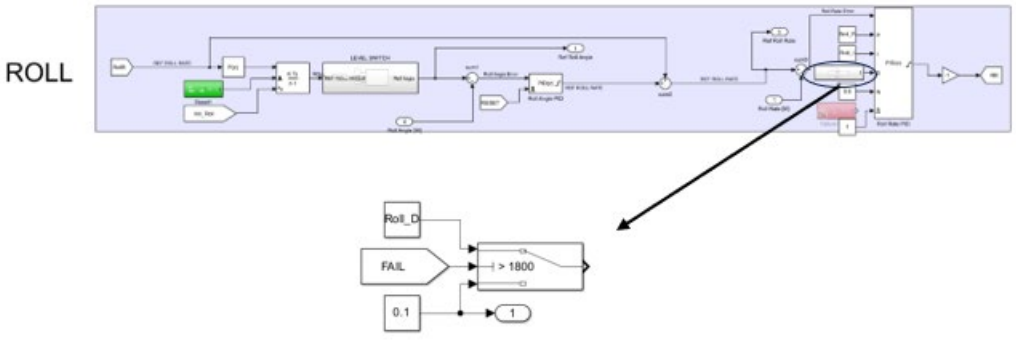

Figure 105. PID reset applied to the controller PIDs

This change in the VP2 controller created the ability to switch from nominal to off-nominal mode in flight without disruption to attitude, altitude, and heading. This has applications in practical testing of failure flight, switching from off-nominal to nominal in flight, and translational flight.

The data from a flight test of these changes is shown in Figure 106, Figure 107, and Figure 108 below. It shows the flight mode change from nominal to off-nominal mode (rotor failure) in flight and the controller commanding controls to counteract the failure.

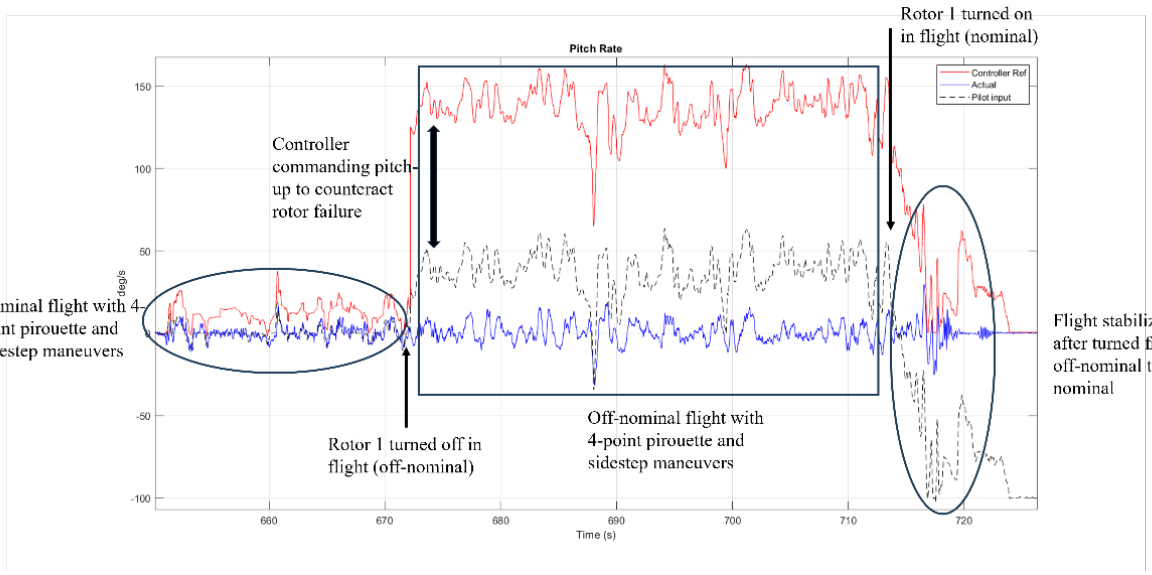

Figure 106. Flight data for failure in hover (pitch)

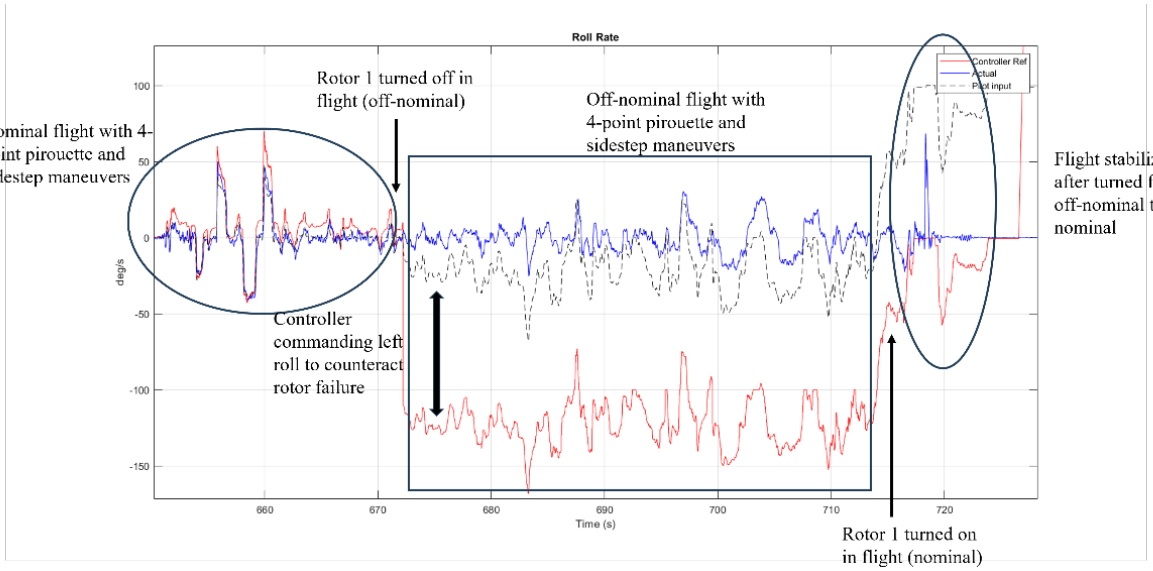

Figure 107. Flight data for failure in hover (roll)

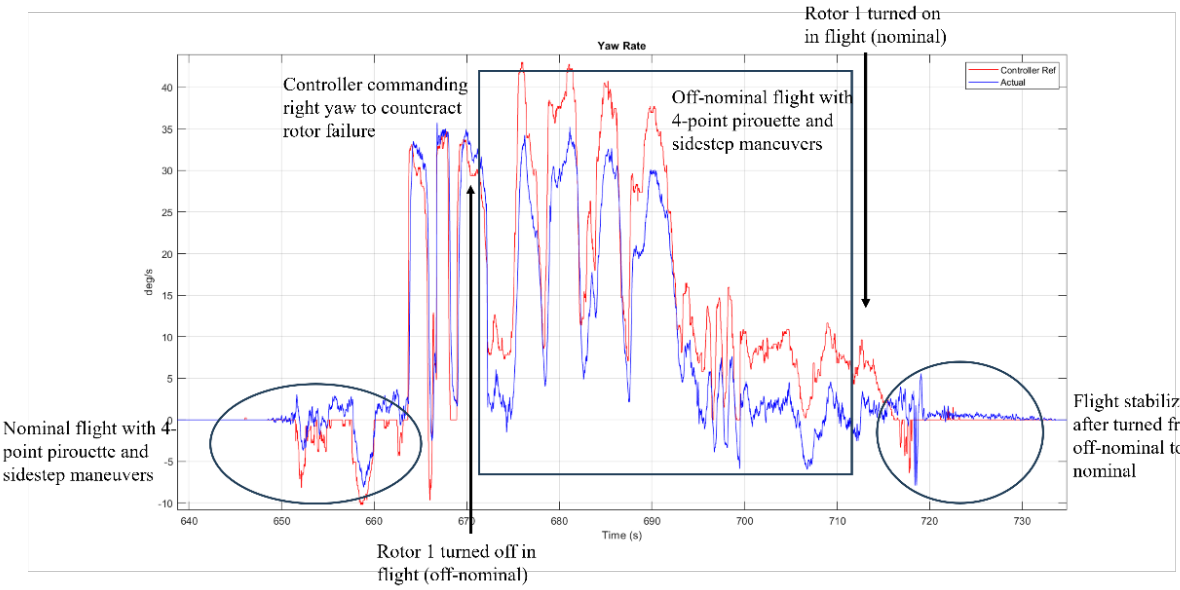

Figure 108. Flight data for failure in hover (yaw)

4.6.5 Frequency sweep testing for system identification

The first set of frequency sweep testing was performed on simulation and Mini PAVER. This test was mainly focused on practicing manual frequency sweeps with the SCAS-ON. The data to be logged for the manual frequency sweep testing are the measured angular rates, attitude in Euler angles, pilot stick inputs, body axes accelerations, mixer inputs, controller reference inputs, attitude reference, linear velocities in NED frame, latitude and longitude and PWM inputs to the 12 servos. All the mentioned data are logged at 250 Hz except for the attitude reference measured and collective, which were logged at 125 Hz. This was done to save memory on the Pixhawk's RAM.

The Flight Control System (FCS) in simple block diagram form for the PAVER flight model can be seen in Figure 109. The mixer inputs $\delta_{col}, \delta_{pmix}, \delta_{qmix}$ *and* δ_{rmix} are taken as inputs for the frequency response and the vehicle states as the measured outputs.

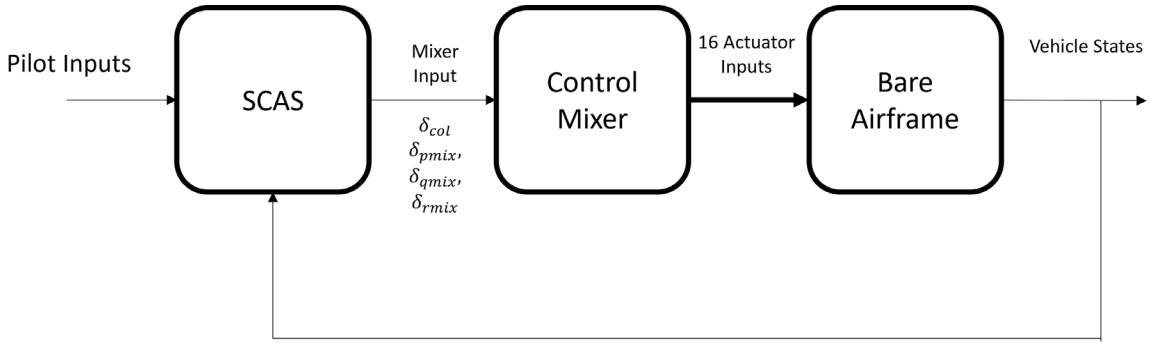

Figure 109. FCS block diagram

The test performed on the Mini PAVER was used to familiarize the researchers with frequency sweep testing and to make sure there the vehicle would not become unstable with increasing frequency. This methodology for the frequency sweep testing is as follows:

- The frequency range for the sweep must be specified. It was determined to be in the range of 0.1 rad/s to 50 rad/s or 0.01 Hz to 2 HZ.
- Each sweep would begin with two long period doublets followed by increasing frequency from low to high and would start and end at trim (hover) condition for at least 3 seconds.
- The amplitude of the frequency would not be constant in manual sweeps but would be constant in automated sweeps.
- Each sweep would be around 15 to 20 seconds in order to properly excite the vehicle dynamics.
- The sweeps would be performed for each control axis independently (roll, pitch, yaw, and heave).
- The test should be conducted ideally in no wind conditions; however, as long as the bias from the wind disturbance is less than 0.3, the resulting identification would be acceptable.
- A mix of multiple manual and automated sweeps will be performed for each axis to gather as much data as possible. This will help with good identification.
- The tests should ideally be performed with the SCAS off; however, due to the unstable dynamics of the vehicle, it is preferable to keep the SCAS on during the sweep. In cases where the SCAS is on, the mixer inputs will be considered as inputs instead of the actual pilot inputs.

- The data recorded should include angular velocities, vehicle attitude, accelerations, linear velocities, pilot inputs, mixer inputs, positions, and altitude. Moreover, the data should be recorded at 1khz.

The following plots represent the flight test data from the frequency sweeps performed on the Mini PAVER. The plots show pilot inputs vs the vehicle response for pitch, roll, and yaw rate. In Figure 110 and Figure 111, the pitch and roll rate response for the frequency sweep can be seen. It is clearly shown that the vehicle follows the pilot inputs very closely for the low frequency inputs, and as the frequency increases, the vehicle response starts to attenuate, although not drastically. However, in the yaw rate, the vehicle response attenuates drastically as the frequency is increased, as seen in Figure 112. This is due to the vehicle's inertia in the yaw axis. This practice test was performed in windy conditions and hence is not useful for system identification, as it has a lot of cross control correlation, such as yaw and roll coupling.

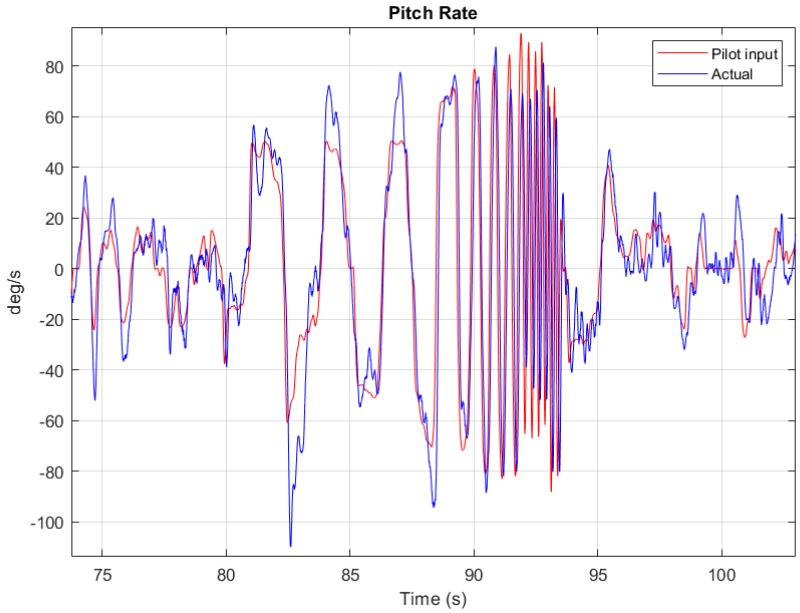

Figure 110. Pitch rate response

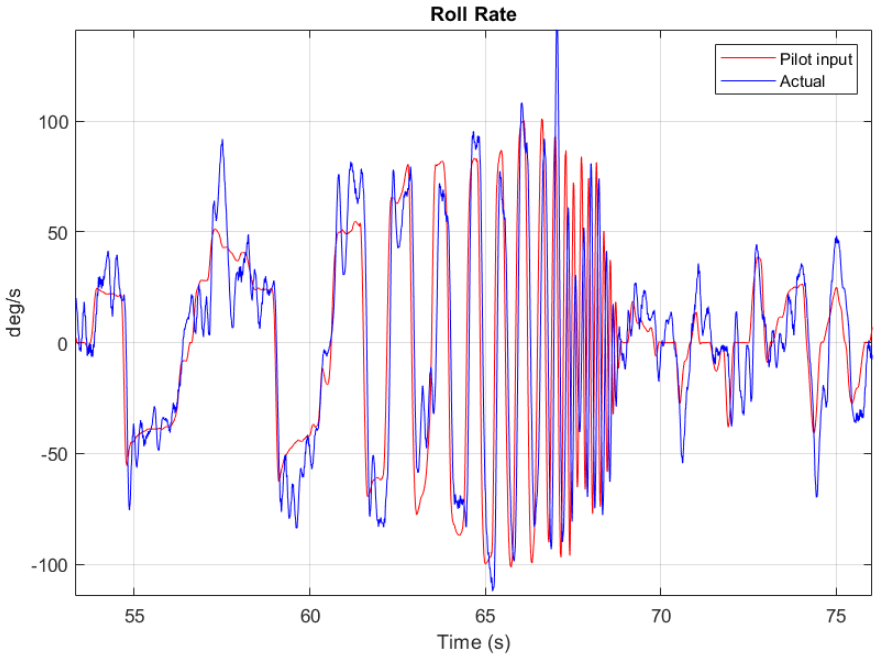

Figure 111. Roll rate response

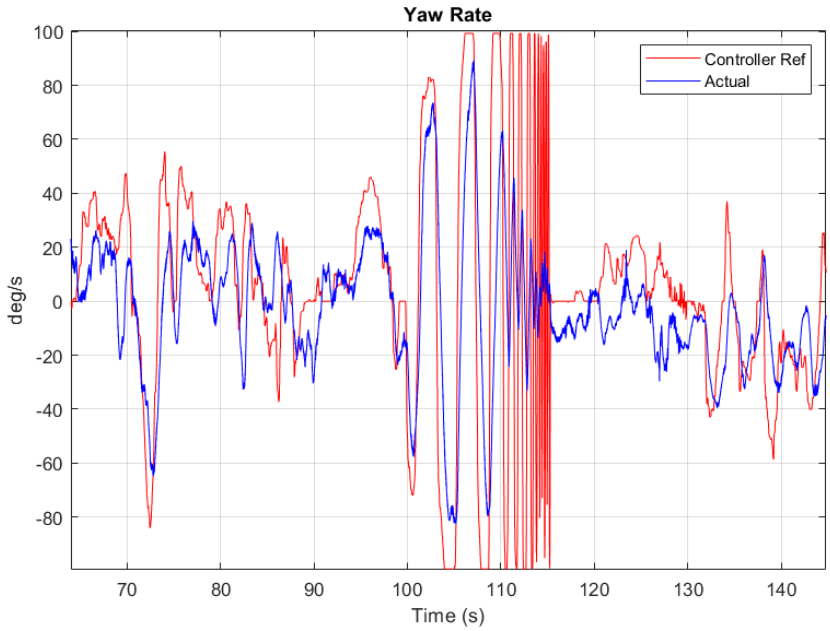

Figure 112. Yaw rate response

After testing the methodology on the Mini PAVER, the frequency sweeps were performed on the PAVER vehicle. These were also performed manually by the pilot. Due to testing area

restrictions, the sweeps at lower frequencies were avoided to prevent collision of the vehicle with the testing cage. The frequency range for the pitch and roll axes was 1.5 rad/s to 45 rad/s, while for the yaw axis it was 0.5 to 22 rad/s. This was due to the huge inertia of the vehicle during yaw. The heave axis was also in the similar range, from 1.5 to 13 rad/s, because the area was also limited in vertical space.

The following plots (Figure 113, Figure 114, Figure 115, Figure 116, Figure 117, and Figure 118) show the sweep data from one of the flight tests. This particular test was performed during calm wind conditions, which were about 8 km/h gusting at the time of the test. Therefore, the signal-to-noise ratio is low and is acceptable for the purpose of system identification.

a.

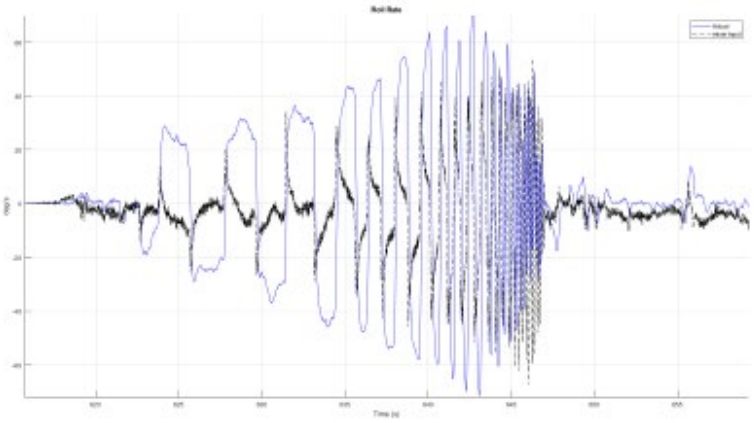

b.

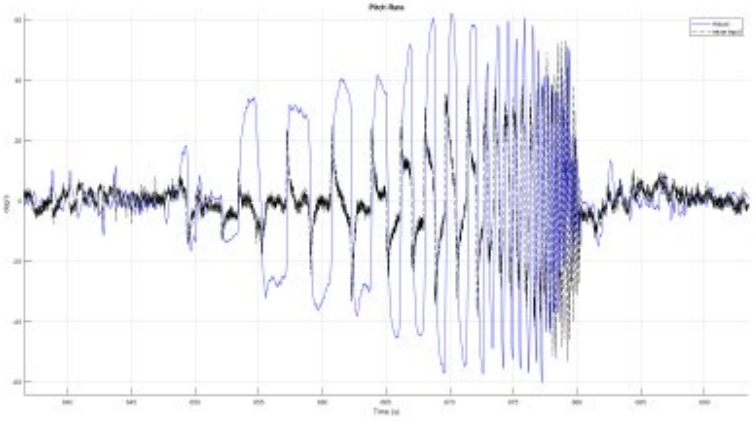

c.

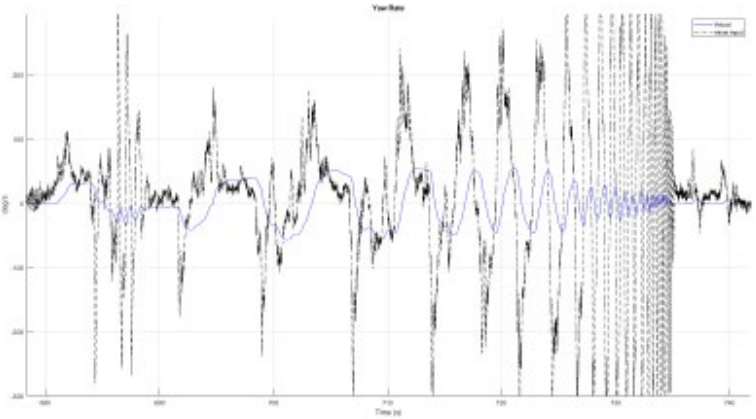

Figure 113. Mixer inputs vs. measured angular rates for roll rate (a), pitch rate (b), and yaw rate (c)

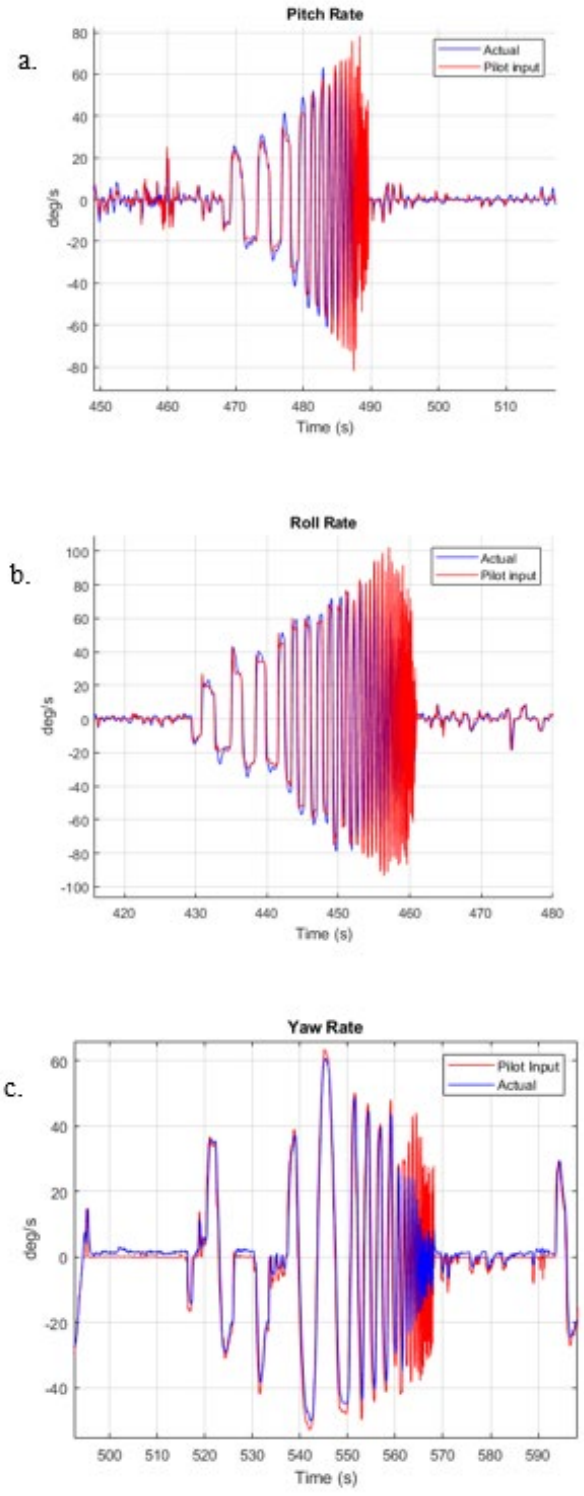

Figure 114. Pilot inputs vs. measured angular rates for pitch rate (a), roll rate (b), and yaw rate (c)

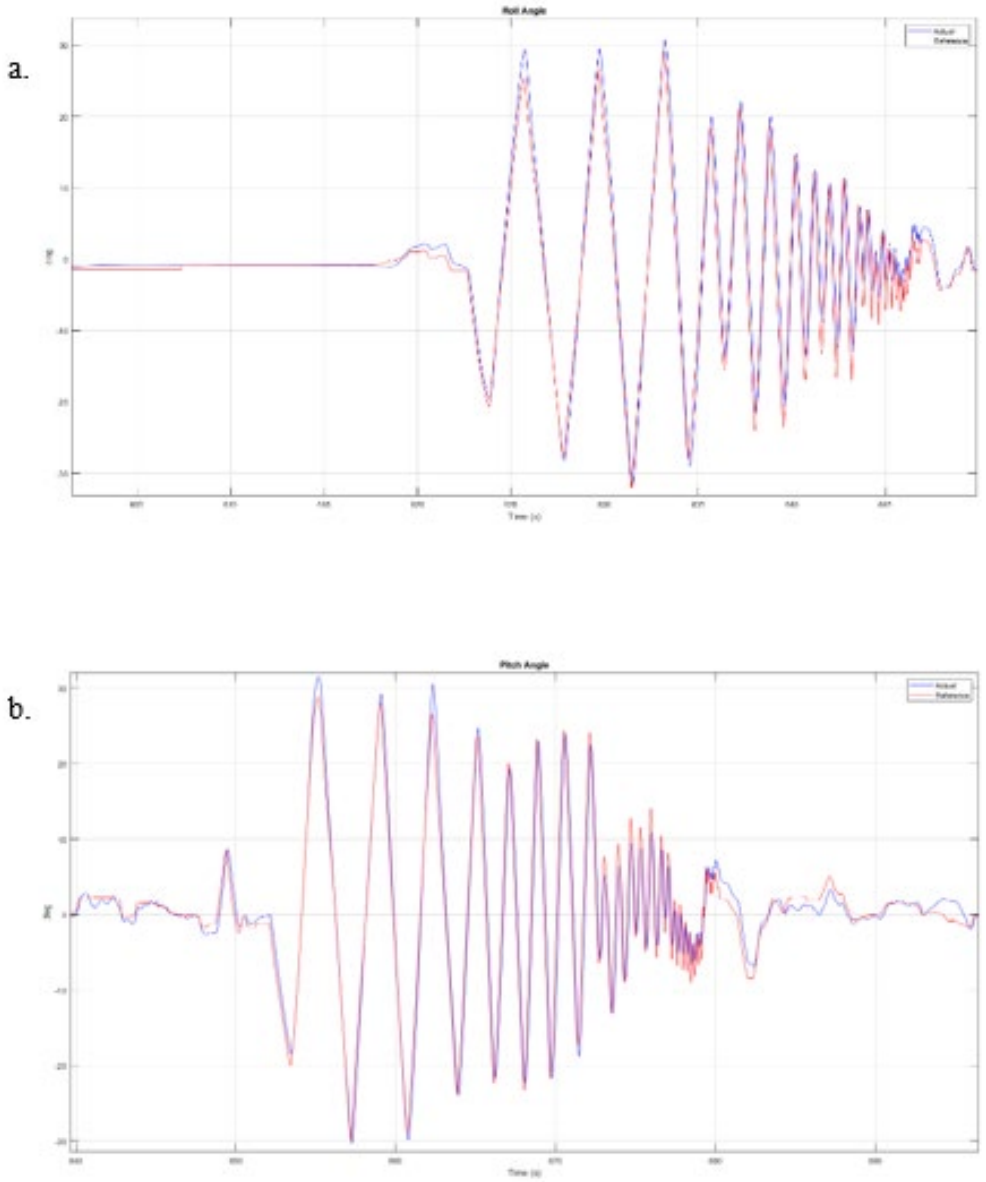

Figure 115. Attitude reference vs. measured roll angle (a) and pitch angle (b)

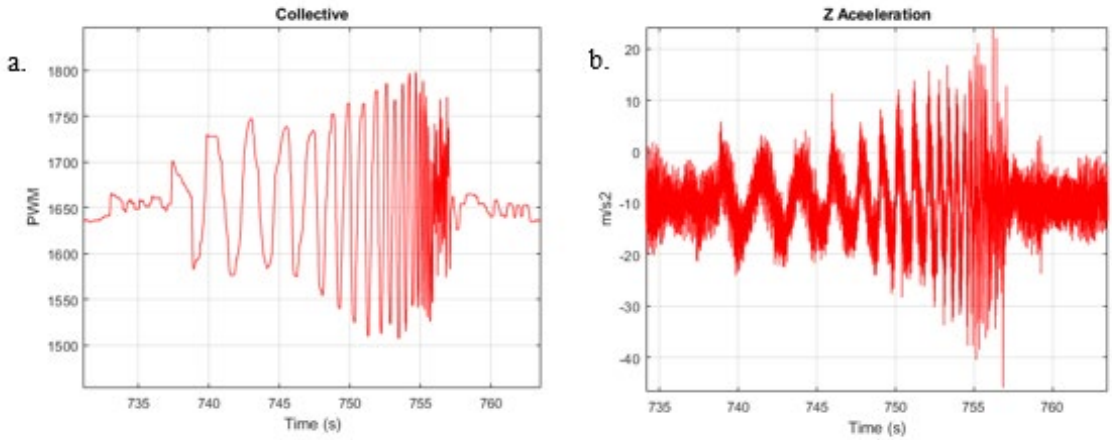

Figure 116. Heave sweep (collective) (a), body acceleration in z-axis (b)

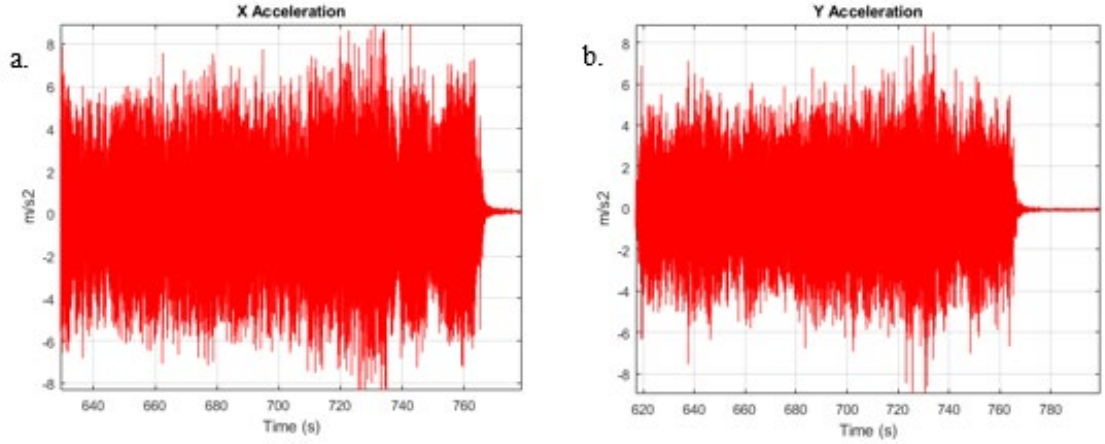

Figure 117. Body accelerations in x and y axes

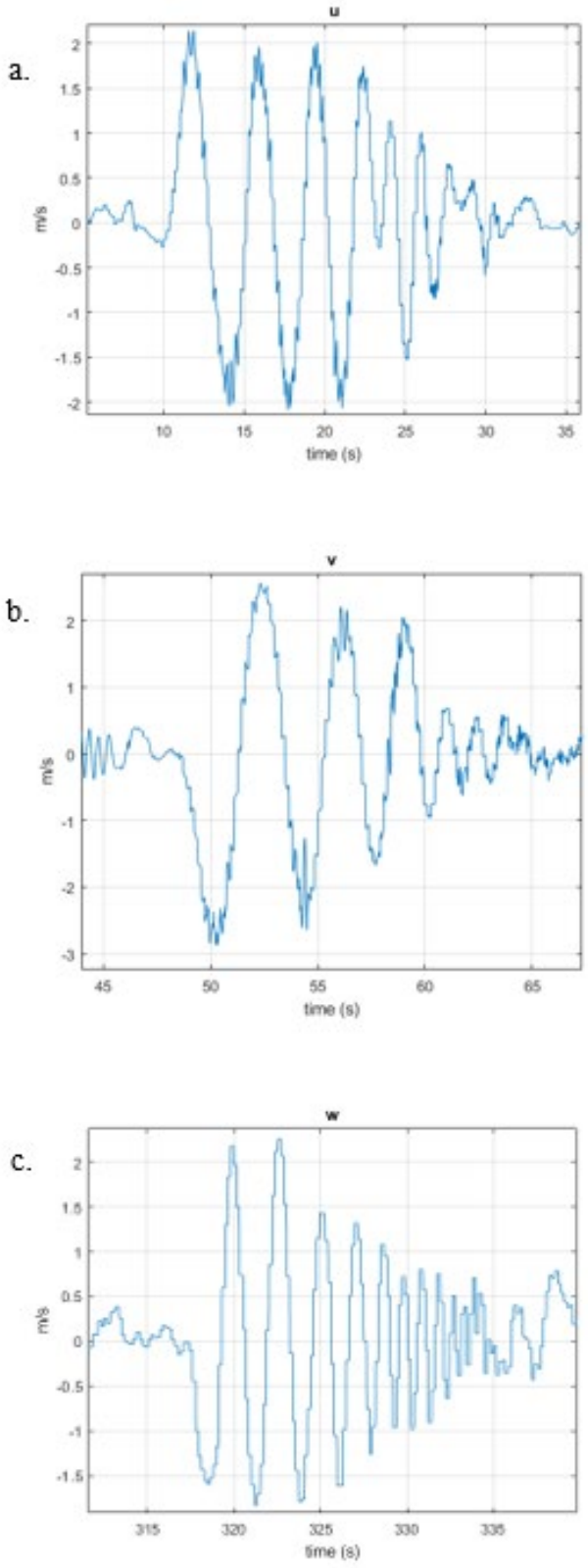

Figure 118. Linear velocities in NED frame

4.6.6 PAVER hardware update

A dozen malfunctioning servos were sent back to the manufacturer for repair at the beginning of Phase 2, and feedback was provided from MKS, the servo manufacturer. Most of the malfunctioning servos had damaged components on the printed circuit boards, likely resulting from voltage spikes or unsteady voltage supplied to the servo. The team was also informed that each servo could consume up to 10A of current, far exceeding the 5A estimation made based on ground testing. Although the PowerBox system has not shown any sign of overcurrent, it is possible for the servos to reach peak current when the team start to test in open field with more aggressive maneuvers.

New voltage regulators (Figure 119) were implemented to address servo power supply issues on the V1 PAVER. Each DEP pod was equipped with one Hobbywing universal battery eliminator circuit (UBEC), capable of supplying 25A continuous and 50A instantaneous to the servo actuators. The UBECs were directly connected to the 12S flight batteries to regulate 50V input into 8.4V output for the servos, eliminating a standalone servo battery and the PowerBox distribution system completely. No auxiliary power was connected to the UBECs, as system redundancy was adequate with four groups of flight batteries supplying power in parallel. Shown in Figure 120 is the installed UBEC undergoing flight test before it can be implemented on both PAVER testbeds.

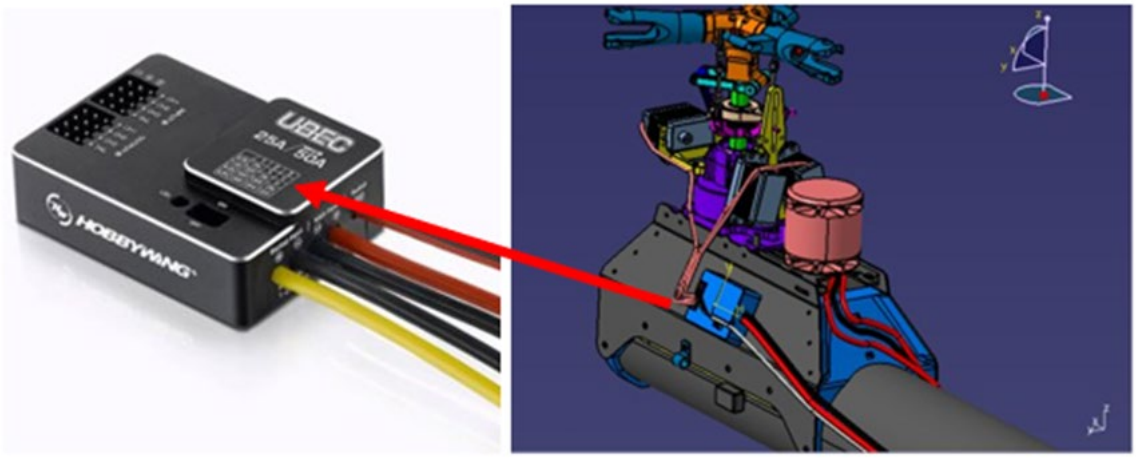

Figure 119. The 25A UBEC being tested on V1 airframe

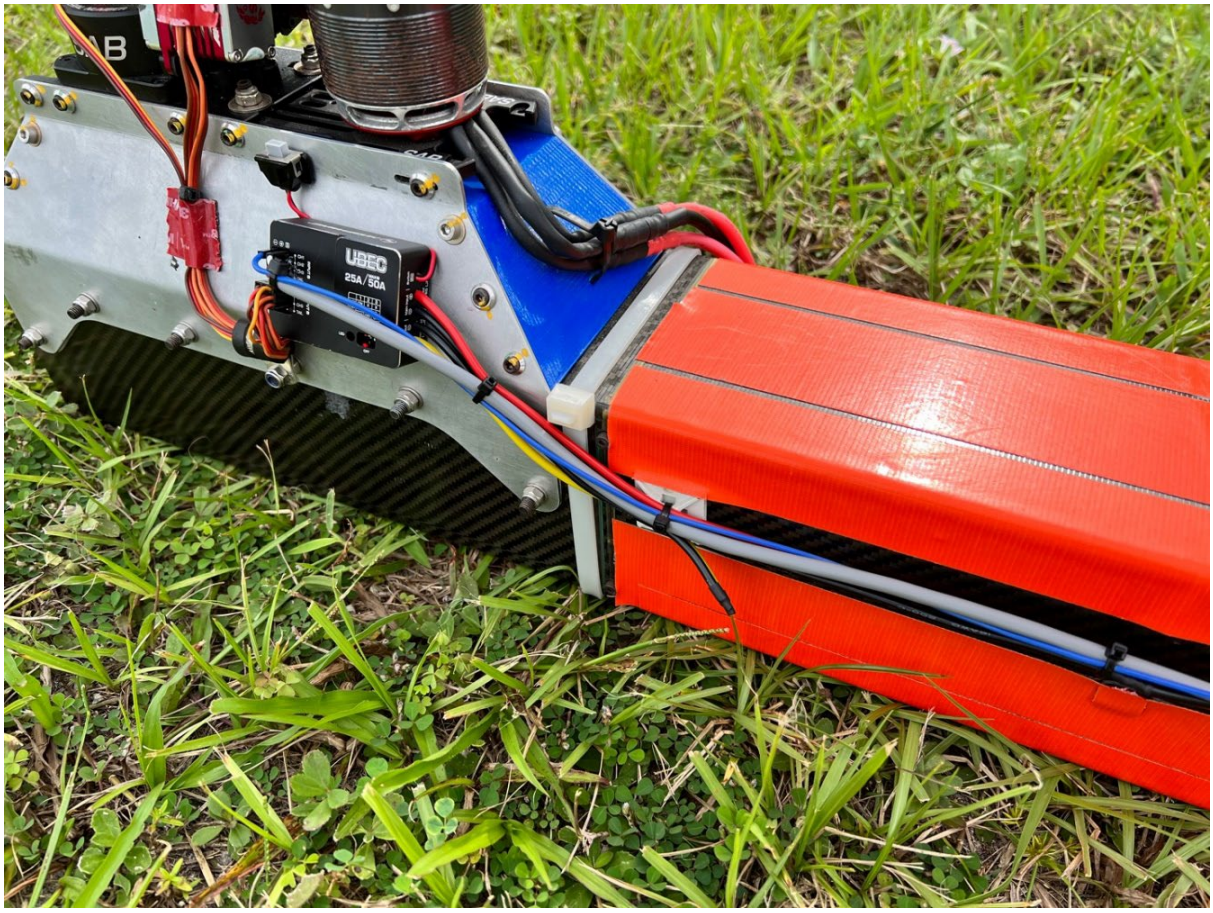

Figure 120. Picture of UBEC installed on the vehicle's DEP pod

As flight testing of failure in hover continued, certain changes were made to the hardware to help get better tracking from the vehicle, less noise, and more disturbance rejection. The flight controller used onboard was changed from Pixhawk Cube Black to Pixhawk 6x, as seen in Figure 121. Further flight testing was done with the new flight controller onboard to facilitate improved off-nominal flights and frequency sweep flights for system identification.

Figure 121. Pixhawk Cube Black (a) and Pixhawk 6x (b)

This flight controller update simplified the electrical wiring of the avionics onboard, which helped to reduce the points of failure during flight testing and the electrical noise generated in form of eddy currents running through the wiring system. The changes, seen between Figure 122 and Figure 123, highlight the improved tidiness of the avionics bay; removing the PowerBox distribution system also eliminated the need for two servo batteries, making for fewer visual inspection points and easier maintenance.

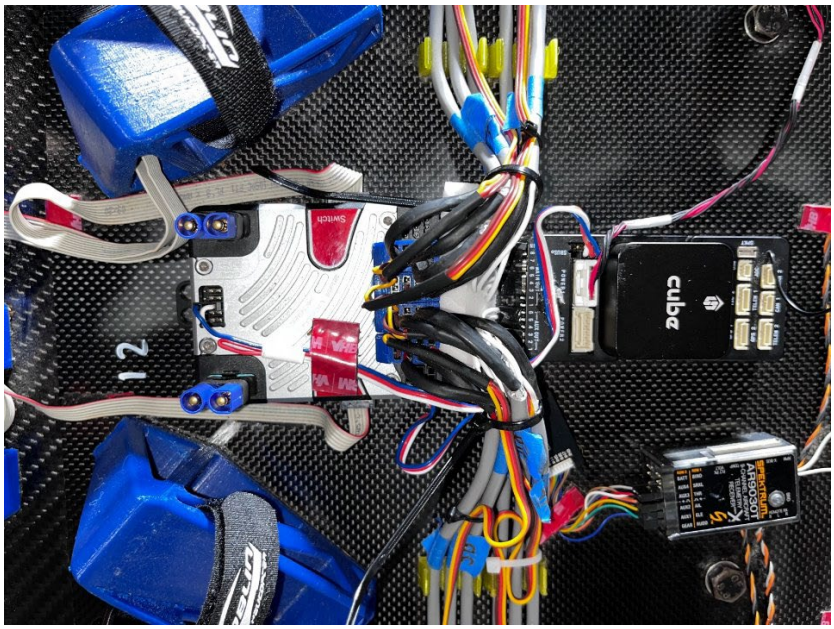

Figure 122. Initial flight avionics system

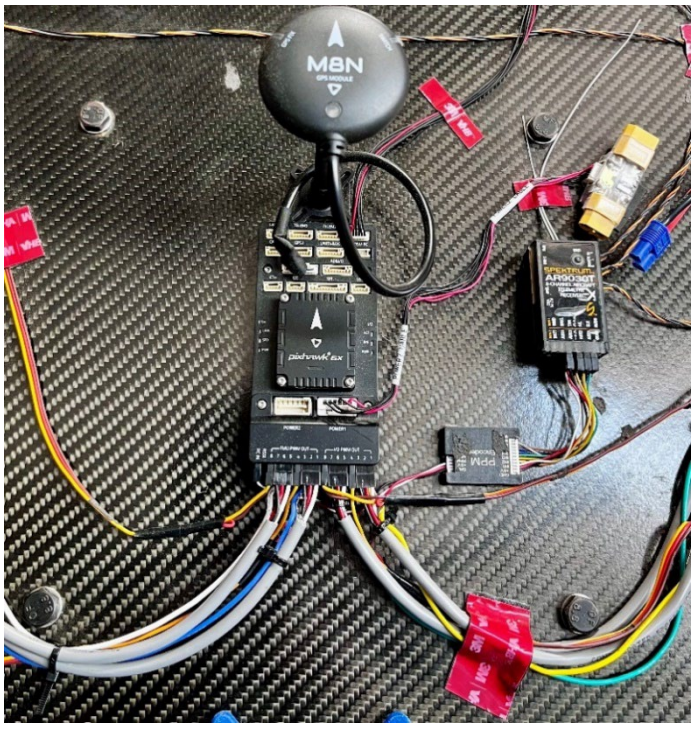

Figure 123. Updated flight avionics system

4.6.7 Lessons learned

This phase saw more flight tests with the updated control laws and new control strategies along with some system identification tests. The VP2 self-level control strategy performed well during flight testing, but it could be improved further by calibrating the flight controller on a flat surface for smoother operation in level flight, most importantly the zero-point calibration done before flight. Optimized PID gains and minimum hardware noise should be considered while operating in this control strategy.

The translational flight control strategy showcased the unique capability of this vehicle. While this control strategy worked, the control laws designed need some tuning and improvement. This is because the PIDs that were tuned for VP2 and VP3 work well individually, but when combined to create translation flight, they must be tuned. Moreover, the increase in cyclic control authority resulted in larger moments and made it difficult for the flight controller to maintain level attitude. Using advanced control laws and control allocation methods would provide stable flight performance.

One of the big milestones achieved was the off-nominal operation of the vehicle. To simulate a failed rotor, one of the rotors was turned off during flight. Though the control law accounted for the failure initially, the issue of integral wind-up still existed. The wind-up would interfere with the controls, progressively leading to loss of control power. This could be avoided by implementing better anti wind-up techniques and more flight tests including forward flight testing.

The data from the frequency sweep testing performed for system identification purposes was acceptable; however, the accelerations showed a lot of noise. This affected the system identification analysis, resulting in a bad identification. This noise was a result of the mechanical vibrations of the vehicle that were picked up by the flight controller. A vibration dampening device could be incorporated below the flight controller for better data clarity. A better tuned noise filter can also help with noise reduction.

4.7 Task G: Validate math models with test data

During Phase 2, the EFRC team used the nonlinear dynamic model to validate and tune the controller gains. The method of using system identification tools to optimize the gains was introduced, where the data from flight test was used to obtain the bare-airframe state-space model. This model was then used to optimize the gains to give better response and handling qualities.

4.7.1 Flight data validation with control equivalent turbulence input model

The dynamic model developed by the EFRC team does a good job of simulating the vehicle. However, due to the lack of a turbulence model, the simulation does not reflect reality. It is more representative of ideal conditions. To improve the fidelity of the dynamic model, the control equivalent turbulence input (CETI) model was implemented. This model is analogous to the Dryden turbulence model, specifically designed for rotorcraft applications. It simulates the effect of turbulence on a rotorcraft operating at hover/low speed conditions. The workflow of implementing the CETI Turbulence model can be seen in Figure 124. The CETI model is inserted after the SCAS and before the mixer inputs to simulate turbulence.

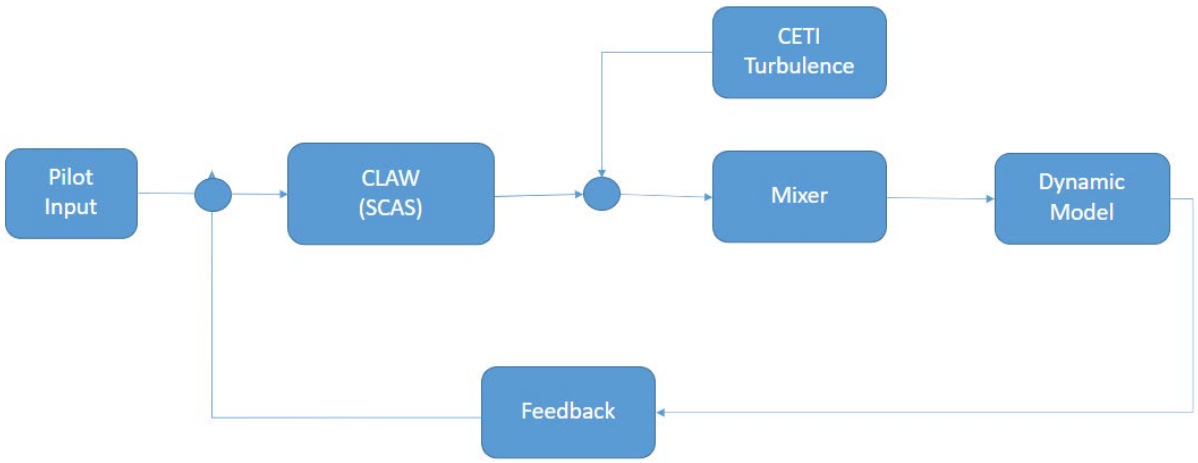

Figure 124. Flight data validation process

For validation, a data set from the PAVER V2 flight test with the VP2 control strategy was taken as an example and validated against the nonlinear dynamic model. Let's consider the case without the CETI turbulence model. This case was validated during Phase 1 and can be seen in Figure 125 below (Collins, et al., 2023). The response of the vehicle tracks the pilot inputs perfectly for the dynamic model while a huge error between the pilot inputs and actual response of the vehicle can be seen. In the next figure, the CETI model was implemented along with a delay of 0.02 seconds and a gain of 1.7 in the feed forward path. This immediately minimized the error between the dynamic model response and the vehicle response for the given pilot inputs. However, some differences between the dynamic model and vehicle responses can still be seen in Figure 125. This is due to the dynamic model not accurately reflecting reality. To improve this, system identification was used to improve the fidelity of the simulation mode.

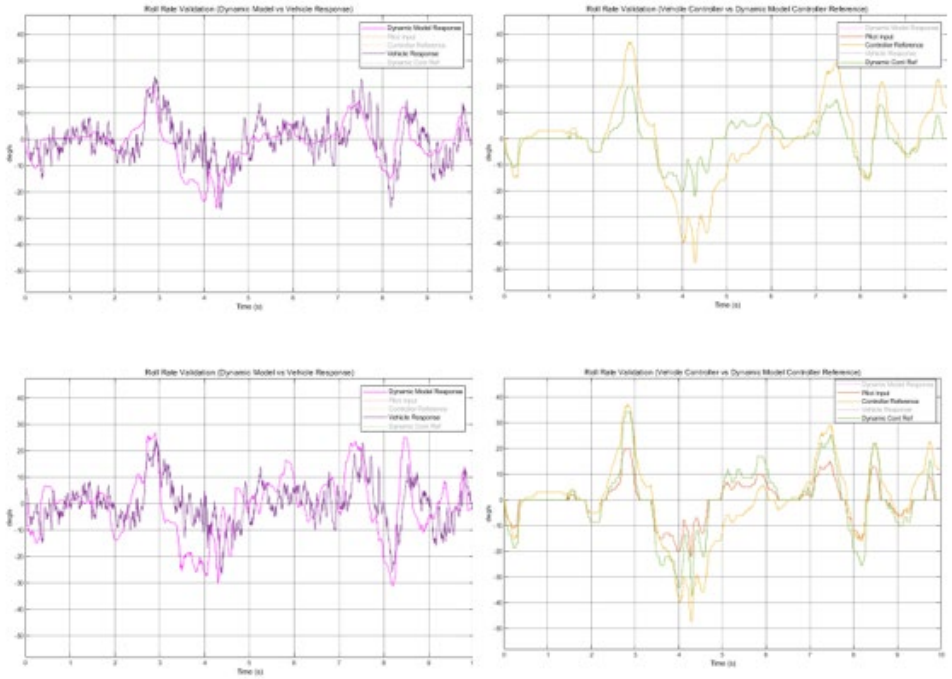

Figure 125. Validation with CETI model and delay

4.7.2 Frequency response analysis

The flight data was transferred over to CIFER to perform frequency response analysis using the FRESPID module to obtain bode plots and coherence of the data. A general guideline on how to decipher the frequency plots is to look at the coherence. If the coherence is close to 1, then it means a good identification, whereas if the coherence is less than 0.6 or close to 0, then it means a bad identification. A basic example is shown in Figure 126.

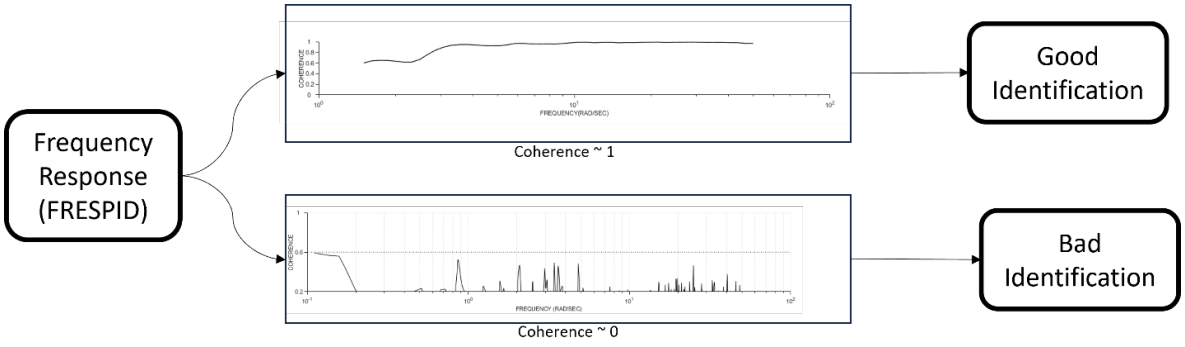

Figure 126. Reading frequency plots

The frequency range was taken as 0.111 to 50 rad/s, and all window sizes were selected. The responses were combined using the COMPOSITE module. The bode plot for roll rate output to

roll rate mixer input ($\frac{p}{\delta_{pmix}}$) and pitch rate output to pitch rate input ($\frac{q}{\delta_{qmix}}$) response is shown below in Figure 127. The coherence starts to be good (≥ 0.6) from around 1.2 rad/s and stays at 1 for the whole frequency range of excitation. This means that the fit is good for the frequency range of application and that the model is indistinguishable from the actual vehicle. This is confirmed by the error plot, where the error goes to 0 for these frequencies.

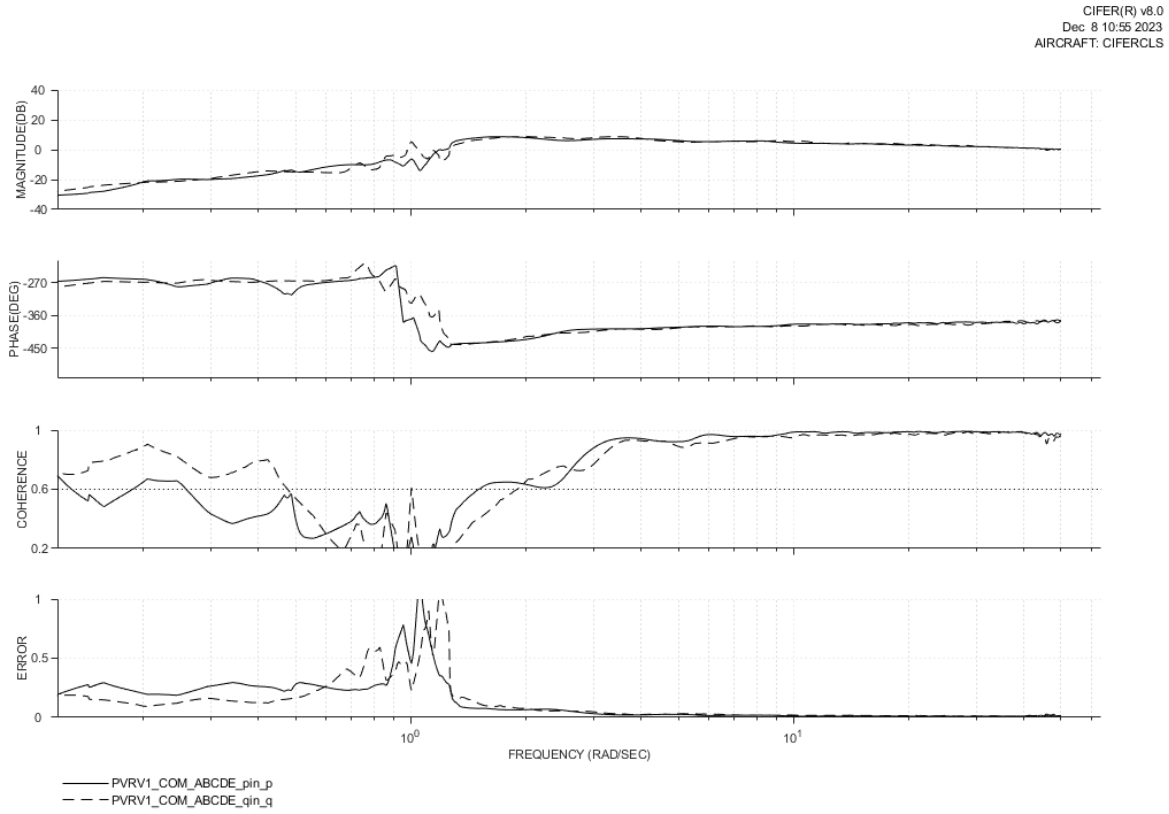

Figure 127. Frequency response bode plot for rate input to measured rate response

The bode plot for roll rate input to measured roll angle $\left(\frac{\phi}{\delta_{pmix}}\right)$ and pitch rate input to measured pitch angle $\left(\frac{\theta}{\delta_{qmix}}\right)$ is given in Figure 128. The coherence and frequency range are similar to the rate response.

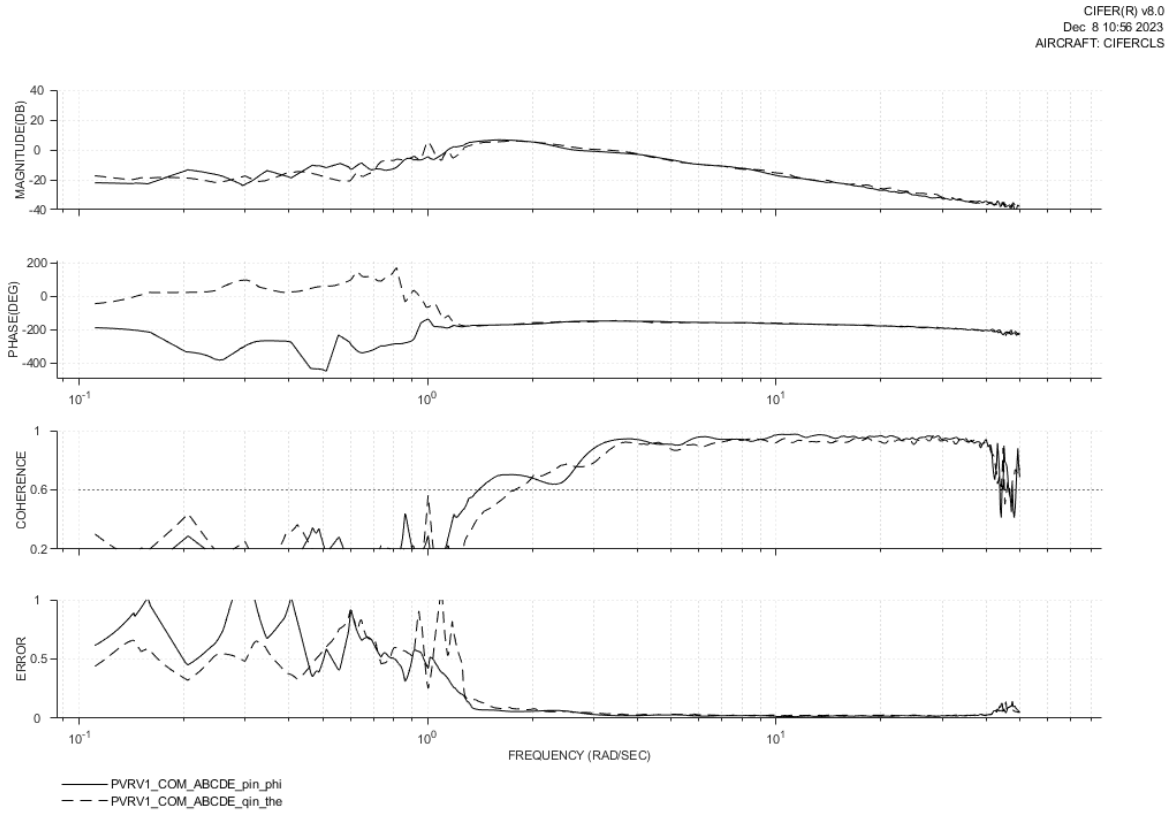

Figure 128. Frequency response bode plot for rate to attitude response

The bode plot for yaw rate input to measured yaw rate $\left(\frac{r}{\delta_{rmix}}\right)$ and yaw rate input to measured yaw angle $\left(\frac{\psi}{\delta_{rmix}}\right)$is given in Figure 129. The $\left(\frac{r}{\delta_{rmix}}\right)$ response, given by the solid line, shows good coherence from 0.5 to 26 rad/s, while $\left(\frac{\psi}{\delta_{rmix}}\right)$ response, given by the dashed line, shows good coherence from 0.5 to 15 rad/s. The coherence degrades for more than 15 rad/s, which may be due to bad data quality.

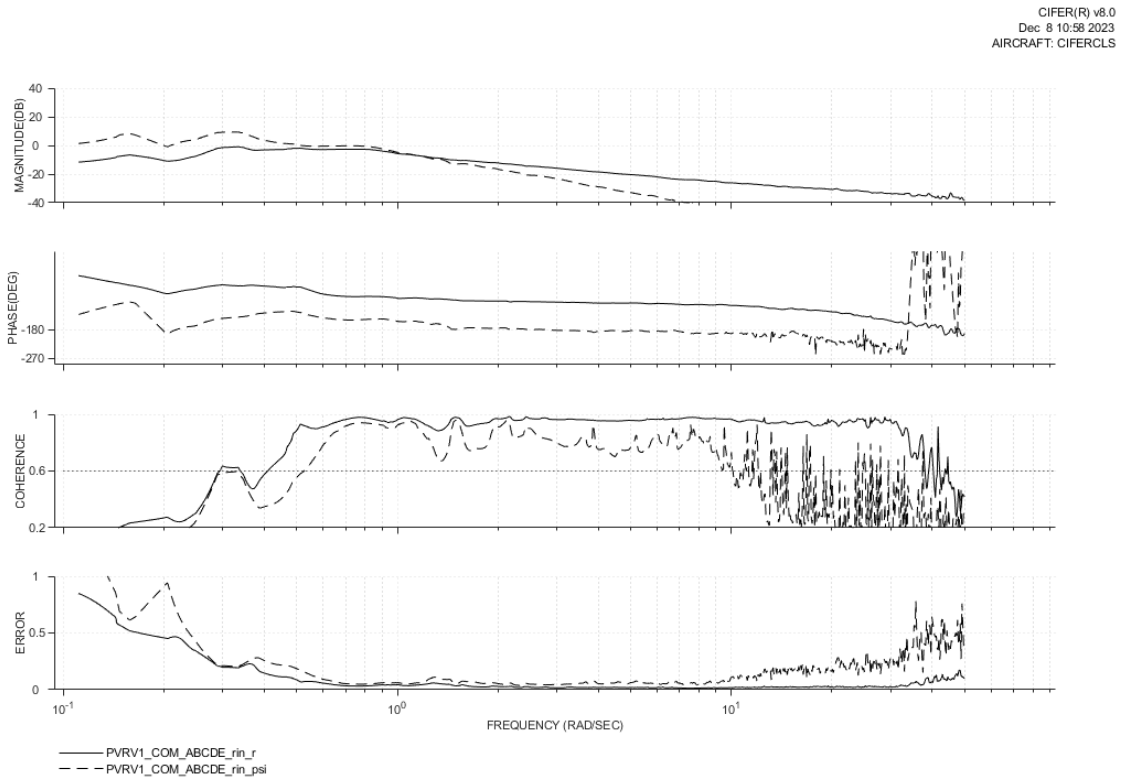

Figure 129. Frequency response bode plot for yaw rate and yaw angle response

The bode plot for collective input to z-acceleration $\left(\frac{az}{\delta_{col}}\right)$ is shown in Figure 130. The response shows good coherence from 1.5 to 13 rad/s.

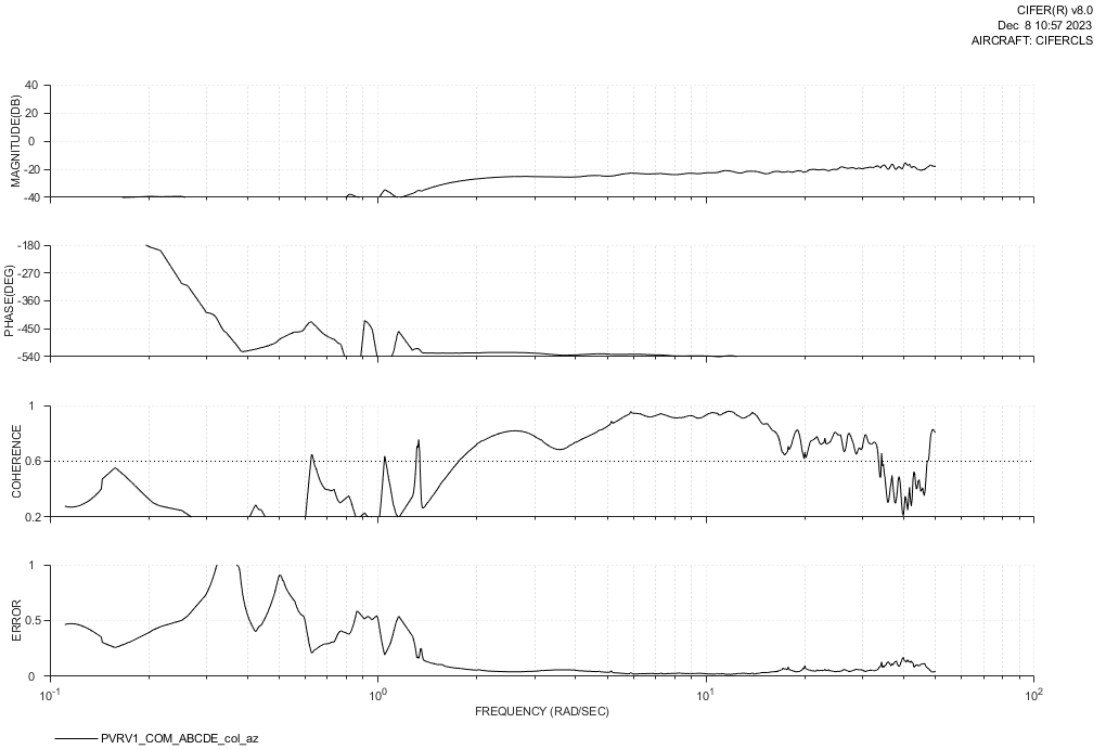

Figure 130. Frequency response bode plot for collective input to z-acceleration

4.7.3 Transfer function model identification

To obtain the initial parameters for stability and control derivatives identification, lower order transfer function models of vehicle dynamics are to be identified from the on-axis responses. This was performed using the NAVFIT module of CIFER. The low-order dynamic models are in the form as shown below.

$$\frac{p}{\delta_{pmix}} = \frac{L_{roll}(s + Y_v)e^{-\tau_{pmix}s}}{s[\zeta, \omega_n]} \quad 78$$

$$\frac{q}{\delta_{qmix}} = \frac{M_{pitch}(s + X_u)e^{-\tau_{qmix}s}}{s[\zeta, \omega_n]} \quad 79$$

$$\frac{r}{\delta_{rmix}} = \frac{N_{yaw}(s)e^{-\tau_{rmix}s}}{s[\zeta, \omega_n]} \quad 80$$

$$\frac{a_z}{\delta_{col}} = Z_{col} e^{-\tau_{col} s} \qquad 81$$

The identification was performed in the frequency range of 0.5-22 rad/s for heave and yaw axes and 1.5-50 rad/s for the pitch and roll axis. The cost function (J) for each axis was calculated in CIFER. The initial conditions for the identification were given for both the numerator and denominator coefficients. The transfer function parameters were used as initial conditions for state-space identification using the DERIVID module in CIFER. A basic input-to-output system of the PAVER vehicle is shown below in Figure 131.

Figure 131. PAVER input-to-output representation

The transfer function model identification was performed using the NAVFIT module. This module uses the responses generated in FRESPID for the input-output relations to get a transfer function fit. The transfer function model for pitch and roll was of second order with ones as initial guesses for the coefficients. The obtained transfer function form for pitch and roll rate response fit is given by equations below. The model fit can be seen from the body plot in Figure 132, where the coherence is good for most of the frequency range.

$$\frac{p}{\delta_{pmix}} = \frac{54.1226s+105.516}{s^2+28.888s-14.8707} e^{-0.0647s} \text{ (or) } \frac{p}{\delta_{pmix}} = \frac{54.1226(1.9496)}{(-0.50591)(29.394)} e^{-0.0647s} \qquad 82$$

$$\frac{q}{\delta_{qmix}} = \frac{52.2954s+107.807}{s^2+26.7189s-12.8219} e^{-0.0173s} \text{ (or) } \frac{q}{\delta_{qmix}} = \frac{52.2954(2.0615)}{(-0.47156)(27.19)} e^{-0.0173s} \qquad 83$$

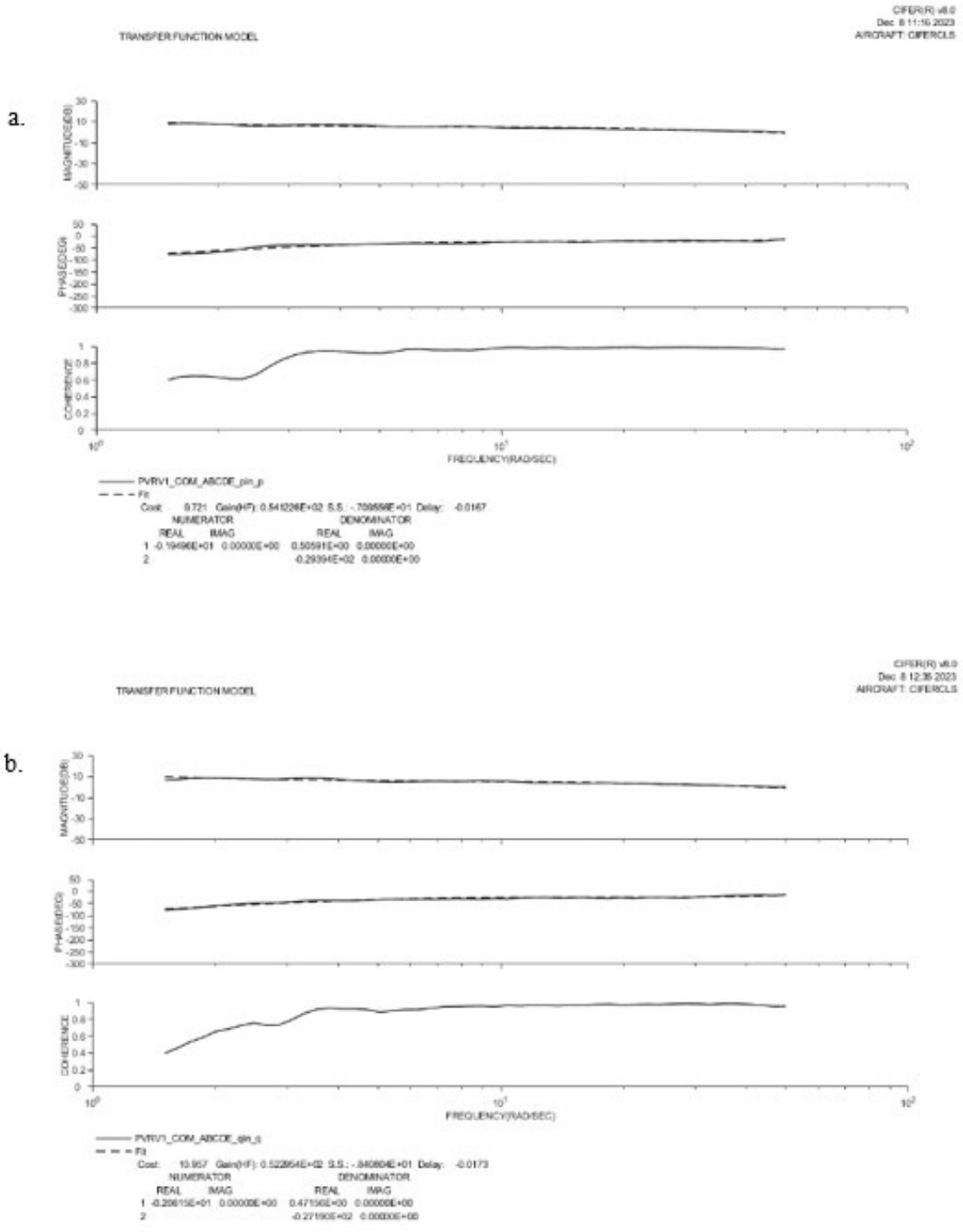

Figure 132. Transfer function model fit (a. roll b. pitch)

The cost function for $\left(\frac{p}{\delta_{pmix}}\right)$ and $\left(\frac{q}{\delta_{qmix}}\right)$ are 9.721 and 10.957 respectively, which, according to the guideline, is lower than 50 ($J \leq 50$). Thus, the model obtained is indistinguishable from the flight data. Both equations and cost functions are almost close, so we can say that these two responses are the same, since the PAVER Quad vehicle is symmetric about the x and y axes. They differ slightly because the frequency sweep was performed manually, and each sweep is different than the other. That could introduce some differences in the excitation.

Similarly, the obtained transfer function for the yaw rate input to yaw rate response $\left(\frac{r}{\delta_{rmix}}\right)$ and the collective input to z-acceleration $\left(\frac{az}{\delta_{col}}\right)$ are obtained as,

$$\frac{r}{\delta_{rmix}} = \frac{0.49599}{s+0.16908} e^{-0.0275s} \text{ (or) } \frac{r}{\delta_{rmix}} = \frac{0.49599}{(0.16908)} e^{-0.0275s} \quad 84$$

$$\frac{az}{\delta_{col}} = \frac{-12850.2}{s+212849} e^{-0.0116s} \text{ (or) } \frac{az}{\delta_{col}} = \frac{-12850.2}{(212850)} e^{-0.0116s} \quad 85$$

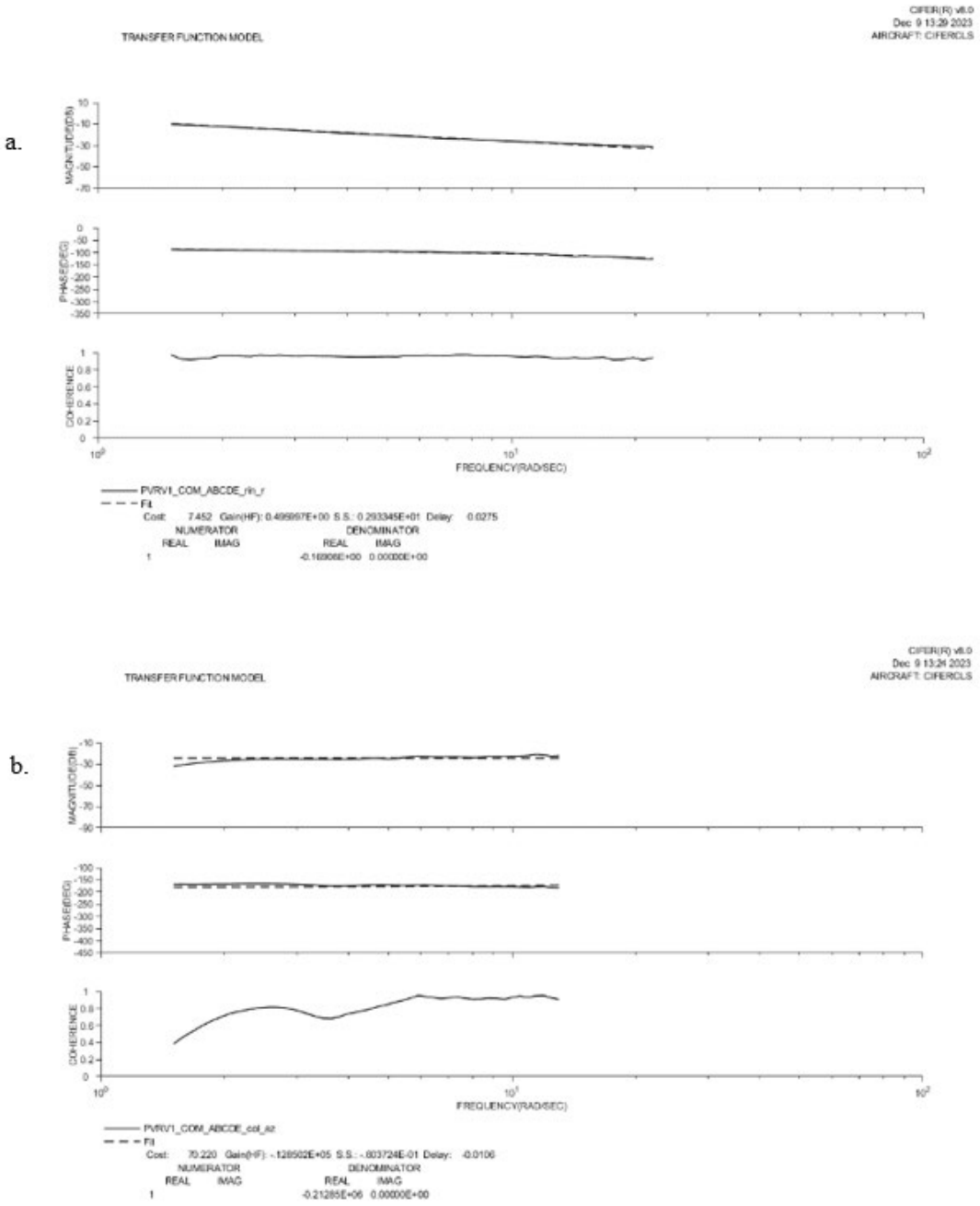

Figure 133. Transfer function model fit for heave (collective) (a) and yaw (b)

The cost function for $\left(\frac{p}{\delta_{pmix}}\right)$ and $\left(\frac{q}{\delta_{qmix}}\right)$ are 7.453 and 70.2 respectively, which, according to the guideline, is lower than 50 ($J \leq 50$) for yaw response. Thus, the model obtained is indistinguishable from the flight data. However, for heave, the cost function is less than 100 but more than 50; therefore, the model obtained is satisfactory. The values from these transfer functions will be used for the state-space model parameters identification using DEIVID.

4.7.4 State-space model identification

The building blocks to get a bare airframe state-space model identified start with defining the equations of motion of the vehicle. A 6DOF model is defined for the PAVER Quad vehicle at hover. The vehicle is modeled using the rigid body equations of motion. The 6DOF equations of motion implemented in CIFER are given by:

$$\dot{u} = X_u u + X_v v + X_w w + a_x + X_p - \left(X_q - W_0\right)q + (X_r + V_0)r - \left(gcos(\theta_0)\right)\theta \quad 86$$

$$\dot{v} = Y_u u + Y_v v + Y_w w + a_y - (Y_r - U_0)r + (Y_p + W_0)p + \left(gcos(\theta_0)\right)\phi \quad 87$$

$$\dot{w} = Z_w w + Z_u u + Z_v v + a_z + \left(Z_p - V_0\right)p - \left(Z_q + U_0\right)q + Z_r r - \left(gsin(\theta_0)\right)\theta \quad 88$$

$$\dot{p} = L_u u + L_v v + L_w w + L_p p + L_q q + L_r r \quad 89$$

$$\dot{q} = M_u u + M_v v + M_w w + M_p p + M_q q + M_r r \quad 90$$

$$\dot{r} = N_u u + N_v v + N_w w + N_p p + N_q q + N_r r \quad 91$$

$$\dot{\phi} = p + rtan\theta \quad 92$$

$$\dot{\theta} = q \quad 93$$

$$\dot{\psi} = rsec\theta \quad 94$$

For the hover condition, the following values are determined to be:

$$U_0 = V_0 = W_0 = \theta_0 = 0 \quad 95$$

The units for these are m/s^2, m/s, deg/s, deg, and PWM for actuator inputs.

4.7.5 Gain optimization

During Phases 1 and 2, the PID gains were tuned manually with the help of simulation and data. However, this process was long and would require multiple flight tests to properly tune the gains. First, the nonlinear dynamic model was linearized at hover for 1800 RPM to get a state-space model, as seen in Figure 134. Keep in mind, this is not a bare airframe state-space model but rather a physics-based linearized state-space model.

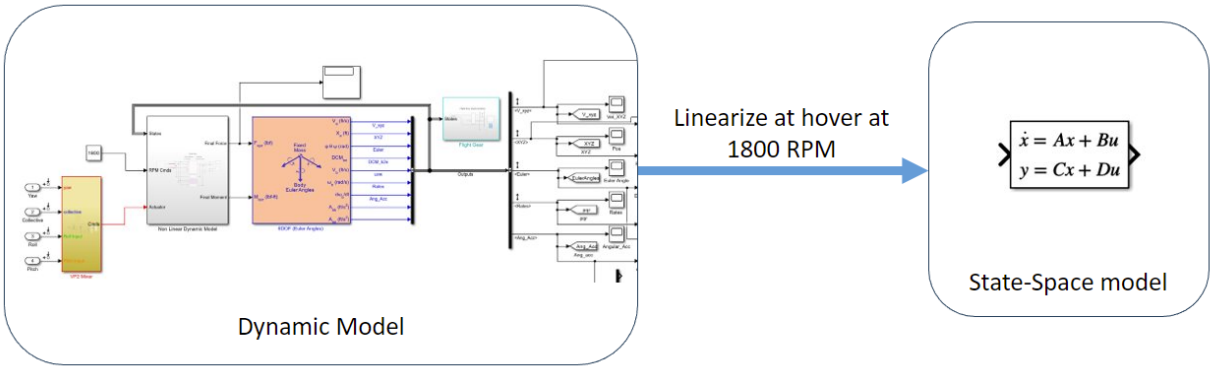

Figure 134. Model linearization at hover

Next, this linear model was used as the aircraft's bare-airframe model, and a controller was designed around it. A control law or SCAS is designed like the cascaded feed forwarded control law but with manual PID gains. This allows the software to set these gains as design parameters and optimizes these values. A PI controller was used for the rate loop, while a P controller is used for the attitude loop, as seen in Figure 135. A longitudinal SCAS was not designed since the gains obtained for the lateral SCAS will be the same for longitudinal SCAS because of the symmetry of a quadcopter. A broken loop switch was implemented between the SCAS and model to evaluate broken loop (open loop) characteristics. A transport delay was used for an equivalent time delay.

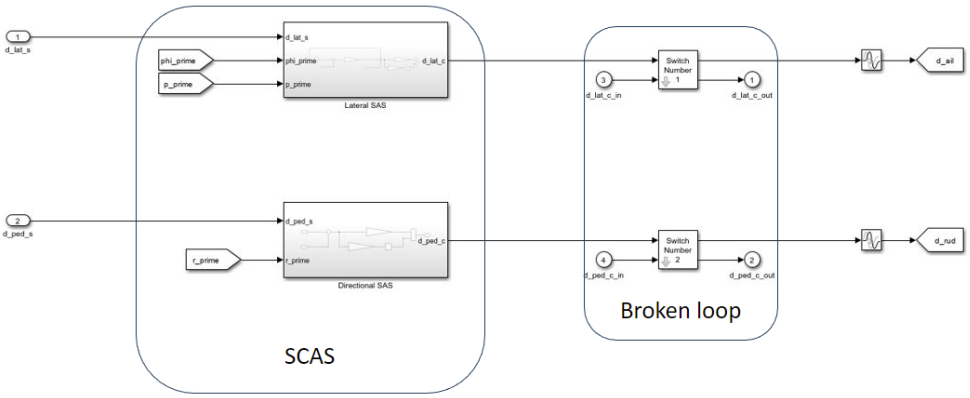

Figure 135. SCAS and broken loop switches

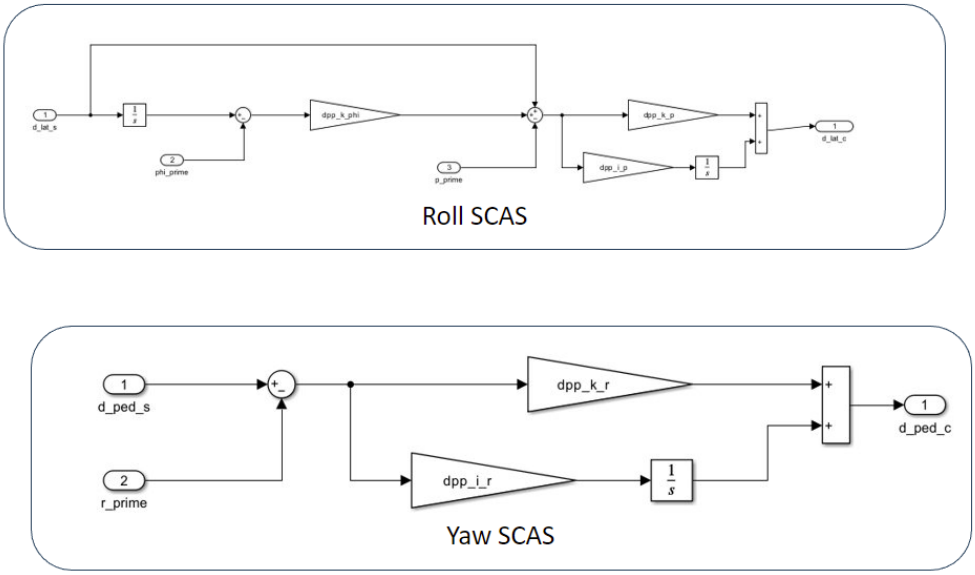

Figure 136. Roll and yaw SCAS

A disturbance input was also implemented to analyze disturbance rejection characteristics, as seen in Figure 137. The inputs to the system are aileron and rudder. In this case, this means roll rate input and yaw rate input (Figure 136).

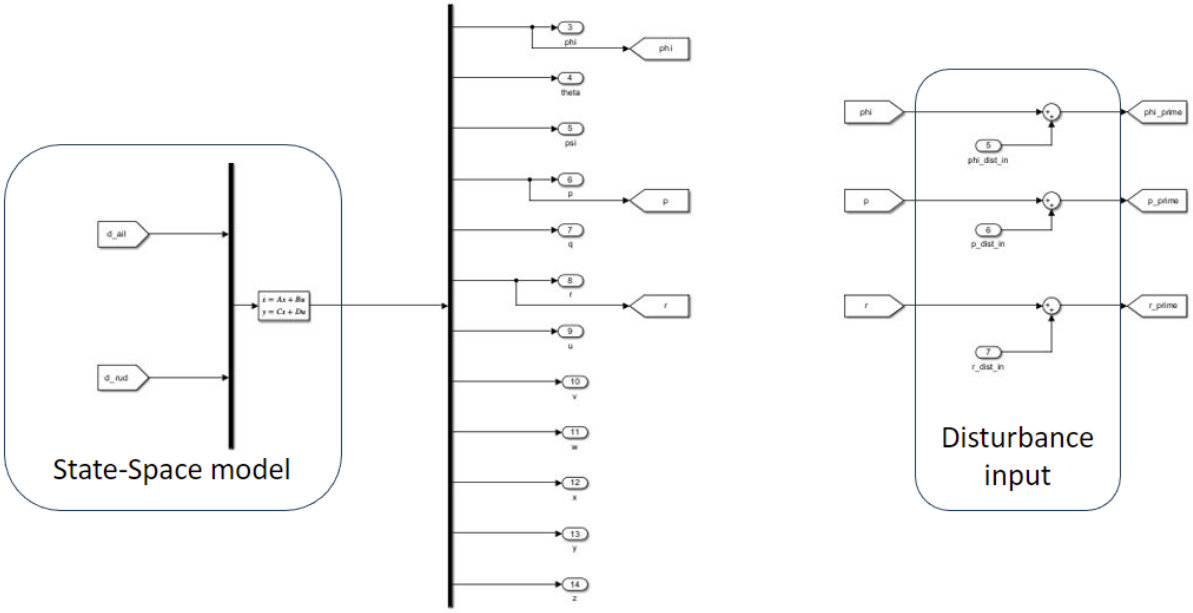

Figure 137. State-space model with disturbance input

Once the problem has been set, the simulation was run with initial gains for several iterations. The initial gains used were the gains currently used in the simulation. After successful run of the optimization, the optimized gains were presented in a design parameters table, as seen in Table 11.

Table 11: Optimized PID gains

K_p	0.6
K_r	1.7
K_ϕ	3.2
K_{p_i}	0.01
K_{r_i}	0.01

4.7.6 Lessons learned

A LOES model for the vehicle was identified as a simpler model. While this model includes the dynamics of the vehicle for a wide range of frequencies, it does not account for higher order

dynamics such as servos, rotor flapping, motor vibrations, and motor lag. This would increase the complexity and fidelity of the model but would include more information about the vehicle dynamics. Using joint input-output (JIO) module within CIEFR instead of FRESPID could be useful for higher order identification.

For the purposes of flight testing, only manual sweeps were conducted due to testing area restrictions. This reduced the maximum value of frequency for the identification, as the pilot could only move his stick as humanly possible. Using automated sweeps could provide a wider range of frequencies and a better signal-to-noise ratio.

4.8 Task H: Develop a trajectory following force and moment prediction process

4.8.1 Nonlinear simulation of control requirements

A nonlinear simulation model of a generic quadrotor vehicle with 6° of freedom was developed. This simulation generates flight trajectories that represent typical MTEs in order to evaluate the resulting control requirements. These flight trajectories are created by defining a reference flight trajectory and using a NLDI controller to make the vehicle follow the reference trajectory. The NLDI controller is implemented using accurate data about the vehicle's parameters and states (e.g., noise-free sensor data), so it can be considered an ideal control law that represents the maneuvering capabilities of the vehicle under idealized conditions. It is worth noting that while a version of the simulation has been developed that includes rotor dynamics (see PAVER section), the simulation results in this section assume that the commanded forces and moments generated by the NLDI controller are implemented directly by the control system. This was done to focus on control requirements that are independent of rotor type (e.g., fixed-pitch, collective pitch, or collective and cyclic pitch) or any specific control allocation.

4.8.2 Vehicle simulation model

The vehicle simulation was developed in the MATLAB/Simulink environment. The simulation model consists of various subsystems, including a block for multirotor vehicle dynamics and a block for guidance and control, which incorporates the NLDI controller. The simulation generates output data for the inertial position (north-east-down), body-referenced inertial velocity components, body-referenced angular rates, and attitude (roll, pitch, and heading) of the vehicle. Additionally, the simulation produces output data for other relevant variables, including the required control forces and moments. Table 12 shows the mass and inertia properties of the simulated multirotor vehicle.

Table 12. Vehicle mass and inertia parameters.

Parameter	Symbol	Value	Units
Weight	W	75	lb
Mass	m	2.329	slug
Moment of Inertia about the X-axis	I_{xx}	10.34	slug-ft^2
Moment of Inertia about the Y-axis	I_{yy}	10.34	slug-ft^2
Moment of Inertia about the Z-axis	I_{zz}	12.56	slug-ft^2
Product of Inertia – XY	I_{xy}	0	slug-ft^2
Product of Inertia – XZ	I_{xz}	0	slug-ft^2
Product of Inertia – YZ	I_{yx}	0	slug-ft^2

The dynamics model assumes that the vehicle behaves as a rigid body, resulting in a set of 12 nonlinear, time-invariant equations of motion that can be expressed in state-space form:

$$\dot{\underline{X}}(t) = \underline{F}\left(\underline{X}(t), \underline{U}(t)\right) \tag{96}$$

The state vector is defined as:

$$\underline{X} = (u, v, w, p, q, r, \phi, \theta, \Psi, x, y, h)^T \tag{97}$$

Where (u, v, w) denote the body-referenced translational velocity components, (p, q, r) represent the body-referenced angular velocity components, (ϕ, θ, Ψ) are the roll, pitch, and yaw (heading) angles, and (x, y, h) denote the inertial position in distance north, distance east, and altitude respectively. The control inputs depend on the type of rotor system used, such as fixed pitch, collective pitch, or collective and cyclic pitch. For example, in the case of a quadcopter with fixed pitch, the controls would correspond to the thrust commanded to each of the four rotor units.

The individual equations of motion are numerically integrated to determine the state variables at every simulation time step. The translational equations of motion take the form:

$$\dot{u} = rv - qw - gsin\theta + \frac{1}{m}\left(T_x^B + F_{x,areo}^B\right) \quad 98$$

$$\dot{v} = -ru + pw + gsin\phi cos\theta + \frac{1}{m}\left(T_y^B + F_{y,areo}^B\right) \quad 99$$

$$\dot{w} = qu - pv + gcos\phi cos\theta + \frac{1}{m}\left(T_z^B + F_{z,areo}^B\right) \quad 100$$

$\left(T_x^B, T_y^B, T_z^B\right)$ represent the components of total thrust generated by the control system, expressed in the vehicle body frame. Similarly, $\left(F_{x,aero}^B, F_{y,aero}^B, F_{z,aero}^B\right)$ corresponds to the components of the aerodynamic force in the body frame.

In this work, the aerodynamic force was modeled as a drag force acting at the CG in the direction of the relative wind at the CG. The vehicle drag force is given by:

$$D = \frac{1}{2}\rho V_a^2 C_d S \quad 101$$

where ρ is the sea-level air density, $C_D S$ represents an estimated flat-plate area for this notional multirotor vehicle, and V_a is the total airspeed, given as the magnitude of the difference between the inertial velocity vector $\underline{V}_{cm}^B$ and the wind velocity vector $\underline{V}_W^B$. The wind velocity vector corresponds to a user-specified steady-state wind vector, which was set to zero in these simulations. The drag force *D*, which acts in the direction of the relative wind, is then expressed in the body frame as follows:

$$F_{x,areo}^B = -D\cos\alpha\sin\beta \quad 102$$

$$F_{y,areo}^B = -Dsin\beta \quad 103$$

$$F_{z,areo}^B = -D\sin\alpha\cos\beta \quad 104$$

Where α and β are the angle of attack and sideslip angles.

The rotational equations of motion, which are obtained by summing external moments about the CG and equating them to the rate of change of angular momentum, take the form:

$$\dot{p} = \frac{1}{I_{xx}} M_x^B + \frac{1}{I_{xx}} (I_{yy} - I_{zz}) qr \quad (105)$$

$$\dot{q} = \frac{1}{I_{yy}} M_y^B - \frac{1}{I_{yy}} (I_{xx} - I_{zz}) pr \quad (106)$$

$$\dot{r} = \frac{1}{I_{zz}} M_z^B + \frac{1}{I_{zz}} (I_{xx} - I_{yy}) pq \quad (107)$$

These equations are simplified due to symmetry, which renders the products of inertia zero. (M_x^B, M_y^B, M_z^B) represent the control moments, resolved into components about each of the body axes. Given that the aerodynamics model only includes a drag force at the CG, and there are no pure aerodynamic moments, no aerodynamic moments are acting about the CG.

The attitude kinematic equations, which are derived by relating the Euler angle rates to the body-referenced angular rates, are given by:

$$\dot{\phi} = p + q \sin\phi \tan\theta + r \cos\phi \tan\theta \quad (108)$$

$$\dot{\theta} = q \cos\phi - r \sin\phi \quad (109)$$

$$\dot{\psi} = q \sin\phi \sec\theta + r \cos\phi \sec\theta \quad (110)$$

Finally, the inertial position kinematic equations, which are derived by transforming the body-referenced inertial velocity components into the inertial north-east-down (NED) frame and integrating them, are given by:

$$\begin{bmatrix} \dot{x} \\ \dot{y} \\ \dot{z} \end{bmatrix} = \begin{bmatrix} V_N \\ V_E \\ V_D \end{bmatrix} = R_B^E \begin{bmatrix} u \\ v \\ w \end{bmatrix} \quad (111)$$

where $R_B^E = (R_E^B)^T$, the transpose of the DCM that relates the inertial axes to the body-fixed axes. The DCM is derived in terms of the roll, pitch, and yaw Euler angles as follows:

$$R_E^B = \begin{bmatrix} 1 & 0 & 0 \\ 0 & \cos\phi & \sin\phi \\ 0 & -\sin\phi & \cos\phi \end{bmatrix} \begin{bmatrix} \cos\theta & 0 & -\sin\theta \\ 0 & 1 & 0 \\ \sin\theta & 0 & \cos\theta \end{bmatrix} \begin{bmatrix} \cos\psi & \sin\psi & 0 \\ -\sin\psi & \cos\psi & 0 \\ 0 & 0 & 1 \end{bmatrix} \quad 112$$

The position kinematic equations are integrated to compute the inertial (NED) position of the vehicle at each simulation time step. Note that the z-axis is in the inertial down direction Z_D, but for the purpose of clarity in presentation, the simulation outputs the altitude $h = -Z_D$.

4.8.3 Guidance and control system

The vehicle simulation is designed to simulate user-defined or preloaded flight trajectories. The reference trajectory is defined in terms of time histories of the inertial (NED) velocity $(V_{N,ref}, V_{E,ref}, V_{D,ref})$. The reference velocity can be defined at any sampling rate, and the vehicle is assumed to travel at a constant heading in the downrange direction. The reference data is generated at a simulation sample rate of 1000 Hz for the control system to track and achieve the desired reference inertial position history.

A control system based on NLDI, also known as feedback linearization, is implemented to enable the vehicle to track the reference trajectories. NLDI is based on the principle that the control input can be used to cancel the inherent nonlinear dynamics of the system and track desired reference trajectories while imposing desirable linear dynamics. The NLDI control laws used in the vehicle simulation are implemented in an outer and inner loop structure. The outer loop represents slower, translational dynamics required to track the reference trajectory, while the inner loop represents faster dynamics associated with stabilizing the attitude of the vehicle. Previous work by the ERAU team has demonstrated the effectiveness of this implementation in simulating multirotor systems.

The outer loop first generates inertial (NED) velocity commands using a PID controller based on the NED position error, which is the difference between the reference position and the vehicle position as would be given by the onboard inertial navigation system (INS):

$$v_{x,com} = K_{P,x}(x_{ref} - x) + K_{I,x}\int_0^t (x_{ref} - x)d\tau + K_{D,x}\frac{d}{dt}(x_{ref} - x) \quad 113$$

$$v_{y,com} = K_{P,y}(y_{ref} - y) + K_{I,y}\int_0^t (y_{ref} - y)d\tau + K_{D,y}\frac{d}{dt}(y_{ref} - y) \quad 114$$

$$v_{z,com} = K_{P,z}\left(z_{ref} - z\right) + K_{I,z}\int_0^t \left(z_{ref} - z\right)d\tau + K_{D,z}\frac{d}{dt}\left(z_{ref} - z\right) \quad 115$$

Inertial acceleration commands are then computed based on the difference between the commanded inertial velocity and the vehicle inertial velocity:

$$a_{x,com} = K_{P,vx}\left(v_{x,com} - v_x\right) + K_{I,vx}\int_0^t \left(v_{x,com} - v_x\right)d\tau + K_{D,vx}\frac{d}{dt}\left(v_{x,com} - v_x\right) \quad 116$$

$$a_{y,com} = K_{P,vy}\left(v_{y,com} - v_y\right) + K_{I,vy}\int_0^t \left(v_{y,com} - v_y\right)d\tau + K_{D,vy}\frac{d}{dt}\left(v_{y,com} - v_y\right) \quad 117$$

$$a_{z,com} = K_{P,vz}\left(v_{z,com} - v_z\right) + K_{I,vz}\int_0^t \left(v_{z,com} - v_z\right)d\tau + K_{D,vz}\frac{d}{dt}\left(v_{z,com} - v_z\right) \quad 118$$

Roll, pitch, and vertical force commands are then generated as follows:

$$\phi_{com} = sin^{-1}\left(\frac{m\left(a_{x,com}\,sin\,\psi - a_{y,com}\,cos\,\psi\right)}{F_{z,com}}\right) \quad 119$$

$$\theta_{com} = sin^{-1}\left(\frac{m\left(a_{x,com}\,cos\,\psi + a_{y,com}\,sin\,\psi\right)}{F_{z,com}\,cos\,\phi}\right) \quad 120$$

$$F_{z,com} = \frac{m\left(a_{z,com} - g\right)}{cos\,\phi\,cos\,\theta} \quad 121$$

The commanded roll and pitch angles serve as inputs to the inner loop, which are then used to generate commanded angular rates. The commanded Euler angle rates are computed using PID controllers operating on the Euler angle errors:

$$\dot{\phi}_{com} = K_{P,\phi}(\phi_{com} - \phi) + K_{I,\phi}\int_0^t (\phi_{com} - \phi)d\tau + K_{D,\phi}\frac{d}{dt}(\phi_{com} - \phi) \quad 122$$

$$\dot{\theta}_{com} = K_{P,\theta}(\theta_{com} - \theta) + K_{I,\theta}\int_0^t (\theta_{com} - \theta)d\tau + K_{D,\theta}\frac{d}{dt}(\theta_{com} - \theta) \quad 123$$

$$\dot{\psi}_{com} = K_{P,\psi}(\psi_{com} - \psi) + K_{I,\psi}\int_0^t (\psi_{com} - \psi)d\tau + K_{D,\psi}\frac{d}{dt}(\psi_{com} - \psi) \quad 124$$

The commanded Euler rates are then converted to commanded body-referenced angular rates:

$$p_{com} = -\dot{\psi}_{com}\, sin\,\theta + \dot{\phi}_{com} \quad 125$$

$$q_{com} = \dot{\psi}_{com}\, sin\,\phi\, cos\,\theta + \dot{\theta}_{com}\, cos\,\phi \quad 126$$

$$r_{com} = \dot{\psi}_{com}\, cos\,\phi\, cos\,\theta - \dot{\theta}_{com}\, sin\,\phi \quad 127$$

Commanded moments about the body axes are then generated from the commanded angular rates using the moment equation

$$\underline{M}^B_{com} = \underline{\omega}^B \times I^B_{cm}\underline{\omega}^B + \underline{\dot{\omega}}_{com} \quad 128$$

where $\underline{\dot{\omega}}_{com} = [\dot{p}_{com} \quad \dot{q}_{com} \quad \dot{r}_{com}]^T$ are commanded body-referenced angular accelerations:

$$\dot{p}_{com} = K_{P,p}(p_{com} - p) + K_{I,p}\int_0^t (p_{com} - p)d\tau + \frac{d}{dt}(p_{com}) \quad 129$$

$$\dot{q}_{com} = K_{P,q}(q_{com} - q) + K_{I,q}\int_0^t (q_{com} - q)d\tau + \frac{d}{dt}(q_{com}) \quad 130$$

$$\dot{r}_{com} = K_{P,r}(r_{com} - r) + K_{I,r}\int_0^t (r_{com} - r)d\tau + \frac{d}{dt}(r_{com}) \quad 131$$

The objective of this simulation study was to determine the required control forces and moments, independent of rotor configuration or control allocation. In practice, these commanded forces and moments would be translated into appropriate control commands for the rotors. The NLDI control law was tuned by adjusting the various PID controller gains to represent an ideal control system with a fast response for tracking the reference trajectories, which approximates the best-case performance of a physical flight control system.

4.9 Task I: Handling qualities evaluation using handling qualities task elements

The flying taxi is an innovative concept in aviation. Hundreds of companies are developing novel versions of eVTOL vehicles with DEP units in various forms, like vectored thrust, multirotor, lift and cruise, etc. To certify these aircraft for private and commercial use, a set of certification standards needs to be created. These vehicles look and work very differently from conventional aircraft and helicopters. Most will be operated via FBW using various classical and modern nondeterministic flight control laws. The certification of these vehicles will be challenging. To address this challenge, this study utilized eVTOL modeling, simulation, and control law analysis to perform virtual experiments that will inform the handling qualities certification process. The methodologies developed will incorporate a mission-oriented approach to define handling qualities MTEs that will serve as a means of compliance with Part 23 certification requirements.

To prototype this methodology for evaluating handling qualities, the simulation model of the PAVER vehicle is used. Due to the weight of the PAVER testbed being greater than 55 pounds, the testbed could not be flown outside the drone cage. Therefore, it was decided to carry out these HQTE experiments in a simulated environment.

For this purpose, the simulator at the EFRC was used with the 6DOF math model of PAVER implemented with Microsoft Flight Simulator as out-the-window view. HQTE courses such as pirouette, hover and land, and sidestep can be created with custom scenery inside the Microsoft Simulator environment. The simulations were run with the pilot-in-the-loop for the pirouette maneuver using the VP2 control strategy, as shown in Figure 138.

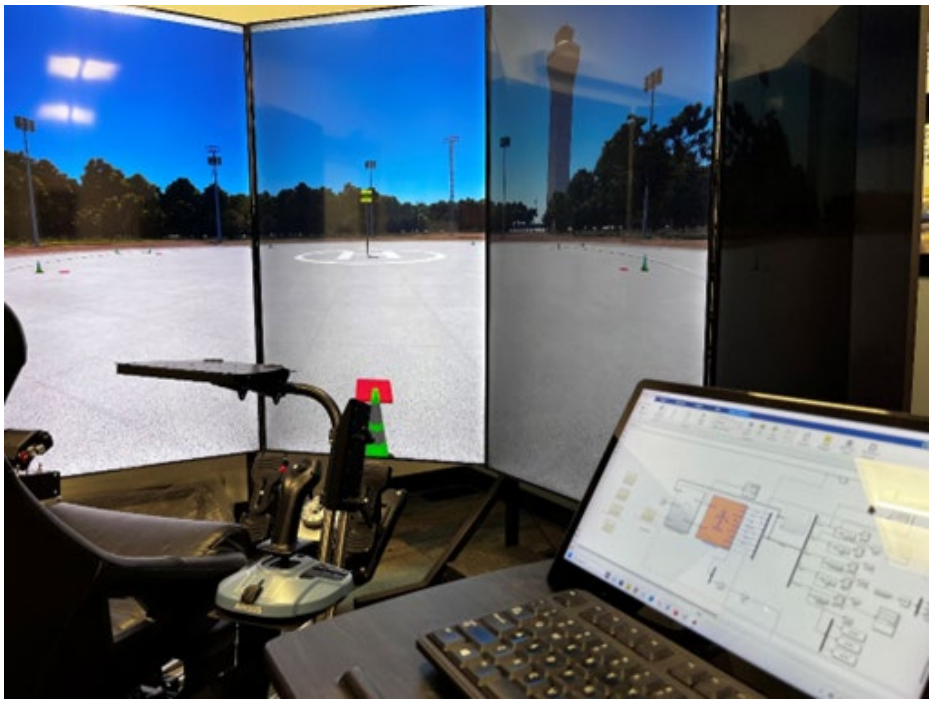

Figure 138. Flight Simulator running PAVER dynamic model

One benefit of using the simulator and flight dynamic model to assess handling qualities is that the performance of the maneuver can be evaluated utilizing data from the execution of the HQTE. As an example, the performance of the pirouette maneuver can be seen in Figure 139. While only the VP2 strategy was evaluated here, the results show that this methodology could easily be applied to test different control strategies and performance under degraded modes of operation in a way that is low risk and at the same time yields quantitative data to aid in the evaluation.

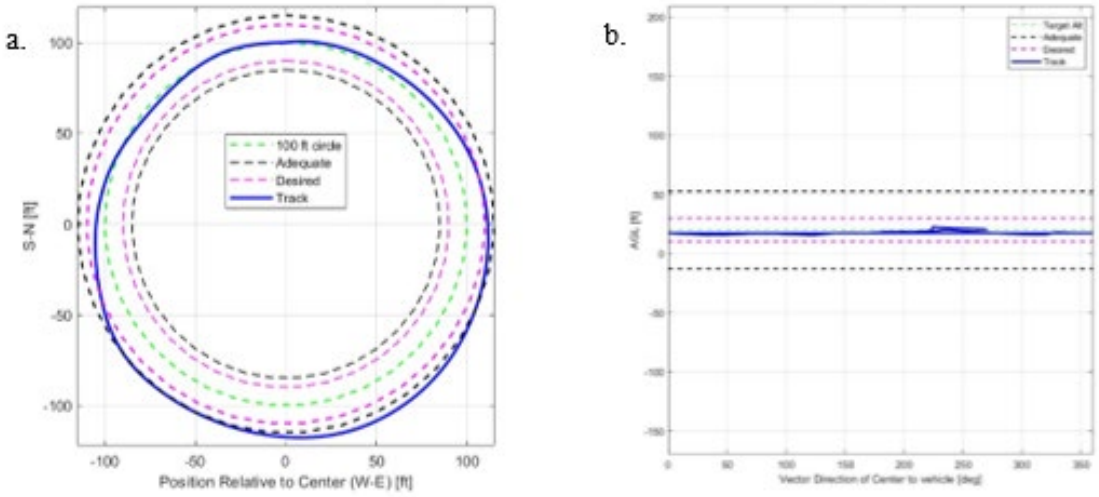

Figure 139. Pirouette HQTE (a) top-down tracking and (b) vertical tracking

5 Performance of mission statement tasks

In closing out Phase 2 of the Integrated Propulsion and Control for Rotorcraft Project, the EFRC has fulfilled the collaborative mission statement objectives crafted with the FAA during Phase 1. Efforts have primarily focused on the development of a hardware-validated flight dynamics simulation to assess different control strategies used to fly MTEs as well as create methodologies that may one day aid and inform specific certification testing at the vehicle level.

Throughout Phases 1 and 2, both rotor and full vehicle simulations for the quadcopter testbed were meticulously crafted. These simulations were pivotal in validating rotor models against real-world data obtained on a specialized RTS. Moreover, they played a critical role in refining various control laws necessary for both nominal and off-nominal flight scenarios, thus aligning with the mission's core directive.

A force and moment envelope methodology not only facilitated the computation of force and moment envelopes for different vehicle configurations, but it also allowed the team to predict potential control challenges, such as situations leading to loss of control. By assuming an "ideal" control law, maximum control power attainable by the vehicle is assessed, enabling proactive evaluation of its capabilities against required tasks. In addition to this, a methodology was developed to display these envelopes in real time to pilots in a way designed to give them an intuitive understanding of the aircraft’s location with respect to its envelope boundaries. This could help pilots avoid accidents resulting from loss of control.

Furthermore, the team’s dedication to academic rigor provoked investigation into control evaluation nuances, including phase and gain margins. Through frequency-based system identification techniques, we obtained a comprehensive understanding of the vehicle's state-space model, which is crucial for optimizing control law gains to meet specified handling quality standards.

In the pursuit of evaluating quadcopter DEP methods of control, various strategies were developed and compared, including constant pitch, collective-only, and collective with cyclic control modes. Extensive analyses encompassing time response assessments, yaw control evaluations, and rotor out scenarios culminated in the identification of the most effective control strategy, particularly in both nominal and off-normal conditions.

Despite regulatory constraints limiting extended forward flight due to weight restrictions and authorization hurdles, the team showcased remarkable adaptability and innovation. Through inventive maneuvers within the confines of the drone cage, such as a HQTE similar to a Pirouette and successfully managing a single rotor failure during hover, the efficacy of cyclic-capable rotor systems on multi-copter platforms was demonstrated.

In essence, our endeavors across Phases 1 and 2 have not only upheld the spirit of the mission statement but also underscored our commitment to advancing rotorcraft technology through rigorous simulation, meticulous control evaluation, and innovative problem-solving.

6 Lessons learned

6.1 Force and moment envelope prediction

The first methodology, which involved the automatic computation of required forces and moments through flight simulation and comparison with the attainable force and moment envelopes, was intended to be a low-cost, low-risk method for predicting handling qualities cliffs without the need for flight testing or any pilot input. While this methodology can predict handling qualities cliffs that could result from running out of control power and/or losing a rotor, it is unable to predict either handling qualities cliffs resulting from dynamic aircraft and/or control law instability or pilot-in-the-loop effects. This is due to the force and moment envelopes at each given state being static in nature.

These limitations led to the development of a second methodology that displays the force and moment envelopes to the pilots as they are flying the vehicle as well as the aircraft’s location with respect to the boundaries of these envelopes. This method combines real-time flight

simulation or flight testing with pilot input. Therefore, it could help uncover a wider range of dynamic handling qualities cliffs as well as alert test pilots when the airplane is about to run out of control power, much like the first methodology. When used with ground-based simulation, it could serve as a means for test pilots to become familiar with the limits of a new aircraft's flight envelope in a safe environment and therefore improve flight test safety once the pilot sets foot in a real test aircraft.

To account for the full range of handling qualities cliffs an aircraft could be expected to encounter, either of the two methods would need to be used in combination with highly realistic aircraft flight dynamics models. During the investigation of the AW609 crash, the engineers were unable to recreate the Dutch roll oscillations that led to the in-flight breakup on the flight simulator. If the flight simulator had been able to recreate these, the accident could have been avoided.

To maximize effectiveness of the first methodology involving required vs. attainable forces and moments prediction, the following changes are recommended:

- Require forces and moments prediction code that can account for different control strategies instead of just the differential collective pitch/RPM control strategy.
- Include dynamic envelopes that consider any delays between when the pilot commands a force or moment from the effectors and when the maximum steady-state forces and moments are achieved.
- Improve computational efficiency to more efficiently analyze configurations with large numbers of effectors and allow for real-time computation of the envelopes. This could be done by finding the minimum number of points required to define the convex hull of these envelopes and feeding the control input combinations associated with these points into the flight simulation model to generate these force and moment envelopes in real time.
- Develop realistic pilot models that can account for how a pilot might respond to a wide range of events, which could include in-flight upsets, wind gusts and turbulence, effector failures, flight control failures, etc.
- Develop realistic flight simulation models that can recreate all the possible situations that could lead to handling qualities cliffs.
- Since the force and moment envelopes are independent from one another, develop an algorithm that will find out which envelope demands the most from the vehicle's

effectors (in the case of PAVER this would be force). Once this envelope is found, a control allocation algorithm would then be used to allocate the vehicle's controls to generate this force, and the moment envelope would be generated using the remaining available control power.

To maximize effectiveness of the second methodology involving the pilot displays, the following changes are recommended:

- The equations used to calculate the lift, drag, thrust, and pitching moment envelope boundaries for a fixed-wing airplane are very simple and computationally efficient. Since eVTOLs often feature multiple rotors and complex control strategies, equations that can efficiently predict the force and moment envelope boundaries of these configurations are necessary.
- Provide realistic flight simulation models that can recreate all the possible situations that could lead to handling qualities cliffs.
- Before using the pilot displays for flight testing, predict all the possible scenarios that could lead to handling qualities cliffs resulting from dynamic situations in addition to those resulting from running out of control power. This is necessary so that the pilot displays can alert pilots when they are approaching such a situation and thereby help avoid loss of control.
- In a high-speed situation, the pilot might have sufficient control authority to generate enough lift to overstress the airframe. Find a way to display structural limits as well as control law limitations to the pilot.

For piloted aircraft, predictions of handling qualities cliffs with actual test pilots in the loop will almost always be more accurate than those carried out by an automated methodology involving a pilot model. Models that can accurately predict how a pilot might respond to a wide range of events are difficult to create, since no two pilots are the same. However, it is predicted that eVTOLs will eventually become autonomous; in such cases, the pilot displays would not be of much use without a human pilot.

6.2 Nonlinear dynamic inversion control allocation method and electric vertical take-off and landing control allocation process

The research was started by understanding the classical approach of control mixing matrix for multirotors with fixed pitch propellers. This matrix is responsible for finding the right combination of RPM to maintain the desired forces and moments. For the PAVER case, the rotor

tests were analyzed, and this classical approach was extended to find the set of RPMs and collective inputs with an improved control mixing relation. Although this set of effector inputs revealed critical information for control, there was a need for a criterion to choose one combination among the set. There are several combinations of RPM and collective input available, so a decision mechanism is important to choose the “best” combination in some criteria. For this reason, cost functions were used to build a criterion to decide the one among the set.

Numerical simulations were conducted with different cost functions. First, a static cost function was implemented to minimize the total collective input usage throughout the test. Then the approach was extended by improving a weighted cost function, which can change the usage of RPM and collective input by a user-defined parameter. The cost functions can vary, and they do not have to be related to control minimization problems only. For that reason, power consumption of rotor tests was evaluated, and a cost function was formulated to express total power consumption of the vehicle by given RPM and collective inputs.

Besides the optimization-based control allocation technique, a frequency-based control allocation approach is added to the report as a different perspective. This concept is inspired by a study that used pitch actuators and RPM control for short-term responses and trim, respectively (Walter A. , McKay, Niemiec, & and Gandhi, 2022). The proposed technique can be modified for this research by deciding how much collective control should be given to the vehicle according to the pilot input, and remaining RPM effector inputs can be found by the control mixing algorithm. Analyzing the frequency content of the pilot inputs and deciding collective/RPM control accordingly can be a different and beneficial allocation topic for future research.

The control allocation problem between RPM and collective input is a simplified problem of PAVER. PAVER also has the advantage of changing the direction of swashplates of its rotors by the cyclic control. This makes it unique because it can compensate for a rotor failure during the flight. Classical allocation techniques of the multirotors with fixed pitch propeller or with fixed RPM cannot compensate for a rotor failure because there are not enough degrees of freedom left for the vehicle. To make the developed control allocation more robust for failures, cyclic rotor tests were evaluated to improve control allocation mixing, which includes cyclic input addition to collective and RPM inputs. A future research topic could involve fully extending the control allocation mixing with the cyclic input.

6.3 Flight tests with prototype vehicles

This phase has seen more flight tests with the updated control laws and new control strategies along with some system identification tests. The VP2 self-level control strategy performed well during flight testing, but it can be improved further by calibrating the flight controller on a flat surface for smoother operation in level flight, most importantly the zero-point calibration done before flight. Optimized PID gains and minimum hardware noise should also be considered while operating in this control strategy.

The translational flight control strategy showcased the unique capability of this vehicle. While this control strategy worked, the control laws designed need some tuning and improvement. This is because the PIDs that were tuned for VP2 and VP3 work well individually, but when combined to create translation flight, they have to be adjusted. Moreover, the increase in cyclic control authority resulted in larger moments and made it difficult for the flight controller to maintain level attitude. Looking into advanced control laws and control allocation methods would provide stable flight performance.

One of the big milestones achieved during this phase was the off-nominal operation of the vehicle. To simulate a failed rotor, one of the rotors was turned off during flight. Though the control law accounted for the failure, the issue of integral wind-up still existed. The wind-up would sometimes interfere with the controls, leading to gradual loss of control power. This could be avoided by implementing better anti wind-up techniques and more flight tests, including forward flight testing.

The data from the frequency sweep testing performed for system identification purposes was acceptable; however, the accelerations showed a lot of noise. This affected the system identification analysis, resulting in a bad identification. This noise was a result of the mechanical vibrations of the vehicle that were picked up by the flight controller. A vibration dampening device can be incorporated below the flight controller for better data clarity. A better tuned noise filter can also help with noise reduction.

6.4 Validate math models with test data

A LOES model for the vehicle was identified as a simpler model. While this model includes the dynamics of the vehicle for a wide range of frequencies, it does not account for higher order dynamics such as servos, rotor flapping, motor vibrations, and motor lag. This would increase the complexity and fidelity of the model, but it would include more information about the vehicle dynamics. Using JIO module within CIFER instead of FRESPID could be useful for higher order identification.

For the purposes of flight testing, only manual sweeps were conducted due to testing area restrictions. This reduced the maximum value of frequency for the identification as the pilot could only move his stick as humanly possible. Using automated sweeps could provide a wider range of frequencies and a better signal-to-noise ratio.

7 Conclusions

With regards to math model development and validation, the methodology to obtain a bare airframe dynamic model was demonstrated and implemented for the PAVER vehicle. Frequency sweep testing was done for both the simulation model and on the actual vehicle. The comparison between the SCAS-off and SCAS-on identification was performed using the dynamic simulation model, and it was seen that the SCAS-off analysis resulted in an unstable system and provided bad coherence through the frequency range. However, the SCAS-on analysis proved that the system is stable, and that the frequency analysis results in good coherence for almost all the frequency ranges. Both the automated and manual sweeps were compared, and the results show that the automated sweeps provide good coherence for the simulation model. The manual sweeps for the PAVER vehicle provided good frequency response and good coherence for the frequency range of applicability. This proves that the SCAS-on identification is preferable for a vehicle when it is unstable in an open-loop design.

A low-order equivalent system of the vehicle was obtained through the frequency responses and was proved to have a low-cost function, which shows good identification and that the obtained transfer function is indistinguishable from the actual vehicle. A bare-airframe state-space model was obtained that represents the bare-airframe dynamic of the vehicle. The gains of the PID controllers were tuned for the simulation model and were optimized. These gains were used for the flight tests performed for system identification that provided gains with good tracking of the pilot inputs.

Two methodologies were developed to assist with early prediction of vehicle handling qualities cliffs. The first methodology predicts whether a given vehicle configuration has sufficient control power to perform a given task. This method was designed to be fully automated and not require a test pilot to fly the vehicle. This method could potentially predict handling qualities cliffs resulting from running out of control power (e.g. one engine out). However, its capability to predict a wider range of handling qualities cliffs resulting from control law issues and/or pilot-in-the-loop effects is very limited. These limitations led to the development of a second methodology, which generates real-time force and moment envelopes for an airplane in the longitudinal direction as the pilot is flying it, either on a simulator or during flight test. Unlike

the first method, this one does bring a pilot into the loop and therefore could be used to predict a wider range of handling qualities cliffs. In addition to alerting the pilot to an upcoming handling qualities cliff during flight test, it could help the pilot become familiar with the aircraft's flight envelope during flight simulation, which could further improve flight test safety.

NLDI controller and the control allocation process allows one to track the pilot commands with a better transient response due to the consideration of system dynamics. It basically provides the opportunity of being able to use the same control structure for different number and placing of actuators. Additionally, overactuation in the vehicle brings into question how the set of control/actuator inputs should be chosen to maintain NLDI commands and requirements. This overactuation and control allocation problem can be solved by different approaches. One is finding an optimal combination among the possible set with respect to some criteria. These criteria can be maintained by some cost functions which can be related to specific requirements, such as control minimization, power minimization, etc.

This phase saw more flight tests with the prototype vehicle, which also showcased the unique capability of the vehicle. A self-level controller was implemented for the VP2 control strategy, which led to the development of the translational controller. This controller allowed the PAVER vehicle to move around linearly without tilting, as most other quadcopter configurations do. This demonstrated the unique capability of the vehicle, which is only possible due to cyclic authority of the rotor blades. The rotor failure during flight testing was a major milestone, as this would not be possible in a conventional quadcopter configuration. The rotorcraft mechanics provided exceptional control authority even in a rotor failure scenario.

8 References

Adams, Z. (2015, December 2). *525 GKY*. (Wikimedia Commons) Retrieved January 10, 2024, from https://commons.wikimedia.org/wiki/File:525_GKY_(31495047476).jpg

(2000). *ADS-33E-PRF.* Redstone Arsenal, Alabama: United States Army Aviation and Missile Command Aviation Engineering Directorate.

Agenzia Nazionale Per La Sicurezza Del Volo. (2016). *Interim Statement - Accident occurred to a AW609 registration marks N609AG, on 30th October 2015, in Tronzano Vercellese (VC), Italy.* Agenzia Nazionale Per La Sicurezza Del Volo.

Bolender, M. A., & Doman, D. B. (2004). Method for Determination of Nonlinear Attainable Moment Sets. *Journal of Guidance, Control, and Dynamics, 27*(5).

Collins, K. B., Anderson, R., Prazenica, R., Merve Dogan, K., Hruswicki, P., Roiati, R., . . . Leal, E. P. (2023). *Integrated propulsion and controls for rotorcraft - Phase 1.* Federal Aviation Administration.

Cooper, & Harper, G. (1969). *The Use of Pilot Rating in the Evaluation of Aircraft Handling Qualities.* NASA.

Cooper, G. E., & Harper, R. P. (1986). Handling Qualities and Pilot Evaluation. *Journal of Guidance, Control, and Dynamics, 9*(5), 515-529.

Das, A., Subbarao, K., & Lewis, F. (2009). Dynamic inversion with zero-dynamics stabilisation for quadrotor control. *IET control theory & applications, vol. 3, no. 3*, (pp. 303–314).

Dikmen, I. C., Arisoy, A., & Temeltas, H. (2009). Attitude control of a quadrotor. *4th International Conference on Recent Advances in Space Technologies.*

Ducard, G. J., & Kryenbühl, P. (2020). Hexacopter Flight Performance Comparison with CCA vs. WCA Control Allocation. . *28th Mediterranean Conference on Control and Automation (MED)*, (pp. pp. 697-702).

Durham, W. C. (1993). Constrained Control Allocation. *AIAA Journal of Guidance, Control, and Dynamics, 16*(4).

Gong, A., Tischler, M. B., & Shalev-Eggert, O. (2023). Flight Dynamics, Control, and Testing of a Coaxial Rotor UAV with Folding Rotor Blades. Vertical Flight Society Forum 79.

Hoffler, K., Martos, B., Bossinger, R., & Duerksen, N. (2023). *Development and Evaluation of Mission Task Elements for Certification of Aircraft with Non-Conventional Control Interfaces.* Federal Aviation Administration.

Jaramillo, J., Yildirim, E., Koru, A. T., Yucelen, T., Pakmehr, M., Dunham, J., & Lu, G. (2022). Experimental Results on Dynamic Attitude Control Allocation for a Hexarotor Platform with Faulty Motors. *AIAA SCITECH 2022 Forum.*

Johansen, T. A., & Fossen, T. I. (2013). Control allocation — A survey. *Automatica*, (pp. 1087-1103).

Kirchengast, M. (2018). Control Allocation Tecniques for Redundantly Actuated Systems. *Graz University of Tecnology.*

Klyde, D. H., Schulze, P. C., Mitchell, D. G., Sizoo, D., Schaller, R., & McGuire, R. (2020). Mission Task Element Development Process: An Approach to FAA Handling Qualities Certification. *AIAA Aviation Forum.* Virtual Event.

Klyde, D., Schulze, C., & Pitoniak, S. (2021). *Development and Evaluation of Mission Task Elements for Certification of Aircraft with Non-Conventional Control Interfaces.* Federal Aviation Administration.

Kurttisi, A., Perera, S. M., & Dogan, K. M. (2023). An Efficient Algorithm to Determine Polynomial Trajectories and Adaptive Control of a Quadcopter. *AIAA Scitech 2023.*

Lavretsky, E., & Wise, K. (2013). Robust adaptive control," in Robust and adaptive control. *Springer*, (pp. 317–353).

Leishman, J. G. (2006). *Principles of Helicopter Aerodynamics.* Cambridge University Press.

Leonardo Helicopters. (n.d.). (New Atlas) Retrieved January 10, 2024, from Leonardo Helicopters: https://helicopters.leonardo.com/en/

Lewis, J. A., & Johnson, E. N. (2020). Limited authority adaptive control architectures with dynamic inversion or explicit model following. *AIAA Scitech 2020 Forum*, (p. 1337).

López, J.-P., López, D.-P., & Allen, M. (2023). Frequency Domain System Identification of a Small Autonomous Helicopter Using CIFER. Vertical FLight Society Forum 79.

Luukkonen, T. (2011). Modelling and control of quadcopter. . *Independent research project in applied mathematics, Espoo, 22.*

Malpica, C., & Barnes, K. (2023). Handling Qualities of Multirotor RPM-Controlled Electric-Vertical Take-Off and Landing (eVTOL) Aircaft for Urban Air Mobility (UAM). Vertical Flight Society.

Malpica, C., & Withrow-Maser, S. (2020). Handling Qualities Analysis of Blade Pitch and Rotor Speed Controlled eVTOL Quadrotor Concepts for Urban. *VFS International Powered Lift Conference.* San Jose, CA.

Marks, A., Whidborne, J., & Yamamoto, I. (2012). Control allocation for fault tolerant control of a VTOL octorotor. *UKACC International Conference on Control Proceedings of the 2012*, (pp. 357-362).

McKillip, Jr., R., Wachspress, D., Hansman, R. J., Sizoo, D., Stadtmueller, T., & Dellmyer, D. (2023). Control Power Margin as a Certification Consideration for Distributed Electric Propulsion (DEP) Aircraft. *Vertical Flight Society's 79th Annual Forum & Technology Display.* West Palm Beach, FL, USA.

Mitchell, D. G., Klyde, D. H., Shubert, M. W., Sizoo, D., & Schaller, R. (2022). Testing for Certification of Urban Air Mobility Vehicles. *AIAA SciTech Forum.* San Diego: AIAA.

Nadell, S., Berger, T., DiMarco, C., & Lopez, M. (2022). System Identification and Stitched Modeling of the ADAPT™ Winged Compound Helicopter Scaled Demonstrator. Vertical Flight Society Forum 78.

Nascimento, P., & Saska, M. (2019). Position and attitude control of multi-rotor aerial vehicles: A survey. *Annual Reviews*, (pp. 129–146).

National Transportation Safety Board. (2018). *Aviation Investigation Final Report DCA16FA199.* National Transportation Safety Board.

NAVAIR. (2020, February 5). *First Navy V-22 Arrives in Patuxent River*. (NAVAIR News) Retrieved January 10, 2024, from https://www.navair.navy.mil/news/First-Navy-V-22-arrives-Patuxent-River/Wed-02052020-1141

Niemiec, R., Gandhi, F., Lopez, M., & Tischler, M. (2020). System Identification and Handling Qualities Predictions of an eVTOL Urban Air. Vertical Flight Society Forum 76.

Oppenheimer, M., Doman, D., & Bolender, M. (n.d.). Control Allocation of Overactuated Systems. *14th Mediterain* .

Padfield, G. (2018). *Helicopter Flight Dynamics: Including a Treatment of Tiltrotor Aircraft.* John Wiley & Sons.

Pei, J., Bassett, G. Z., Grisham, J., Finch, P., Toniolo, M., Miller, L., & Pamadi, B. (2018). Generic Control Allocation Toolbox for Preliminary Vehicle Design. *2018 Modeling and Simulation Technologies Conference.* Atlanta.

Peters, D. A., & HaQuang, N. (1988). Dynamic Inflow for Practical Applications. *Journal of the American Helicopter Society, 33*.

Razvi, S., Collins, K., Anderson, R., & Agrawal, S. (2023). Development of Control Laws for a Large Multi-Rotor eVTOL Using RPM, Collective, and Cyclic Control Allocation Methods. Vertical Flight Society.

Roiati, R., Collins, K., & Anderson, R. (2023). Development and Performance Evaluation of a Multi-Rotor eVTOL Using RPM, Collective, and Cyclic Control in Failure State. Vertical Flight Society.

Rothlaar, P. M., Murphy, P. C., Bacon, B. J., Gregory, I. M., Grauer, J. A., Busan, R. C., & Croom, M. A. (2014). NASA Langley Distributed Propulsion VTOL Tilt-Wing Aircraft Testing, Modeling, Simulation, Control, and Flight Test Development. *AIAA Aviation Technology, Integration and Operations (ATIO) Conference.* Atlanta.

Schulze, P. C., Klyde, D. H., Mitchell, D. G., Sizoo, D., Schaller, R., & McGuire, R. (2020). Mission Task Element Development Process: An Approach to FAA Handling Qualities Certification. *AIAA Aviation Forum.* American Institute of Aeronautics and Astronautics.

Shin, Y. (2005). Neural network based adaptive control for nonlinear dynamic regimes. *Georgia Institute of Technology.*

Singh, P. (2023). Flight Dynamics and Control of the Butterfly eVTOL Aircraft in Hover. Vertical Flight Society.

Söpper, M., Zhang, J., & Holzapfel, F. (2021). Attainable Moment Set Optimization to Support Configuration Design: A Required Moment Set Based Approach. *Applied Sciences, 11*(8).

Söpper, M., Zhang, J., Bähr, N., & Holzapfel, F. (2021). Required Moment Sets: Enhanced Controllability Analysis for Nonlinear Aircraft Models. *Applied Sciences, 11*(8).

Tischler, M. B., & Remple, R. K. (2012). *Aircraft and Rotorcraft System Identification: Engineering Methods with Flight Test Examples.* AIAA.

Tischler, M. B., Berger, T., Ivler, C. M., Mansur, M. H., Cheung, K. K., & Soong, J. Y. (2017). *Practical Methods for Airfract and Rotorcraft Flight Control Design: An Optimization-Based Approach.* AIAA.

Tischler, M., Blanken, C., Ivler, & Christina. (n.d.). *Aeronautical Design Standard-33E(PRF).*

United States Army. (2000). ADS-33E-PRF. Redstone Arsenal, AL: United States Army Aviation and Missile Command Aviation Engineering Directorate.

United States Department of Defense. (2004). *Flying Qualities of Piloted Aircraft, MIL-STD-1797B.* United States Department of Defense.

Vertical Flight Society. (2023, October 10). *VFS Electric VTOL Directory Hits 900 Concepts*. Retrieved from Electric VTOL News by the Vertical Flight Society: https://evtol.news/news/vfs-electric-vtol-directory-hits-900-concepts

Walter, A., McKay, M., Niemiec, R., & and Gandhi, F. (2022). Hover Dynamics & Flight Control of a UAM-Scale Quadcopter with Hybrid RPM & Collective Pitch Control. *Proceedings of the Vertical Flight Society 78th Annual Forum,.*

Walter, A., Mckay, M., Niemiec, R., Gandhi, F., & Berger, T. (2023). Hover Dynamics and Flight Control of a UAM-Scale Quadcopter with Hybrid RPM and Collective Pitch Control. *Journal of the American Helicopter Society.*

Walter, A., McKay, M., Niemiec, R., Gandhi, F., & Ivler, C. (2020). Hover Handling Qualities of Fixed-Pitch, Variable-RPM Quadcopters with Increasing Rotor Diameter. *VFS 76th Annual Forum & Technology Display.* Virginia Beach, VA.

Wise, K. A., Brinker, J. S., Calise, A. J., Enns, D. F., Elgersma, M. R., & Voulgaris, P. (1999). Direct adaptive reconfigurable flight control for a tailless advanced fighter aircraft. *International Journal of Robust and Nonlinear Control, vol. 9, no. 14*, (pp. 999–1012).